FEDERAL UNIVERSITY OF JUIZ DE FORA
GRADUATE PROGRAM IN COMPUTATIONAL MODELING

Noemi Zeraick Monteiro

Mathematical biology models incorporating memory kernels via ordinary, delay, and fractional differential equations

Juiz de Fora

2026

Noemi Zeraick Monteiro

Mathematical biology models incorporating memory kernels via ordinary, delay, and fractional differential equations

Thesis submitted to the Graduate Program in Computational Modeling at the Federal University of Juiz de Fora, as partial fulfillment of the requirements for the degree of Doctor in Computational Modeling. Concentration area: Applied Mathematics.

Advisor: Prof. Dr. Sandro Rodrigues Mazorche

Coadvisor: Prof. Dr. Rodrigo Weber dos Santos

Juiz de Fora

2026

Noemi Zeraick Monteiro

Mathematical biology models incorporating memory kernels via ordinary, delay, and fractional differential equations

Tese apresentada ao Programa de Pós-Graduação em Modelagem Computacional da Universidade Federal de Juiz de Fora como requisito parcial à obtenção do título de Doutora em Modelagem Computacional. Área de concentração: Modelagem Computacional.

Aprovada em 26 de março de 2026.

BANCA EXAMINADORA

Prof. Dr. Sandro Rodrigues Mazorche - Orientador e Presidente da Banca
Universidade Federal de Juiz de Fora

Prof. Dr. Rodrigo Weber dos Santos - Coorientador e Membro titular interno
Universidade Federal de Juiz de Fora

Prof. Dr. Rubens de Figueiredo Camargo - Membro titular externo
Universidade Estadual Paulista "Júlio de Mesquisa Filho" - Câmpus Bauru

Prof. Dr. Alfonso Bueno-Orovio - Membro titular externo
University of Oxford

Prof. Dr. Kevin Burrage - Membro titular externo
Queensland University of Technology

Prof. Dr. Grigori Chapiro - Membro titular interno
Universidade Federal de Juiz de Fora

Prof. Dr. Bernardo Martins Rocha - Membo titular interno
Universidade Federal de Juiz de Fora

Juiz de Fora, 29/03/2026.

Documento assinado eletronicamente por **Alfonso Bueno Orovio**, **Usuário Externo**, em 30/03/2026, às 12:14, conforme horário oficial de Brasília, com fundamento no § 3º do art. 4º do Decreto nº 10.543, de 13 de novembro de 2020.

Documento assinado eletronicamente por **Grigori Chapiro**, **Professor(a)**, em 30/03/2026, às 13:12, conforme horário oficial de Brasília, com fundamento no § 3º do art. 4º do Decreto nº 10.543, de 13 de novembro de 2020.

Documento assinado eletronicamente por **Rodrigo Weber dos Santos**, **Professor(a)**, em 30/03/2026, às 15:49, conforme horário oficial de Brasília, com fundamento no § 3º do art. 4º do Decreto nº 10.543, de 13 de novembro de 2020.

Documento assinado eletronicamente por **kevin burrage**, **Usuário Externo**, em 31/03/2026, às 04:33, conforme horário oficial de Brasília, com fundamento no § 3º do art. 4º do Decreto nº 10.543, de 13 de novembro de 2020.

Documento assinado eletronicamente por **Rubens de Figueiredo Camargo**, **Usuário Externo**, em 01/04/2026, às 07:36, conforme horário oficial de Brasília, com fundamento no § 3º do art. 4º do Decreto nº 10.543, de 13 de novembro de 2020.

Documento assinado eletronicamente por **Bernardo Martins Rocha**, **Professor(a)**, em 01/04/2026, às 18:11, conforme horário oficial de Brasília, com fundamento no § 3º do art. 4º do Decreto nº 10.543, de 13 de novembro de 2020.

Documento assinado eletronicamente por **Sandro Rodrigues Mazorche**, **Professor(a)**, em 01/04/2026, às 18:43, conforme horário oficial de Brasília, com fundamento no § 3º do art. 4º do Decreto nº 10.543, de 13 de novembro de 2020.

A autenticidade deste documento pode ser conferida no Portal do SEI-Ufjf (www2.ufjf.br/SEI) através do ícone Conferência de Documentos, informando o código verificador **2925646** e o código CRC **7A0E2387**.

Ficha catalográfica elaborada através do programa de geração
automática da Biblioteca Universitária da UFJF,
com os dados fornecidos pelo(a) autor(a)

Zeraick Monteiro, Noemi.
Mathematical biology models incorporating memory kernels via ordinary, delay, and fractional differential equations / Noemi Zeraick Monteiro. -- 2026.
181 p. : il.

Orientador: Sandro Rodrigues Mazorche
Coorientador: Rodrigo Weber dos Santos
Tese (doutorado) - Universidade Federal de Juiz de Fora, Instituto de Ciências Exatas. Programa de Pós-Graduação em Modelagem Computacional, 2026.

1. Memory effect. 2. Mathematical biology. 3. Electrophysiology. 4. Fractional calculus. 5. Mittag-Leffler functions. I. Rodrigues Mazorche, Sandro, orient. II. Weber dos Santos, Rodrigo, coorient. III. Título.

To my beloved family, especially Dad Jorge, Mom Laila, Brother Thiago, and Niece Abigail.

ACKNOWLEDGEMENTS

It is impossible to adequately express my gratitude to all who contributed: my family, for their love, patience, prayers, inspiration, and unconditional support; my extended family of friends, helpers, and brothers and sisters in Christ, who lovingly support me every day; Rodrigo and Sandro, my advisors in the last four and sixteen (!) years, respectively, to whom I can never fully repay my debt of gratitude; my defense committee, for honoring me with their time, corrections, and suggestions; my colleagues and professors, who are part of my life and my education; our funders — CAPES, FAPEMIG, CNPq, and UFJF; the giants referenced in the bibliography; you who are reading this right now. To everyone involved, thank you very much. Paraphrasing C. S. Lewis, good relations are the instrument by which God reveals to each the beauties of all the others.

My Lord made all this possible. *"To God only wise, be glory through Jesus Christ for ever. Amen." Romans 16:27*

“**Three verses that describe my career well are Psalm 111:2-4:** *The works of the Lord are great, sought out of all them that have pleasure therein. His work is honorable and glorious: and his righteousness endures for ever. He has made his wonderful works to be remembered: the Lord is gracious and full of compassion.*”

James P. Keener, recognized as a pioneer in mathematical physiology and cardiology.

ABSTRACT

Biological systems frequently exhibit non-exponential dwell times and delay distributions. While chains of ordinary differential equations, delay systems, and fractional calculus formulations have been used to incorporate memory effects, a unified and biologically consistent framework connecting these paradigms remains lacking.

This thesis presents a general memory kernel formulation that integrates ordinary, delayed, and fractional differential systems into a unified structure. By representing memory using integral kernels with statistically interpretable distributions, the study shows that these modeling approaches lie on a continuous spectrum determined by the shape of the time-delay kernel, while retaining physical interpretability. In particular, the generalized gamma Mittag-Leffler distribution is introduced as a versatile kernel that can capture both exponential and heavy-tailed fractional characteristics, while also describe statistical moments.

The proposed structure is explored analytically and numerically in several applications, including population dynamics, epidemiology, pharmacokinetics, and electrophysiology. It is demonstrated that memory kernels induce complex behaviors in simple models. These effects can lead to phenomena such as multi-wave epidemic dynamics, and oscillations in cardiac action potentials, known as early afterdepolarizations. Rather than acting as an external periodic forcing, memory reshapes the phase-space geometry of trajectories, thus modulating the dynamics.

By recognizing memory in biological models as more than a mathematical adjustment, but as a structural expansion of phase space through hidden variables and degrees of freedom, this thesis clarifies the relationship between Markovian and non-Markovian systems. Furthermore, it establishes consistent and physically grounded fractional formulations, contributing to the rigorous application of fractional calculus in biological modeling and thereby reducing common sources of misinterpretation. Taken together, these results provide a unified basis for the analysis of complex behaviors across diverse disciplines.

Keywords: Memory Effect. Mathematical Biology. Electrophysiology. Fractional Calculus. Mittag-Leffler functions.

RESUMO

Sistemas biológicos frequentemente exibem tempos de permanência e distribuições de atraso (delay) não exponenciais. Embora cadeias de equações diferenciais ordinárias, sistemas com atraso e formulações de cálculo fracionário tenham sido utilizados para incorporar efeitos de memória, ainda carece de um arcabouço unificado e biologicamente consistente que conecte esses paradigmas.

Esta tese apresenta uma formulação geral baseada em núcleos de memória que integra sistemas diferenciais ordinários, com atraso e fracionários em uma estrutura unificada. Ao representar a memória por meio de núcleos integrais com distribuições estatisticamente interpretáveis, o estudo mostra que essas abordagens de modelagem situam-se em um espectro contínuo determinado pela forma do núcleo de atraso no tempo, ao mesmo tempo em que preservam a interpretabilidade física. Em particular, a distribuição gama Mittag-Leffler generalizada é introduzida como um núcleo versátil capaz de capturar tanto características exponenciais quanto comportamentos fracionários de cauda pesada, além de permitir uma interpretação em termos de momentos estatísticos.

A estrutura proposta é explorada analítica e numericamente em diversas aplicações, incluindo dinâmica de populações, epidemiologia, farmacocinética e eletrofisiologia. Demonstra-se que núcleos de memória induzem comportamentos complexos em modelos simples. Esses efeitos podem levar a fenômenos como dinâmicas epidêmicas com múltiplas ondas e oscilações em potenciais de ação cardíacos, conhecidas como pós-despolarizações precoces. Em vez de atuar como forçante periódico externo, a memória reorganiza a geometria do espaço de fases das trajetórias, modulando, assim, a dinâmica do sistema.

Ao reconhecer a memória em modelos biológicos como algo além de um simples ajuste matemático — isto é, como uma expansão estrutural do espaço de fases por meio de variáveis ocultas e graus de liberdade adicionais — esta tese contribui para o esclarecimento da relação entre sistemas markovianos e não markovianos. Além disso, estabelece formulações fracionárias consistentes e fisicamente fundamentadas, contribuindo para a aplicação rigorosa do cálculo fracionário na modelagem biológica e, consequentemente, reduzindo fontes comuns de má interpretação. Em conjunto, esses resultados fornecem uma base unificada para a análise de comportamentos complexos em diferentes áreas do conhecimento.

Palavras-chave: Efeito memória. Biologia matemática. Eletrofisiologia. Cálculo fracionário. Funções de Mittag-Leffler.

LIST OF FIGURES

LIST OF TABLES

CONTENTS

1 INTRODUCTION

Many biological systems are not purely “state-determined” by the present: their current response can depend on how they were driven in the past. This history dependence is often described under the umbrella of memory effects. In particular settings, the phenomenon in which the current state of a system depends not only on present conditions but also on past history is called hysteresis (5). Hysteresis and related memory effects appear across scales (6), from ecosystems and populations (7, 8), to epidemiology (9), and to molecular and cellular processes (10).

In biological and population models, memory implies that cells, molecules, organisms, or entire communities retain information about past events in a way that influences present and future dynamics. The main goal of this thesis is to unify and complement biologically relevant modeling frameworks for memory, emphasizing approaches that remain interpretable and usable in data-driven applications. A central perspective adopted throughout this thesis is that such memory effects can be systematically represented through memory kernels, which encode how past states influence present dynamics.

Two main mechanisms of memory motivate this work, both of which can be naturally expressed within a kernel-based framework. The first is non-exponential dwell times. In many real systems, waiting times in a state (*e.g.*, the time to recovery, the time until loss of immunity, or residence time in a binding site) are not well described by an exponential distribution, and therefore cannot be captured by memoryless (Markovian) dynamics. This perspective already appears implicitly in pioneering epidemiological modeling through explicit dependence on the time since infection, as in the works of Kermack and McKendrick (11), and in early population dynamics ideas associated with Volterra (12). Despite the dominance of Markovian models due to their mathematical tractability, several methods have been developed to address non-Markovian regimes. For example, in (13) a non-Markovian SIS epidemic model on complex networks was proposed with general (arbitrary) infectivity and recovery functions; numerical results demonstrated its relevance by fitting first-wave COVID-19 data in Italy, Spain, and the UK (14). Outside epidemiology, non-exponential dwell times also play an important role. Single-particle tracking experiments, for instance, have reported truncated power-law distributions of residence times for DNA-binding species in living cells (15). From a modeling perspective, such non-exponential waiting times naturally lead to distributed memory kernels, where the influence of past states is weighted according to the underlying dwell-time distribution.

The second major source of memory is the presence of delays. In population dynamics, delays may arise from maturation or gestation, food storage, threshold effects, and reaction times (16). Delays have also been linked to mechanisms such as feeding times and hunger effects in predator–prey interactions (17), as well as the time needed for resources to regenerate (*e.g.*, vegetation recovery in grazing systems) (18). A key qualitative fact is that delays can fundamentally alter system behavior: stability, instability, and the emergence of periodic or chaotic oscillations may depend critically on the delay values (19). A broad overview of such impacts across population dynamics, epidemiology, physiology, immunology, neural networks, and cell kinetics is discussed in (20). In electrophysiology, memory-like effects have also been discussed in the context of voltage-gated ion channels, which are transmembrane proteins that open and close in response to changes in membrane voltage (21). In the kernel-based framework, general delay effects can be interpreted as particular cases of distributed memory kernels. This provides a concrete setting in which the same kernel-based formalism can be used to reinterpret classical electrophysiological models in terms of effective memory.

The central claim of this thesis is that memory kernels provide a unifying mathematical language for these modeling paradigms. Kernel-based formulations naturally connect renewal/waiting-time descriptions, delay differential equations, Volterra-type integral models, and fractional-order dynamics. Within this perspective, classical ordinary differential equations, delay differential equations, distributed-delay models, and fractional formulations arise from distinct choices of the memory kernel. This unifying viewpoint is developed not only for population and epidemiological systems, but also for computational electrophysiology, where macroscopic conductances can exhibit effective dependence on past voltage trajectories even when microscopic gating is modeled as a memoryless Markov process. Computational physiology is an interdisciplinary field that develops and uses computational models to describe and simulate biological functions. The branch of physiology that investigates the electrical properties of cells and tissues is electrophysiology.

Specific objectives of this thesis include:

- Develop and consolidate fractional-calculus-based approaches for non-exponential waiting times and distributed delays, while preserving physical units and interpretability.
- Establish explicit connections between ordinary, delay, and fractional differential models through a unified kernel-based representation.
- Perform analytical and numerical studies, fit real data, and interpret the biological meaning of memory effects in concrete applications.
- Investigate how different choices of memory kernels translate into electrophysiological properties in neuronal and cardiac models.

1.1 STRUCTURE OF THE THESIS

Chapter 2 introduces a modeling approach derived from non-exponential waiting-time distributions, particularly Mittag-Leffler-based, emphasizing physical consistency and interpretability. We discuss mean waiting times and asymptotic behavior and apply the framework to propose a new fractional SIRS model. This model describes a population of Susceptible, Infectious, and Recovered individuals with temporary immunity so that recovered individuals eventually return to the susceptible class. Numerical experiments illustrate the resulting dynamics.

Next, Chapter 3 establishes the core theoretical result of the thesis: it demonstrates that classical ODE, discrete-delay, and fractional models arise as special cases of a unified framework based on a gamma Mittag–Leffler memory kernel, starting from logistic growth. We classify kernel regimes, analyze asymptotic behavior, and present supporting numerical simulations. The resulting fractional formulations preserve dimensional consistency and explicitly link parameters to past states. The approach is validated by reproducing COVID-19 infection dynamics in Australia, Brazil, and Peru.

Building on this foundation, Chapters 4 and 5 apply the constructed framework to electrophysiological systems. These chapters explore how different choices of memory kernels translate into distinct physiological behaviors.

Voltage-gated ion channels transition between conduction states in response to changes in voltage, shaping ionic currents and the action potential (AP). While microscopic gating is often represented as a Markov process, population-level conductances exhibit an effective dependence on past voltage trajectories (21), motivating delay and kernel-based formulations. In Chapter 4, we propose a simple AP model formulated as a single delay differential equation (DDE) driven by sodium and potassium conductances. The Hodgkin-Huxley study of the squid giant axon is a foundational neuronal model in electrophysiology (22). This model accurately replicates essential features of a standard Hodgkin-Huxley AP, such as sodium and potassium conductance profiles, responses below and above the threshold, and the all-or-nothing principle. This principle describes a binary response in which the stimulus either induces a complete depolarization ("all") with a waveform that remains mostly unchanged regardless of the stimulus strength or has no effect ("nothing"). The delay-based formulation also enables explicit analytical approximations for strength–interval relations and for the relationship between spike frequency and sustained stimulus amplitude. Finally, by varying the memory kernel, we connect the discrete-delay description to other representations of macroscopic channel memory, including linear-chain (Erlang) ODE systems, continuous-time Markov chain (CTMC) models, and fractional formulations.

Chapter 5 applies kernel-based memory to cardiac phenomenological models. In cardiac electrophysiology, early afterdepolarizations (EADs) are abnormal depolarizations during the AP plateau and are associated with arrhythmia risk. Standard memoryless two-variable phenomenological models often fail to generate EADs. We develop a framework that extends Hodgkin–Huxley-type formulations using gamma Mittag–Leffler distributed delays, and we show how this mechanism can induce EAD-like oscillations in generalized versions of the FitzHugh–Nagumo (cardiac adaptation (23)), Mitchell–Schaeffer (24), and Karma (25) models. The emergence of oscillations is analyzed through the fractional parameters and through the mean and variance of the memory kernels, together with stability observations and numerical results.

Chapters 6 and 7 synthesize the theoretical and practical implications of this approach, discussing methodological principles, limitations, and future directions. Chapter 6 presents general discussions on good practices and common pitfalls in fractionalization, kernel modeling, and biological applications. Chapter 7 addresses limitations and outlines future directions, including partially developed results on the generation of EADs through geometric modifications of cardiac models and on the relationship between complex distributed delays and ODE formulations via phase-type distributions. Finally, Chapter 8 presents the concluding remarks.

The thesis includes five appendices covering: proofs of the theorems stated in Section 2.1; positivity and equilibrium results for a fractional Susceptible-Infectious-Recovered (SIR) model (26); additional analysis and simulations for the general logistic structure in Chapter 3 (including a numerical study of the gamma Mittag–Leffler PDF kernel); further EAD examples in the generalized FitzHugh–Nagumo model; and a geometric justification for the Mitchell–Schaeffer and Karma adaptations used to generate EADs.

1.2 CONTRIBUTIONS

The PhD candidate's research resulted in the following papers and presentations during the program period:

Full articles published in journals

1. MONTEIRO, N. Z.; MAZORCHE, S. R. Limitations and applications in a fractional Barbalat's Lemma. **Fractional Calculus and Applied Analysis**, v. 26, n. 1, p. 253-275, 2023.

2. CAMMAROTA, D.; MONTEIRO, N. Z.; MENEZES, R.; FORT, H.; SEGURA, A. M. Lotka–Volterra model with Allee effect: equilibria, coexistence and size scaling of maximum and minimum abundance. **Journal of Mathematical Biology**, v. 87, n. 6, p. 82, 2023.

3. MONTEIRO, N. Z.; MAZORCHE, S. R.; SANTOS, R. W. Positivity and equilibrium in a fractional SIR model with Mittag-Leffler memory. **Trends in Computational**

and Applied Mathematics, v. 25, p. e01789, 2024.

4. MONTEIRO, N. Z.; PEREIRA, R. R.; ROCHA, B. M.; SANTOS, R. W.; MAZORCHE, S. R.; LOULA, A. F. D. A novel second-order ADI Scheme for solving epidemic models with cross-diffusion. **Journal of Computational Science**, v. 81, p. 102341, 2024.
5. MONTEIRO, N. Z.; SANTOS, R. W.; MAZORCHE, S. R. Constructive fractional models through Mittag-Leffler functions. **Computational & Applied Mathematics**, v. 43, n. 4, 2024.
6. MONTEIRO, N. Z.; SANTOS, R. W.; MAZORCHE, S. R. Bridging the gap between models based on ordinary, delayed, and fractional differential equations through integral kernels. **Proceedings of the National Academy of Sciences**, v. 121, n. 19, p. e2322424121, 2024.
7. MONTEIRO, N. Z.; SANTOS, R. W.; MAZORCHE, S. R. Ion channel memory drives cardiac early afterdepolarizations in fractional models. **Mathematics**, v. 13, n. 10, p. 1585, 2025.
8. MONTEIRO, N. Z.; SANTOS, R. W. Revisiting the modeling of cell electrophysiology using a delay-based equation. **Nonlinear Dynamics**, 114, 521, 2026.

Published/organized books or editions

1. CAMARGO, R. F.; OLIVEIRA, E. C.; MONTEIRO, N. Z. **Equações fracionárias: métodos analíticos e numéricos**. Sociedade Brasileira de Matemática, 2025.

Full papers published in conference proceedings

1. MONTEIRO, N. Z.; MAZORCHE, S. R. Lema de Barbalat fracionário: limitações e aplicações. **Proceeding Series of the Brazilian Society of Computational and Applied Mathematics**, v. 9, n. 1, 2022.
2. COUTO, G. M.; MONTEIRO, N. Z.; SANTOS, R. W. Accelerating Simulations of Cardiac Arrhythmias through Robust Numerical Techniques and Parallel Computing. In: **Simpósio Brasileiro de Computação Aplicada à Saúde (SBCAS)**. SBC, 2023. p. 72-77. **(Award-winning work at SBCAS 2023)**
3. MAZORCHE, S. R.; MONTEIRO, N. Z. Pontos de equilíbrio e estabilidade em um modelo SIR fracionário construído com funções de Mittag-Leffler. **Proceeding Series of the Brazilian Society of Computational and Applied Mathematics**, v. 10, n. 1, p. 2-7, 2023.

4. COUTO, G. M., MONTEIRO, N. Z., ROCHA, B. M., SANTOS, R. W. Accelerating the Simulations of Cardiac Arrhythmia with a Second-Order Numerical Method and High-Performance Computing. In: **International Conference on Computational Science and Its Applications**. Cham: Springer Nature Switzerland, 2023. p. 103-113.

Abstracts published in conference proceedings and posters

1. MELO, M. P.; MONTEIRO, N. Z.; CAMARGO; R. F. Equações Diferenciais Fracionárias com Ajuste Dimensional. **Proceeding Series of the Brazilian Society of Computational and Applied Mathematics**, v. 10, n. 1, 2023.
2. MONTEIRO, N. Z.; MAZORCHE, S. R *et al.* **Semana Matemática & Estatística UFJF - Dia do Cálculo Fracionário.** Federal University of Juiz de Fora, Brazil, 2024. (Several posters about our work were displayed)

Conference oral presentations

1. MONTEIRO, N. Z.; MAZORCHE, S. R. Novel quarantine and behavioral fractional SIR-type models. In: **Brazilian Symposium on Fractional Calculus**, 2024. Presented by N. Z. MONTEIRO.
2. MONTEIRO, N. Z.; DOS SANTOS, R. W. Computational Electrophysiology. **Global July**, Federal University of Juiz de Fora, Brazil, 2024. Presented by R. W. dos SANTOS and N. Z. MONTEIRO.
3. MONTEIRO, N. Z.; DOS SANTOS, R. W.; MAZORCHE, S. R. Modeling Ion Channel Delays with Fractional Calculus Reveals Early Afterdepolarizations Mechanisms. 52^{nd} **international Computing in Cardiology conferecence (CinC)**, São Paulo, Brazil, 2025. Presented by N. Z. MONTEIRO.

Although several chapters are based on published works, the thesis is organized as a coherent progression centered on a unified modeling perspective. This structure is intended to guide the reader from fundamental concepts to applications, while maintaining a consistent mathematical and conceptual pillar throughout the thesis.

1.3 BACKGROUNDS

Some background information about memory kernels, fractional calculus, and electrophysiology is provided in the following sections.

1.3.1 Memory Kernels

Let $f(t)$ be a signal, and $w(t)$ a variable that depends on the history of $f(t)$. We can generally express $w(t)$ as a Volterra convolution (16):

$$w(t) = \int_0^t \kappa(s)f(t-s)ds = \int_0^t \kappa(t-s)f(s)ds; \qquad \kappa(t) \geq 0, \int_0^\infty \kappa(s)ds = 1. \tag{1.1}$$

The kernel κ acts as a weight for the past of the signal f. For example, with a Dirac delta centered at zero, we have $w(t) = \int_0^t \delta_0(t-s)f(s)ds = f(t)$, and the past does not influence $w(t)$. If we use a Dirac delta centered at τ, we obtain $w(t) = f(t-\tau)$, a discrete delay.

Systems of ordinary differential equations (ODEs) can implicitly employ exponential memory kernels of type $\kappa(t) = \exp\left(-t/\tau\right)/\tau$. Based on (27), $w(t)$ formulated as:

$$w(t) = \int_0^t \frac{1}{\tau} \exp\left(-\frac{1}{\tau}(t-s)\right) f(s)ds + w_0 \exp\left(-t/\tau\right) \tag{1.2}$$

is equivalent to the ODE:

$$\frac{dw}{dt} = \frac{f(t) - w}{\tau}. \tag{1.3}$$

The solution of this differential equation converges continuously to f with a delay characterized by the time constant τ.

The integral form $\int_0^t \kappa(s)f(t-s)ds = \int_0^t \kappa(t-s)f(s)ds$ can also be utilized in stochastic processes, where κ is a permanence probability kernel. For instance, consider the density function of the random variable X, which represents the waiting time of the individuals or materials represented by $y(t)$ in the equation:

$$y'(t) + ry(t) = g(y(t), t), \qquad y(0) = y_0, \qquad r > 0. \tag{1.4}$$

It can be expressed as:

$$f(t;r) = \begin{cases} re^{-rt}, & t \geq 0, \\ 0, & t < 0, \end{cases} \tag{1.5}$$

with its cumulative function given by:

$$F(t;r) = \begin{cases} 1 - e^{-rt}, & t \geq 0, \\ 0, & t < 0. \end{cases} \tag{1.6}$$

As X has an exponential distribution, then its conditional probability follows:

$$\Pr(X > s + t \mid X > s) = \Pr(X > t) \text{ for all } s, t \geq 0. \tag{1.7}$$

In fact, we have:

$$\Pr(X > s + t \mid X > s) = \frac{\Pr(X > s + t \cap X > s)}{\Pr(X > s)} = \frac{e^{-r(s+t)}}{e^{-rs}} = e^{-rt}. \tag{1.8}$$

This property is related to the Markovian memoryless property, where the next state of a process depends only on the present state and not on past states. If the interarrival or waiting times are not exponentially distributed, then we have a non-Markovian model (28).

The kernel framework highlights how delays and memory kernels offer a unified and flexible foundation for describing a wide spectrum of stochastic or deterministic biological dynamics within a unified formalism. Indeed, the kernel modeling viewpoint serves as a connection between classical ODE systems with exponential kernels, chain-trick representations with Erlang/hypoexponential kernels, CTMC-based models with phase-type kernels, and fractional formulations with heavy-tailed or multimodal kernels.

1.3.2 Fractional Calculus

Two powerful and extensively studied methods for incorporating the influence of the past into mathematical models are DDEs and fractional differential equations (FDEs).

FDEs provide a natural framework for incorporating past information into mathematical models. Unlike classical integer-order equations, FDEs involve nonlocal fractional derivatives that inherently encode memory effects. This nonlocality enables the influence of past states to persist in the present dynamics, making FDEs particularly suitable for systems with memory (5, 29).

In this setting, the order of the derivative determines the shape and intensity of memory. For example, the contribution of past times in operators with fractional orders $\alpha \in (0, 1]$ admits a statistical interpretation (5). Another geometric consequence of fractional derivatives is that the resulting trajectories are non-autonomous and may exhibit self-intersections in the phase space.

Often, a fractional model is designed in the so-called *ad hoc* manner: a classical model is generalized by allowing the integer order of the derivative to be arbitrary. However, this practice can lead to some physical misinterpretation, and previous works study ways to construct fractional models with biological meaning (30, 31, 32, 33). From a modeling perspective, the intrinsic relationship between changing kernels in integral equations and the emergence of fractional models is often overlooked. This gap does not stem from a lack of solid theory. In fact, at the turn of the 20th century, prominent researchers possessed profound knowledge of fractional calculus functions and operators, as well as integral equations. Notably, there was a significant correspondence between the Swedish mathematician Gösta Mittag-Leffler and his colleague Vito Volterra over nearly forty years (34). Mittag-Leffler was also E. I. Fredholm's doctoral advisor, and the most commonly used linear integral equations belong to the integral equations of Fredholm or

Volterra (35). In the late 20th century, comprehensive books such as (36) expanded the theory in FC and integral equations. General operators in FC research were discussed in works such as (37, 38, 39, 40). Additionally, significant advances in operational calculation for general fractional derivatives with Sonine kernels are recently outlined in works such as (41, 42). Notably, the fractional Poisson process and Mittag-Leffler distributed waiting times have been studied by researchers such as (43, 44, 45, 46, 47), and related references. However, a broader constructive theory is not commonly discussed.

1.3.2.1 Preliminaries

Basic definitions and results in fractional calculus (FC) are presented below, and are based on classical references such as (48, 49, 36, 50, 51, 52). Consider $[a, b]$ a real interval and α be a real number such that $0 \leq n-1 < \alpha \leq n$, with $n \in \mathbb{N}$.

Definition 1.1 (Riemann-Liouville integral in finite intervals)**.** *The Riemann-Liouville integral of order α is defined to $t \in [a, b]$ as*

$$I^{\alpha}_{a+} f(t) = \frac{1}{\Gamma(\alpha)} \int_a^t (t-\theta)^{\alpha-1} f(\theta) d\theta. \tag{1.9}$$

In this work, we utilize mainly the fractional Riemann-Liouville derivative due to its analytical properties, despite the several definitions available for fractional derivatives. However, we also present the definition of the Caputo fractional derivative:

Definition 1.2 (Riemann-Liouville derivative in finite intervals)**.** *The Riemann-Liouville derivative of order α is defined to $t \in [a, b]$ as*

$$D^{\alpha}_{a+} f(t) = D^n [I^{n-\alpha}_{a+} f(t)] = \frac{1}{\Gamma(n-\alpha)} \left(\frac{d^n}{dt^n} \right) \int_a^t (t-\theta)^{n-\alpha-1} f(\theta) d\theta \,, \tag{1.10}$$

where D^n is the derivative of integer order n.

Definition 1.3 (Caputo derivative in finite intervals)**.** *The Caputo derivative of an arbitrary order α is set to $t \in [a, b]$ by:*

$${}^{C}D^{\alpha}_{a+} f(t) = I^{n-\alpha}_{a+} [D^n f(t)] = \frac{1}{\Gamma(n-\alpha)} \int_a^t (t-\theta)^{n-\alpha-1} \frac{d^n}{d\theta^n} f(\theta) d\theta \,.$$

Now, we present the Mittag-Leffler functions. The classical Mittag-Leffler function with one parameter is a generalization of the exponential function. Due to its significance in solving numerous fractional differential equations, it has earned the nickname "queen of special functions" in the field of FC, with the functions associated with it referred to as its "court" (4). Its relevance in FC is akin to the importance of the exponential function in classical calculus. Here is the definition of the three-parameter Mittag-Leffler function, also known as the Prabhakar function, and its particular cases with 1 and 2 parameters:

Definition 1.4 (Mittag-Leffler functions)**.** *Let $z \in \mathbb{C}$, and three parameters $\alpha, \beta \in \mathbb{C}$, $\rho \in \mathbb{R}$ such that $Re(\alpha) > 0, Re(\beta) > 0$, $\rho > 0$. The Mittag-Leffler function with three parameters is defined by*

$$E_{\alpha,\beta}^{\rho}(z) = \sum_{k=0}^{\infty} \frac{(\rho)_k}{\Gamma(\alpha k + \beta)} \frac{z^k}{k!}, \tag{1.11}$$

where $(\rho)_k$ is the Pochhammer symbol, defined by $(\rho)_k = \Gamma(\rho + k)/\Gamma(\rho)$.

When $\rho = 1$, we have $(\rho)_k = k!$. In this case, the two-parameter Mittag–Leffler function is recovered and denoted as $E_{\alpha,\beta}^{1}(t) = E_{\alpha,\beta}(t)$. When $\rho = \beta = 1$, we obtain the classical Mittag-Leffler function, denoted as $E_{\alpha,1}^{1}(t) = E_{\alpha,1}(t) = E_{\alpha}(t)$. The behavior of the Mittag-Leffler function $E_{\alpha}(-t^{\alpha})$, commonly used in applications, is presented in Figure 1.1. The exponential function is obtained as a particular case when $\alpha = \beta = \rho = 1$.

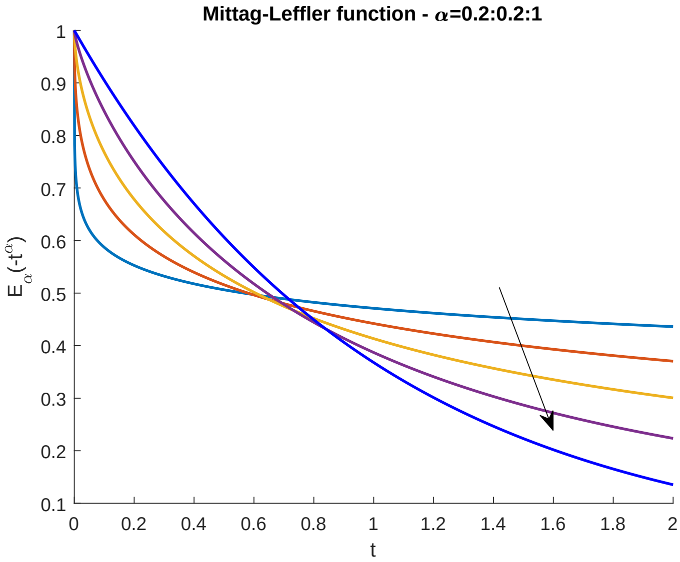

Figure 1.1 – The arrow shows the growth direction of α from 0.2 to 1 in increments of 0.2. The dark blue line represents the exponential function. Note that, when α is less than 1, the decay is faster in the beginning but slower in the end, characterizing a heavy-tailed distribution.

Next, we present the formulas for the Laplace transform:

Proposition 1.1 (Laplace transform of the Riemann-Liouville integral)**.** *The Laplace transform of the fractional Riemann-Liouville integral is given by*

$$\mathcal{L}[I_{0+}^{\alpha} f(t)](s) = s^{-\alpha} \mathcal{L}[f(t)](s). \tag{1.12}$$

Proposition 1.2 (Laplace transform of the Riemann-Liouville derivative)**.** *The Laplace transform of the fractional Riemann-Liouville derivative is given by*

$$\mathcal{L}[D_{0+}^{\alpha} f(t)](s) = s^{\alpha} \mathcal{L}[f(t)](s) - \sum_{k=0}^{n-1} s^{n-1-k} g^{(k)}(0), \tag{1.13}$$

where $g(t) = I_{0+}^{n-\alpha} f(t)$*. If* $f(t)$ *is sufficiently smooth, for instance, continuous, then* $g^{(k)}(0) = 0$ *(53), and* $\mathcal{L}[D_{0+}^{\alpha} f(t)](s) = s^{\alpha}\mathcal{L}[f(t)](s)$*.*

Proposition 1.3 (Laplace transform of the Caputo derivative)**.** *The Laplace transform of the arbitrary-order Caputo derivative is given by:*

$$\mathcal{L}[{}^{C}D_{0+}^{\alpha} f(t)](s) = s^{\alpha}\mathcal{L}[f(t)](s) - \sum_{k=0}^{n-1} s^{\alpha-1-k} f^{(k)}(0). \tag{1.14}$$

Proposition 1.4 (Laplace transform of the Mittag-Leffler function of a real variable)**.** *For* $\lambda \in \mathbb{R}$ *and* $s^{\alpha} > |\lambda|$*, the Laplace transform of the function* $t^{\beta-1}E_{\alpha,\beta}(-\lambda t^{\alpha})$*, with* $t \in [0, \infty]$ *and* $\alpha, \beta \geq 0$*, is given by:*

$$\mathcal{L}[t^{\beta-1}E_{\alpha,\beta}(-\lambda t^{\alpha})](s) = \frac{s^{\alpha-\beta}}{s^{\alpha}+\lambda}. \tag{1.15}$$

Finally, some useful Lemmas:

Lemma 1.1 (Derivatives of the Mittag-Leffler function)**.** *The following identity is valid:*

$$\frac{d^k}{dz^k} E_{\alpha,\beta}^{\rho}(z) = (\rho)_k E_{\alpha,\beta+\alpha k}^{\rho+k}(z). \tag{1.16}$$

Particularly,

$$\frac{d}{dz} E_{\alpha}(z) = E_{\alpha,1+\alpha}^{2}(z). \tag{1.17}$$

Lemma 1.2 (Riemann-Liouville derivative of Mittag-Leffler function)**.** *The Riemann-Liouville derivative and the Mittag-Leffler function follow the relation*

$$D_{0+}^{\alpha}[t^{\beta-1}E_{\mu,\beta}(\lambda t^{\mu})](x) = t^{\beta-\alpha-1}E_{\mu,\beta-\alpha}(\lambda x^{\mu}). \tag{1.18}$$

Particularly,

$$D_{0+}^{1-\alpha}[E_{\alpha}(\lambda t^{\alpha})](x) = t^{\alpha-1}E_{\alpha,\alpha}(\lambda x^{\alpha}). \tag{1.19}$$

Lemma 1.3 (Composition of operators)**.** *Let* $\alpha > 0$*. If there exists some* $\psi \in L_1[a, b]$ *such that* $f(t) = I_{a+}^{\alpha}\psi(t)$*, then*

$$I_{a+}^{\alpha}\ D_{a+}^{\alpha} f(t) = D_{a+}^{\alpha}\ I_{a+}^{\alpha} f(t) = f(t) \tag{1.20}$$

almost everywhere.

1.3.2.2 Mittag-Leffler distribution

The Mittag-Leffler distribution is a type of continuous probability distribution represented by a parameter r and an order $0 < \alpha \leq 1$. Its density function can be expressed as:

$$f_{\alpha}(t; r) = \begin{cases} r^{\alpha}t^{\alpha-1}E_{\alpha,\alpha}(-(rt)^{\alpha}) & , \ t \geq 0, \\ 0 & , \ t < 0. \end{cases} \tag{1.21}$$

Its cumulative function (54), as illustrated in Figure 2.9, is given by:

$$F_\alpha(t;r) = \begin{cases} 1 - E_\alpha(-(rt)^\alpha) & , \ t \geq 0, \\ 0 & , \ t < 0. \end{cases} \tag{1.22}$$

Figure 2.11 shows the PDF for $q = 0.6$ and $r = 1$. Figure 2.10 exhibits the corresponding cumulative distribution function, given by:

$$F_\alpha(t;r_1,r_2) = \begin{cases} 1 - E_\alpha(-(r_1 t)^\alpha)e^{-r_2 t} & , \ t \geq 0, \\ 0 & , \ t < 0. \end{cases} \tag{1.23}$$

The fractional Poisson process is an intuitive generalization of the Poisson process and is intrinsically related to the FC, as studied in (44, 45), and other references. The waiting times J_n of the fractional Poisson process satisfy the equation:

$$P(J_n > t) = E_\alpha(-\lambda t^\alpha), \tag{1.24}$$

for $0 < \alpha \leq 1$, where E_α represents the one-parameter Mittag-Leffler function. The function $E_\alpha(-\lambda t^\alpha)$ reduces to the exponential function $e^{-\lambda t}$ when $\alpha = 1$. The time between events in a fractional Poisson process follows the Mittag-Leffler distribution. The heavy-tail behavior of this distribution when $\alpha < 1$ suggests that outliers have a higher probability of occurring compared to the exponential case. This can be particularly relevant in fields like epidemiology, where a long recovery time may not be as unlikely. For $\alpha < 1$, the mean of the Mittag-Leffler distribution is infinite.

1.3.2.3 Numerical scheme

For discretization and implementation of fractional operators in MATLAB or Python, we constructed a numerical scheme similar to $L1$ (48). The time interval $[a,t]$ is discretized as $a = t_0 < t_1 < \cdots < t_n = t$, where the time steps ΔT have the same size. For the Riemann-Liouville integral and $\alpha > 1$, we perform the following discretization:

$$\begin{aligned} I_{a+}^{\alpha-1} f(t_j) &= \frac{1}{\Gamma(\alpha-1)} \int_a^{t_j} (t_j - \theta)^{\alpha-2} f(\theta) d\theta \\ &= \frac{1}{\Gamma(\alpha-1)} \left[\sum_{k=0}^{j-1} f(t_{k+1}) \left[\frac{-(t_j-\theta)^{\alpha-1}}{\alpha-1} \right] \Bigg|_{t_k}^{t_{k+1}} \right] \\ &\simeq \frac{\Delta T^{\alpha-1}}{\Gamma(\alpha)} \left[\sum_{k=0}^{j-1} f(t_{k+1}) [(j-k)^{\alpha-1} - (j-k-1)^{\alpha-1}] \right], \end{aligned} \tag{1.25}$$

where $t_i = i\Delta T + t_0$ for all $i \in \{0, 1, \cdots, n\}$.

For the Riemann-Liouville derivative and $\alpha < 1$, we perform the following discretization:

$$\begin{aligned} D_{a+}^{1-\alpha} f(t_j) &= \frac{1}{\Gamma(\alpha)}\left(\frac{d}{dt_j}\right)\int_a^{t_j}(t_j-\theta)^{\alpha-1}f(\theta)d\theta \\ &\simeq \frac{1}{\Gamma(\alpha)}\frac{\int_a^{t_{j+1}}(t_{j+1}-\theta)^{\alpha-1}f(\theta)d\theta - \int_a^{t_j}(t_j-\theta)^{\alpha-1}f(\theta)d\theta}{\Delta T} \\ &\simeq \frac{\Delta T^{\alpha-1}}{\Gamma(\alpha+1)}\left[\sum_{k=0}^{j-1} f(t_k)[(j-k+1)^\alpha - 2(j-k)^\alpha + (j-k-1)^\alpha] + f(t_j)\right]. \end{aligned} \tag{1.26}$$

1.3.3 Electrophysiology

A significant number of cells in our body rely on electrical impulses for communication and for performing essential functions such as contraction, information processing, secretion, and other vital tasks. These excitable cells include neurons, responsible for transmitting and processing information; cardiomyocytes, the heart muscle cells that regulate the heartbeat; skeletal muscle cells, which control voluntary movements; smooth muscle cells, found in organs such as the gastrointestinal tract and blood vessels, which handle involuntary movements; and certain endocrine cells that release hormones in response to electrical activity. These cells are called excitable because, when exposed to a stimulus, they respond with an electrical pulse known as an action potential (AP).

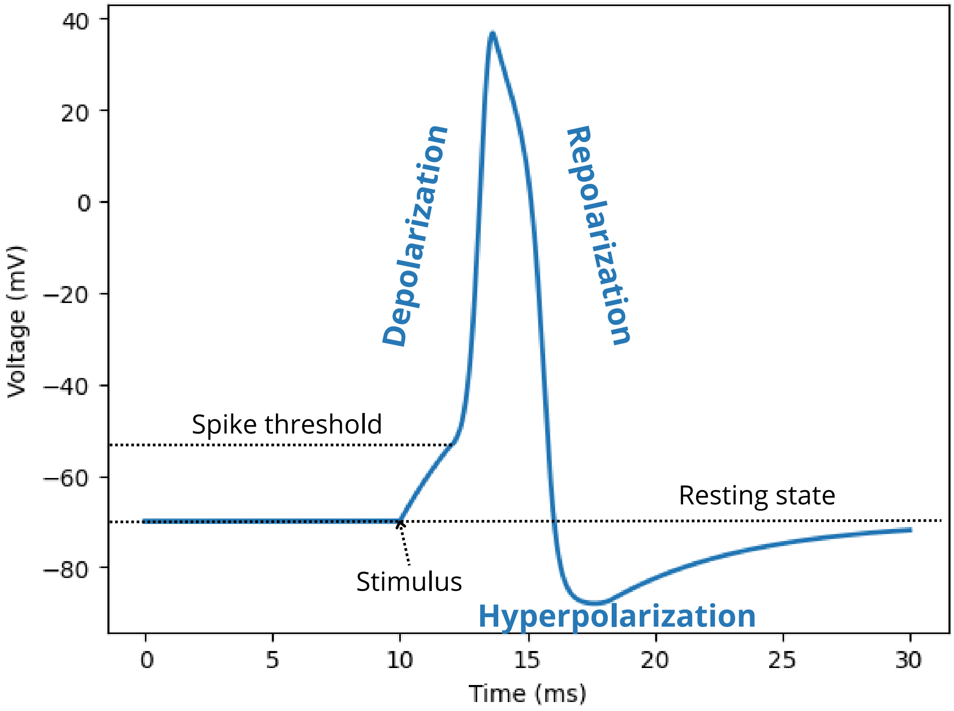

Figure 1.2 – A schematic diagram illustrating the phases of a standard neuronal AP over time.

An AP is an electrical pulse that represents the variation of the electric potential difference across the membrane over time. In this context, we denote the transmembrane electric potential by V, where $V = V_{\text{in}} - V_{\text{out}}$. Here, V_{in} represents the intracellular electric potential, while V_{out} represents the extracellular potential. Voltage-gated ion channels are essential for the generation of the AP. These ion channels are protein structures embedded within the membrane that selectively allow ions to pass through. They are highly specific, permitting only certain ions to flow from one side of the membrane to the other. For example, sodium ion channels allow sodium ions (Na^+) to pass, giving rise to a sodium current, I_{Na}. Voltage-gated channels possess electrical properties that allow them to change conformation in response to alterations in the electric field across the membrane. The gating of sodium and potassium channels is particularly essential for understanding the AP, as discussed in Chapter 4.

Figure 1.2 presents how the electric potential difference of one neuron may evolve with time to form an AP, or electric pulse. When normal electrical activity is disrupted, vital functions are compromised.

2 WAITING TIME DISTRIBUTIONS AND MITTAG-LEFFLER DECAYS

In this chapter, we present a method developed in our publication (55) for creating meaningful fractional generalizations of a wide range of differential equations, with a particular focus on compartmental models. A previous attempt in this direction was made in (56), which resulted in fractional differential compartmental systems without mass imbalance, allowing for separate integration of rates and the use of multiple orders. However, there were unresolved issues related to unit changes and physical interpretation. More recently, (57, 58) addressed these concerns by developing fractional compartmental models using continuous-time random walks (CTRW). Here, we offer a simpler approach to introducing memory effects through fractional derivatives, without requiring a strong background in stochastic processes or CTRW.

We propose to include memory effects via fractional derivatives for the ODE initial value problem:

$$y'(t) + ry(t) = g(y(t), t), \quad y(0) = y_0, \quad r > 0. \tag{2.1}$$

The most common practice for constructing the fractional version of this ODE is to replace the integer derivative with an arbitrary-order derivative, typically the Caputo derivative with an order of $\alpha \in (0, 1]$. This version is referred to as an *ad hoc* fractional model, as the change is made directly to the order of the derivative. When doing this, one may adjust the units by raising the parameters to the power of α or multiplying the fractional derivative by a time constant. Denoting g^α as the g function with constants raised to the power of α, and τ as a time constant, these two corrections, when applied to Eq. (2.1), can be summarized as:

$$^{C}D^{\alpha}_{0+}y = -r^{\alpha}y + g^{\alpha}(y, t), \quad \tau^{\alpha-1}\, {}^{C}D^{\alpha}_{0+}y = -ry + g(y, t). \tag{2.2}$$

The fractional models mentioned above expand on the original ODE model by incorporating memory effects, which can replicate important phenomena, as demonstrated in (59, 60, 61, 62, 63). However, these common *ad hoc* practices can lead to drawbacks such as mass imbalance, unit issues, problems with positivity or monotonicity, and difficulties in physical interpretation. Several of these concerns are addressed in (33, 64, 65), and related references.

To circumvent these issues, we propose a constructive modeling approach. We extend an exponential kernel to Mittag-Leffler based kernels and create meaningful fractional models that generalize the ODE in Eq. (2.1). In fact, the ODE (2.1) can also be written as an integral equation:

$$y(t) = \int_0^t e^{-r(t-\tau)} g(y(\tau), \tau) d\tau + e^{-rt} y_0, \tag{2.3}$$

where e^{-rt} is related to the decay or removal of y at the rate r. Generalizing this exponential permanence probability kernel with a Mittag-Leffler kernel $\kappa(t) = E_\alpha(-(rt)^\alpha)$, or considering two removal rates, one memoryless and another with memory, through a kernel $\kappa(t) = E_\alpha(-(r_1 t)^\alpha)e^{-r_2 t}$, we obtain comprehensive fractional models of type:

$$y' = -r^\alpha D^{1-\alpha} y + g(y,t), \quad y' = -r_1^\alpha e^{-r_2 t} D^{1-\alpha}(e^{r_2 t} y) - r_2 y + g(y,t). \tag{2.4}$$

This modeling approach maintains the physical units, the original variables, and parameters. This chapter is structured as follows: In Section 2.1, we present the proposed method and the resulting Riemann-Liouville and Caputo models. These results, obtained using Laplace transform techniques, generalize the integer order results from (66). We also analyze the asymptotic behavior of these models and the mean waiting time. In Section 2.2, we demonstrate the technique with the epidemic model SIRS and present numerical results. In Section 2.3, we examine the relationship between the method and waiting time distributions when replacing exponential kernels with Mittag-Leffler kernels.

2.1 METHODS AND RESULTS

The proposed method is applied to differential equations of the form (2.1). Hereafter, we write y instead of $y(t)$ for conciseness. These ODEs encompass exponential behavior, logistic growth, and certain master equations of compartmental models (where r can be, for instance, the recovery rate), among many important models. In physical applications, g is referred to as the disturbing function or excitation. For further study of this first-order differential equation with Laplace Transform techniques, readers can refer to the reference (66).

The ODE (2.1) is equivalent to the integral equation given by

$$y = \int_{-\infty}^{t} e^{-r(t-\tau)} g(y,\tau) d\tau + e^{-rt} c. \tag{2.5}$$

The constant c depends on the limit of y as $t \to -\infty$. When studying memory effects, it is important to ensure that all past information is known (67). Therefore, we assume that all past information until $t = 0$ is null. The initial conditions are a topic of extensive discussion, and further details can be found in (68, 69). Additionally, when constructing integral Eq. (2.3) as a known influx, it is useful to assume the presence of a unit impulse at $t = 0$. Since the preliminary relation between $g(y,t)$ and y is unknown, we follow the approach outlined in (66), obtaining Eq. (2.3).

Events such as death, birth, or recovery from a disease can be represented by the decay parameter r. In terms of waiting times, the function e^{-rT} represents the survival function, indicating the influence of age T on the event. At time T, the initial amount y_0 decays to $e^{-rT} y_0$, and for $t > 0$, any additional income introduced at a rate $g(y(t),t)$ also decays by $e^{-r(T-t)}$ at time $T > t$.

Viewing the permanence probability at age T, the term $e^{-rt}y_0$ represents the surviving individuals/material from 0 to t. The exponential distribution of waiting times adheres to the memoryless property (see Eq. (1.8)). Memory effects can be incorporated by replacing the exponential decay with a more general permanence probability kernel κ:

$$y = \int_0^t \kappa(t-\tau)g(y,\tau)d\tau + \kappa(t)y_0. \tag{2.6}$$

We assume that the functions κ and g are sufficiently regular so that y is absolutely continuous.

2.1.1 Constructing fractional models

To fractionalize Eq. (2.6), we first consider $\kappa(t) = E_\alpha(-(rt)^\alpha)$, where $\alpha \in (0,1]$. The integer-order model is recovered when $\alpha = 1$. This generalization reveals long-memory dynamics, which is discussed further in Section 2.3.

The fractional models obtained are described in the following Theorem:

Theorem 2.1. *If the kernel in Eq.* (2.6) *is given by* $\kappa(t) = E_\alpha(-(rt)^\alpha)$*, the corresponding differential model is given by:*

$$y' = -r^\alpha D^{1-\alpha}y + g(y,t), \tag{2.7}$$

in terms of the Riemann-Liouville fractional derivative.

In terms of the Caputo fractional derivative, the model can be written as:

$$^C D^\alpha y = -r^\alpha y + I^{1-\alpha}g(y,t). \tag{2.8}$$

Proof. See Appendix A. ☐

In many applications, multiple rates act simultaneously. For example, a death rate occurs alongside a recovery rate. In this scenario, we can assume that only one of the rates exhibits a long-memory effect. Therefore, we consider a kernel that is the product of a Mittag-Leffler function with a scale parameter r_1 and an exponential function with parameter r_2. In this case, $\kappa(t) = E_\alpha(-(r_1t)^\alpha)e^{-r_2t}$.

Theorem 2.2. *If the kernel in Eq.* (2.6) *is given by* $\kappa(t) = E_\alpha(-(r_1t)^\alpha)e^{-r_2t}$*, the corresponding differential model is given by:*

$$y' = -r_1^\alpha e^{-r_2t}D^{1-\alpha}(e^{r_2t}y) - r_2y + g(y,t), \tag{2.9}$$

in terms of the Riemann-Liouville fractional derivative.

In terms of the Caputo fractional derivative, the model can be written as:

$$e^{-r_2t}\,{}^C D^\alpha(e^{r_2t}y) = -r_1^\alpha y + e^{-r_2t}I^{1-\alpha}(e^{r_2t}g(y,t)). \tag{2.10}$$

Proof. See Appendix A. □

It is worth noting that $D^{1-\alpha}$ has units of time$^{\alpha-1}$ and r^{α} has units of time$^{-\alpha}$; therefore, the units are consistent.

2.1.2 Asymptotic Behavior

In the analysis of fractional differential equations, not all stability conditions have an intuitive correlation with the results of integer-order classical equations due to the nonlocality and specific features of FC (70). In the case we are studying, the equation contains two derivative orders, 1 and $1-\alpha$ (or α), which presents several difficulties in the classical analysis of equilibria. In this section, we seek equilibrium states y^* such that $y \to y^*$ as $t \to \infty$. In other words, we are studying the asymptotic behavior of the models represented by Eq. (2.7) (corresponding to Eq. (2.8)) and Eq. (2.9) (corresponding to Eq. (2.10)).

Theorem 2.3. *If $y \to y^*$ as $t \to \infty$ in Eq.* (2.7)*, then*

$$\lim_{t\to\infty} g(y,t) = 0 \tag{2.11}$$

if $\alpha < 1$.

On the other hand, if $y \to y^*$ as $t \to \infty$ in Eq. (2.8)*, then we must have:*

$$y^* = r^{-\alpha} \lim_{t\to\infty} I^{1-\alpha} g(y,t). \tag{2.12}$$

Proof. See Appendix A. □

Particularly, Eq. (2.12) implies Eq. (2.11) with additional hypotheses (71). However, these conditions are necessary but not always sufficient and may be irrelevant in certain cases. When $\alpha = 1$, the relation in Eq. (2.12) yields the integer result:

$$y^* = r^{-1} \lim_{t\to\infty} g(y,t). \tag{2.13}$$

When working with Eq. (2.9), a more significant result about asymptotic behavior is observed.

Theorem 2.4. *If $y \to y^*$ when $t \to \infty$ in Eq.* (2.9) *and Eq.* (2.10)*, then*

$$y^* = (r_1^{\alpha} r_2^{1-\alpha} + r_2)^{-1} \lim_{t\to\infty} g(y,t). \tag{2.14}$$

Proof. See Appendix A. □

We have demonstrated that if there are asymptotically stable equilibria of models (2.7) and (2.8), as well as (2.9) and (2.10), they are determined by the relations (2.11)-(2.12) and (2.14), respectively. However, the stability of these states has not been proven yet. The formal analysis of stability poses challenges, but progress can be made by utilizing the theory of Volterra integrals (see (72, 73)).

2.1.3 Mean waiting time

The mean waiting time, or expected waiting time (expectation) for an object in a dynamic system is the time the object is expected to spend before leaving the system permanently. When $r_2 > 0$, there is a finite expectation for the removal of y:

Theorem 2.5. *The mean waiting time for y in the model described by Eq.* (2.9) *or Eq.* (2.10) *is given by:*

$$\eta = \frac{r_2^{\alpha-1}}{r_2^{\alpha} + r_1^{\alpha}}. \tag{2.15}$$

It is undefined if $r_2 = 0$, i.e., the mean waiting time is not finite in the case of Eq. (2.7) *and Eq.* (2.8).

Proof. See Appendix A. □

We propose a parameter $q \in [0, 1]$ such that:

$$r_1 = qr \quad ; \qquad r_2 = (1-q)r. \tag{2.16}$$

If $q = 1$, we recover the case of Eq. (2.7). If $q = 0$, we recover the integer case because $E_\alpha(0) = 1$. With this new parameter, we have:

$$\eta = \frac{(1-q)^{\alpha-1} r^{\alpha-1}}{q^\alpha r^\alpha + (1-q)^\alpha r^\alpha} = \frac{(1-q)^{\alpha-1}}{q^\alpha + (1-q)^\alpha} \frac{1}{r}. \tag{2.17}$$

For each α, there might be a q such that $\eta = 1/r$, then the mean waiting time remains the same after fractionalization. For this, we must have:

$$(1-q)^{\alpha-1} = q^\alpha + (1-q)^\alpha. \tag{2.18}$$

Note that $q = 0$ is a trivial solution. If $q \neq 0$, we must have:

$$(1-q)^{\alpha-1} = q^{\alpha-1}, \tag{2.19}$$

from which

$$\alpha = 1 \qquad \text{or} \qquad q = 1/2. \tag{2.20}$$

Thus, for all $\alpha < 1$, the mean waiting time is the same as those of the integer case if, and only if, $r_2 = r$ and $r_1 = 0$, or $r_2 = r_1 = r/2$. Moreover, if $q \to 1$, then $\eta \to \infty$. This leads to the following Proposition:

Proposition 2.1. *In the model* (2.9)*, let* $q \in [0,1]$ *be such that* $r_1 = qr$ *and* $r_2 = (1-q)r$*. The mean time of removal, or mean waiting time, is given for* $q \in [0,1)$ *by:*

$$\eta = \frac{(1-q)^{\alpha-1}}{q^{\alpha} + (1-q)^{\alpha}} \eta_r, \tag{2.21}$$

where $\eta_r = 1/r$ *is the mean waiting time of the integer case, i.e., when* $\alpha = 1$*. If* $\alpha < 1$*,*

- $\eta = \eta_r$ *if* $q = 0$ *or* $q = 1/2$*;*
- $\eta < \eta_r$ *if* $q \in (0, 1/2)$*;*
- $\eta > \eta_r$ *if* $q \in (1/2, 1)$*;*
- $\lim_{q \to 1^-} \eta = +\infty$.

The graph in Figure 2.1 shows the behavior of η/η_r*.*

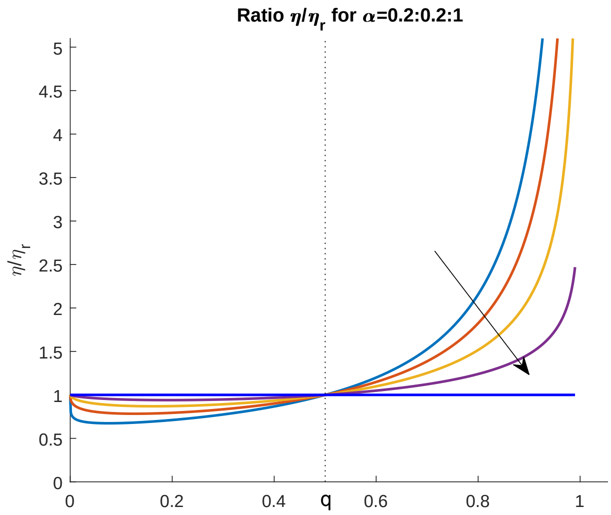

Figure 2.1 – The arrow indicates the direction of growth of α, ranging from 0.2 to 1 at regular intervals of 0.2. When $\alpha = 1$, the mean waiting time is the same for all q. As α decreases, the mean waiting time is lower for the initial values of q and quickly increases as q approaches 1. Note that $\eta = \eta_r$ for $q = 0$ and $q = 1/2$, regardless of the value of α.

2.2 APPLICATION

In this section, we demonstrate how to derive a new fractional SIRS model from the theory presented. The model considers a constant population N divided into susceptible, infectious, and recovered classes. Let $S(t)$, $I(t)$, and $R(t)$ be the populations of susceptible, infectious, and recovered with immunity classes, respectively. The model is called an SIRS model since susceptibles become infectious, recover with temporary immunity, and eventually become susceptible again once the immunity is lost.

In (74), a SIRS model with a time delay in the recovered class and a nonlinear incidence rate is proposed. The initial population that is still immune at time t is denoted as $R_0(t)$. The probability of remaining recovered and immune t time units after recovery is represented by $P(t) := 1 - H(t-\omega)$, where H is the Heaviside step function. Here, ω is a fixed period of immunity after which a recovered person reenters the susceptible compartment. This model is described as:

$$\begin{cases} S'(t) = -R_0'(t) + \gamma I(t-\omega) - \dfrac{\Omega}{N} I^p(t)S(t), \\ I'(t) = \dfrac{\Omega}{N} I^p(t)S(t) - \gamma I(t), \\ R'(t) = R_0'(t) + \gamma I(t) - \gamma I(t-\omega), \end{cases} \tag{2.22}$$

where we define $I(t) = 0$ for $t < 0$ to facilitate notation.

Here, p is a positive constant near to 1 that accounts for nonlinear incidence rate caused, for instance, by saturation or multiple exposures before infection. $1/\gamma$ represents the average infectious period, and Ω is the contact rate. We introduce a memory effect into the infection by using a Mittag-Leffler distributed waiting time in the infectious compartment. Additionally, we replace the step-size immunity function with a smooth immunity decay (see Figure 2.2), which enables the inclusion of a second fractional derivative in the model instead of the delayed reentry of infectious individuals in S.

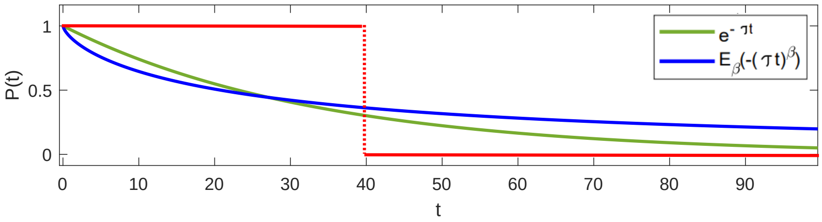

Figure 2.2 – The probability $P(t)$ for the step type is shown in red on the plot, along with its smoothing using exponential and Mittag-Leffler functions, with $\beta = 0.7$ and $\tau = 0.03$.

For $t > 0$, and $I(0) = I_0 > 0$, the integral equation for $I(t)$ is given by:

$$I(t) = I_0 e^{-\gamma t} + \int_0^t \frac{\Omega}{N} I^p(y)S(y)e^{-\gamma(t-y)}dy. \tag{2.23}$$

We extend the infectious period distribution from exponential to Mittag-Leffler, yielding the equation:

$$I'(t) = \frac{\Omega}{N} I^p(t)S(t) - \gamma^\alpha D^{1-\alpha} I(t). \tag{2.24}$$

We can interpret $\gamma^\alpha D^{1-\alpha} I(t)$ as the rate from I to R with memory. By letting $\alpha \to 1$, we can recover the integer case. For all $t > 0$, the integral equation for $R(t)$ is:

$$R(t) = R_0(t) + \gamma \int_0^t I(y)P(t-y)dy. \tag{2.25}$$

Instead of a sudden shift in the immune response, we can propose an exponential decline in the likelihood of remaining recovered and immune, denoted by $P(t) = e^{-\tau t}$. By defining R_0 as the initial fraction of recovered individuals, we can express $R_0(t) = R_0 e^{-\tau t}$, resulting in the equation:

$$R(t) = R_0 e^{-\tau t} + \gamma \int_0^t I(y) e^{-\tau(t-y)} dy. \tag{2.26}$$

In this case, τ represents the rate at which recovered individuals become susceptible. It is also possible to generalize this exponential using a Mittag-Leffler function, $P(t) = E_\beta(-(\tau t)^\beta)$, with $\beta \in (0, 1]$. This generalization can slow down the loss of immunity in individuals who have recovered, as illustrated in Figure 2.2.

Then, we have:

$$R(t) = R_0 E_\beta(-(\tau t)^\beta) + \gamma^\alpha \int_0^t D^{1-\alpha} I(y) E_\beta(-(\tau(t-y))^\beta) dy. \tag{2.27}$$

Using the Laplace convolution denoted by $\star$, we get:

$$R(t) = R_0 E_\beta(-(\tau t)^\beta) + \gamma^\alpha D^{1-\alpha} I(t) \star E_\beta(-(\tau t)^\beta). \tag{2.28}$$

Calculating the derivative by Leibniz's rule and using Laplace transform techniques as before, we obtain:

$$R'(t) = \gamma^\alpha D^{1-\alpha} I(t) - \tau^\beta D^{1-\beta} R(t), \tag{2.29}$$

where $\tau^\beta D^{1-\beta} R(t)$ is the rate from R to S with memory.

As β approaches 1, we observe exponential behavior, and τ can be interpreted as the rate of immunity loss.

Then, the new model is given by:

$$\begin{cases} S'(t) = \tau^\beta D^{1-\beta} R(t) - \dfrac{\Omega}{N} I^p(t) S(t), \\ I'(t) = \dfrac{\Omega}{N} I^p(t) S(t) - \gamma^\alpha D^{1-\alpha} I(t), \\ R'(t) = \gamma^\alpha D^{1-\alpha} I(t) - \tau^\beta D^{1-\beta} R(t). \end{cases} \tag{2.30}$$

We can also consider vital dynamics. The rates of births and natural deaths are both equal to ξ, as commonly simplified. Therefore, the probability of being infectious should be understood as the probability of being both infectious and alive. Similarly, the probability of a recovered person being immune should be understood as the probability of being immune and alive. In this case, the model is given by:

$$\begin{cases} S'(t) = \xi N + \tau^\beta e^{-\xi t} D^{1-\beta}(R(t) e^{\xi t}) - \dfrac{\Omega}{N} I^p(t) S(t) - \xi S(t), \\ I'(t) = \dfrac{\Omega}{N} I^p(t) S(t) - \gamma^\alpha e^{-\xi t} D^{1-\alpha}(I(t) e^{\xi t}) - \xi I(t), \\ R'(t) = \gamma^\alpha e^{-\xi t} D^{1-\alpha}(I(t) e^{\xi t}) - \tau^\beta e^{-\xi t} D^{1-\beta}(R(t) e^{\xi t}) - \xi R(t). \end{cases} \tag{2.31}$$

Theorem 2.6. *In model Eq.* (2.31)*, we have a disease-free equilibrium:*

$$S^* = N, \quad I^* = 0, \quad R^* = 0. \tag{2.32}$$

An endemic (nontrivial) equilibrium corresponds to persistence of the disease, and is obtained by:

$$S^* = \frac{\gamma^\alpha \xi^{1-\alpha} + \xi}{\frac{\Omega}{N}(I^*)^{p-1}}, \quad R^* = \frac{\gamma^\alpha \xi^{1-\alpha} I^*}{\tau^\beta \xi^{1-\beta} + \xi}, \tag{2.33}$$

where I^* *for* $p \neq 1$ *is a root in* $\mathbb{R}^+$ *of the function*

$$f(x) = N\frac{\gamma^\alpha \xi^{1-\alpha} + \xi}{\Omega} x^{1-p} + \left[\frac{\gamma^\alpha \xi^{1-\alpha}}{\tau^\beta \xi^{1-\beta} + \xi} + 1\right] x - N. \tag{2.34}$$

In the case where $p = 1$*,* I^* *is given by:*

$$I^* = \frac{\tau^\beta \xi^{1-\beta} + \xi}{\gamma^\alpha \xi^{1-\alpha} + \tau^\beta \xi^{1-\beta} + \xi} N \left[1 - \frac{\gamma^\alpha \xi^{1-\alpha} + \xi}{\Omega}\right]. \tag{2.35}$$

Proof. The asymptotic equilibria (S^*, I^*, R^*) of Eq. (2.31) are studied by letting

$$\begin{cases} 0 = \xi N + \tau^\beta \lim_{t\to\infty} \left[e^{-\xi t} D^{1-\beta}(R(t) e^{\xi t})\right] - \frac{\Omega}{N}(I^*)^p S^* - \xi S^*, \\ 0 = \frac{\Omega}{N}(I^*)^p S^* - \gamma^\alpha \lim_{t\to\infty} \left[e^{-\xi t} D^{1-\alpha}(I(t) e^{\xi t})\right] - \xi I^*, \\ 0 = \gamma^\alpha \lim_{t\to\infty} \left[e^{-\xi t} D^{1-\alpha}(I(t) e^{\xi t})\right] - \tau^\beta \lim_{t\to\infty} \left[e^{-\xi t} D^{1-\beta}(R(t) e^{\xi t})\right] - \xi R^*. \end{cases} \tag{2.36}$$

Following the limit calculation presented, for instance, in (67) and in Eq. (3.8), this implies

$$\begin{cases} 0 = \xi N + \tau^\beta \xi^{1-\beta} R^* - \frac{\Omega}{N}(I^*)^p S^* - \xi S^*, \\ 0 = \frac{\Omega}{N}(I^*)^p S^* - \gamma^\alpha \xi^{1-\alpha} I^* - \xi I^*, \\ 0 = \gamma^\alpha \xi^{1-\alpha} I^* - \tau^\beta \xi^{1-\beta} R^* - \xi R^*. \end{cases} \tag{2.37}$$

If $I^* = 0$, we can get a disease-free equilibrium:

$$S^* = N, \qquad I^* = 0, \qquad R^* = 0. \tag{2.38}$$

If $I^* \neq 0$,

$$S^* = \frac{\gamma^\alpha \xi^{1-\alpha} + \xi}{\frac{\Omega}{N}(I^*)^{p-1}}, \qquad R^* = \frac{\gamma^\alpha \xi^{1-\alpha} I^*}{\tau^\beta \xi^{1-\beta} + \xi}. \tag{2.39}$$

Then,

$$\frac{\gamma^\alpha \xi^{1-\alpha} + \xi}{\frac{\Omega}{N}(I^*)^{p-1}} + \frac{\gamma^\alpha \xi^{1-\alpha} I^*}{\tau^\beta \xi^{1-\beta} + \xi} + I^* = N, \tag{2.40}$$

and, for $p \neq 1$, we need to solve $f(x) = 0$ in $\mathbb{R}^+$, with $f(x)$ given in Eq. (2.34). In the specific case where $p = 1$, follows Eq. (2.35) from Eq. (2.40). □

The number of endemic equilibria can be studied following (74), section 3. For $p = 1$, the endemic equilibrium can be written as

$$\begin{cases} S^* = N\dfrac{\gamma^\alpha \xi^{1-\alpha} + \xi}{\Omega}, \\ I^* = \dfrac{\tau^\beta \xi^{1-\beta} + \xi}{\gamma^\alpha \xi^{1-\alpha} + \tau^\beta \xi^{1-\beta} + \xi}[N - S^*], \\ R^* = \dfrac{\gamma^\alpha \xi^{1-\alpha}}{\gamma^\alpha \xi^{1-\alpha} + \tau^\beta \xi^{1-\beta} + \xi}[N - S^*], \end{cases} \tag{2.41}$$

and is feasible if $\Omega > \gamma^\alpha \xi^{1-\alpha} + \xi$.

Therefore, based on classical formulations, we introduce a quantity denoted as $\Re_0$ to assess the viability of the endemic equilibrium. It is computed as:

$$\Re_0 = \frac{\Omega}{\gamma^\alpha \xi^{1-\alpha} + \xi}. \tag{2.42}$$

The $\Re_0$ value is independent of the distribution of immunity, the exponent $1 - \beta$, and the time scale τ. Regardless of the value of p, the theory for the model in Eq. (2.31) leads to the following proposition:

Proposition 2.2. *If $\xi > 0$, the mean time of remaining in the infectious compartment is given by:*

$$\eta = \frac{\xi^{\alpha-1}}{\xi^\alpha + \gamma^\alpha}. \tag{2.43}$$

2.2.1 Numerical results

Using $N = 10^6$, in Figures 2.3-2.4, we illustrate the impact of the parameters α and β on the dynamics of the I compartment in model Eq. (2.30). We assume that $\xi < \gamma$. In Figure 2.3, as α decreases, the waiting-time kernel exhibits a heavier tail, implying slower decay of the memory term and thus a longer effective residence time in the infectious compartment. On the other hand, as β decreases, a heavier-tailed immunity loss distribution is introduced, meaning that a fraction of individuals retains immunity for significantly longer periods.

In Figures 2.5 to 2.8, we demonstrate the effect of the orders α (infection memory), β (immunity loss), and the nonlinearity parameter p on the trajectories. All curves tend to the calculated equilibria shown in red. We consider $p = 1$ in Figures 2.5 to 2.7, so the equilibrium I^* is calculated by Eq. (2.41). When $\xi = \gamma$, the equilibrium is the same for all α since $\gamma^\alpha \xi^{1-\alpha}$ becomes constant. As shown in Figure 2.5, when α decreases, there are more infected individuals in the endemic state, whereas decreasing β has the opposite effect, as seen in Figure 2.6. The parameters α and β play dual roles: decreasing α prolongs infection, increasing endemic levels, while decreasing β prolongs immunity, reducing the endemic equilibrium.

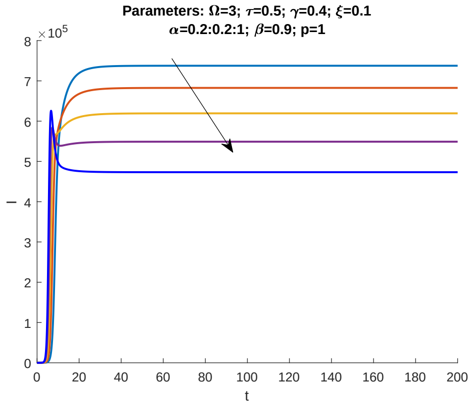

Figure 2.3 – When α is smaller, the memory kernel exhibits a heavier tail, indicating a greater mean waiting time in the I compartment. Note the trajectory of I approaches a sigmoidal (logistic-like) shape.

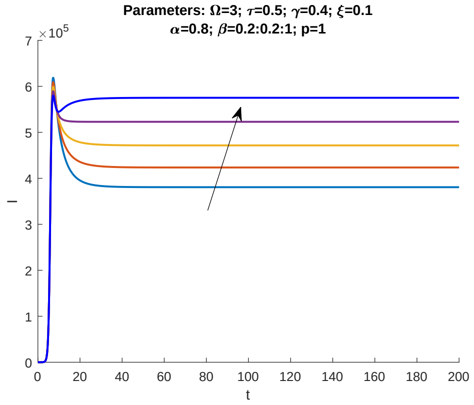

Figure 2.4 – When β is smaller, the I equilibrium is lower, as recovered individuals lose immunity more slowly. Notice that the non-abrupt loss of immunity inhibits the periodic behavior of the original model.

In Figure 2.7, since $\xi = \tau$, the equilibrium is invariant with respect to β because $\tau^{\beta}\xi^{1-\beta}$ is constant in Eq. (2.41). Additionally, note in Figure 2.6 a self-intersection of the trajectory. Within this parameter set, Eq. (2.34) may admit two positive solutions when $p > 1$. In such cases, the larger root is selected for Figure 2.8, as it corresponds to the biologically relevant endemic equilibrium, typically associated with stability (74).

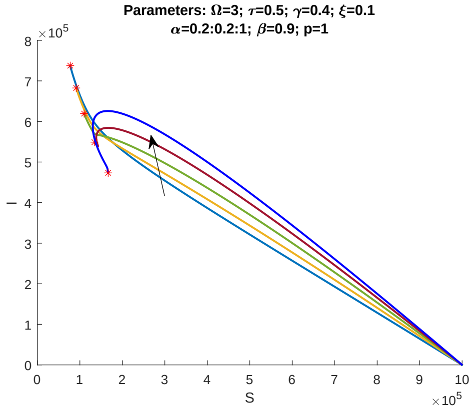

Figure 2.5 – When α is smaller, there are more infected people in endemic equilibrium.

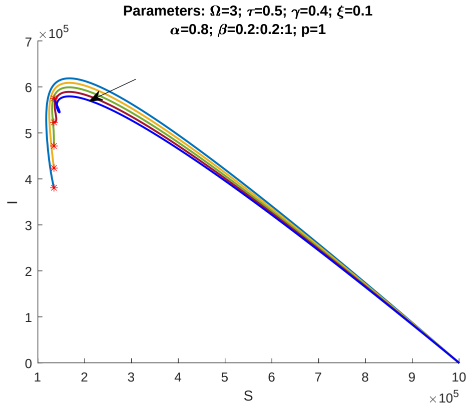

Figure 2.6 – When β is smaller, there are fewer infected people in endemic equilibrium.

2.3 DISCUSSION

In this chapter, the main goal was to create models with long-memory by extending exponential distributions to Mittag-Leffler-based distributions. The proposed method is outlined in Table 2.1.

The original models we study follow the exponential distribution for the waiting times to removal. These models are memoryless (see Section **1.3.1**). In contrast, the

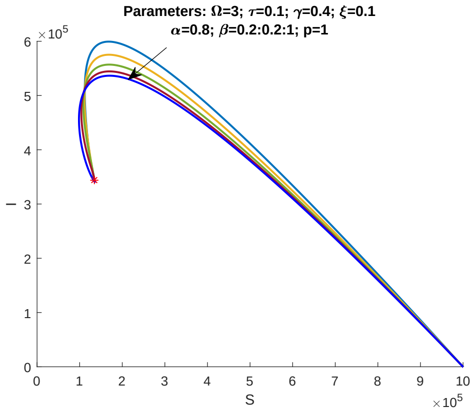

Figure 2.7 – When $p = 1$ and $\xi = \tau$, the endemic equilibrium is the same for all β because $\tau^{\beta}\xi^{1-\beta}$ is constant in Eq. (2.41).

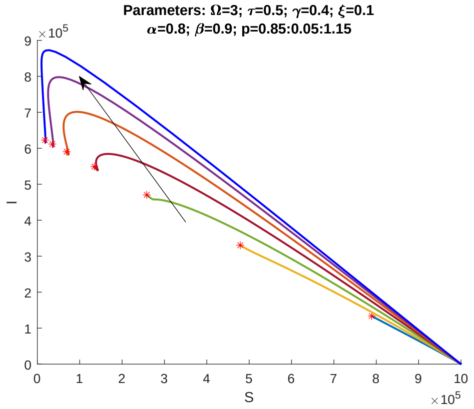

Figure 2.8 – The number of infected individuals in endemic equilibrium increases as p increases in the interval [0.85, 1.15].

Models of type $y(t) = \int_0^t \kappa(t-\tau)g(y,\tau)d\tau + \kappa(t)y_0$

$\kappa(t), t \geq 0$	**Differential Equation**	**Asymp. Eq. (if it exists)**	**Mean**
e^{-rt}	$y' = -ry + g(y,t)$	$y^* = r^{-1} \lim_{t\to\infty} g(y,t)$	r^{-1}
$E_\alpha(-(rt)^\alpha)$	$y' = -r^\alpha D^{1-\alpha} y + g(y,t)$ ${}^C D^\alpha y(t) = -r^\alpha y + I^{1-\alpha} g(y,t)$	$\lim_{t\to\infty} g(y,t) = 0$ (if $\alpha < 1$) $y^* = r^{-\alpha} \lim_{t\to\infty} I^{1-\alpha} g(y,t)$	∞
$E_\alpha(-(r_1 t)^\alpha)e^{-r_2 t}$	$y' = -r_1^\alpha e^{-r_2 t} D^{1-\alpha}(e^{r_2 t} y) - r_2 y + g(y,t)$ ${}^C D^\alpha (e^{r_2 t} y) = -r_1^\alpha e^{r_2 t} y + I^{1-\alpha}(e^{r_2 t} g(y,t))$	$y^* = (r_1^\alpha r_2^{1-\alpha} + r_2)^{-1} \lim_{t\to\infty} g(y,t)$	$\frac{r_2^{\alpha-1}}{r_2^\alpha + r_1^\alpha}$

Table 2.1 – The several memory kernels and their corresponding differential equations (ordinary or fractional), as well as their asymptotic behavior and the mean waiting time to removal.

fractional models exhibit a long-memory property.

When more than one removal mechanism is present, the parameter r of the PDF (*1.3.2.2*) can be decomposed into two independent rates: a rate $r_1 = qr$, associated with the long-memory Mittag–Leffler component, and a memoryless rate $r_2 = (1-q)r$, where $0 \leq q \leq 1$. For an order $0 < \alpha \leq 1$, the distribution is expressed as:

$$f_\alpha(t; r_1, r_2) = \begin{cases} r_1^\alpha t^{\alpha-1} E_{\alpha,\alpha}(-(r_1 t)^\alpha) e^{-r_2 t} + r_2 E_\alpha(-(r_1 t)^\alpha) e^{-r_2 t} & , \ t \geq 0, \\ 0 & , \ t < 0. \end{cases} \tag{2.44}$$

Generally, we can consider n independent removal rates, where $n-1$ are exponentially distributed and one follows a Mittag-Leffler waiting time distribution. In this scenario, the cumulative distribution function is given by:

$$F_\alpha(t; r_1, r_2, \cdots, r_n) = \begin{cases} 1 - E_\alpha(-(r_1 t)^\alpha) e^{-(r_2 + r_3 + \cdots + r_n)t} & , \ t \geq 0, \\ 0 & , \ t < 0. \end{cases} \tag{2.45}$$

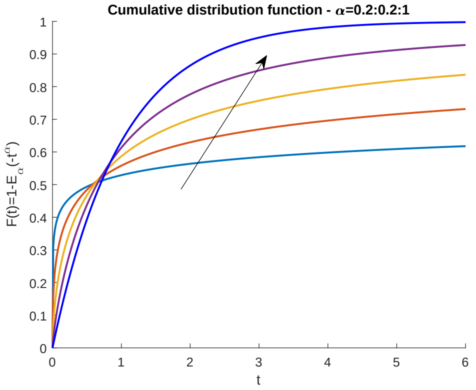

Figure 2.9 – The cumulative function (1.22) for $r = 1$. Observe that the lower the value of α, the greater the value of F in the first moments and the lower the value of F in the tail.

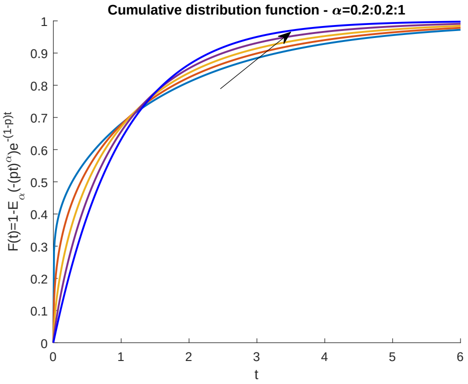

Figure 2.10 – The cumulative function (1.23) for $r = 1$ and $q = 0.55$. Again, the lower the value of α, the greater the value of F in the first moments and the lower the value of F in the tail.

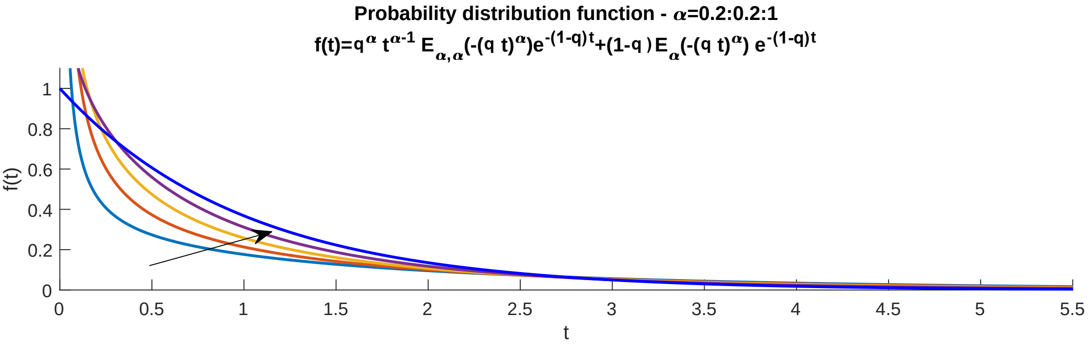

Figure 2.11 – The PDF (2.44) for $r = 1$ and $q = 0.55$. Compared to the classic PDF, it is more likely to be removed in the early moments due to the singularity at $t = 0$ for $\alpha < 1$. However, it is less likely for the subsequent moments. Due to the heavy-tailed behavior, the probability of removal takes longer to decrease over time.

2.3.1 Continuous-time random walks approach

Seminal works such as (43) and (75) have shown that fractional master equations are a special case within the theory of CTRW, with distributed Mittag-Leffler waiting times. However, translating this theory into biological models, such as compartmental models, is not straightforward. To address this issue, (57) proposed a systematic approach for including fractional derivatives into compartment models by deriving deterministic governing equations from an underlying physical stochastic process.

Our approach aligns with the work of (57) and their previous references, as it is based on the concept of distributed Mittag-Leffler waiting times and allows us to construct fractional compartmental models, as in Section 2.2. However, our aim is to provide a practical construction that goes beyond the language of CTRW and offers a simple alternative to the *ad hoc* approach commonly used by applied mathematicians to fractionalize models (*e.g.*, (76),(77)). Additionally, although (57) focuses on compartmental models, our proposal can be applied to non-compartmental models that, for instance, do not have a finite population, as the source term g is general in Eq. (2.6).

2.3.2 Sonine kernels and generalized fractional derivatives

The paper (41) discusses the utilization of Sonine kernels in general fractional integrals and derivatives on function spaces with an integrable singularity at zero. A Sonine kernel $\kappa(x)$ satisfies the condition that there exists another kernel $\ell(x)$ such that

$$\int_0^x \ell(x-t)\kappa(t)dt = 1, \quad x > 0. \tag{2.46}$$

An integral operator of the form

$$\mathbf{K}\varphi := \int_{-\infty}^x \kappa(x-t)\varphi(t)dt, \quad x \in \mathbb{R} \tag{2.47}$$

is called a Sonine integral operator if κ is a Sonine kernel.

Specifically, the kernel $\kappa(t) = E_\alpha(-(r_1 t)^\alpha)e^{-r_2 t}$, where $\alpha < 1$ and $r_1 > 0$, can be considered a Sonine kernel as it is a singular, locally integrable, completely monotone function (41). In general, for any Sonine kernel with an integrable singularity at zero, Eq. (2.6) can be expressed as

$$y' = \mathbb{D}_{(K)}g + \kappa'(t)y_0, \tag{2.48}$$

where $\mathbb{D}_{(K)}$ represents a general fractional derivative of convolution type, defined in the Riemann-Liouville sense. A similar formulation can be applied in the Caputo sense. In particular, for the specific kernel $\kappa(t) = E_\alpha(-(r_1 t)^\alpha)e^{-r_2 t}$, the resulting derivative $\mathbb{D}_{(K)}$ is neither a classical Riemann-Liouville nor a Caputo fractional derivative. Additionally, in Eq. (2.48), the fractional derivative is applied to the function g, not to y as in our modeling:

$$y' = -r_1^\alpha e^{-r_2 t} D^{1-\alpha}(e^{r_2 t}y) - r_2 y + g(y,t). \tag{2.49}$$

Therefore, this approach is not directly related to our proposal, but the connection between the two different approaches can be explored in future research.

2.3.3 Limitations and extensions

We have not yet demonstrated the stability of the equilibria. This issue may be addressed by using the theory of Volterra integrals, as discussed in (72, 73).

Another limitation is that our example in Section 2.2 is a system, but the approach is based on each scalar equation: the equation for I, where we generalize an exponential to a Mittag-Leffler waiting time, and the equation for R, where we consider a smooth immunity behavior instead of a step function. We hypothesize that Theorem 2.1 is also effective when y is a vector in Eq. (2.3), through the use of the Mittag-Leffler function applied to matrices (78). However, when considering multiple rates, as in Theorem 2.2, for R_1 and R_2 matrices, *i.e.*, for

$$Y = \int_0^t E_\alpha(-(R_1(t-\tau))^\alpha)e^{-R_2(t-\tau)}g(Y,\tau)d\tau + E_\alpha(-(R_1 t)^\alpha)e^{-R_2 t}y_0, \tag{2.50}$$

it is necessary to ensure the commutativity in certain parts of Eq. (A.13). Although some cases can be easier, say if R_1 and R_2 are diagonals, future research should aim to clarify central aspects in suitable matrix spaces.

The proposed method can be applied to any differential equation of the form $y'(t) = f(y(t), t)$. This is equivalent to Eq. (2.1), where $g(y(t), t) = f(y(t), t) + \lambda y(t)$, for any $\lambda > 0$. This general approach introduces a new parameter, λ, the relationship of which with the original model is unclear. Therefore, the applicability of this approach depends on the original model and possible interpretations for λ.

2.3.3.1 New results in a SIR model

In Appendix B, we examine the SIR model introduced in (32), with the aim of extending previous results and presenting new findings (26). In an SIR model, individuals transition from being susceptible to becoming infectious, and then recover with lifelong immunity. We show that a fractional model of the same type, formulated within the framework of CTRW, can be derived from the theory developed in this chapter. This connection clarifies the role of the proposed generalizations within the context of the classical SIR model.

In addition to formulating the model, we establish the non-negativity of solutions and analyze the behavior of the compartments S and R. In particular, we prove monotonicity in the limiting case where $\gamma \equiv 0$. This result is consistent with the expected biological interpretation. Furthermore, we investigate the equilibrium points of the system, proving global asymptotic stability of the disease-free equilibrium and local asymptotic stability of the endemic equilibrium.

2.3.4 Concluding remarks

In this chapter, we proposed a method that leverages Mittag-Leffler kernels to generalize exponential distributions in a wide range of ODE models. We illustrate this approach by developing an SIRS epidemiological model and presenting numerical results. Our findings suggest that this modeling approach is a valuable tool for creating meaningful fractional models while preserving physical units and interpretations.

In the next chapter, we extend this perspective by showing that such fractional formulations are particular instances of a more general framework based on integral memory kernels. This transition allow us to place ordinary, delayed, and fractional models within a single unified structure.

3 BRIDGING THE GAP BETWEEN MODELS BASED ON ORDINARY, DELAYED, AND FRACTIONAL DIFFERENTIAL EQUATIONS THROUGH INTEGRAL KERNELS

This chapter presents the central theoretical contribution of the thesis. Building on the fractional constructions introduced in Chapter 2, the key idea is that the influence of past states on present dynamics can be represented through a kernel function, whose specific form determines the qualitative behavior of the system. In this context, classical memoryless models, discrete delays, distributed delays, and fractional formulations correspond to different choices of this kernel. This unified perspective not only clarifies the relationships between existing modeling approaches but also provides a systematic way to construct new models by selecting appropriate kernel functions.

As discussed in the introduction, delays play a fundamental role in population dynamics. We proceed with our work in (79) to demonstrate, starting from the logistic model structure, that classical, delayed, and fractional models are special cases of a framework using a gamma Mittag-Leffler memory kernel.

Assume, without loss of generality, that the carrying capacity of a population y is equal to one, and that delays or the influence of the past appear in the logistic equation in a Volterra convolution form:

$$y'(t) = ry(t)\left(1 - \int_0^t \kappa(t-\tau)y(\tau)d\tau\right). \tag{3.1}$$

This type of formulation dates back to (80). Eq. (3.1) indicates that the growth rate at time t depends on population sizes at previous times $\tau < t$ in a distributed (or weighted) manner, where the weights are defined by the delay kernel κ. In Eq. (3.1), discrete or distributed delays that follow continuous distribution functions can be considered (81). Previously, distributed delays in the logistic equation have been extensively explored (*e.g.*, (16, 82)). However, to the best of our knowledge, no existing framework currently integrates the principles of FC with integro-differential models of population growth.

Ordinary differential equations

If we set $\kappa(t) = \delta_0(t)$ (Dirac delta kernel), we assume that only the present state of y influences the vital rates of the population, leading to the classical logistic model: $y' = ry(1 - y(t))$. On the other hand, if we consider Erlang distributed delays, *i.e.*, a gamma distribution parameterized by a positive integer parameter β, we end up with a system of $\beta + 1$ ODEs. By incorporating memory effects in this specific manner, we can include past information while maintaining a Markovian model. This is accomplished by introducing additional variables that introduce delays in their interactions continuously, a technique known as the "chain trick," which has been utilized in previous studies (83, 84, 2).

As seen before, two powerful and extensively studied methods for incorporating the influence of the past into mathematical models are DDEs and FDEs. For example, when we set $\kappa(t) = \delta_\mu$ (a Dirac delta centered at μ), we obtain the delayed logistic equation, commonly known as Hutchinson's equation: $y' = ry(1 - y(t - \mu))$.

A new general framework

The dynamics of solutions of (3.1) and their inherent relationship with the shape of the memory kernel remain relatively unexplored in the literature. This work aims to address this gap by demonstrating how classical, fractional, delayed, and ODE system-based models can all be viewed as specific instances within a broader memory-based approach. To achieve this, we leverage the probability distribution functions associated with the generalized gamma Mittag–Leffler distribution as our delay kernels. The gamma Mittag–Leffler distribution emerges as a generalization that simultaneously encompasses classical exponential memory, phase-type/Erlang structure, heavy-tailed fractional behavior, and mean/variance control, as discussed in the following sections.

A key highlight of this framework is its capacity to facilitate the development of new fractional models while providing a comprehensive understanding of the implications of non-integer derivatives and integrals in the solution. We also delve into the examination of asymptotic behavior. The approach is validated by reproducing real-world phenomena, such as the infection dynamics of COVID-19 in different countries.

3.1 NEW MATHEMATICAL MODELS BASED ON THE GAMMA MITTAG-LEFFLER PROBABILITY DISTRIBUTION FUNCTION

Consider the generalized gamma Mittag–Leffler probability distribution function (85) in the form:

$$\kappa(x) = \begin{cases} Cx^{\beta-1}e^{-ax}E_{\alpha,\beta}(-\lambda x^{\alpha}), & x \geq 0 \\ 0, \quad \text{elsewhere}, \end{cases} \tag{3.2}$$

where $C = a^{\beta} + a^{\beta-\alpha}\lambda$ is a normalizing factor, and one of the following conditions must hold:

- $a = 0, \lambda > 0$ and $0 < \alpha = \beta \leq 1$;
- $-a^{\alpha} < \lambda \leq 0$, $a > 0$, $\alpha, \beta > 0$;
- $0 \leq \lambda < a^{\alpha}$, $a > 0$, $0 < \alpha \leq 1$, and $\alpha \leq \beta$.

A brief numerical study of this function is found in Appendix C. We use the gamma Mittag-Leffler distribution (3.2) as a memory kernel, rewriting Eq. (3.1) as

$$y' = ry\left(1 - \int_0^t C(t-\tau)^{\beta-1}e^{-a(t-\tau)}E_{\alpha,\beta}(-\lambda(t-\tau)^{\alpha})y(\tau)d\tau\right) \tag{3.3}$$

Next, we utilize the fractional Riemann-Liouville integral and derivative. By applying the properties of the Mittag-Leffler functions and Laplace transforms, we obtain the following system:

$$\begin{cases} y' = ry(1 - Ce^{-at}D^{1-\beta}(e^{at}w)), \\ w' = y - \lambda e^{-at}D^{1-\alpha}(e^{at}w) - aw. \end{cases} \tag{3.4}$$

The general model (3.4) is unit-consistent and maintains the interpretation of variation rates, as long as the left side remains a classical derivative. It is important to emphasize that this approach differs from the classical substitution of integer-order derivatives with fractional ones, as discussed in Appendix C.

We observe that the parameter α primarily affects the right tail of the distribution, leading to a slower convergence to equilibrium for smaller values of α, as depicted in Figure 3.1.B (purple). Conversely, the parameter β mainly influences the mode of the kernel, resulting in increased overshoots when β is larger (compare, for instance, the green curve with $\beta = 3.4$ and the light blue curve with $\beta = 0.05$ in Figure 3.1.B). The parameters a and λ are associated with the velocity of the memory kernel. Further details on numerical studies and simulations exploring parameter sensitivity analysis can be found in Appendix C.

3.1.1 Asymptotic Equilibria

If $a > 0$, the feasible equilibrium can be obtained directly from Eq. (3.4). Besides the trivial equilibrium, we need to examine the following limit:

$$C \lim_{t\to\infty} e^{-at}D^{1-\beta}(e^{at}w) = 1. \tag{3.5}$$

To solve this limit, let us denote $\mathcal{L}\{w(t)\}(s) = W(s)$. For $a > 0$, we have:

$$\mathcal{L}\{e^{-at}D^{1-\beta}(e^{at}w)\} = (s+a)^{1-\beta}W((s-a)+a) \tag{3.6}$$

$$= a^{1-\beta}W(s) + (1-\beta)a^{-\beta}sW(s) + \mathcal{O}(s^2)W(s). \tag{3.7}$$

Assuming that the conditions of the Final Value Theorem (66) are met, we obtain:

$$\begin{aligned} &\lim_{t\to\infty}[e^{-at}\, D^{1-\beta}(e^{at}w)] \\ &= \lim_{s\to 0}[a^{1-\alpha}sW(s) + (1-\beta)a^{-\beta}s^2W(s) + \mathcal{O}(s^3)W(s)] \\ &= a^{1-\beta}w^*. \end{aligned} \tag{3.8}$$

In the system (3.4), the only equilibrium other than 0 must satisfy the following conditions:

$$\begin{cases} y^* = \lambda a^{1-\alpha}w^* + aw^* = 1, \\ w^* = C^{-1}a^{\beta-1}. \end{cases} \tag{3.9}$$

The stability of the non-null equilibrium $y^* = 1$ is discussed in Appendix C. Still, the instability of the equilibrium for "long" delays is a key observation. For example, in the case of Erlang-distributed delays with $\lambda = 0$ and $\beta = n \in \mathbb{N}^*$, (16) proves that the equilibrium is unstable if the mean of the distribution is $\mu > 4/r$. Recall from Eq. (3.1) that r represents the speed of dynamics. Therefore, long delays, in comparison to this dynamics, tend to have a destabilizing effect, either by facilitating oscillations or slowing down the approach to equilibrium.

3.2 LINKING THE CLASSICAL MODEL, SYSTEMS OF ODES, DELAYED AND FRACTIONAL LOGISTIC MODELS

We outline how single DDEs, ODEs, and FDEs systems are derived from the general structure of Eq. (3.4). In Figure 3.1.C, we display several kernels defined from Eq. (3.2) with a mean of $\mu = 1$, given by Eq. (3.22), except for the classical logistic kernel with a mean of $\mu = 0$, and the Mittag-Leffler PDF, where $a = 0$ and the mean is infinite. The kernels illustrated in Figure 3.1.C produce the logistic responses depicted in Figure 3.1.A-B.

3.2.1 Classical logistic model

If $\kappa(t) = \delta_0(t)$ (see Figure 3.1.C, dark blue), then Eq. (3.1) represents the classical logistic model. This is a limiting case of system (3.4) if $\lambda = 0$, $\beta = 1$ and $C = a = n$, for $n \in \mathbb{N}^*$. In fact, the kernels become a sequence of the form ne^{-nt}, which is a Dirac sequence. Therefore, as $n \to \infty$, the system tends towards the classical logistic equation. Figure 3.1.A illustrates the classical logistic response where the solution increases monotonically until reaching equilibrium.

3.2.2 ODE systems: Erlang probability distribution function kernels

The gamma distribution can be used as a delay kernel by setting $\lambda = 0$ in Eq. (3.2). This leads to the equation:

$$y'(t) = ry\left(1 - \int_0^t \frac{a^\beta}{\Gamma(\beta)}(t-\tau)^{\beta-1}e^{-a(t-\tau)}y(\tau)d\tau\right), \tag{3.10}$$

where $\beta > 0$. For $\beta = n \in \mathbb{N}^*$, which characterizes Erlang distributions (86), the model can be expressed as a system of $(n+1)$ ODEs using a technique known as the linear chain trick (83). Actually, by setting $\beta = 1$ in Eq. (3.10), we define:

$$v(t) = \int_0^t ae^{-a(t-\tau)}y(\tau)d\tau. \tag{3.11}$$

The memory kernel $\kappa_1(t) = ae^{-at}$ is commonly referred to as the weak kernel (16). Differentiating, we obtain:

$$v'(t) = ay(t) - av(t) = \frac{y(t) - v(t)}{\mu}, \tag{3.12}$$

where $\mu = 1/a$ is the mean of the distribution. Therefore, for $\beta = 1$, the integro-differential Eq. (3.10) is equivalent to the following system:

$$\begin{cases} y' = ry(1 - v), \\ v' = \dfrac{y - v}{\mu}. \end{cases} \tag{3.13}$$

With the so-called strong kernel κ_2 (16), obtained with $\beta = 2$, we can establish an equivalence between Eq. (3.10) and the 3-dimensional system:

$$\begin{cases} y' = ry(1 - z), \\ v' = \dfrac{2(y - v)}{\mu}, \\ z' = \dfrac{2(v - z)}{\mu}. \end{cases} \tag{3.14}$$

By considering an inductive approach, we observe that

$$\frac{d}{dt}\int_0^t \frac{a_n^n}{(n-1)!}(t-\tau)^{n-1}e^{-a_n(t-\tau)}y(\tau)d\tau \tag{3.15}$$

$$= a_n\Bigg(\int_0^t \frac{a_n^{n-1}}{(n-2)!}(t-\tau)^{n-2}e^{-a_n(t-\tau)}y(\tau)d\tau \tag{3.16}$$

$$-\int_0^t \frac{a_n^n}{(n-1)!}(t-\tau)^{n-1}e^{-a_n(t-\tau)}y(\tau)d\tau\Bigg), \tag{3.17}$$

which leads to the conclusion that Eq. (3.10) is equivalent to an $(n+1)$-dimensional system of ODEs. This approach is not applicable if n is not an integer, as discussed in (84).

In Figure 3.1.C, the second kernel represents the strong memory Erlang PDF for $\beta = 2$ and mean 1. The logistic response is illustrated in Figure 3.1.A (orange). The delay induces an overshoot and oscillations; however, the equilibrium remains the same.

3.2.3 Delayed differential model

With $\lambda = 0$ and $\beta = n \in \mathbb{N}^*$ as before, we choose the constants a_n conveniently to maintain the mean of the distribution at μ. Therefore, defining $\kappa_n(t) = a_n^n t^{n-1}e^{-a_n t}/(n-1)!$, we have $\kappa_n \to \delta(t - \mu) =: \delta_\mu$ (see Figure 3.1.C for $\mu = 1$), and the $(n+1)$-dimensional system of ODEs tends to the delayed logistic equation:

$$y' = ry\left(1 - y(t - \mu)\right), \tag{3.18}$$

as $n \to \infty$. Note the oscillatory behavior in Figure 3.1.A (yellow).

3.2.4 Special cases of fractional models

3.2.4.1 Mittag-Leffler distributed delays

By setting $0 < \alpha = \beta \leq 1$ and $a = 0$, we obtain the fractional Poisson process described in Eq. (1.24), where the kernel represents the probability density function of the Mittag-Leffler distribution. This leads to the formulation of Eq. (3.1) as:

$$y' = ry\left(1 - \int_0^t \lambda(t-\tau)^{\alpha-1}E_{\alpha,\alpha}(-\lambda(t-\tau)^{\alpha})y(\tau)d\tau\right), \tag{3.19}$$

resulting in the logistic model with Mittag-Leffler distributed delays given by:

$$\begin{cases} y' = ry(1 - \lambda D^{1-\alpha}w), \\ w' = y - \lambda D^{1-\alpha}w. \end{cases} \tag{3.20}$$

As α approaches 1, we recover exponentially distributed delays. Mittag-Leffler kernels indicate that the population growth rate depends on both present and past states, with a decreasing impact over time. In Figure 3.1.C (purple), the right tail of the Mittag-Leffler distribution's PDF is higher than other distributions, although it decreases more rapidly initially. The slow approach to equilibrium is due to the heavy tail of the memory kernel, as shown in Figure 3.1.B.

3.2.4.2 Gamma distributed delays

By setting $\lambda = 0$, as in Eq. (3.23), we obtain gamma-distributed delays (see (3.10)), which corresponds to the model:

$$\begin{cases} y' = ry(1 - Ce^{-at}D^{1-\beta}(e^{at}w)), \\ w' = y - aw. \end{cases} \tag{3.21}$$

This kernel does not have a Mittag-Leffler term, but the model is still fractional provided that $\beta \notin \mathbb{N}$, *i.e.*, provided that the kernel is not an Erlang PDF. The solutions generated by these kernels allow interpolation between the solutions generated by the ODE systems from Erlang PDF kernels. In Figures 3.1.B-3.1.C, we show the response and the kernel for $\beta = 3.4$ (green).

The ODEs and DDEs models have already been studied in the literature, but the fractional models are new. We propose FC tools for addressing a large family of memory kernels, which can be chosen adequately for each biological system.

3.2.5 Mean and variance

For $a > 0$, the mean μ and the variance σ^2 of the gamma Mittag-Leffler distribution (85) are given by:

$$\mu = \frac{\beta}{a} - \frac{\lambda\alpha}{a(a^\alpha + \lambda)}, \qquad \sigma^2 = \frac{\beta}{a^2} - \frac{\lambda\alpha[(\alpha+1)a^\alpha + \lambda]}{a^2(a^\alpha + \lambda)^2}. \tag{3.22}$$

For $a = 0$, there is no finite mean or variance.

Note that when $\beta \leq 1$, the memory kernel (3.2) is weak in the sense that the present is the most influential moment in the growth rate. On the other hand, if $\beta > 1$, we have $\kappa(0) = 0$, and a strong memory kernel, in the sense that the distribution mode is not zero. Moreover, since $\partial\mu/\partial\beta = 1/a$ and $\partial\sigma^2/\partial\beta = 1/a^2$, the mean and the variance increase as β increases. Thus, increasing the parameter β increases the window of the memory (σ^2) and how remote it is (μ).

Another interesting analysis is to see that $\partial\mu/\partial\lambda = -\alpha a^{\alpha-1}/(a^\alpha + \lambda)^2 < 0$, and $\partial\sigma^2/\partial\lambda = -\alpha a^{\alpha-2}[(\alpha+1)a^\alpha + \lambda(1-\alpha)]/(a^\alpha + \lambda)^3 < 0$ within the established hypotheses. This indicates that increasing λ implies a decrease in the mean and in the variance, as expected.

Finally, we note that for any $\mu, \sigma^2 \in (0, \infty)$, there is at least one choice of parameters that sets the mean and variance of the memory kernel to μ and σ^2, respectively. An immediate option is to set

$$\lambda = 0, \qquad a = \frac{\mu}{\sigma^2}, \qquad \beta = \mu a = \frac{\mu^2}{\sigma^2}. \tag{3.23}$$

This choice is independent of α and corresponds to the gamma memory kernel $Ct^{\beta-1}e^{-at}$ and the model Eq. (3.21).

These findings demonstrate how incorporating fractional models expands the range of phenomena that can be effectively represented. In Figure 3.1.D, the extension of the proposed model is illustrated. In the classical model, both the mean and variance of the memory kernel are zero. DDE allow memory with any mean but with a zero variance. In Erlang PDF, since $\mu = \beta/a$ and $\sigma^2 = \beta/a^2$, $\beta = \mu^2/\sigma^2$ must be an integer. Therefore, each $\beta = n$ corresponds to a branch of a parabola $\mu^2 = n\sigma^2$ in the plane $\mu \times \sigma^2$. The limit as $n \to \infty$ is the axis $\sigma^2 = 0$, *i.e.*, the DDE case. Fractional models are the only of the presented cases that can span the entire $\mu \times \sigma^2$ plane.

3.3 CLASSIFYING THE KERNELS

The gamma Mittag-Leffler PDF memory kernel (3.2) can be categorized into six regions and their boundaries based on the following characteristics:

- The sign of λ: Note that, from (3.22), a negative λ corresponds to a higher variance, leading to smaller overshoots and oscillations in the solution.

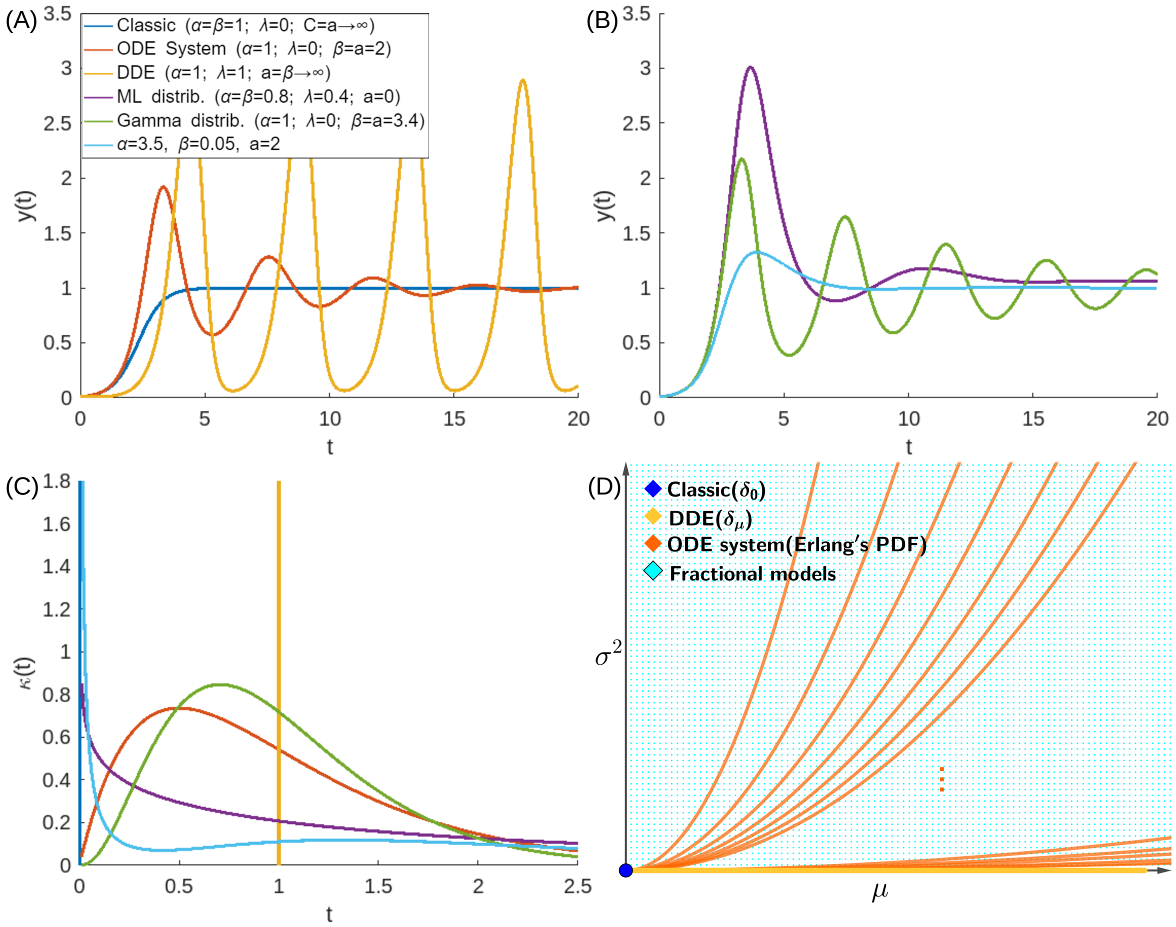

Figure 3.1 – Panels **(A)**-**(B)** displays the logistic responses for kernels (panel **(C)**) defined from (3.2) with a mean of $\mu = 1$, except for the classical case ($\mu = 0$) and ML distributed delays (infinite mean). The delayed equation, the ODE system, and the gamma-distributed delayed model are generated by strong memory kernels, while the other kernels represent weak memory. Panel **(D)** illustrates the plane $\mu \times \sigma^2$ of the kernel κ. In the classical case (blue dot), both the mean and the variance are null: $\mu = \sigma^2 = 0$. The DDE case (yellow) corresponds to $\sigma^2 = 0$ and is the limiting case of the ODE systems generated by Erlang PDF memory kernels (orange). In fact, once $\mu = \beta/a$ and $\sigma^2 = \beta/a^2$ in Erlang PDF, then $\beta = \mu^2/\sigma^2$ must be an integer. Each $\beta = n$ corresponds to a branch of a parabola $\mu^2 = n\sigma^2$, with the limit being the axis $\sigma^2 = 0$.

- Weak and strong memory kernels: A weak memory kernel has a distribution mode of zero, while a strong memory kernel has a non-zero mode, determined by $\beta \leq 1$ or $\beta > 1$, respectively. Generally, a weak memory kernel results in asymptotically stable behavior.
- Unimodal or multimodal kernels: The presence of multiple peaks after the first distribution peak indicates a break in monotonicity. Subsection C.3.A explains the origin of these multiple modes using the Mittag-Leffler series. Some general kernels exhibit multimodal behavior, as illustrated in Figures 3.2 and C.10.

The six regions and their frontiers are illustrated in Figure 3.2 and are described

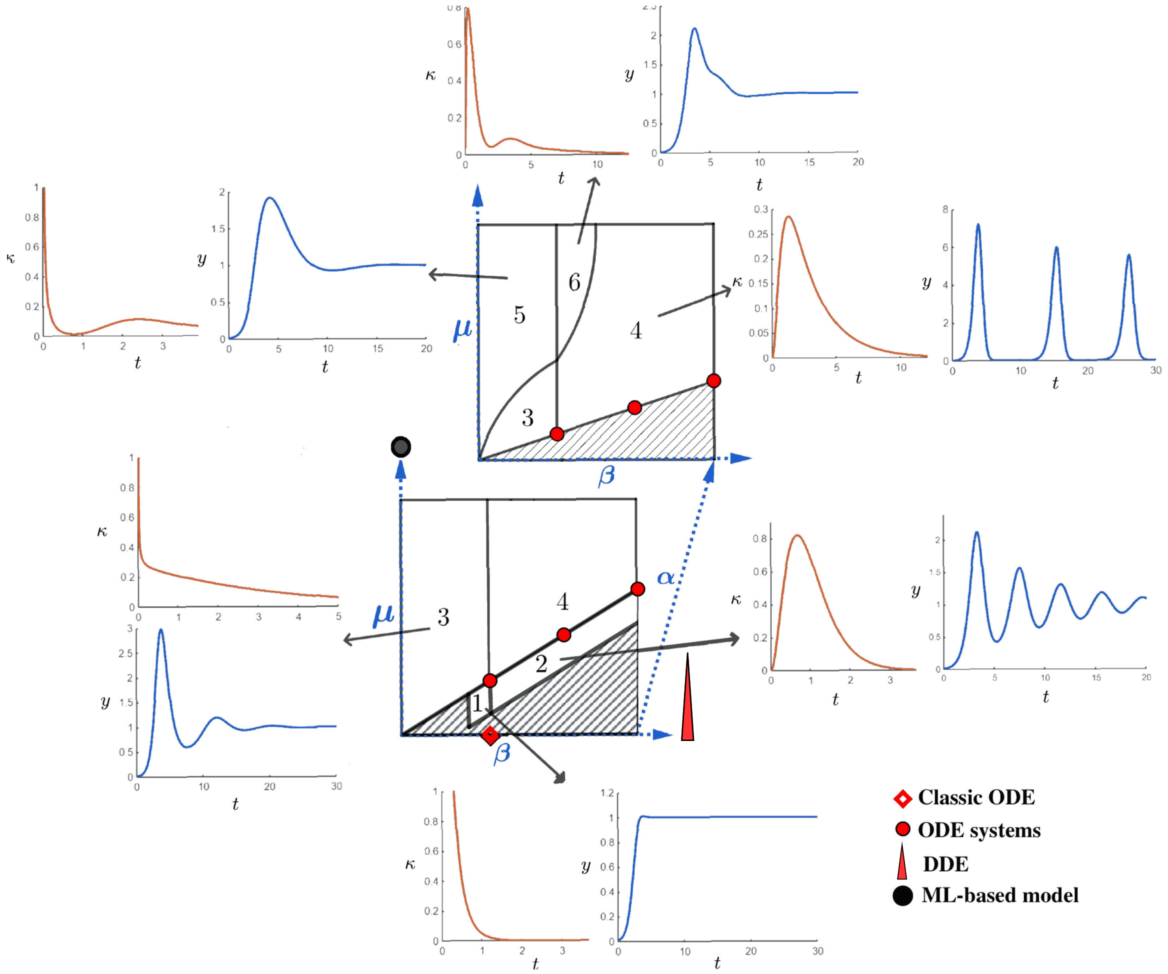

Figure 3.2 – A visual map displaying different types of kernels and their logistic responses. The map is divided into two planes, with the horizontal and vertical axes representing the parameters β and μ, respectively. The parameter α increases upwards, with a higher value at the top plane. The parameter a is fixed in both planes' simulations, but it is not fixed in the classical cases of δ_0, δ_μ, and Mittag-Leffler PDF. The hatched region in both planes indicates that kernel hypotheses are not satisfied. Each region from 1 to 6 is associated with a simulation example, illustrating a kernel from that region and its respective logistic response using an arrow. The lines dividing regions with $\lambda > 0$ and $\lambda < 0$ (*e.g.*, the frontier between regions 1 and 3) are lines where $\lambda = 0$, corresponding to gamma PDF kernels. In this case, the corresponding models can be fractional but are not related to α. Some special kernels are marked in red: the diamond illustrates the limiting classical kernel, red dots represent Erlang PDF kernels, where $\beta \in \mathbb{N}^*$ and $\lambda = 0$, and the triangle in $\beta \to \infty$ indicates the region of DDE kernels. Additionally, the black dot corresponds to the limiting case $\mu \to \infty$, where the kernel is a Mittag-Leffler PDF.

as follows:

1) Weak unimodal kernels with $\lambda > 0$: These kernels are the closest to the classical delta Dirac kernel, with a mode at zero and small variance.

2) Strong unimodal kernels with $\lambda > 0$: These kernels have a mean other than zero and small variance. In the limiting case, they approximate kernels of type δ_μ, inducing oscillations similar to those of the delayed logistic equation.

3) Weak unimodal kernels with $\lambda < 0$: Kernels in this region are singular (mode equals zero) but do not have small variance. Their decay relates to Mittag-Leffler decay types.

4) Strong unimodal kernels with $\lambda < 0$: These kernels have a mean other than zero and can consider a large memory window. This reveals interesting behaviors, such as "almost extinction" between waves.

5) Weak multimodal kernels with $\lambda < 0$: These kernels are singular but have other small peaks, making them multimodal kernels. They allow consideration of other important points (peaks) from the past.

6) Strong multimodal kernels with $\lambda < 0$: These kernels can also be considered multimodal, allowing behaviors worth noting in the solution, such as a secondary plateau after the main overshoot.

Figure 3.2 also highlights the locations of the memory kernels for the classical logistic equation, DDEs, systems of ODEs (Erlang kernel), and other particular cases in this parameterized map:

a) The limiting classical kernel δ_0 (logistic ODE) can be obtained when $\beta = 1$, $\mu = 0$, and $a \to \infty$. In Figure 3.2, it is illustrated by a red diamond on the β axis.

b) In the frontiers where $\lambda = 0$, the delay follows gamma distributions. These continuous delay distributions were studied, for instance, in (2, 87, 88, 89), but were not linked before to fractional models.

c) In the frontiers where $\lambda = 0$, delays that are Erlang distributed are obtained when $\beta \in \mathbb{N}^*$. In Figure 3.2, these kernels are marked with red dots. As discussed previously, in this case, the model can be written as a system of ODEs.

d) The kernel δ_μ is the limiting case when $\lambda = 0$, and $\beta \in \mathbb{N}^*$ is such that $\beta \to \infty$. With these kernels, illustrated as a red triangle in Figure 3.2, we obtain classical DDEs. The ODE case can also be achieved on the basis of the triangle.

e) When $a = 0$, $0 < \alpha = \beta \leq 1$, and $\mu \to \infty$, the delays are Mittag-Leffler distributed, as discussed in Section 3.2 and illustrated in Figure 3.2 as a black dot. This case was previously explored in the literature in (90).

3.4 MODELING THE SPREAD OF COVID-19 WITH MEMORY KERNELS

We demonstrate the ability to reproduce real data using the new models by utilizing a COVID-19 dataset (91). The MATLAB routine *lsqnonlin* was used to solve the nonlinear least-squares problem and fit the curve to the active cases data.

3.4.1 Motivation

The motivation for using the logistic equation in modeling epidemics relies on the Susceptible-Infected (SI) model. It can be viewed as a simplification of the Susceptible–Infected (SI) model (11), where the infection dynamics are described by $I'(t) = bS(t)I(t) - gI(t)$, with b representing infectivity and g indicating the recovery rate. If g is negligible compared to $bS(t)$, resulting in $R(t) \approx 0$, the primary dynamic lies in the infection. The percentage of susceptible and infectious individuals at time t is denoted by $S(t)$ and $I(t)$, respectively. With $R(t)$ being negligible, $S(t) + I(t) \approx 1$, the total population. Notably, the model simplifies to a classical logistic model given by

$$I'(t) = bI(t)(1 - I(t)). \tag{3.24}$$

In this simplification, I must monotonically increase without surpassing N in order for S to remain non-negative. However, stepping beyond the compartmental SI framework, this simple logistic equation motivates us to replicate oscillatory patterns of real data from COVID-19 infection dynamics.

While we do not aim to delve into the complexities of modeling a complex disease such as COVID-19 with a logistic equation, the linear chain trick discussed in Section 3.2 illustrates how delays can be represented by introducing new differential equations and variables into a model. Therefore, incorporating a general delay kernel in a logistic equation based on the SI model is related to explicitly modeling other dynamics or compartments through systems of ODEs. Our findings demonstrate that the generalized memory kernel can capture the intricate dynamics of COVID-19 in several countries.

3.4.2 Results

In Figure 3.3, we present optimization results for modeling COVID-19 active cases in different scenarios and countries, by adjusting the parameters a, α, β, r, and λ in the model (3.4). We used MATLAB to solve a Least Squares problem using the FDIPA optimization algorithm (92).

The real data is displayed in black, while the green and blue lines represent the solutions of the ODE system with $\beta + 1$ equations (β ranging from 1 to 10) and the general framework (3.4), respectively. We have rescaled the solution $I(t)$ according to the data of each country.

In Figure 3.3.A, we present the optimization results for 25 weeks of COVID-19 infection dynamics in Australia. For this dataset, the simpler Erlang PDF memory kernel with $\beta = 3$ (corresponding to 4 ODEs) shows results almost as accurate as those of the general kernel. As shown in Table 3.1, the means of the two kernels are both approximately $\mu = 2.4$. The general kernel, which belongs to region 2 in Figure 3.2, reduces the Erlang fitting error in approximately 22%.

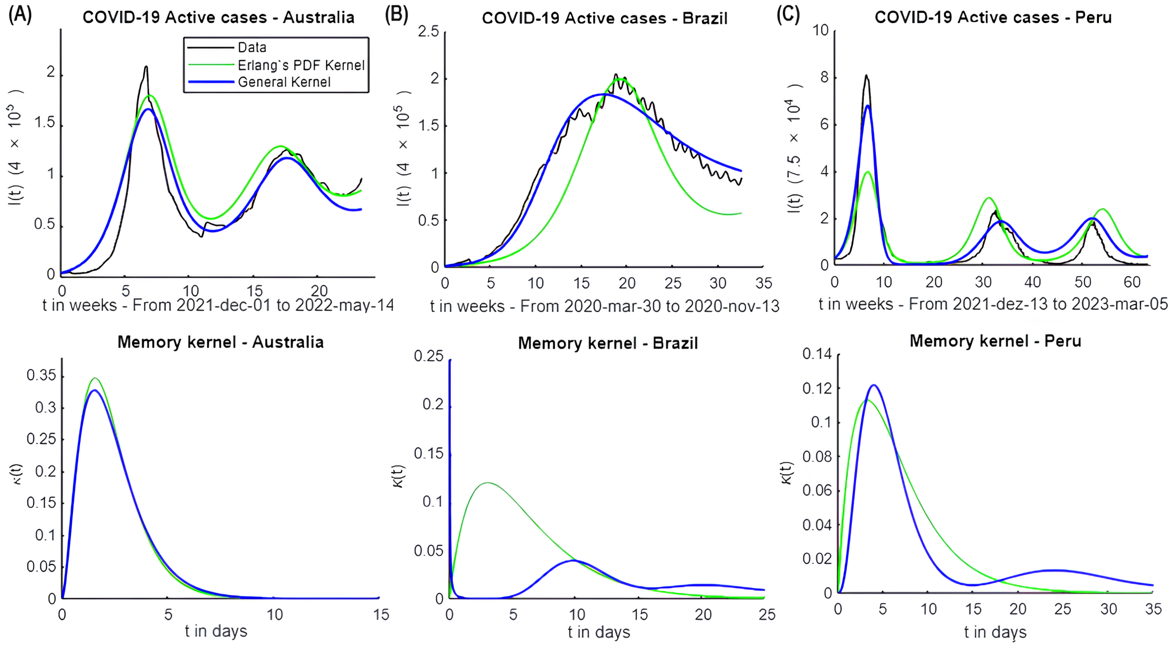

Figure 3.3 – **(A)** Fitting of the reported active cases of two waves of COVID-19 in Australia, along with the respective memory kernels (Erlang PDF and general kernels) at the bottom. **(B)** Fitting of the first COVID-19 wave in Brazil and the corresponding memory kernels. **(C)** Fitting of the reported active cases of three waves of COVID-19 in Peru, with corresponding memory kernels. The optimal parameters for each case are presented in Table 3.1.

	Erlang's PDF Kernel ($\lambda = 0$)						**General Kernel**							
	a	β	r	μ	σ^2	Error	a	α	β	r	λ	μ	σ^2	Error
Australia	1.2797	3	0.7335	2.3442	1.8319	2.6682	1.0816	1.0002	2.7540	0.7320	0.1693	2.4209	2.1381	2.1854
Brazil	0.3286	2	0.3378	6.0864	18.5222	5.4316	1.5382	16.0270	0.0100	0.4749	-499.9997	10.5577	228.1278	1.5725
Peru	0.3058	2	0.5591	6.5402	21.3873	20.0169	0.7144	14.2949	3.8475	0.6226	-0.0021	12.4110	207.3036	11.2104

Table 3.1 – Optimal parameters used in Figure 3.3, and respective mean, variance, and fitting errors. The mean and variance are calculated by Eq. (3.22). For each country and memory kernel, the corresponding nonlinear least-square minimization problem was solved five times, from which the solution with the smallest error was chosen.

In Figure 3.3.B, the optimization results are displayed for Brazil's data over 35 weeks. In this case, the Erlang PDF kernel was unable to describe the rounded shape of the wave, a characteristic that was well captured by the general kernel. Note that the general kernel is singular but non-monotonic. In fact, it belongs to region 5 in Figure 3.2 and combines the features of a Mittag-Leffler PDF singularity and decay with an Erlang PDF peak. As shown in Table 3.1, the variance of the general kernel is greater than the mean squared, which cannot be achieved with Erlang PDF memory kernels, as $\beta = \mu^2/\sigma^2 \geq 1$. In this case, the fitting error is reduced by a factor of 3.6 with the new formulation. The mode of the Erlang PDF kernel is about three days. In the general multimodal kernel, the dynamics is mainly influenced by the present (mode at 0) and the second mode at $t = 10$ days. This can be interpreted as an average main influence over the past 5 days. A third mode at $t = 20$ days also influences the dynamics.

Finally, Figure 3.3.C displays the optimization results for Peru's data over 65 weeks. The 'almost extinction' behavior of the solution is well captured by both the Erlang and the general kernel. However, the general kernel, from region 6 of Figure 3.2, more effectively captures the significantly different amplitudes of the three infection peaks. Moreover, the response of the general kernel allows the second wave to be lower than the third. These features result in a decrease in the fitting error by a factor of 1.8, equivalent to a 44% reduction. The modes of the two memory kernels are around the third and fourth days.

The means of the general memory kernels for Australia, Brazil, and Peru's data fitting are 2.4209, 10.5577, and 12.4110, respectively. These values are believed to be related to the duration of the waves in each region. In Brazil, the peak of the first wave is reached around the twenty-fourth week; in Australia, around the sixth week; and in Peru, the peak of the second wave is reached around the thirty-second week. The mean of each kernel is aligned with half the time until the peak in each country and is influenced by the recovery time for each wave, differences in under-reporting in each region, and variations in population sizes.

Furthermore, the modes of the kernels, falling within the range $[2, 5]$, align with the incubation period of COVID-19 and delays in notification (see, for instance, (93)). This emphasizes how delays can influence the dynamics of infection cases.

3.5 DISCUSSION

We have shown how to build ODE, DDE, and FDE models as specific instances of a comprehensive logistic model. This model is based on a gamma Mittag-Leffler probability distribution function acting as a memory kernel. The gamma Mittag-Leffler PDF kernel extends both weak and strong memory kernels, such as the Dirac delta and Erlang PDF, leading to coherent models in dimension and physical interpretation. This extension enables a direct link between past states and present dynamics while preserving the notion of flux, as the left side of the formulated equations maintains an integer order derivative.

3.5.1 Related works and summary

In Figure 3.1, it is evident that each generated model exhibits unique characteristics, offering a valuable opportunity to exploit these traits depending on the specific phenomena under investigation. This connection between the physical interpretation of the kernel and the diverse dynamics of the solutions underscores the versatility of integral kernels in modeling complex systems. While mathematical theories concerning integral kernels have been relatively well-established, as evidenced by seminal works such as (16, 37, 94), there remains a considerable gap compared to other mathematical frameworks covered in this study, with limited practical application. Although gamma distributions of time delays were employed in practical settings before, such as in pharmacokinetics (2), their explicit connection to FC has not been established until now. References such as (87) also explore the utilization of gamma distributions in modeling excitatory and inhibitory meanfield interactions in neuronal populations, while (88) and (89) delve into the incorporation of gamma-distributed delays to model delayed reactions in human drivers and neuronal dynamics, respectively. Additionally, Mittag-Leffler-distributed delays have been utilized to investigate drug responses in tumor models (90).

Results linking the suitable kernel choice for logistic behavior, given by (3.1), are summarized in Table 3.2. Particularly, the models in Table 3.2 with noninteger values for α and β are novel. The viable asymptotic equilibria are consistent across all cases, as discussed in Sections 3.1 and S.1.A.

	General kernel	General system
	$\kappa(t) = Ct^{\beta-1}e^{-at}E_{\alpha,\beta}(-\lambda t^{\alpha})$	$\begin{cases} y' = ry(1 - Ce^{-at}D^{1-\beta}(e^{at}w)), \\ w' = y - \lambda e^{-at}D^{1-\alpha}(e^{at}w) - aw \end{cases}$
	Special case	Respective system
Dirac delta kernel δ_0: Classical logistic	$\lambda = 0; \beta = 1, C = a \in \mathbb{N}^*, C \to \infty$	$y' = ry(1 - y)$
Erlang PDF kernel: ODE system	$\lambda = 0; \beta \in \mathbb{N}^*$	$\begin{cases} y' = ry(1 - v_\beta), \\ v_1' = \dfrac{\beta(y - v_1)}{\mu}, \\ \vdots \\ v_i' = \dfrac{\beta(v_{i-1} - v_i)}{\mu}, \\ \vdots \\ v_\beta' = \dfrac{\beta(v_{\beta-1} - v_\beta)}{\mu} \end{cases}$
Dirac delta kernel δ_μ: Delay equation	$\lambda = 0; \beta \in \mathbb{N}^*; a = \beta/\mu; \beta \to \infty$	$y' = ry(1 - y(t - \mu))$
Gamma distributed delays	$\lambda = 0$	$\begin{cases} y' = ry(1 - a^{\beta}e^{-at}D^{1-\beta}(e^{at}w)), \\ w' = y - aw \end{cases}$
Mittag-Leffler distributed delays	$0 < \alpha = \beta \leq 1; a = 0$	$\begin{cases} y' = ry(1 - \lambda D^{1-\alpha}w), \\ w' = y - \lambda D^{1-\alpha}w \end{cases}$

Table 3.2 – Logistic-based models with the general gamma Mittag-Leffler memory kernel and special cases. We highlight that the novel general framework encompasses the most well-known models, such as the classical and delayed ones, as well as new fractional models.

We have also developed a classification of kernels within the general framework and their respective solutions (refer to Figure 3.2). This classification enables us to explore the connection between the memory window and the significance of each past time in the current dynamics, and to observe how it impacts the behavior of the model solution.

3.5.2 COVID-19

To demonstrate the practical applicability of our proposed framework, we utilize the generalized gamma Mittag-Leffler memory kernel in a simple SI model to replicate COVID-19 infection data. The outcomes successfully capture the intricate dynamics of COVID-19 across three distinct countries. Moreover, analyzing the adjusted kernels provides valuable insights into how past events influence infection dynamics. For instance, we observe that the primary modes of the adjusted kernels are within the range [2, 5], aligning with the known COVID-19 incubation period and delays in notification (as documented in (93)). Similarly, the means of the adjusted kernels are proportional to the time to the infection peak in each of the three countries. This underscores the versatility of our generalized kernel-based structure in accurately characterizing the multifaceted dynamics inherent in COVID-19 infections.

The predominant approach for modeling COVID-19 involves the use of multi-compartmental models with numerous variables or subpopulations (95, 96, 97, 98). These models typically consist of a large system of ODEs that introduce time constants in a Markovian manner. As previously mentioned, these ODE systems represent particular cases of our general approach, particularly the instances involving Erlang kernels as discussed in Section 3.2.

3.5.3 Extensions

In this work, we have focused on generalizing the logistic model. Immediate extensions of the work include the possibility of adding the Allee Effect to the proposed model, as well as generalizing the memory kernel as a weighted sum of PDFs. Both extensions are presented in Appendix C. Another possible kernel is the uniform delay distribution (99), which can be analyzed with the same tools presented here.

Most importantly, although we initially utilized the logistic equation as a framework, the proposed construction can serve as a versatile technique to incorporate memory effects into any ODE. In fact, any delayed differential equation in the form

$$y'(t) = f(t, y(t), y(t-\tau)) \tag{3.25}$$

can be generalized with gamma Mittag-Leffler-distributed delays as

$$y'(t) = f\left(t, y(t), Ce^{-at}D^{1-\beta}(e^{at}w)\right), \tag{3.26}$$

$$w'(t) = y(t) - \lambda e^{-at}D^{1-\alpha}(e^{at}w) - aw(t), \tag{3.27}$$

where w is an auxiliary variable.

To explore the generalization mentioned above, we illustrate with an example from pharmacokinetics, an area where FC has been successfully applied. For instance, (65) demonstrated that in a simple two-compartment system, changing the order of the derivatives can lead to inconsistent systems and violate mass balance. In a related article from the same year (56), the authors proposed a consistent fractional kinetics modeling approach. They first integrated the ordinary system to derive a system of integral equations and then fractionalized the integrals. While this approach is intriguing, it does not directly address delayed responses as in the construction we present here. Our approach introduces delay in a general manner, enabling the use of diverse modeling frameworks, including systems of ODEs, DDEs, and FDEs. In addition to clarifying the underlying mechanisms, it extends the work presented in (2).

In pharmacokinetics and pharmacodynamics, delays can occur during the absorption phase as it takes time for the drug to be transported from the depot site to the central compartment after extravascular administration. Additionally, the desired effect of the drug may be further delayed in relation to the drug concentration in the central compartment (2). Transit compartment models have been widely used to describe these delayed outcomes (see an example in Figure 3.4.A). As noted in (2), while the transit compartment model approach can effectively capture a variety of data, it has several disadvantages, such as the manual determination of the number of compartments and the inability to adequately describe complex features.

To address these drawbacks, (2) proposed the use of a distributed delay approach to model input feedings and delayed drug effects (1). A particular application was described for modeling the absorption of sorafenib in patients with solid tumors after oral administration. The model aims to describe enterohepatic circulation and absorption delay. First, it is developed a transit-compartmental approach, describing the model as:

$$x_1'(t) = S(t) - k_{tr}x_1(t), \tag{3.28}$$

$$x_i'(t) = k_{tr}x_{i-1}(t) - k_{tr}x_i(t), \qquad i = 2, \cdots, n, \tag{3.29}$$

$$A_a'(t) = k_{tr}x_n(t) - k_{tr}A_a(t) + k_{BA_a}(t)B(t), \tag{3.30}$$

$$A'(t) = k_{tr}A_a(t) - k_e(1-f)A(t) - k_{AB}fA(t), \tag{3.31}$$

$$B'(t) = k_{AB}fA(t) - k_{BA_a}(t)B(t), \tag{3.32}$$

where $S(t)$ represents the dose rate given at time t. The compartment A is the central compartment, A_a is the absorption compartment, and B is the gallbladder compartment. The parameter k_{AB} represents the first-order rate at which the drug is excreted from the central compartment to the gallbladder compartment, while k_{BA_a} represents the rate at which the drug is periodically released from the gallbladder compartment to the absorption compartment. The parameter f represents the fraction of the drug transferred from the central compartment to the gallbladder compartment, and k_e is the first-order elimination rate from the central compartment (see Figure 3.4.A). According to (1), the best way to describe the absorption delay was via three transit compartments. As seen before, this is equivalent to considering an Erlang-distributed delay with $\beta = 3$ (see Eq. (3.10)).

The purpose of (2) was to enhance the model by incorporating a gamma-distributed delay without linking it to FC as in Eq. (3.21). This involves replacing the transit compartments for absorption with a single term $\int_0^t g(\tau)S(t-\tau)d\tau$, where g represents the PDF of the gamma distribution with rate parameter k_{tr} and shape parameter β, which can be any positive number (refer to Figure 3.4.B). By fixing k_{tr} and varying β, the mean of the delay distribution varies proportionally with β. The study demonstrated that β can be reliably estimated, eliminating the need to manually test different structural models to find an appropriate one, as required by the compartmental models approach.

Our new framework (Figure 3.4.C) enables us to enhance the approach introduced in (2) by incorporating a gamma Mittag-Leffler distribution. In this case, the new differential equation for A_a is given by:

$$A_a' = Ce^{-k_{tr}t}D^{1-\beta}(e^{k_{tr}t}w) - k_{tr}A_a + k_{BA_a}B, \tag{3.33}$$

where $C = k_{tr}^{\beta} + k_{tr}^{\beta-\alpha}\lambda$, and w is an auxiliary variable such that

$$w' = S - \lambda e^{-k_{tr}t}D^{1-\alpha}(e^{k_{rt}t}w) - k_{tr}w. \tag{3.34}$$

In this generalization, the mean of the delay distribution is obtained by (3.22). As previously mentioned, when $\lambda = 0$, we revert to the gamma-distributed delay shown in Figure 3.4.B. Furthermore, if $\beta \in \mathbb{N}^*$, we recover the compartmental model depicted in Figure 3.4.A.

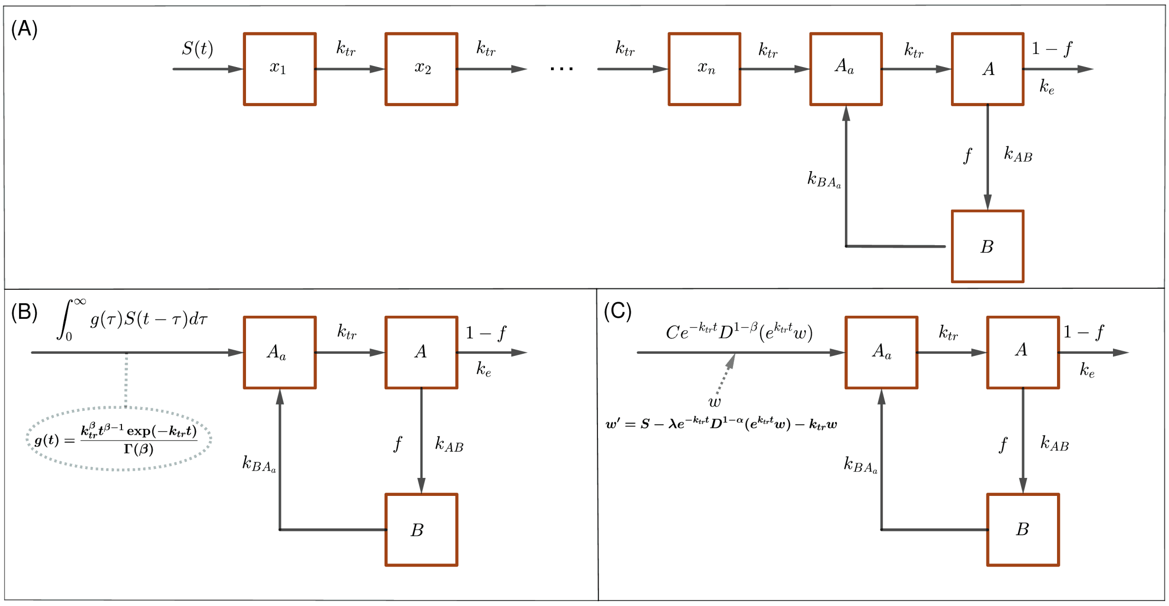

Figure 3.4 – The diagram shows models that describe the delayed absorption of cancer drugs with enterohepatic circulation. Panel **(A)** illustrates a compartmental model to describe the delayed absorption (1), where k_{tr} is the transition rate between transit compartments $x_1, \cdots, x_n$. In panel **(B)**, the absorption delay is generalized with a delay kernel g. In (2), g is the PDF of a gamma distribution. Panel **(C)** uses our FC approach to describe the absorption delay with a gamma Mittag-Leffler distribution. If $\lambda = 0$, the gamma-distributed delay of panel **(B)** is recovered, and if, in addition, $\beta \in \mathbb{N}^*$, we recover the compartmental model of panel **(A)**.

3.5.4 Limitations and future works

We explored a new mathematical framework across three distinct application scenarios: population dynamics, epidemiology, and pharmacokinetics. A meticulous and comprehensive sensitivity analysis was conducted for population dynamics, as illustrated in Figures 3.1 and 3.2. In the context of COVID-19 application, we successfully correlated the principal modes and mean values of the adjusted distributions with key factors such as the COVID-19 incubation period, delays in notification, and time to the first infection peak. However, the mechanistic interpretations of each parameter within our general formulation were specific to the application at hand. In future works, it would be beneficial to explore methods for interpreting the parameters of the pharmacokinetics model (3.33)-(3.34) and the generalization outlined in Eq. (3.26) in a manner similar to that presented in Figures 3.1 and 3.2.

3.6 METHODS

3.6.1 Model description

We derive our mathematical models using the gamma Mittag-Leffler probability distribution function as the kernel in Eq. (3.1).

3.6.1.1 Gamma Mittag–Leffler probability distribution function

The Mittag-Leffler distribution can be extended to the gamma Mittag–Leffler distribution (85). We consider the generalized gamma Mittag–Leffler probability distribution function in the form of (3.2).

3.6.1.2 Proof

To prove that (3.2) describes a PDF, we must ensure positivity and $\int_0^\infty f(x)dx = 1$. We examine each condition:

- $a = 0, \lambda > 0$ and $0 < \alpha = \beta \leq 1$

  In this case, the PDF of the fractional Poisson process is described in Eq. (1.24).

- $-a^\alpha < \lambda \leq 0$, $a > 0$, $\alpha, \beta > 0$

  The positivity of $f(x)$ depends on the positivity of C once $-\lambda x^\alpha \geq 0$ for $x \geq 0$, which implies $\lambda > -a^\alpha$.

  Under the same condition, we can utilize the Laplace transform of $x^{\beta-1}E_{\alpha,\beta}(-\lambda x^\alpha)$ (4), resulting in:

  $$\int_0^\infty C x^{\beta-1} e^{-ax} E_{\alpha,\beta}(-\lambda x^\alpha) dx = C \frac{a^{\alpha-\beta}}{a^\alpha + \lambda} = 1. \tag{3.35}$$

- $0 \leq \lambda < a^\alpha$, $a > 0$, $0 < \alpha \leq 1$, and $\alpha \leq \beta$

  With these hypotheses, $E_{\alpha,\beta}(-\lambda x^\alpha)$ is completely monotonic (4); in particular, it is positive. The constant C is also positive, so $f(x)$ is positive. Furthermore, it has a Laplace transform as shown in Eq. (3.35).

3.6.1.3 A general logistic model

The PDF of the gamma Mittag-Leffler distribution (3.2) can be used as a memory kernel $\kappa(t) = f(t)$, which transforms (3.1) into (3.3).

By applying the properties of the Mittag-Leffler functions and Laplace transforms using fractional Riemann-Liouville integral and derivative, we obtain:

$$\begin{aligned} y' &= ry - ryCe^{-at}\mathcal{L}^{-1}\left[\mathcal{L}\left[t^{\beta-1}E_{\alpha,\beta}(-\lambda t^{\alpha})\right]\mathcal{L}[e^{at}y]\right] && (3.36)\\ &= ry - ryCe^{-at}\mathcal{L}^{-1}\left[\frac{s^{\alpha-\beta}}{s^{\alpha}+\lambda}\mathcal{L}[e^{at}y]\right] && (3.37)\\ &= ry - ryCe^{-at}\mathcal{L}^{-1}\left[s^{1-\beta}\mathcal{L}\left[\int_0^t E_{\alpha}(-\lambda(t-\tau)^{\alpha})e^{a\tau}y(\tau)d\tau\right]\right] && (3.38)\\ &= ry - ryCe^{-at}D^{1-\beta}(e^{at}w), && (3.39) \end{aligned}$$

where

$$w = \int_0^t E_{\alpha}(-\lambda(t-\tau)^{\alpha})e^{-a(t-\tau)}y(\tau)d\tau. \tag{3.40}$$

Next, we differentiate using Leibniz's rule and utilize

$$\begin{aligned} E_{\alpha,\alpha}(z) &= \sum_{k=0}^{\infty}\frac{k!}{\Gamma(\alpha k+\alpha)}\frac{z^k}{k!} && (3.41)\\ &= \sum_{k=0}^{\infty}\frac{(\alpha k+\alpha)k!}{\Gamma(\alpha k+\alpha+1)}\frac{z^k}{k!} = \alpha E^2_{\alpha,1+\alpha}(z). && (3.42) \end{aligned}$$

By using Lemma 1.1, we arrive at

$$w' = y - \int_0^t \left(\lambda(t-\tau)^{\alpha-1}E_{\alpha,\alpha}(-\lambda(t-\tau)^{\alpha}) + aE_{\alpha}(-\lambda(t-\tau)^{\alpha})\right)e^{-a(t-\tau)}y(\tau)d\tau, \tag{3.43}$$

which leads to the logistic model with gamma Mittag-Leffler distributed delays as given by (3.4).

Note that, if $\alpha > 1$, we have $D^{1-\alpha} = I^{\alpha-1}$, where $I^{\alpha-1}$ is the fractional Riemann-Liouville integral of order $\alpha - 1$. The same applies if $\beta > 1$, where $D^{1-\beta} = I^{\beta-1}$. Additionally, the model can be expressed using the Caputo derivative. For sufficiently smooth functions, Riemann-Liouville and Caputo fractional derivatives satisfy the following relationship (52):

$${}^{C}D^{\alpha}f(t) = D^{\alpha}f(t) - \sum_{k=0}^{n-1}\frac{f^{(k)}(0)t^{k-\alpha}}{\Gamma(k-\alpha+1)}, \tag{3.44}$$

where $0 \leq n-1 < \alpha \leq n$, with $n \in \mathbb{N}$. In particular, if both α and β are less than or equal to 1, and the solutions are assumed to be absolutely continuous, then the model (3.4) can be expressed using the Caputo fractional derivative instead of the Riemann-Liouville derivative, provided that $w(0) = 0$.

In the following chapters, we explore the unifying viewpoint constructed in this chapter within the context of electrophysiology. We apply the kernel-based framework to describe how memory effects influence observable physiological phenomena.

4 REVISITING THE MODELING OF CELL ELECTROPHYSIOLOGY USING MEMORY KERNELS

In this chapter, we apply the unified kernel-based framework developed previously to the modeling of cell electrophysiology. The central idea remains unchanged: the present state of the system depends on its past through a memory kernel. We explore our publication (100) and discuss how memory structure influences electrophysiological phenomena.

An action potential (AP), defined in Subsection **1.3.3**, is driven primarily by the activity of voltage-gated ion channels in the cell membrane. In neurons, simple models suggest that the initial rapid depolarization is triggered by the opening of voltage-gated sodium channels, while the repolarization phase is controlled by their inactivation and the opening of potassium channels (101). The relationship between membrane potential and channel states is inherently history-dependent. Macroscopic conductances at time t depend on channel-state occupancies shaped by the past transmembrane voltage trajectory, which can be represented through memory kernels (with discrete delays as a simple limiting case).

In Section 4.1, we introduce a novel mathematical model for AP generation based on a single DDE, building upon the work of Rameh, Cherry, and Santos (2020) (27). Despite its simplicity, this conductance-based model is suitable for modeling excitable cells and captures key electrophysiological features, including subthreshold, suprathreshold, and all-or-nothing behaviors, as discussed in Subsection **4.2.1**. The compact memory-based representation enables transparent mathematical decompositions and the derivation of closed-form approximations for experimentally relevant refractory metrics (*e.g.*, strength–interval curves) in terms of explicit interpretable parameters, as discussed in Subsection **4.2.2**. Subsection **4.2.3** further explores the response to prolonged or constant stimuli.

In Section 4.3, we discuss different types of memory kernels and how the proposed framework connects to classical ODE-based cell models, including Hodgkin-Huxley (HH) and CTMC formulations. We also outline extensions to FC models. HH-type models represent channel kinetics using additional ODE state variables (gating probabilities) that converge towards voltage-dependent steady states. In contrast, our DDE formulation explicitly incorporates history dependence through discrete delays, corresponding to Dirac kernels in a general Volterra memory-kernel description. By substituting the Dirac kernel with other kernel families, the same framework can recover ODE “linear-chain” (Erlang) representations and naturally link to CTMC-based models (via phase-type kernels). Fractional kernels offer an extension capable of representing long-tailed memory when supported by data.

Conclusions and final discussions are presented in Section 4.4.

4.1 A SIMPLE MATHEMATICAL MODEL FOR THE ACTION POTENTIAL

We present a simple mathematical description of the dynamics of the transmembrane potential V during an AP using a reduced differential formulation. Figure 4.1 illustrates the key components of our model: a cell enclosed by a membrane and ion channels for sodium and potassium. Background (leak) currents I_{Kb} and I_{Nab} represent the potassium and sodium currents that persist even when the cell is at resting steady state. On the other hand, voltage-gated ion channels regulate the movement of potassium and sodium ions across the cell membrane in response to changes in the membrane's electrical potential, resulting in potassium current I_{K} and sodium current I_{Na}.

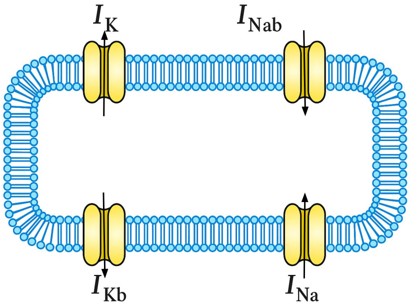

Figure 4.1 – A schematic diagram illustrating the current flows across the cell membrane in the proposed model.

By conservation of charge, for an isolated cell the net transmembrane current satisfies $C_{\mathrm{m}} dV/dt + I_{\mathrm{Na}} + I_{\mathrm{Nab}} + I_{\mathrm{K}} + I_{\mathrm{Kb}} - I_{\mathrm{stim}} = 0$, where I_{stim} is the stimulus current. To describe the relationship between electric current and electric potential, we adopt a linear Ohmic formulation for ionic currents. For example, for background sodium, we use:

$$I_{\mathrm{Nab}} = G_{\mathrm{Nab}}\,(V - V_{\mathrm{Na}}), \tag{4.1}$$

where V is the transmembrane potential, G_{Nab} is the sodium background conductance, and V_{Na} is the sodium Nernst potential. Similar equations can be applied to other currents. By using these equations, we can derive:

$$C_{\mathrm{m}} \frac{dV}{dt} + (G_{\mathrm{K}} + G_{\mathrm{Kb}})\,(V - V_{\mathrm{K}}) + (G_{\mathrm{Na}} + G_{\mathrm{Nab}})\,(V - V_{\mathrm{Na}}) - I_{\mathrm{stim}} = 0. \tag{4.2}$$

4.1.1 Voltage-gated ion channels

In 1952, Hodgkin and Huxley conducted experiments to observe and document voltage-dependent conductance changes (22), which were later interpreted as channel gating (102). These experiments provided insights into how transmembrane voltage influences ion channel gating, the process of channel opening and closing. The classical Hodgkin-Huxley (HH) model describes an AP by considering voltage-gated ion channels and their probabilities of being closed, open, or inactivated. The transitions between states of the gates are determined by time-varying rates. The model is represented by the ODE:

$$C_{\mathrm{m}}\frac{dV}{dt}+C_{\mathrm{K}}n^4\left(V-V_{\mathrm{K}}\right)+C_{\mathrm{Na}}m^3h\left(V-V_{\mathrm{Na}}\right)+C_{\mathrm{L}}\left(V-V_{\mathrm{L}}\right)-I_{\mathrm{stim}}(t)=0. \tag{4.3}$$

Here, n, m, and h are dimensionless probabilities described by a set of three differential equations, all following the general form of Eq. (4.43). Specifically, each gating variable satisfies

$$\frac{dn}{dt}=\alpha_n(1-n)-\beta_n n=\frac{\left(\frac{\alpha_n}{\alpha_n+\beta_n}\right)-n}{\frac{1}{\alpha_n+\beta_n}}, \tag{4.4}$$

$$\frac{dm}{dt}=\alpha_m(1-m)-\beta_m m=\frac{\left(\frac{\alpha_m}{\alpha_m+\beta_m}\right)-m}{\frac{1}{\alpha_m+\beta_m}}, \tag{4.5}$$

$$\frac{dh}{dt}=\alpha_h(1-h)-\beta_h h=\frac{\left(\frac{\alpha_h}{\alpha_h+\beta_h}\right)-h}{\frac{1}{\alpha_h+\beta_h}}, \tag{4.6}$$

where the functions α and β are given by

$$\alpha_n(V)=\frac{0.01(10-V)}{\exp\left(\frac{10-V}{10}\right)-1},\quad \beta_n(V)=0.125\exp\left(-\frac{V}{80}\right), \tag{4.7}$$

$$\alpha_m(V)=\frac{0.1(25-V)}{\exp\left(\frac{25-V}{10}\right)-1},\quad \beta_m(V)=4\exp\left(-\frac{V}{18}\right), \tag{4.8}$$

$$\alpha_h(V)=0.07\exp\left(-\frac{V}{20}\right),\quad \beta_h(V)=\frac{1}{\exp\left(\frac{30-V}{10}\right)+1}. \tag{4.9}$$

Depolarization corresponds to a shift of the membrane potential V (with $V = V_{\mathrm{in}} - V_{\mathrm{out}}$) from its negative resting value towards zero (*i.e.*, becoming less negative and possibly positive), reflecting a net increase of intracellular positive charge due to inward ionic currents. This is usually caused by an influx of sodium ions, while repolarization is the return to the resting steady-state membrane potential, primarily driven by an outflow of potassium ions and the inactivation of sodium channels. During the hyperpolarization phase, voltage-gated potassium channels that are still open cause the membrane potential to drop below the resting potential before stabilizing. Finally, all voltage-gated channels close.

The HH gating equations for sodium channels can be derived based on the assumption that sodium channels have three activation gates and one inactivation gate, each of which can be in a closed or open state. If these gates operate independently, the fraction of open Na^+ channels is represented as m^3h. For potassium channels, if there are four n gates per channel and all must be open for K^+ to flow, the fraction of open potassium channels is n^4 (103).

4.1.2 Simple delay-based models for ion channels

Figure 4.2 illustrates the opening of potassium channels in response to changes in transmembrane voltage. Panel B shows that potassium conductance increases with voltage. This relationship can be mathematically represented by the potassium channel conductance as a function of voltage, denoted as $G_{\mathrm{K}}(V(t))$. A simple linear model can capture the positive correlation between voltage and potassium conductance:

$$G_{\mathrm{K}}(V) = C_{\mathrm{K}} V, \tag{4.10}$$

where C_{K} represents a constant linear coefficient. Two modifications are introduced. First, we introduce a shift by replacing V with $V - V_{\mathrm{th}}$. This adjustment results in a threshold for the opening of potassium channels. We introduce the Heaviside step function $H(X)$, defined as:

$$H(X) = \begin{cases} 0, & X < 0 \\ 1, & X \geq 0. \end{cases} \tag{4.11}$$

This yields the simplified potassium conductance model:

$$G_{\mathrm{K}}(V) = C_{\mathrm{K}}\ (V - V_{\mathrm{th}})\ H(V - V_{\mathrm{th}}). \tag{4.12}$$

The Heaviside function ensures that $G_{\mathrm{K}}(V)$ remains non-negative even if $V < V_{\mathrm{th}}$, thereby maintaining physically meaningful conductance values. Using the HH model as a reference, we discuss how conductances respond to changes in membrane voltage. Accordingly, the second modification in the construction of the model pertains to the response time of ion channels to changes in transmembrane voltage.

In Figure 4.2.A, it is observed that the increase in G_{K} following a voltage pulse occurs gradually over time. To account for finite channel response times (*i.e.*, non-instantaneous relaxation toward equilibrium), we introduce a delay parameter τ_{K} is introduced, such that $G_{\mathrm{K}}(t) = G_{\mathrm{K}}(V(t - \tau_{\mathrm{K}}))$. Thus, the conductance at time t depends on the voltage at an earlier time $t - \tau_{\mathrm{K}}$.

With this adjustment, the potassium current gating model is finalized as:

$$G_{\mathrm{K}}(V) = C_{\mathrm{K}}\ (V(t - \tau_{\mathrm{K}}) - V_{\mathrm{th}})\ H(V(t - \tau_{\mathrm{K}}) - V_{\mathrm{th}}). \tag{4.13}$$

This equation can be rewritten as

$$G_{\mathrm{K}}(V) = C_{\mathrm{K}}\ n(t - \tau_{\mathrm{K}}), \tag{4.14}$$

by introducing a normalized and dimensionless gating variable n:

$$n(t) = \frac{(V(t) - V_{\mathrm{th}})\ H(V(t) - V_{\mathrm{th}})}{V_{\mathrm{Na}} - V_{\mathrm{th}}}. \tag{4.15}$$

At this point, we rescale C_{K} accordingly so that it has units of $\mathrm{mS} \cdot \mathrm{cm}^{-2}$.

Figure 4.2 also illustrates how sodium channels open in response to changes in the transmembrane voltage. Initially, the conductance of sodium channels increases after a voltage shift but eventually decreases. As with potassium channels, the peak sodium current also increases with the pulse amplitude, leading to the recruitment of more sodium channels to open as the transmembrane voltage increases. This phase is known as the activation phase of sodium channels. As a simplifying assumption, we take sodium and potassium channels to share the same activation threshold. We describe sodium channel activation using a simple model:

$$m(t) = \frac{(V(t) - V_{\text{th}})H(V(t) - V_{\text{th}})}{V_{\text{Na}} - V_{\text{th}}}. \tag{4.16}$$

However, unlike potassium channels, sodium channels undergo an inactivation phase. This phase is characterized by a decrease in voltage-dependent conductance to zero as the voltage pulse amplitude increases. The inactivation phase can be represented by the model:

$$h(t) = \frac{(V_{\text{cut}} - V(t))\ H(V_{\text{cut}} - V(t))}{V_{\text{cut}} - V_{\text{K}}}, \tag{4.17}$$

where V_{cut} represents the threshold at which voltage-dependent sodium channels become inactivated. Note that there is a negative relationship between h and the voltage pulse. As the voltage V increases, the value of h decreases until it reaches zero, with $h = 0$ indicating complete inactivation of the sodium channels. By incorporating delays in the activation and inactivation responses to changes in voltage V, a simple model for the gating of sodium channels can be established:

$$G_{\text{Na}}(V) = C_{\text{Na}}\ m(V(t - \tau_{\text{m}}))\ h(V(t - \tau_{\text{h}})). \tag{4.18}$$

Here, C_{Na} denotes the linear relationship between voltage and conductance changes, τ_{m} governs the activation speed, and τ_{h} represents the inactivation phase delay. In Figure 4.2.B, the lower panel shows $G_{\text{Na}} + G_{\text{Nab}}$ in red as a function of V without delays. It displays a parabolic shape between V_{th} and V_{cut}, and is zero elsewhere. This representation effectively captures the initial rise in sodium conductance during activation, followed by a decline during inactivation as V continues to rise.

A key feature of the model is the role of delays in shaping the AP. Experimental observations show that the activation of sodium channels is the quickest response to a voltage step, while the opening of potassium channels and the inactivation of sodium channels are much slower processes. Without these different time scales, sodium channels would activate and inactivate instantly, disrupting the depolarization phase. Similarly, instant potassium channel opening would lead to rapid repolarization, counteracting sodium influx before full depolarization. These delays ensure the characteristic shape of the AP, with a rapid upstroke driven by sodium activation and a slower repolarization phase controlled by potassium channel activation and sodium inactivation. This construction provides a minimal delay-based alternative to HH-type models, capturing essential electrophysiological features with reduced dimensionality, as explored next.

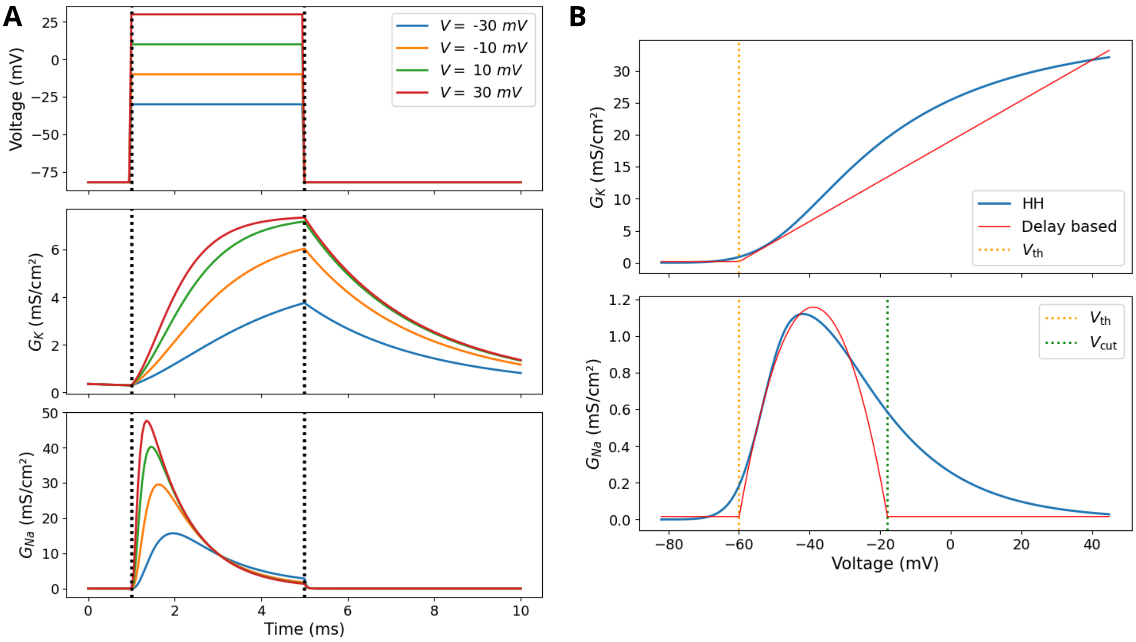

Figure 4.2 – Typical delay-based results of voltage-dependent ionic conductances compared with the HH model. **(A)** Time-dependent responses of potassium (G_{K}) and sodium (G_{Na}) conductances to step changes in membrane potential (top panel), for different voltage amplitudes. The delayed activation and inactivation reproduce the characteristic temporal hierarchy observed experimentally: rapid sodium activation followed by slower potassium activation and sodium inactivation. The average ranges we used to fit the delay values in DDE model were obtained from voltage clamp experiments using the classical HH model. **(B)** Static conductance–voltage relationships. The potassium conductance (top) exhibits a monotonic increase above the threshold V_{th}, while sodium conductance (bottom) displays a non-monotonic profile due to activation and inactivation. The proposed delay-based model (red) captures the qualitative behavior of the HH model (blue) with reduced complexity, vanishing beyond V_{cut}.

4.1.3 A delay-based model for the action potential

The simplified model for the AP is obtained by combining the elements introduced above, resulting in the following equations:

$$\begin{aligned} C_{\mathrm{m}}\frac{dV}{dt} &+ (G_{\mathrm{Kb}} + C_{\mathrm{K}}\ n(t-\tau_{\mathrm{K}}))\ (V - V_{\mathrm{K}}) \\ &+ (G_{\mathrm{Nab}} + C_{\mathrm{Na}}\ m(t-\tau_{\mathrm{m}})\ h(t-\tau_{\mathrm{h}}))\ (V - V_{\mathrm{Na}}) - I_{\mathrm{stim}}(t) = 0, \quad t > 0, \qquad (4.19) \\ V(t) &= V_0, \quad t \le 0. \qquad (4.20) \end{aligned}$$

The following algebraic equations complement this delay differential equation:

$$n(t) = m(t) = \frac{(V(t) - V_{\mathrm{th}})\ H(V(t) - V_{\mathrm{th}})}{V_{\mathrm{Na}} - V_{\mathrm{th}}}, \qquad (4.21)$$

$$h(t) = \frac{(V_{\mathrm{cut}} - V(t))\ H(V_{\mathrm{cut}} - V(t))}{V_{\mathrm{cut}} - V_{\mathrm{K}}}. \qquad (4.22)$$

Despite consisting of a single differential equation and 12 parameters (V_{K}, V_{Na}, C_{m}, V_{th}, V_{cut}, G_{Kb}, C_{K}, τ_{K}, G_{Nab}, C_{Na}, τ_{m}, τ_{h}), some of which biologically determined, this model can accurately replicate an AP, sodium and potassium conductance variations over time, and other crucial mechanisms.

Figure 4.3.A illustrates a typical AP, while panel B shows the evolution of sodium and potassium conductances over time. Sodium conductance rapidly increases at the onset of depolarization, reaching a peak before inactivating, while potassium conductance rises more slowly and remains elevated during repolarization, aiding in restoring the membrane potential to its resting value.

The normalized gating variables in Figure 4.3.C illustrate the rapid activation of sodium, followed by its inactivation, and the activation of potassium. In this parameter setting (refer to Table 4.1), sodium inactivation is the last gating variable to recover.

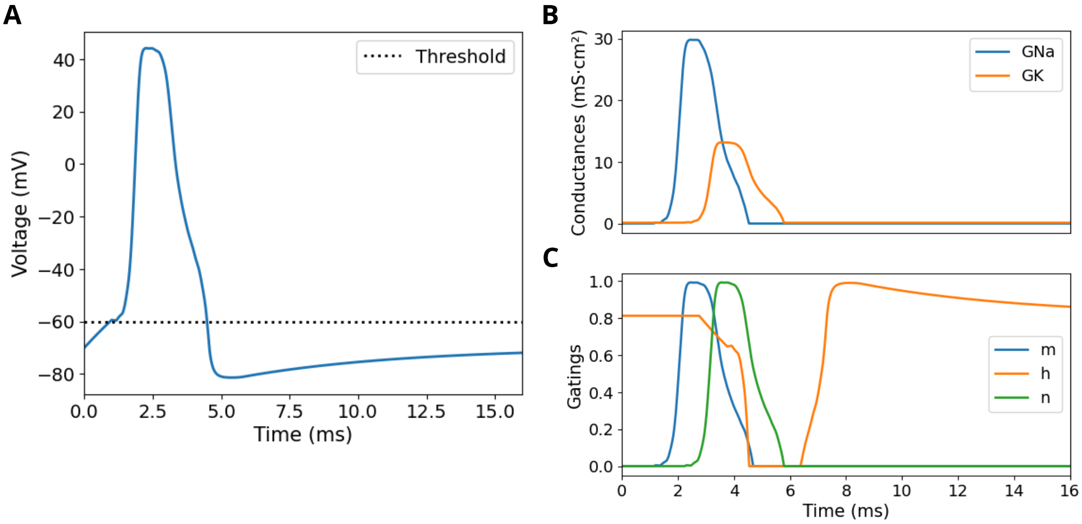

Figure 4.3 – The typical neuron AP behavior triggered by the constructed delay-based model is shown. Panel **(A)** depicts the transmembrane voltage over time and the threshold. A 1 ms stimulus of 11.5 μA/cm^2 was applied at time 0. Panel **(B)** shows the evolution in sodium and potassium conductances. Panel **(C)** displays the gating variables m (sodium channel activation), h (sodium channel inactivation), and n (potassium channel activation).

4.2 ACTION POTENTIAL FEATURES OF THE NEW DDE-BASED MODEL

Despite its simplicity, our conductance-based model captures key electrophysiological features of neurons, including all-or-nothing behavior, the refractory period, and the response to prolonged stimuli, as discussed next.

4.2.1 Subthreshold, suprathreshold and all-or-nothing behaviors

For subthreshold stimuli (small amplitude or short duration), the membrane potential shows passive responses. In this case, the voltage depolarizes in proportion to the applied current but does not trigger an AP. When $V < V_{\mathrm{th}}$, V satisfies the linear differential equation

$$C_\mathrm{m}\frac{dV}{dt} + G_\mathrm{Kb}\;(V - V_\mathrm{K}) + G_\mathrm{Nab}\;(V - V_\mathrm{Na}) - I_\mathrm{stim}(t) = 0. \tag{4.23}$$

This equation can be rewritten to allow an explicit solution by defining the total conductance as $G_\mathrm{b} = G_\mathrm{Kb} + G_\mathrm{Nab}$ and the steady-state voltage V_eq given by:

$$V_\mathrm{eq}(t) = \frac{G_\mathrm{Kb}V_\mathrm{K} + G_\mathrm{Nab}V_\mathrm{Na} + I_\mathrm{stim}(t)}{G_\mathrm{b}}. \tag{4.24}$$

When activated, the inward stimulus increases the equilibrium V_eq. The solution for $V(t)$, considering that V_eq is constant in the interval from t_0 to t, follows an exponential approach towards V_eq:

$$V(t) = V_\mathrm{eq} + (V_0 - V_\mathrm{eq})e^{-(t-t_0)/\tau}, \tag{4.25}$$

where t_0 represents the initial time of each phase and $\tau = C_\mathrm{m}/G_\mathrm{b}$. When the stimulus is removed at $t = \Delta t$, the initial condition is updated to $V_0 = V(\Delta t)$ and V_eq diminishes. The membrane capacitance ensures that voltage changes occur over a characteristic timescale given by the time constant τ. Figure 4.4.A illustrates this subthreshold behavior.

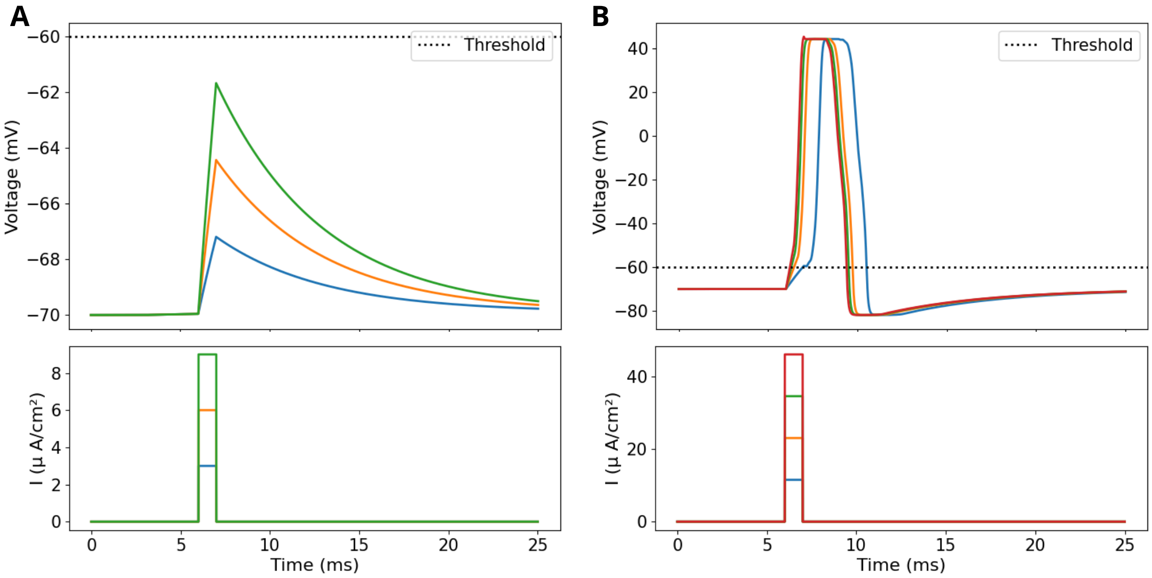

Figure 4.4 – The AP waveform is related to the amplitude of the current density I_stim with a duration of 1 ms. In panel **(A)**, subthreshold stimuli result in purely passive responses of the membrane potential. Panel **(B)** shows suprathreshold behaviors. The results highlight the all-or-nothing property.

For suprathreshold stimuli, the behavior of the upstroke can also be analytically modeled. Assuming the time constants τ_h and τ_K are long, we can consider $V(t - \tau_\mathrm{h})$ and $V(t - \tau_\mathrm{K})$ as approximately constant and equal to V_th. This results in the inactivation variable remaining at $\overline{h} = V_\mathrm{cut} - V_\mathrm{th}$ and the potassium conductance can be approximated by its background value G_{Kb}. Additionally, when τ_{m} is small, we can consider $V(t-\tau_{\mathrm{m}}) \approx V(t)$. Consequently, the sodium conductance follows:

$$G_{\mathrm{Na}}(V) = C_{\mathrm{Na}}\, \overline{h}\, (V - V_{\mathrm{th}})\ H(V - V_{\mathrm{th}}). \tag{4.26}$$

Once the membrane potential V surpasses V_{th}, the sodium conductance significantly increases, dominating the dynamics of V. Substituting this into the membrane equation and neglecting the small contributions from G_{Nab}, G_{Kb}, and I_{stim}, we obtain:

$$C_{\mathrm{m}}\, \frac{dV}{dt} = -C_{\mathrm{Na}}\, \overline{h}\, (V - V_{\mathrm{th}})\ (V - V_{\mathrm{Na}}). \tag{4.27}$$

The right-hand side vanishes at $V = V_{\mathrm{th}}$ or $V = V_{\mathrm{Na}}$, which are equilibrium points (unstable and stable, respectively). If the initial voltage V_0 is slightly above the threshold, the solution moves away from V_{th} towards V_{Na} during the AP upstroke. The solution for the depolarization phase has a closed analytical expression:

$$V(t) = V_{\mathrm{th}} + \frac{V_{\mathrm{Na}} - V_{\mathrm{th}}}{1 + Be^{-r(t-t_0)}}, \tag{4.28}$$

where

$$B = \frac{V_{\mathrm{Na}} - V_0}{V_0 - V_{\mathrm{th}}}, \qquad r = \frac{C_{\mathrm{Na}}\overline{h}}{C_{\mathrm{m}}}(V_{\mathrm{Na}} - V_{\mathrm{th}}). \tag{4.29}$$

This is a logistic-type curve (sigmoid or S-shape) transitioning from $V_0 = V_{\mathrm{th}} + \epsilon$, for a small $\epsilon > 0$ at $t = t_0$, to V_{Na} as t increases.

Figure 4.4.B demonstrates how the AP waveform remains largely unchanged even when the amplitude of I_{stim} is increased fourfold. Further increases in I_{stim} may cause noticeable changes in the AP shape but would be beyond physiological ranges.

4.2.2 Refractory period

The primary factor responsible for refractory behavior is sodium inactivation. Sodium channels open rapidly during the AP but quickly enter an inactivated state, preventing immediate reopening even with membrane depolarization. Potassium channels also contribute to the refractory period by remaining open after the AP, hyperpolarizing the membrane and making it more difficult to trigger a new AP (22).

Figure 4.5.A illustrates the relative refractory period in which voltage-gated potassium channels close before the inactivation phase of sodium channels ends. In Figure 4.5.B, we adjusted the time constants to $\tau_{\mathrm{h}} = 1.5$ and $\tau_{\mathrm{K}} = 2.5$. This panel uses a deliberately non-physiological second stimulus amplitude as a diagnostic illustration: it highlights that, during incomplete recovery, delayed potassium activation together with residual sodium inactivation can dominate the net current balance and prevent a second full upstroke even when a large inward stimulus is applied. Note that refractoriness relates to recovery “memory times” (τ_h and τ_K), which makes it possible to connect refractory behavior to explicit kinetic parameters.

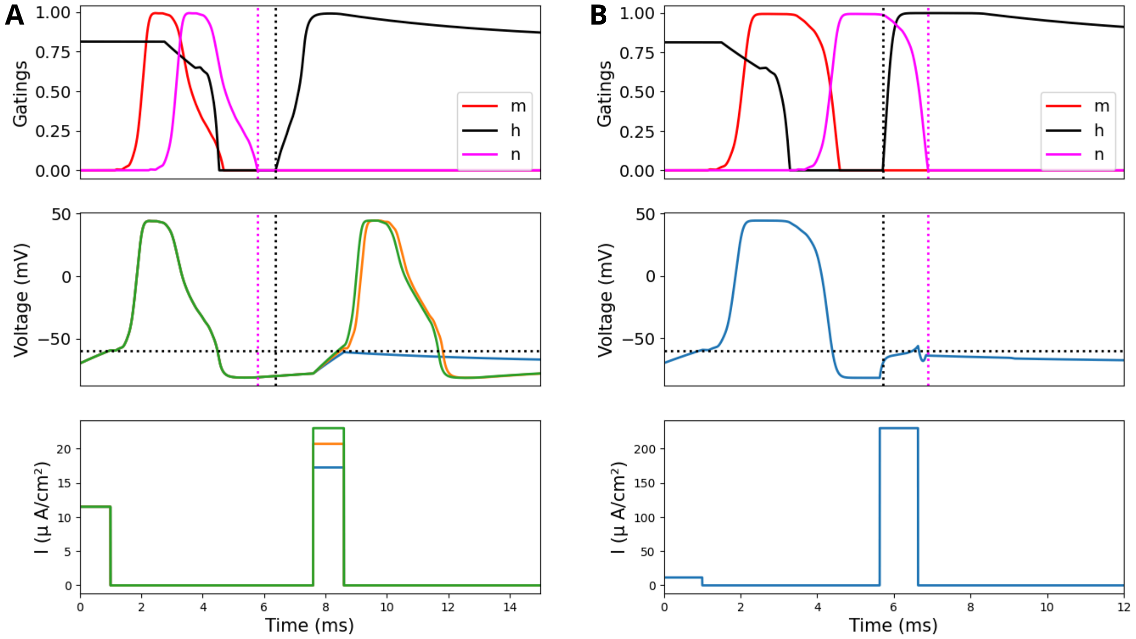

Figure 4.5 – The horizontal dotted lines indicate the threshold $V_{\mathrm{th}} = -60$ mV, while the vertical dotted lines represent the closure of potassium gated-channels and the end of the sodium inactivation period. The first stimulus has an amplitude of $11.5\,\mu\mathrm{A/cm}^2$. Standard parameters are taken from Table 4.1. **(A)** illustrates the refractory period operation when voltage-gated potassium channels close before the sodium channel inactivation phase ends. **(B)** In this simulation, $\tau_{\mathrm{h}} = 1.5$ and $\tau_{\mathrm{K}} = 2.5$. The voltage response to inputs when the second stimulus has a non-biological amplitude of $20 \times 11.5\,\mu\mathrm{A/cm}^2$ is shown.

4.2.2.1 Strength-interval relation

The strength-interval curve provides information about a neuron's excitability, showing the threshold stimulus strength required to generate an AP at various recovery time intervals after the initial stimulus (104, 105).

Consider a stimulus I_{stim} lasting 1 ms applied t^* ms after the initial stimulus. We assume that $h(t^*+1) > 0$ and approximate $V(t-\tau_{\mathrm{m}}) \approx V(t)$. Let us consider the case where the voltage-gated potassium channel is closed at time t^*. From t^* to t^*+1, the following inequality holds:

$$C_{\mathrm{m}} \frac{dV}{dt} \geq -G_{\mathrm{Kb}}\,(V - V_{\mathrm{K}}) - G_{\mathrm{Nab}}\,(V - V_{\mathrm{Na}}) + I_{\mathrm{stim}}. \tag{4.30}$$

The inequality reflects the possibility of an inward sodium current before t^*+1 if the sodium inactivation phase has already ended. Using Eq. (4.25), we can deduce that:

$$V(t^*+1) \geq V_{\mathrm{eq}} + (V(t^*) - V_{\mathrm{eq}})\, e^{-1/\tau}, \tag{4.31}$$

where

$$V_{\mathrm{eq}} = \frac{G_{\mathrm{Kb}} V_{\mathrm{K}} + G_{\mathrm{Nab}} V_{\mathrm{Na}} + I_{\mathrm{stim}}}{G_{\mathrm{b}}} = V_{\mathrm{eq}}^* + \frac{I_{\mathrm{stim}}}{G_{\mathrm{b}}}, \tag{4.32}$$

for

$$V_{\text{eq}}^* = \frac{G_{\text{Kb}}V_{\text{K}} + G_{\text{Nab}}V_{\text{Na}}}{G_{\text{b}}}. \tag{4.33}$$

To ensure that $V(t^*+1) > V_{\text{th}}$ and trigger the second AP, we can use the inequality above to estimate the minimum amplitude of the second stimulus:

$$I_{\text{stim}} \approx \left[(V_{\text{th}} - V_{\text{eq}}^*) - \left(V(t^*) - V_{\text{eq}}^*\right) e^{-1/\tau}\right] \frac{G_{\text{b}}}{(1 - e^{-1/\tau})}. \tag{4.34}$$

In a general scenario, the voltage-gated potassium channels remain open until time $t^* + \epsilon$, where $0 \leq \epsilon \leq 1$. Based on biological and numerical evidence, we assume that no significant voltage change occurs while potassium channels remain open until the end of the second stimulus, *i.e.*, when $\epsilon = 1$. By substituting $e^{-1/\tau}$ with $e^{-(1-\epsilon)/\tau}$ in the denominator of Eq. (4.34), we obtain:

$$I_{\text{stim}} \approx \left[(V_{\text{th}} - V_{\text{eq}}^*) - \left(V(t^*) - V_{\text{eq}}^*\right) e^{-1/\tau}\right] \frac{G_{\text{b}}}{(1 - e^{-(1-\epsilon)\tau})}. \tag{4.35}$$

When ϵ approaches 1, the necessary stimulus increases indefinitely, indicating the absolute refractory phase. The black curve in Figure 4.6 represents the numerically generated strength-interval curve. The red points correspond to the analytical approximations for the minimal current.

In the first case, where the stimulus begins after the potassium channels are closed, the analytical approximations align well. In the second case, the required stimulus is overestimated, but the approximations follow a similar pattern.

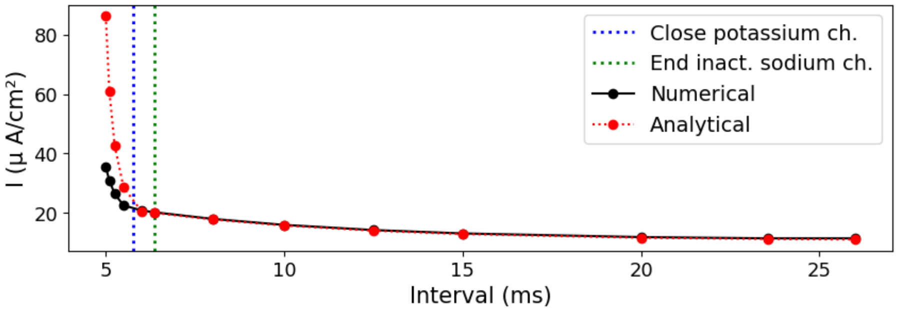

Figure 4.6 – Strength-interval curve displaying intervals measured from the initial stimulus application. The closure of potassium channels and the end of the inactivation phase are marked by vertical dotted lines. The red points indicate analytical approximations for the minimum current.

4.2.3 Train of action potentials

The response of a neuron to a prolonged or constant stimulus can generate multiple APs. As the amplitude of the stimulus increases, the frequency of APs also increases, as illustrated in Figure 4.7. The frequency is more responsive to changes when the amplitude is small, reaching a maximum frequency as the amplitude increases. Numerically, we observed the onset of repetitive firing for a constant stimulus of $1.6641\,\mu\text{A/cm}^2$.

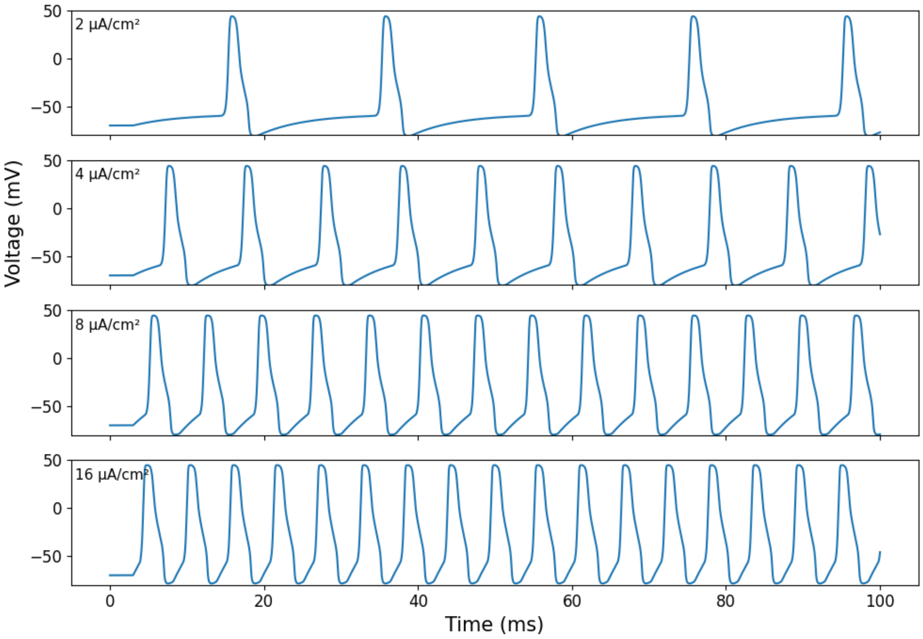

Figure 4.7 – The response of the membrane voltage to a prolonged stimulus of different amplitudes.

To mathematically analyze the frequency of APs, we consider a stimulus I_{stim} in the model given by Eqs. (4.19)-(4.20). For simplicity, we focus on the primary factors affecting the firing period and neglect sodium activation and inactivation delays. The firing period T_{stim} can be divided into three phases:

$$T_{\text{stim}} = t_{\text{fast}} + t_{\text{recovery}} + t_{\text{slow}}, \tag{4.36}$$

where t_{fast} accounts for the fast depolarization time when the potential changes from V_{th} to its peak; t_{recovery} accounts for the repolarization time from the peak to the minimum potential at hyperpolarization, V_r; and the time duration t_{slow} represents the passive depolarization of the membrane potential from the hyperpolarized reset voltage V_r to the firing threshold V_{th}. The slow depolarization time t_{slow} is the key variable that significantly varies with the stimulus current I_{stim}.

Following recovery, with low potassium conductance (considering τ_{K} significantly smaller than t_{slow}) and inactivated sodium, the membrane passively integrates the stimulus. By defining $G_{\text{b}} = G_{\text{Nab}} + G_{\text{Kb}}$ as previously, the voltage dynamics are described by Eq. (4.23). Starting from $V_0 = V_r$, the minimum hyperpolarization voltage, the solution, similar to Eq. (4.25), is given by:

$$V(t) = V_{\text{eq}} + (V_r - V_{\text{eq}})e^{-t/\tau}, \quad \tau = \frac{C_{\text{m}}}{G_{\text{b}}}. \tag{4.37}$$

The time t_{slow} is defined as the duration for $V(t)$ to reach the threshold V_{th}. Since $V_r - V_{\text{eq}} < 0$, $V(t)$ increases from V_r to V_{eq}, indicating firing if the input I_{stim} is sufficient for $V_{\text{eq}} > V_{\text{th}}$, where V_{eq} depends on I_{stim} and is given by Eq. (4.24). By solving for t_{slow} we obtain:

$$t_{\text{slow}}(I_{\text{stim}}) = \tau \ln \left(\frac{V_{\text{eq}}(I_{\text{stim}}) - V_r}{V_{\text{eq}}(I_{\text{stim}}) - V_{\text{th}}} \right). \tag{4.38}$$

Therefore, when the amplitude of I_{stim} is sufficient for $V_{\text{eq}} > V_{\text{th}}$, t_{slow} is a decreasing function of the magnitude of the inward stimulus current, and so is the total firing period. The other components of the period show minimal sensitivity to I_{stim}, making this mechanism the primary driver of frequency modulation. When t_{slow} is not considerably greater than τ_{K} and the potassium voltage-gated channels are still open during this time, this approximation is still valid, as the frequency tends to a plateau.

Using the parameters presented in Table 4.1, our numerical results yield the approximations $t_{\text{fast}} + t_{\text{recovery}} \approx 4.3$ ms and $V_r \approx -79$ mV. Figure 4.8 shows the frequency calculated numerically as a function of the stimulus amplitude compared to the values obtained with the above approximations, *i.e.*, using Eq. (4.38) and $T_{\text{stim}} = t_{\text{slow}}(I_{\text{stim}}) + 4.3$. The analytical approximation demonstrates significant accuracy. For the stimulus of $35\,\mu\text{A/cm}^2$, the analytical approximation gives us 206 spikes per second, compared to the 200 spikes calculated numerically.

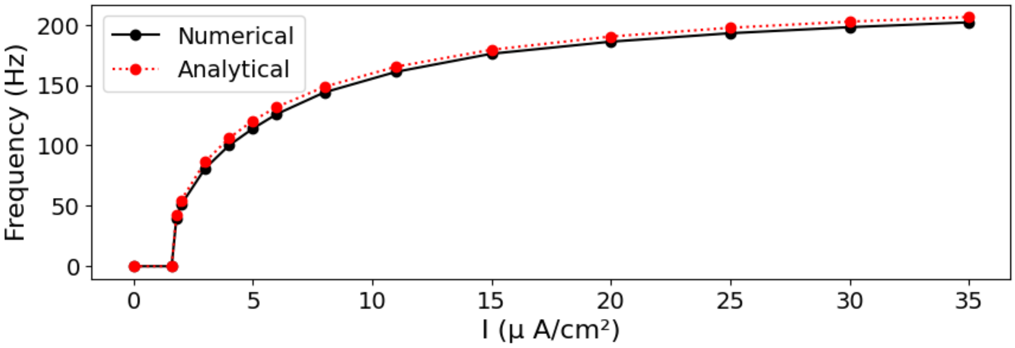

Figure 4.8 – The frequency of the membrane voltage response to a prolonged stimulus of varying amplitudes is measured in peaks per second (hertz).

In addition, autonomous firing, or a train of pulses, can occur even in the absence of an external stimulus when the equilibrium potential V_{eq} exceeds the threshold V_{th}. This regime can be induced by adjusting parameters such as the background sodium current (G_{Nab}) or the background potassium current (G_{Kb}). For instance, maintaining $G_{\text{Nab}} = 0.016$ and using $G_{\text{Kb}} = 0.072$, we have $V_{\text{eq}} \approx -59 > V_{\text{th}}$, and Figure 4.9 illustrates the resulting autonomous firing.

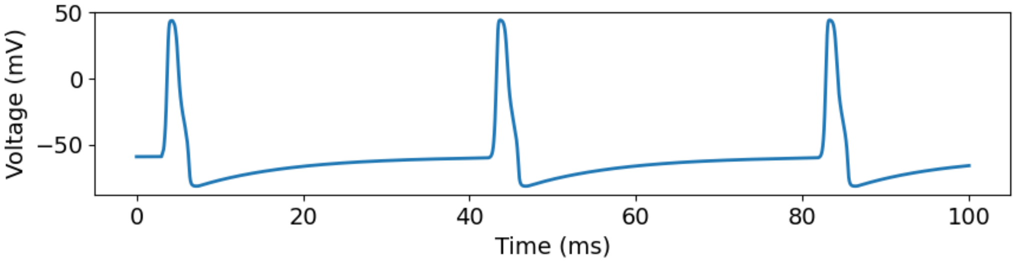

Figure 4.9 – Autonomous firing when $V_{\mathrm{eq}} > V_{\mathrm{th}}$.

4.3 ODE MODELS AND MEMORY KERNELS

We employ discrete delays to model voltage-gated ion channels, whereas Hodgkin and Huxley (22) adopted a continuous formulation. Both approaches can be viewed as particular cases of a more general representation based on delay kernels.

In Eq. (1.1), the kernel κ acts as a weighting function over the past of the signal f. For example, with the Dirac delta distribution centered at zero, δ_0, we have $w(t) = \int_0^t \delta_0(t-s)f(s)ds = f(t)$, so that no past dependence is present. In our model, we use a Dirac delta centered at τ, resulting in $w(t) = f(t-\tau)$, a discrete delay.

Consider, for instance, the HH model (Eq. (4.3)) and the FitzHugh-Nagumo (FHN) model, obtained by assuming a cubic nullcline for v and a linear nullcline for w:

$$\xi \frac{dV}{dt} = f(V) - w + I_{\mathrm{stim}}, \tag{4.39}$$

$$\frac{dw}{dt} = V - \gamma w, \tag{4.40}$$

where $f(V) = V(1-V)(V-a)$, with $0 < a < 1$, $\xi \ll 1$. Typical parameter values are $a = 0.1$, $\gamma = 0.5$, and $\xi = 0.01$ (103).

Both models implicitly employ exponential memory kernels of the form $\kappa(t) = \exp\left(-t/\tau\right)/\tau$. This kernel introduces an average delay of τ while continuously weighting the past of f with exponentially decaying weights. Following (27), $w(t)$ can be written as:

$$w(t) = \int_0^t \frac{1}{\tau} \exp\left(-\frac{1}{\tau}(t-s)\right) f(V(s))ds + w_0 \exp\left(-t/\tau\right), \tag{4.41}$$

which is equivalent to the ODE

$$\frac{dw}{dt} = \frac{f(V(t)) - w}{\tau}. \tag{4.42}$$

The solution converges to $f(V(t))$ with characteristic time scale τ. The gating formulation in the original HH model extends this concept, with the relaxation time of the gating variable w depending on the membrane potential V:

$$\frac{dw}{dt} = \frac{f(V(t)) - w}{\tau(V(t))}. \tag{4.43}$$

In this scenario, we also have a kernel-based formulation for a gating variable w (see also Section **5.1.2**):

$$w(t) = \int_0^t \frac{f(V(s))}{\tau(V(s))} \exp\left(-\int_s^t \frac{1}{\tau(V(\xi))} d\xi\right) ds + w_0 \exp\left(-\int_0^t \frac{1}{\tau(V(\xi))} d\xi\right). \qquad (4.44)$$

Therefore, ODEs, particularly those used in the HH formalism, and Volterra convolutions can be formulated equivalently under appropriate assumptions.

To make explicit that gating variables depend on the past of $V(t)$, we replace the exponential kernels in the HH-like models with Dirac delta function. By doing so, a general HH-type ODE system of the form:

$$\begin{cases} \dfrac{dV}{dt} = g(V(t)) + w(t), \\ \dfrac{dw}{dt} = \dfrac{f(V(t)) - w(t)}{\tau}, \end{cases} \qquad (4.45)$$

simplifies to:

$$\frac{dV}{dt} = g(V(t)) + f(V(t - \tau)). \qquad (4.46)$$

The two formulations above are closely related and can be viewed as first-order approximations of each other. Assuming that f is smooth, we can consider the Taylor expansion around $t - \tau$:

$$f(V(t)) = f(V(t - \tau)) + \tau \frac{d}{dt}\Big(f(V(t - \tau))\Big) + O(\tau^2). \qquad (4.47)$$

Define the auxiliary variable $w(t) := f(V(t - \tau))$. Then, using the first-order approximation:

$$f(V(t)) \approx f(V(t - \tau)) + \tau \frac{d}{dt}\Big(f(V(t - \tau))\Big) = w(t) + \tau \frac{dw(t)}{dt}, \qquad (4.48)$$

we obtain Eq. (4.42). By substituting $w(t) = f(V(t - \tau))$ into the first equation of Eq. (4.45), we recover the delayed formulation Eq. (4.46). Therefore, Eq. (4.45) and Eq. (4.46) are consistent first-order approximations of the same memory effect: the present voltage dynamics depends on a filtered (relaxing) or lagged version of $f(V)$.

This connection clarifies the modeling meaning of “delay” used in this work: a discrete lag provides the simplest representation of history dependence, whereas the HH-type gating-variable ODE corresponds to an exponential (weak) memory kernel.

4.3.1 Fitting to the Hodgkin-Huxley model

As seen before, in HH-type models, the gating variables follow exponential relaxation times. In the DDE model Eq. 4.19, the gating variables use discrete delays:

$$n(t-\tau_{\mathrm{K}}) = \frac{(V(t-\tau_{\mathrm{K}})-V_{\mathrm{th}})\ H(V(t-\tau_{\mathrm{K}})-V_{\mathrm{th}})}{V_{\mathrm{Na}}-V_{\mathrm{th}}}, \tag{4.49}$$

$$m(t-\tau_{\mathrm{m}}) = \frac{(V(t-\tau_{\mathrm{m}})-V_{\mathrm{th}})\ H(V(t-\tau_{\mathrm{m}})-V_{\mathrm{th}})}{V_{\mathrm{Na}}-V_{\mathrm{th}}}, \tag{4.50}$$

$$h(t-\tau_{\mathrm{h}}) = \frac{(V_{\mathrm{cut}}-V(t-\tau_{\mathrm{h}}))\ H(V_{\mathrm{cut}}-V(t-\tau_{\mathrm{h}}))}{V_{\mathrm{cut}}-V_{\mathrm{K}}}. \tag{4.51}$$

Also, we replaced the leak current of the HH model, $C_{\mathrm{L}}\ (V-V_{\mathrm{L}})$, with the two background currents of sodium and potassium. These two approaches can be written in an equivalent form. Indeed,

$$I_{\mathrm{Kb}}+I_{\mathrm{Nab}} = G_{\mathrm{Kb}}(V-V_{\mathrm{K}})+G_{\mathrm{Nab}}(V-V_{\mathrm{Na}}) = G_{\mathrm{b}}(V-V_{\mathrm{L}}), \tag{4.52}$$

where $G_{\mathrm{b}} = G_{\mathrm{Kb}}+G_{\mathrm{Nab}}$ and

$$V_{\mathrm{L}} = \frac{G_{\mathrm{Kb}}V_{\mathrm{K}}+G_{\mathrm{Nab}}V_{\mathrm{Na}}}{G_{\mathrm{b}}}. \tag{4.53}$$

In the HH model simulation, the leak current has a Nernst potential of $V_L = -59.4$ mV and a leakage conductance of $C_L = 0.3\,\mathrm{mS}\cdot\mathrm{cm}^{-2}$. For the DDE model, we chose $G_{\mathrm{Kb}} = 9.5\cdot G_{\mathrm{Nab}}$ to ensure that the equilibrium in Eq. (4.24) matches the resting potential $V_{\mathrm{eq}} = -70$ mV.

Our model accurately reproduces the standard HH action potential and its corresponding conductances, as shown in Figure 4.10.A-B. The Nernst potentials for potassium and sodium are set at $V_{\mathrm{K}} = -82$ mV and $V_{\mathrm{Na}} = 45$ mV for both models. The initial condition is $V_0 = V_{\mathrm{eq}} = -70$ mV, and the applied stimulus has an amplitude of $11.5\,\mu\mathrm{A/cm}^2$ for 1 ms. All other DDE model parameters are listed in Table 4.1. The parameters of the HH model were taken from (22).

Figure 4.10.C shows the gating variables of the two models. Note that the binary effects of the Heaviside functions sharpen the behavior of the gating variables in model Eq. (4.19)-(4.20).

4.3.2 Chain-trick, Markov chains and Fractional models

As seen in the previous chapter, a link can be established between the proposed DDE formulation and other modeling frameworks such as linear-chain and FC formulations. The linear-chain (Erlang) approximation (83, 2), also known as the method of stages, refers to the standard representation of an Erlang distributed memory kernel as a finite cascade

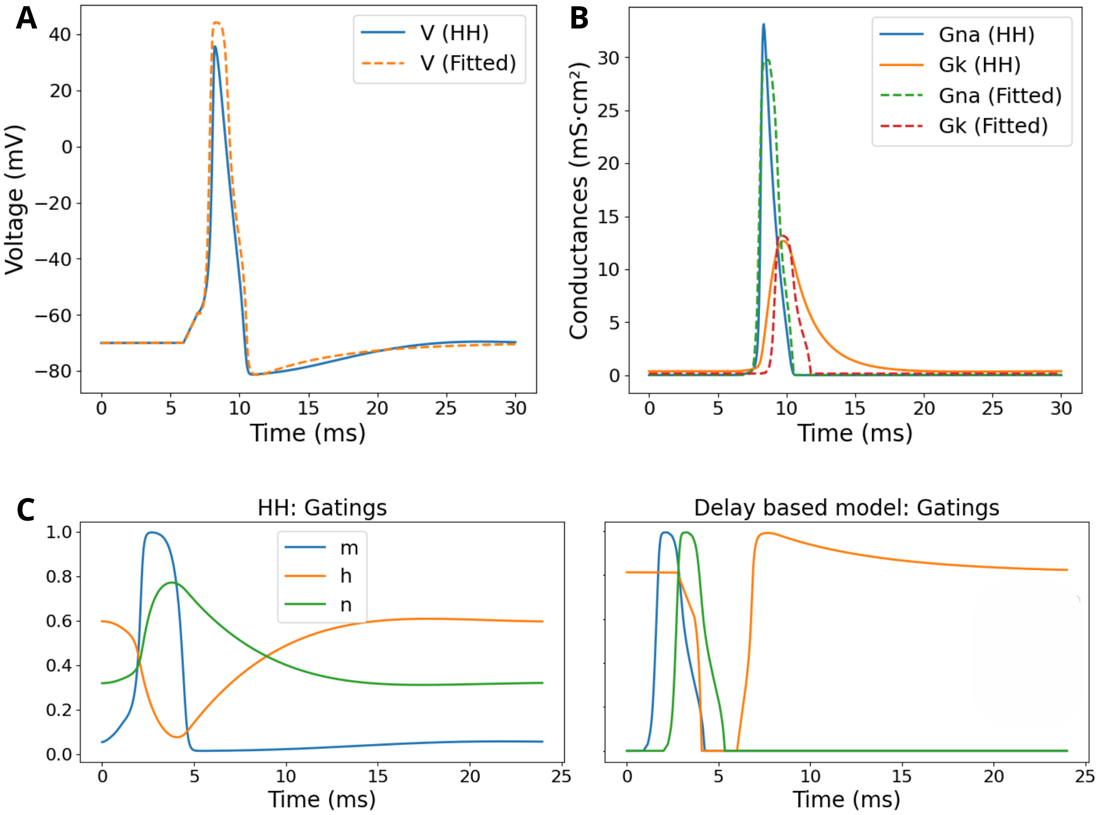

Figure 4.10 – The model Eq. (4.19)-(4.20) is fitted to the HH model by adjusting both the voltage (panel **(A)**) and conductances (panel **(B)**). Panel **(C)** displays the gating variables of the two models for the adjusted parameters.

Parameter	**Fitted and fixed (*) values**
V_{K} (*)	-82 mV
V_{Na} (*)	45 mV
G_{Nab}	$0.016\ \mathrm{mS}\cdot\mathrm{cm}^{-2}$
G_{Kb}	$9.5\cdot G_{\mathrm{Nab}} = 0.152\ \mathrm{mS}\cdot\mathrm{cm}^{-2}$
C_{Na}	$36.96\ \mathrm{mS}\cdot\mathrm{cm}^{-2}$
C_{K}	$13.125\ \mathrm{mS}\cdot\mathrm{cm}^{-2}$
τ_{m}	0.199 ms
τ_{h}	2.758 ms
τ_{K}	1.3 ms
V_{cut}	-18 mV
V_{th} (*)	-60 mV
C_{m} (*)	$1.0\,\mu\mathrm{F}\ \cdot\mathrm{cm}^{-2}$

Table 4.1 – Fitted and fixed parameters for Eq. (4.19)-(4.20).

of first-order ODE “stages”. This approach preserves the prescribed mean relaxation time. By the FC formulation, we mean a nonlocal-in-time generalization in which the memory kernel exhibits long tails. This provides a compact parameterization of long-memory relaxation when such behavior is supported by experimental data. It is presented here as an optional extension rather than as the classical baseline for ion-channel kinetics.

In this section, we assume that sodium channels are extremely fast, corresponding to $\tau_{\mathrm{m}} = \tau_{\mathrm{h}} = 0$ in model (4.19). We first define an auxiliary variable related to the gating variable n that accounts for potassium activation with memory:

$$w(t) = \int_0^t \kappa_{\tau_{\mathrm{K}}}(s)\, n(t-s)\, ds. \tag{4.54}$$

In the proposed DDE framework, the kernel κ is a Dirac delta. Replacing the Dirac delta with an exponential memory kernel $\kappa(t) = e^{-t/\tau_{\mathrm{K}}}/\tau_{\mathrm{K}}$ for the slow variable w, we obtain a two-variable ODE system:

$$\begin{cases} C_{\mathrm{m}} \dfrac{dV}{dt} = -G_{\mathrm{K}}(w)\ (V - V_{\mathrm{K}}) - G_{\mathrm{Na}}(V)\ (V - V_{\mathrm{Na}}) + I_{\mathrm{stim}}, \\ \dfrac{dw}{dt} = \dfrac{n(t) - w}{\tau_{\mathrm{K}}}, \\ G_{\mathrm{K}}(w) = G_{\mathrm{Kb}} + C_{\mathrm{K}}\, w, \\ G_{\mathrm{Na}}(V) = G_{\mathrm{Nab}} + C_{\mathrm{Na}}\ (V - V_{\mathrm{th}})\ (V_{\mathrm{cut}} - V)\ H(V - V_{\mathrm{th}})\ H(V_{\mathrm{cut}} - V). \end{cases} \tag{4.55}$$

This reduced model contains the core structure of the phenomenological FHN system (106). The cubic nonlinearity in V captures the rapid depolarization associated with sodium channel activation, while the slow variable w describes potassium-mediated repolarization dynamics.

Moreover, cascades of processes can be described by chains of delays (107, 108, 109). In electrophysiological systems, cascades of reactions and processes are very common. For example, in cardiac myocytes, the calcium current (I_{CaL}) is partially inactivated by intracellular calcium, which rises only after the increase of I_{CaL}, itself triggered by depolarization of the transmembrane voltage (110). Similarly, ion channel gating may depend on intracellular messengers that are activated in successive biochemical steps (111).

To illustrate this concept, let us examine how potassium channels respond to changes in transmembrane voltage as a series of two interconnected processes. The voltage initially influences an intermediate variable y with a delay of τ_{y}, and then y affects a second variable w with a delay of τ_{w}, which ultimately modulates the effective potassium conductance G_{K}:

$$\begin{cases} C_{\mathrm{m}} \dfrac{dV}{dt} = -G_{\mathrm{K}}(w)\ (V - V_{\mathrm{K}}) - G_{\mathrm{Na}}(V)\ (V - V_{\mathrm{Na}}) + I_{\mathrm{stim}}, \\ \dfrac{dy}{dt} = \dfrac{n(t) - y}{\tau_{\mathrm{y}}}, \\ \dfrac{dw}{dt} = \dfrac{y - w}{\tau_{\mathrm{w}}}, \end{cases} \tag{4.56}$$

where G_{K} and G_{Na} are defined as in Eq. (4.55).

The corresponding kernel is expressed as

$$\kappa(t) = \frac{1}{\tau_{\mathrm{w}} - \tau_{\mathrm{y}}}\Big(e^{-t/\tau_{\mathrm{w}}} - e^{-t/\tau_{\mathrm{y}}}\Big), \quad t \geq 0, \tag{4.57}$$

referred to as the hypoexponential or generalized Erlang distribution (112), with a mean of $\tau_{\mathrm{w}} + \tau_{\mathrm{y}}$ and a standard deviation of $\sqrt{\tau_{\mathrm{w}}^2 + \tau_{\mathrm{y}}^2}$.

When the two delays are equal ($\tau = \tau_{\mathrm{y}} = \tau_{\mathrm{w}}$), the dynamics of w is equivalent to applying a delay kernel to $n(t)$ given by an Erlang distribution with a mean of 2τ, a standard deviation of $\sqrt{2}\,\tau$, and a mode at τ. Such a kernel is often referred to as a strong kernel, in contrast to the exponential or weak kernel, $\kappa(t) = \tau^{-1}e^{-t/\tau}$.

The linear-chain construction can be interpreted probabilistically as multi-stage kinetics that induces a hypoexponential residence-time distribution before occupancy accumulates in the open state. This stochastic process is called a continuous-time Markov chain (CTMC). It satisfies the Markov property: the conditional distribution of the future $X(t+s)$ of a random variable X given the present $X(s)$ and the past $X(u)$ for times $0 < u \leq s$, depends only on the present time s (113).

The same equations are derived for the three-state Markov process shown below:

$$S_1 \xrightarrow{\alpha_1} S_2 \xrightarrow{\alpha_2} O,$$

with $S_1 = n - y$, $S_2 = y - w$ and $O = w$. [1] We define α_1 and α_2 as the transition rates between the three states such that $\tau_{\mathrm{y}} = 1/\alpha_1$ and $\tau_{\mathrm{w}} = 1/\alpha_2$. In this unidirectional two-step chain, the intermediate stages have exponential residence (relaxation) times with means τ_{y} and τ_{w}, resulting in a hypoexponential passage-time distribution from S_1 to O (Erlang when $\alpha_1 = \alpha_2$).

These probabilistic states can be interpreted as microscopic configurations of an ion channel, where each state corresponds to a distinct protein conformation representing a local minimum in the channel's energy landscape. In this interpretation, the transition rates between microstates determine the characteristic residence and relaxation time scales, and thus the effective memory (kernel) parameters at the macroscopic level, within a framework traditionally employed in ion channel modeling (115). These Markov-type models are based on the assumption that transitions between states depend only on the present channel conformation, and are often associated with experimentally observed mechanisms of channel movement (116).

However, the CTMC above has a structural limitation since it only allows forward transitions and, related to a phase-type distribution (117), requires the last state to be an absorbing one. To overcome this restriction, we can move beyond the chain-trick

---

[1] We have assumed that V is constant; thus, n is also constant. For a general time-varying $V(t)$, additional reservoir state formulations and open CTMC (114) are required to describe the bidirectional probability exchange between the chain and its environment.

modelling paradigm and adopt a more general CTMC formulation, proposing the following three-state Markov process:

$$S_1 \underset{\beta_1(V)}{\overset{\alpha_1(V)}{\rightleftharpoons}} S_2 \underset{\beta_2(V)}{\overset{\alpha_2(V)}{\rightleftharpoons}} O,$$

where $\alpha_1(V)$, $\alpha_2(V)$, $\beta_1(V)$, and $\beta_2(V)$ are the voltage-dependent rates governing the transitions between the channel's microstates S_1, S_2, and O.

Rewriting the potassium conductance as $G_{\mathrm{K}}(O) = G_{\mathrm{Kb}} + C_{\mathrm{K}}\, O$, we can derive the following new model:

$$\begin{cases} C_{\mathrm{m}} \dfrac{dV}{dt} = -G_{\mathrm{K}}(O)\ (V - V_{\mathrm{K}}) - G_{\mathrm{Na}}(V)\ (V - V_{\mathrm{Na}}) + I_{\mathrm{stim}}, \\ \dfrac{dS_1}{dt} = -\alpha_1(V)\, S_1 + \beta_1(V)\, S_2, \\ \dfrac{dS_2}{dt} = \alpha_1(V)\, S_1 - \Big(\beta_1(V) + \alpha_2(V)\Big)\, S_2 + \beta_2(V)\, O, \\ \dfrac{dO}{dt} = \alpha_2(V)\, S_2 - \beta_2(V)\, O. \end{cases}$$

By using the constraint $S_1 + S_2 + O = 1$, we can simplify the system to:

$$\begin{cases} C_{\mathrm{m}} \dfrac{dV}{dt} = -G_{\mathrm{K}}(O)\ (V - V_{\mathrm{K}}) - G_{\mathrm{Na}}(V)\ (V - V_{\mathrm{Na}}) + I_{\mathrm{stim}}, \\ \dfrac{dS_2}{dt} = \alpha_1(V) - \Big(\alpha_1(V) + \beta_1(V) + \alpha_2(V)\Big)\, S_2 + \Big(\beta_2(V) - \alpha_1(V)\Big)\, O, \\ \dfrac{dO}{dt} = \alpha_2(V)\, S_2 - \beta_2(V)\, O. \end{cases} \tag{4.58}$$

Consider the scenario where the voltage dependence only affects the first forward and backward rates:

$$\alpha_1 = a_1\, n(V), \qquad \beta_1 = b_1\, (1 - n(V)),$$

while the rates α_2 and β_2 remain constant. By choosing the parameters $(a_1, \alpha_2, b_1, \beta_2)$ appropriately, we can create a three-state CTMC with an effective memory kernel that has a specified mean. For calibration (rates fixed; $n = 0.8$), we calculate an activation-time kernel by considering O as absorbing. In this scenario:

$$\kappa_O(t) = \frac{\alpha_1 \alpha_2}{\lambda_2 - \lambda_1}\Big(e^{-\lambda_1 t} - e^{-\lambda_2 t}\Big),$$

where $\lambda_{1,2}$ are the eigenvalues of the transient subgenerator. This kernel is used solely to match a target mean μ; simulations involve integrating the reversible CTMC (Eq. (4.58)).

The CTMC presented here is more flexible than the chain-trick (Erlang) formulation. After adjusting the steady-state activation $O_\infty(V)$ and aligning with a target mean time scale (using the $n \equiv 0.8$ calibration kernel), one additional degree of freedom is available. We utilize β_2 to parameterize this freedom and readjust the other rates to satisfy both constraints, resulting in different transient (bi-exponential) shapes while maintaining the same steady-state behavior and mean.

Furthermore, another modeling formulation enhances the flexibility of generating memory kernels with several shapes using only a few parameters: fractional differential equations (79, 118). Recall that w was defined as a Volterra convolution in Eq. (4.54). As presented in Chapter 3, a versatile and comprehensive choice for the kernel is the generalized Gamma Mittag-Leffler function:

$$\kappa(t) = C\, t^{\beta-1} e^{-at} E_{\alpha,\beta}(-\lambda t^{\alpha}), \quad t \geq 0,$$

where $E_{\alpha,\beta}(\cdot)$ represents the two-parameter Mittag-Leffler function and C is a normalization constant. This formulation encompasses the exponential, gamma, Delta Dirac, and classical Mittag-Leffler distributions as particular or limiting cases (79).

The dynamics of V and w can be equivalently described by the fractional differential equations:

$$\begin{cases} C_{\mathrm{m}} \dfrac{dV}{dt} = -G_{\mathrm{K}}(w)\ (V - V_{\mathrm{K}}) - G_{\mathrm{Na}}(V)\ (V - V_{\mathrm{Na}}) + I_{\mathrm{stim}}, \\ \dfrac{dw}{dt} = n(t) - \lambda\, e^{-at}\, D^{1-\alpha}\Big(e^{at} w\Big) - a\, w, \\ G_{\mathrm{K}}(w) = G_{\mathrm{Kb}} + C_{\mathrm{K}} C\, e^{-at}\, D^{1-\beta}\Big(e^{at} w\Big), \\ G_{\mathrm{Na}}(V) = G_{\mathrm{Nab}} + C_{\mathrm{Na}}\ (V - V_{\mathrm{th}})\ (V_{\mathrm{cut}} - V)\ H(V - V_{\mathrm{th}})\ H(V_{\mathrm{cut}} - V). \end{cases} \tag{4.59}$$

where D^{α} is the Riemann-Liouville derivative of order α.

As seen in Chapter 3, for $a > 0$, the mean and the variance of the distribution have analytical expressions. By varying the parameters α and β, the kernel can smoothly transition from exponential to stretched-exponential and power-law forms, resulting in long-memory and heavy tails that cannot be captured by a finite number of Markov states. In certain combinations, the kernel can become multimodal, describing non-monotonic memory where past events at specific times regain influence on current dynamics. In contrast to the 3-state CTMC, the fractional Gamma Mittag-Leffler kernel can replicate any desired mean and variance. It spans a continuum of relaxation times, enabling the modeling of complex memory effects observed in experimental data.

Figure 4.11 illustrates examples of kernels and solutions for the initial DDE and the four different models we described in this section: HH-like with exponential and Erlang memory kernels, Markov chain-based, and fractional models, all with the same biological parameters and mean $\mu = 1.2$. It reflects the diversity of delay-based formulations.

4.4 DISCUSSION

While HH-type models represent channel kinetics through additional ODE state variables (gating probabilities) with voltage-dependent relaxation times, we pursue an

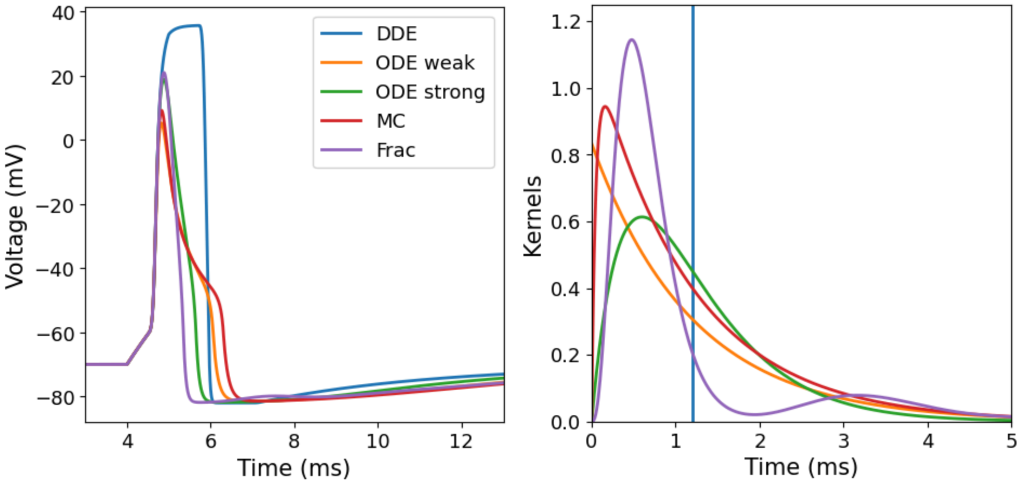

Figure 4.11 – Examples of solutions and kernels for the presented DDE model (Eq. (4.19)) and the four different models we developed in this section: HH-like with weak and strong memory kernels (Eq. (4.55) and Eq. (4.56) with $\tau = \tau_{\mathrm{y}} = \tau_{\mathrm{w}}$, respectively), Markov chain-based (Eq. (4.58)) and fractional (Eq. (4.59)). The same biological parameters and mean $\mu = 1.2$ are considered. For the Markov-chain model, the kernel shown is the activation-time (first-passage) kernel; the voltage trace "MC" is obtained by integrating the reversible CTMC model.

alternative viewpoint: channel kinetics are explicitly written in terms of discrete or distributed delays that combine both latency and relaxation into equilibrium. In our formulation, gating is described by punctual delays (Dirac kernels) and, more generally, by Volterra memory kernels. This has two practical consequences. First, the dominant kinetic times appear explicitly as delay/kernel parameters, enabling compact analytical approximations for biologically meaningful quantities (*e.g.*, strength-interval curves and stimulus-frequency relations) without tracking multiple auxiliary ODE states.

Secondly, the kernel viewpoint serves as a unified bridge between classical ODE gating (exponential kernels), chain-trick representations (Erlang/hypoexponential kernels), CTMC-based models (phase-type kernels), and fractional formulations (heavy-tailed or multimodal kernels). When a single discrete delay is insufficient (*e.g.*, when multiple kinetic time scales contribute comparably or when relaxation times vary strongly along trajectories), the same framework can be systematically enriched by transitioning from a Dirac kernel to distributed kernels (exponential, Erlang/hypoexponential, phase-type/CTMC, or fractional kernels), as discussed in Section 4.3. Therefore, the delay-based model aims to provide a concise and interpretable representation of channel latency/memory along with a systematic approach to enhance the memory structure when necessary.

The use of weak and strong gamma-distributed delays has been explored in neuronal dynamics, particularly as models of interspike intervals (89, 119), and more recently in a modified FHN (120). The cascade of linear ODEs generated by Erlang kernels with integer shape parameters has also been beneficial in modeling several cellular processes, such as calcium cycling (110, 121) and signal transduction (109, 122).

HH/Markov ODE models are the natural choice when the objective is to interpret or manipulate explicit channel-state probabilities (*e.g.*, state-dependent block, mutation effects associated with specific transitions, or mechanistic pharmacology). In contrast, the delay representation developed here captures excitability, refractoriness, stimulus–frequency modulation, and propagation phenomena in a compact form, while rendering the dominant kinetic time scales explicit as memory parameters. This delay-based ionic formulation also extends naturally to spatially distributed neuron models, as illustrated in Figure 4.12, which provides new opportunities for research.

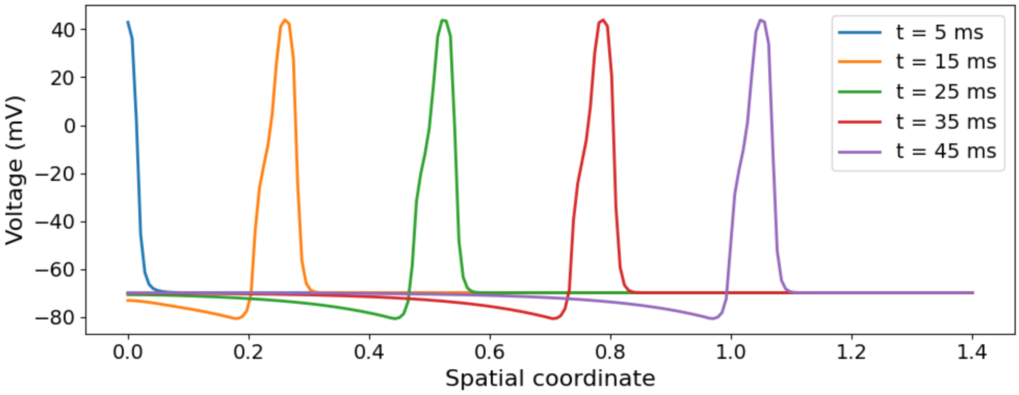

Figure 4.12 – Solutions of the 1D cable equation for the DDE model (Eq. (4.19)) at various time snapshots. The cable equation is given by $C_\text{m}\dfrac{\partial V}{\partial t} = \dfrac{a}{2R_i}\dfrac{\partial^2 V}{\partial x^2} - I_\text{ion}(t) + I_\text{stim}(t)$, with I_ion representing the sum of the ionic currents. We use an axon radius $a = 0.01$ cm and axial resistivity $R_i = 35.4\,\Omega\cdot\text{cm}$, and Neumann boundary condition. The parameters of the ionic model are given in Table 4.1.

Particularly, CTMCs allow the steady-state response to match classical HH behavior while tuning the mean and making the choice of memory kernel variance more flexible. This flexibility enables the model to reproduce a wide spectrum of stochastic or deterministic channel dynamics within a unified formalism. Altogether, the presented framework highlights how delays and memory kernels offer a unified and flexible foundation for describing cellular electrophysiology within a common mathematical structure.

Furthermore, employing a gamma Mittag–Leffler probability density function as the memory kernel naturally leads to fractional models, further extending modeling flexibility, for instance, allowing independent control of the mean and variance (see Chapter 3). In this regime, kernels can become multimodal, capturing richer temporal dependencies and nonlocal memory effects. Fractional formulations have enabled compact two-dimensional cardiac models to reproduce complex behaviors, such as early afterdepolarizations, as demonstrated in the next chapter.

5 ION CHANNEL MEMORY DRIVES CARDIAC EARLY AFTERDEPOLARIZATIONS IN FRACTIONAL MODELS

This chapter continues the application of the kernel-based framework to electrophysiological systems, focusing on cardiac models. Within the unified perspective established in Chapter 3, this approach allows us to investigate how changes in the temporal structure of memory can lead to qualitatively new behaviors, such as mixed-mode oscillations.

Cardiac myocytes are able to respond to an external stimulus by generating an AP. Figure 5.1 shows a typical cardiac AP. The plateau and the absence of hyperpolarization are among the key differences from the neuronal APs discussed in Section **1.3.3** and Chapter 4. In Phase 0, the cell is stimulated, and the transmembrane potential rapidly becomes more positive in a process known as depolarization. In Phase 1, the membrane potential undergoes a brief repolarization. Following this, in Phase 2, the transmembrane potential enters the plateau phase, where it slowly decays. During the fast repolarization phase (Phase 3), the potential returns toward its resting value, reaching the resting state in Phase 4.

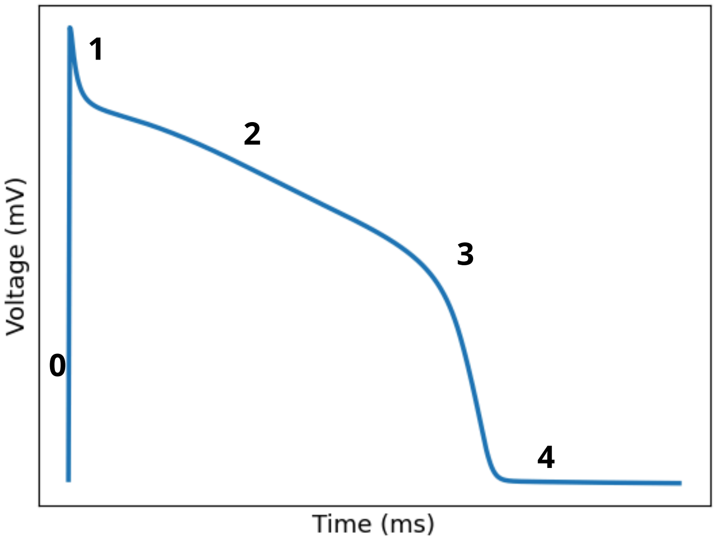

Figure 5.1 – Typical cardiac action potential and its phases.

Early afterdepolarizations (EADs) are abnormal depolarizations that can occur during the plateau phase of the cardiac AP and are associated with life-threatening arrhythmias. Although they have been studied extensively since the 20th century (*e.g.*, (123, 124)), they remain an active area of research in both experimental and computational settings due to the potential of EADs to induce dangerous cardiac rhythms like extrasystoles and tachycardia. Some recent studies include (125) on the determinants of EAD properties in ventricular myocyte models, (126) on the mechanism of arrhythmogenesis driven by EADs in cardiac tissue, and (127) on the roles of calcium cycling and its interaction with voltage in the genesis of EADs in cardiac myocyte models.

Studying EADs in simplified cardiac models is a fundamental research focus, as shown in (3). The study explores the emergence and evolution of EADs in a reduced three-variable Luo-Rudy model. From a dynamical systems perspective, EADs can manifest as mixed-mode oscillations, a dynamic behavior where a system alternates between small- and large-amplitude oscillations, as noted by (128). Traditional two-variable models such as Karma, Mitchell-Schaeffer, and FHN struggle to replicate EADs due to their simple trajectory structure. In essence, they inherently rely on memoryless exponential kernels, and two-dimensional autonomous systems are generally unable to exhibit mixed-mode oscillations. To achieve the rich alternation between small and large oscillations, at least three dimensions and multiple time scales are typically required.

In recent years, there has been a growing interest in generating mixed-mode oscillations using models that involve fractional derivatives. For example, (129) obtained mixed-mode oscillations from a two-variable system near a Hopf-like bifurcation, while (130) investigated the emergence of mixed-mode oscillations and canard explosion in a fractional-order FHN model. Additionally, spiking and bursting patterns of fractional-order Izhikevich mode have been discussed in (131), and mixed-mode oscillations based on complex canard explosion in a fractional-order FHN model have been presented in (132). The relationship between mixed-mode oscillations generated by fractional derivatives and the proximity to the Hopf-like bifurcation point has also been explored in (133). Furthermore, (134) has discussed the pattern dynamics behavior of a fractional vegetation-water model in arid flat environments, and (135) discussed Hopf bifurcation and transitions of firing activities in a fractional-order FitzHugh-Rinzel system with multiple time delays.

Based on our publication (118), we explore the generation of EADs by modifying the memory kernel of the slow variable in this type of model using tools from FC. Unlike previous research, our approach does not replace integer-order derivatives with fractional ones; instead, it extends the exponential kernel to the gamma Mittag-Leffler probability density function, thereby introducing Riemann–Liouville fractional derivatives on the right-hand side of the differential equations. Although assigning direct biological meaning to each parameter is challenging, simplified scenarios such as the gamma kernel were studied to link EAD occurrence to the mean and variance of memory kernels. In this case, EADs were found to occur when slight changes in the mean or variance of the kernel lead to an increased influence of recent voltage values on potassium currents during repolarization. Mathematically, EADs arise when the system's trajectory approaches an unstable spiral or limit cycle in the corresponding integer-order model. The introduction of fractional operators, which render the system non-autonomous, allows trajectories to self-intersect in the phase plane and thereby enables the generation of mixed-mode oscillations.

The chapter is structured as follows: Section 5.1 presents the methods. It examines the connection between equations of the form

$$\frac{dw}{dt} = \frac{w_\infty(u) - w}{\tau_w(u(t))} \tag{5.1}$$

and memoryless exponential kernels. This enables us to explore how simplified two-dimensional cardiac models with HH-type equations can be extended with gamma Mittag-Leffler distributed delays, resulting in fractional models.

5.1 MATHEMATICAL METHODS

5.1.1 Delay Kernels

When a model depends on the history of a function $y(t)$ with a distributed delay weight, delays (the influence of past states) typically appear in a Volterra convolution form (16):

$$\int_0^t \kappa(s)y(t-s)ds = \int_0^t \kappa(t-s)y(s)ds; \qquad \kappa(t) \geq 0, \int_0^\infty \kappa(s)ds = 1. \tag{5.2}$$

Consider the generalized gamma Mittag–Leffler probability distribution function (PDF) as described by Eq. (3.2). This distribution function spans exponential, gamma, and Mittag-Leffler regimes. A brief analysis of the effects of the parameters can be found in Section C.2.

We use the gamma Mittag-Leffler distribution (3.2) as a memory kernel, rewriting Eq. (5.2) as:

$$\int_0^t \kappa(t-s)y(s)ds = \int_0^t C(t-s)^{\beta-1}e^{-a(t-s)}E_{\alpha,\beta}(-\lambda(t-s)^\alpha)y(s)ds. \tag{5.3}$$

As shown in Chapter 3, Laplace transforms and the analytical properties of FC can be used to derive a general formulation for the convolution Eq. (5.3), obtaining:

$$\int_0^t \kappa(t-s)y(s)ds = Ce^{-at}D^{1-\beta}(e^{at}w), \tag{5.4}$$

$$\frac{dw}{dt} = y - \lambda e^{-at}D^{1-\alpha}(e^{at}w) - aw. \tag{5.5}$$

In this formulation, we have:

$$w = \int_0^t E_\alpha(-\lambda(t-\tau)^\alpha)e^{-a(t-\tau)}y(\tau)d\tau. \tag{5.6}$$

For $a > 0$, the mean μ and the variance σ^2 of a gamma Mittag-Leffler distribution (85) are given by the expressions in Eq. (3.22). For $a = 0$, we are in the case of the Mittag-Leffler distribution, for which there is no finite mean or variance. Note that if $\beta \leq 1$, the memory kernel (3.2) is weak, where the current time has the greatest influence on the rate of the phenomenon. Conversely, for $\beta > 1$, we have the so-called strong memory kernels, where $\kappa(0) = 0$ and the distribution mode is not zero.

As cited in previous chapters, a key observation is that, for any positive values of μ and σ^2, there exists at least one parameter set that yields the prescribed mean and variance of the memory kernel to μ and σ^2, respectively. This highlights how the incorporation of fractional models can accurately represent a wide range of phenomena.

The next subsections describe how the gamma Mittag-Leffler PDF memory kernels can be incorporated into the HH equation type.

5.1.2 Delays in Hodgkin-Huxley's Equation Type

Although the generation and propagation of signals have been extensively studied by physiologists over the past 100 years, one of the most important milestones is the work of Alan Hodgkin and Andrew Huxley (22), who developed the first quantitative model of action potentials. Their model was originally used to explain the AP in the giant axon of a squid nerve cell, but the ideas have been extended and applied to a wide variety of excitable cells. The HH theory is notable not only for its influence on electrophysiology but also on applied mathematics in general.

We analyze a HH-type equation (see also Section 4.3). Let us denote an arbitrary gate variable as w, associated with the differential equations:

$$\frac{du}{dt} = f(u, w), \tag{5.7}$$

$$\frac{dw}{dt} = \frac{w_\infty(u) - w}{\tau_w(u)}. \tag{5.8}$$

Define $\mu = \exp\left(\int_0^t \frac{1}{\tau_w(u(s))} ds\right)$, and note that:

$$\frac{d\mu}{dt} = \frac{\mu}{\tau_w(u)}. \tag{5.9}$$

From (5.8), we have:

$$\mu\frac{dw}{dt} + \mu\frac{w}{\tau_w(u)} = \mu\frac{w_\infty(u)}{\tau_w(u)}, \tag{5.10}$$

$$\frac{d(\mu w)}{dt} = \mu\frac{w_\infty(u)}{\tau_w(u)}. \tag{5.11}$$

So, assuming $w \equiv 0$ for $t \leq 0$, we have:

$$\mu w = \int_0^t \frac{\mu(s) w_\infty(u(s))}{\tau_w(u(s))} ds, \tag{5.12}$$

$$w = \int_0^t \frac{w_\infty(u(s))}{\tau_w(u(s))} \exp\left(-\int_s^t \frac{1}{\tau_w(u(\xi))} d\xi\right) ds. \tag{5.13}$$

The special case in which $\tau_w \equiv \tau$ corresponds to the case described by Rameh, Cherry, and dos Santos (27), in which

$$w = \int_0^t \frac{w_\infty(u(s))}{\tau} \exp\left(-\frac{1}{\tau}(t-s)\right) ds. \tag{5.14}$$

The relation (5.14) leads to the conclusion that (5.8) corresponds to a convolution with an exponential kernel of form $\frac{1}{\tau} \exp\left(-\frac{1}{\tau}(t-s)\right)$, which is associated with a memoryless waiting-time distribution. We can use a general delay kernel κ to express w as:

$$w = \int_0^t w_\infty(u(s))\kappa(t-s)ds. \tag{5.15}$$

Particularly, if $\kappa = \delta_\tau$, a Dirac delta centered at $\tau \geq 0$, we have

$$w = w_\infty(u(t-\tau)). \tag{5.16}$$

In this case, the differential system (5.7) and (5.8) reduces to a DDE:

$$\frac{du}{dt} = f(u, w_\infty(u(t-\tau))). \tag{5.17}$$

By using special types of kernels, such as a gamma Mittag-Leffler PDF memory kernel, we can derive fractional general electrophysiological models, as described in Chapter 4 and in the next subsection.

5.1.3 Fractional Cardiac Models

The models considered here capture the essential dynamics of an AP in a simplified form, using only two variables: one fast (u) and one slow (w). The fast variable is referred to as the excitation variable, while the slow variable is known as the recovery variable.

The variable w represents slow inactivation of sodium and calcium channels, as well as slow activation of potassium channels. Specifically, if the evolution of w is governed by

$$\frac{dw}{dt} = \frac{w_\infty(u) - w}{\tau}, \tag{5.18}$$

and $w(0) = 0$, then w admits the representation given in Eq. (5.14). This corresponds to an exponentially weighted (memoryless) dependence on u.

In the previous sections, we discussed generalizing this kernel using the gamma Mittag-Leffler PDF (3.2) as a memory kernel. Eqs. (3.4)and (5.5) allow us to express w as

$$w = \int_0^t w_\infty(u(s))\kappa(t-s)ds = Ce^{-at}D^{1-\beta}(e^{at}\overline{w}), \tag{5.19}$$

where

$$\frac{d\overline{w}}{dt} = w_\infty(u) - \lambda e^{-at}D^{1-\alpha}(e^{at}\overline{w}) - a\overline{w}. \tag{5.20}$$

The memoryless model is obtained by setting $\alpha = \beta = 1$, $\lambda = 0$, $a = 1/\tau$, and $w = \overline{w}/\tau$. Simplifying the notation by dropping the overline, the general fractional HH-type model is described by

$$\frac{du}{dt} = f(u, Ce^{-at}D^{1-\beta}(e^{at}w)), \tag{5.21}$$

$$\frac{dw}{dt} = w_\infty(u) - \lambda e^{-at}D^{1-\alpha}(e^{at}w) - aw. \tag{5.22}$$

This framework allows modification of the memory dependence of the voltage for sodium and calcium slow inactivation, as well as potassium slow activation. The new parameters are denoted as α, β, λ, and a. The parameter τ does not appear explicitly in the fractional formulation, but, in general, a and λ are inversely related to the characteristic time scale τ. Additionally, the model can be expressed using the Caputo derivative. For sufficiently smooth functions, Riemann-Liouville and Caputo fractional derivatives satisfy the relationship Eq. (3.44). In particular, if α and β are both less than or equal to 1, and solutions are assumed to be absolutely continuous, then the model (5.21) and (5.22) can be expressed using the Caputo fractional derivative instead of the Riemann-Liouville derivative, provided that $w(0) = 0$.

The next section presents the fractional extension of three two-variable cardiac models, along with numerical results.

5.2 FRACTIONAL FITZHUGH-NAGUMO, MITCHELL-SCHAEFFER AND KARMA MODELS, AND THE EMERGENCE OF EADS

The differential equations for the slow variable of traditional two-variable FitzHugh-Nagumo (FHN), Mitchell-Schaeffer (MS), and Karma models have the form of Eq. (5.18). These models are implicitly constructed with memoryless exponential memory kernels, which are known to be unable to reproduce mixed-mode oscillations. In this section, we present the emergence of EADs in adapted versions of these models when the memory kernel of the slow variable is modified as discussed in the previous section.

Figure 5.2 illustrates examples of APs with EADs in the 3D reduced version of the Luo-Rudy model (3) and in the three 2D fractional models presented in this paper.

5.2.1 Fractional FitzHugh-Nagumo Model

We use the FHN equations (136) to model the ionic current. The solution waveform of the FHN system exhibits hyperpolarization of the potential in the refractory period. However, this feature is not characteristic of the myocyte AP and may adversely affect its recovery properties, especially in reentrant activation patterns. To adapt the model to the cardiac AP problem, the hyperpolarization is suppressed using an adaptation first

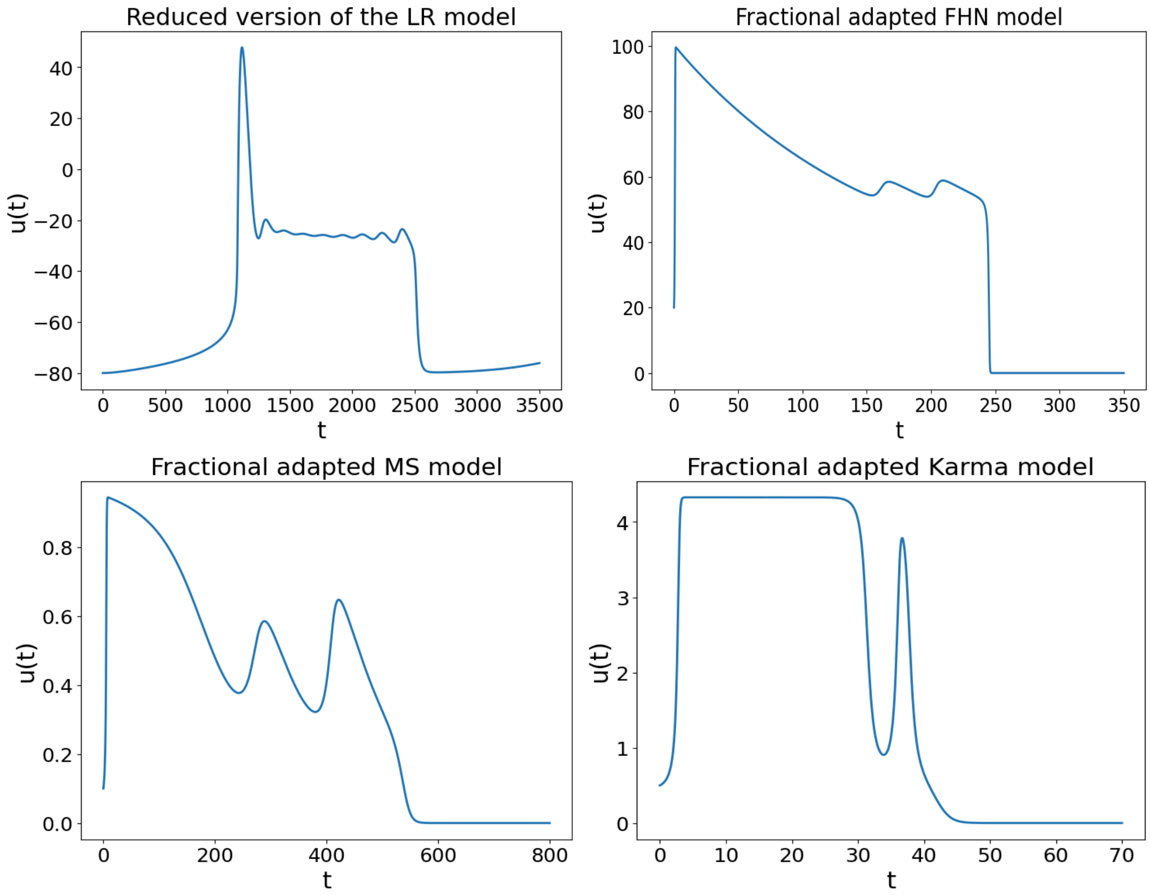

Figure 5.2 – The emergence of EADs was observed in a simplified 3D version of the Luo-Rudy model (3) and in 2D fractional models based on the adapted FHN, MS, and Karma cardiac models.

presented by Rogers and McCulloch in 1994 (23), leading to the following equations:

$$\frac{du}{dt} = -Gu\left(1 - \frac{u}{u_{th}}\right)\left(1 - \frac{u}{u_p}\right) - \eta_1 uw + I_{\text{stim}}, \tag{5.23}$$

$$\frac{dw}{dt} = \eta_2\left(\frac{u}{u_p} - \eta_3 w\right) = \frac{\xi u - w}{\tau}, \tag{5.24}$$

where G, η_1, η_2, and η_3 are positive coefficients, I_{stim} is the input current, u_{th} is the threshold, and u_p is the peak potential. We have $\tau = \frac{1}{\eta_2\eta_3}$ and $\xi = \frac{\tau\eta_2}{u_p} = \frac{1}{\eta_3 u_p}$.

Consider $\gamma = \frac{1}{\tau} = \eta_2\eta_3$. The function w implicitly incorporates past values of the voltage with exponential weighting. In fact, the system of ODEs Eqs. (5.23) and (5.24) is equivalent to the integral representation:

$$\frac{du}{dt} = -Gu\left(1 - \frac{u}{u_{th}}\right)\left(1 - \frac{u}{u_p}\right) - \eta_1 uw + I_{\text{stim}}, \tag{5.25}$$

$$w = \int_0^t \gamma e^{-\gamma(t-s)} \xi u(s) ds. \tag{5.26}$$

We generalize this using a delay kernel $\kappa(t)$:

$$\frac{du}{dt} = -Gu\left(1 - \frac{u}{u_{th}}\right)\left(1 - \frac{u}{u_p}\right) - \eta_1 u \int_0^t \kappa(t-s)\xi u(s) ds + I_{\text{stim}}. \tag{5.27}$$

Using the gamma Mittag-Leffler PDF (3.2) as $\kappa(t)$, Eqs. (5.21) and (5.22) allow us to obtain the generalized fractional FHN model:

$$\text{Generalized FHN}\begin{cases} \dfrac{du}{dt} & = -Gu\left(1-\dfrac{u}{u_{th}}\right)\left(1-\dfrac{u}{u_p}\right) - \eta_1 Cue^{-at}D^{1-\beta}(e^{at}w) + I_{\text{stim}}, \\ \dfrac{dw}{dt} & = \xi u - \lambda e^{-at}D^{1-\alpha}(e^{at}w) - aw. \end{cases} \tag{5.28}$$

If $\alpha = \beta = 1$, $a = \gamma$, and $\lambda = 0$, with the rescaling $w := w/\tau$, we recover the classical model. We consider the initial conditions $w(0) = 0$ and $u(0) = 20$ to account for the initial input current. From now on, we omit the term I_{stim} for brevity.

When we use the gamma Mittag-Leffler PDF to generalize the memory kernel, it reveals the emergence of EADs. The following simulations are conducted with a set of parameters largely derived from (137):

$$G = 1.704, \eta_1 = 4.4, \eta_2 = 0.012, \eta_3 = 1, u_{th} = 13, u_p = 100. \tag{5.29}$$

Seeking minimal models in which EADs emerge, we find the possibility of this phenomenon with simple Mittag-Leffler distributed delays. This occurs in the case $\alpha = \beta$ and $a = 0$ in Eq. (5.28):

$$\text{FHN - ML Kernel}\begin{cases} \dfrac{du}{dt} & = -Gu\left(1-\dfrac{u}{u_{th}}\right)\left(1-\dfrac{u}{u_p}\right) - \eta_1 CuD^{1-\alpha}w, \\ \dfrac{dw}{dt} & = \xi u - \lambda D^{1-\alpha}w. \end{cases} \tag{5.30}$$

In this case, there is no finite mean or variance (79), although the memory kernel can be close to exponential during the AP interval. Figure 5.3A shows the emergence of EADs when $\alpha = \beta = 0.998$, with a pacing period of 700, ms. Note that the number of spikes of the first AP is different, but the subsequent APs also exhibit EADs. The comparison of the classic and the new AP is illustrated in Figure 5.3B, and Figure 5.3C compares the memory kernels. The fractional AP exhibits slower initial repolarization than the classic AP, which relates to a smaller numerical mean in the first moments. In fact, for a shorter delay, the gating variable w relates to a more recent smaller voltage and can be relatively weaker than expected. Once $\beta < 1$, the memory kernel is singular. The singularity is not evident because the kernel decays rapidly at first moments. The fractional and classic trajectories are compared in Figure 5.3D. The self-intersections of the fractional trajectory are clear. We highlight that the second coordinate when the trajectories are plotted is the convolution of Eq. (5.19). We cannot compare the w variable directly because w was redefined between Eqs. (5.20) and (5.22).

Another case arises when $\alpha = 1$ and $\lambda = 0$, which corresponds to a simple gamma memory kernel. In this case, the fractional Riemann- Liouville derivative only appears in the differential equation of the voltage:

$$\text{FHN - Gamma Kernel}\begin{cases}\dfrac{du}{dt} &= -Gu\left(1-\dfrac{u}{u_{th}}\right)\left(1-\dfrac{u}{u_p}\right)-\eta_1 Cue^{-at}D^{1-\beta}(e^{at}w),\\ \dfrac{dw}{dt} &= \xi u - aw.\end{cases} \tag{5.31}$$

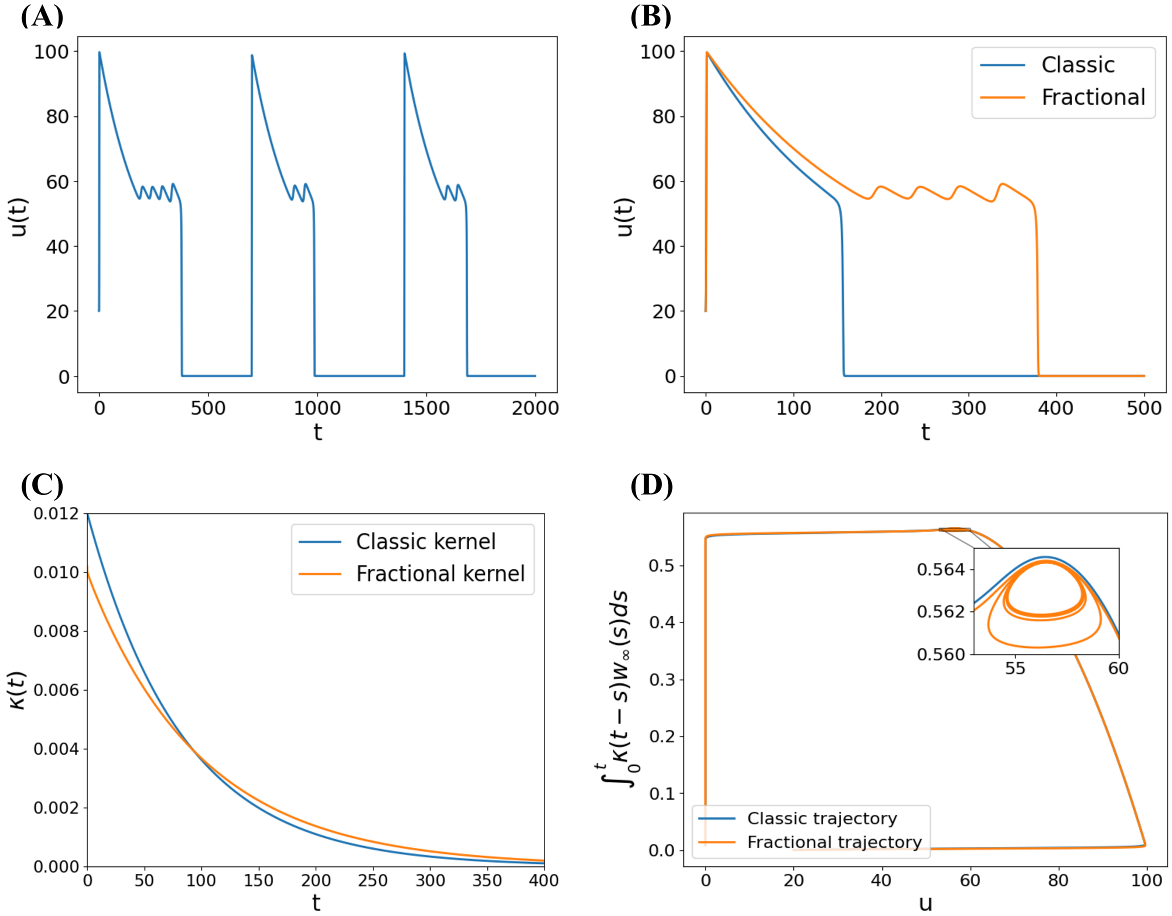

Figure 5.3 – Solution of the model (5.30) with Mittag-Leffler memory kernel, for parameters $\alpha = \beta = 0.998$, $a = 0$, and $\lambda = 0.01$. **(A)** AP with the emergence of EADs for three stimuli at a pace of 700 ms. **(B)** Comparison of memoryless AP and AP with the emergence of EADs, showing slower initial repolarization in the latter. **(C)** Comparison of exponential and Mittag-Leffler distributed memory kernels, given by $\lambda t^{\alpha-1}E_{\alpha,\alpha}(-\lambda t^{\alpha})$. The fractional memory kernel is singular once $\alpha = \beta < 1$, but decreases rapidly initially. However, they intersect, and the fractional kernel surpasses the exponential kernel. **(D)** Comparison of classic and fractional trajectories, showing autointersections in the latter.

We can also obtain EADs when $\beta = 1$. In this case, the fractional Riemann-Liouville derivative only appears in the differential equation of the slow variable:

$$\frac{du}{dt} = -Gu\left(1-\frac{u}{u_{th}}\right)\left(1-\frac{u}{u_p}\right)-\eta_1 Cuw, \tag{5.32}$$

$$\frac{dw}{dt} = \xi u - \lambda e^{-at}D^{1-\alpha}(e^{at}w) - aw. \tag{5.33}$$

Examples of the emergence of EADs for these specific simplifications and other combinations are shown in Appendix D. In the following subsections, we propose to adjust two other two-variable cardiac models, namely the MS and Karma models, to have a phase portrait similar to the FHN cardiac model discussed earlier, thus exhibiting similar properties. This adaptation, along with the incorporation of the gamma Mittag-Leffler PDF delay kernel, enables these models to also exhibit the emergence of EADs.

5.2.2 Fractional Adapted Mitchell-Schaeffer Model

In (24), Mitchell and Schaeffer introduced and studied a model for the electrical activity of the cardiac membrane with an inward and an outward current. The model contains two functions of time: the transmembrane potential or voltage $u(t)$ and a gating variable $w(t)$, which satisfy the following ODEs:

$$\frac{du}{dt} = w\frac{u^2(1-u)}{\tau_{in}} - \frac{u}{\tau_{out}}, \tag{5.34}$$

$$\frac{dw}{dt} = \begin{cases} \frac{1-w}{\tau_{open}}, & u < u_{gate} \\ \frac{-w}{\tau_{close}}, & u > u_{gate}. \end{cases} \tag{5.35}$$

We propose a model, which we call an adapted version of the MS model, described by

$$\frac{du}{dt} = w\frac{u^2(1-u)}{\tau_{in}} - \frac{u}{\tau_{out}}, \tag{5.36}$$

$$\frac{dw}{dt} = \frac{2}{\tau_{open}+\tau_{close}}(u_{gate} - u - w). \tag{5.37}$$

We should consider the initial conditions $w(0) = 1$ and $u(0) = 1$ to account for the initial input current. However, the initial condition $w(0) = 1$ is not consistent with the convolution described in Eq. (5.15). To address this, we suggest a variable transformation $w \mapsto 1 - w$ to ensure that $w(0) = 0$. The model is reformulated as

$$\frac{du}{dt} = (1-w)\frac{u^2(1-u)}{\tau_{in}} - \frac{u}{\tau_{out}}, \tag{5.38}$$

$$\frac{dw}{dt} = \frac{2}{\tau_{open}+\tau_{close}}(1 + u - u_{gate} - w). \tag{5.39}$$

The simulations were conducted with parameters largely derived from (24):

$$\tau_{in} = 0.3, \tau_{out} = 6, u_{gate} = 0.67, \tau_{open} = 120, \tau_{close} = 150. \tag{5.40}$$

The method of generalization via the gamma Mittag-Leffler PDF kernel (see Eqs. (5.21) and (5.22)) leads to the fractional model:

$$\text{Generalized MS} \begin{cases} \dfrac{du}{dt} & = (1 - Ce^{-at}D^{1-\beta}(e^{at}w))\dfrac{u^2(1-u)}{\tau_{in}} - \dfrac{u}{\tau_{out}}, \\ \dfrac{dw}{dt} & = 1 + u - u_{gate} - \lambda e^{-at}D^{1-\alpha}(e^{at}w) - aw. \end{cases} \tag{5.41}$$

Generalizing the memory kernel with the gamma Mittag-Leffler probability density function enables the formation of EADs. An example is illustrated in Figure 5.4A. Figure 5.4B compares the kernels. When $\beta < 1$, the gamma Mittag-Leffler kernel is singular and is above the classic memory kernel initially. It crosses the classic kernel near 100 ms. Finally, the comparison between the fractional and the classic trajectory is depicted in Figure 5.4C. Note that the AP repolarizes faster initially. This is related to a greater numerical mean in the first moments, as mentioned above.

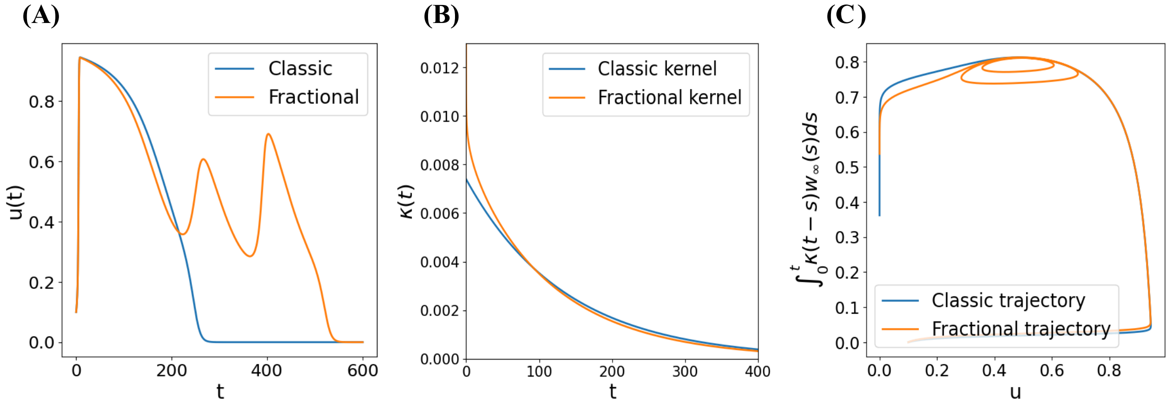

Figure 5.4 – Solution of the model Eq. (5.41) with a gamma Mittag-Leffler distributed memory kernel, for parameters $\alpha = 0.9$, $\beta = 0.95$, $a = \frac{2}{\tau_{open}+\tau_{close}}$, $\lambda = 0.1 \cdot a$. **(A)** Comparison of memoryless AP and AP with EAD emergence. **(B)** Comparison of exponential and gamma Mittag-Leffler distributed memory kernels. The fractional memory kernel is singular when $\beta < 1$, but decreases rapidly and they intersect in the time interval of interest. **(C)** Comparison of classic and fractional trajectories, showing autointersections in the latter.

5.2.3 Fractional Adapted Karma Model

The Karma model is based on an analysis of the Noble model, with the fast gate variables eliminated adiabatically. The model consists of two variables: a fast variable related to the membrane voltage and a slow gate variable. This model was first introduced by Alain Karma in 1993 (25) to demonstrate spiral wave breakup due to alternans. The fast variable u represents the voltage, while w represents the combined effects of sodium slow inactivation and potassium slow activation:

$$\frac{du}{dt} = -u + \left[1 + 4\gamma - \left(\frac{w}{w^*}\right)^{xm}\right] h(u), \tag{5.42}$$

$$\frac{dw}{dt} = \begin{cases} -\epsilon w, & u < 1 \\ \epsilon(1-w), & u > 1, \end{cases} \tag{5.43}$$

where $h(u) = (u^2 - \delta u^3)/\alpha_1$. The wave-front insensitivity is controlled by the parameter xm, indicating the weak dependence of the wave-front velocity on the slow variable, which regulates the AP duration.

We propose a model that we call an adapted version of the Karma model, as described by the following equations:

$$\frac{du}{dt} = -u + \left[1 + 4\gamma - \left(\frac{w}{v^*}\right)^{xm}\right] \frac{u^2 - \delta u^3}{\alpha_1}, \tag{5.44}$$

$$\frac{dw}{dt} = \begin{cases} -\epsilon w, & u < 1 \\ \epsilon(u - 1 - w), & u > 1. \end{cases} \tag{5.45}$$

We consider the initial conditions $w(0) = 0$ and $u(0) = 0.5$ to account for the initial input current. Most parameters used in the simulations are based on the literature (*e.g.*, (25, 138, 48, 49, 36, 50, 51, 52, 4, 16, 85, 27, 136, 139)). The parameters for the model are defined as follows:

$$\alpha_1 = 9.5, \gamma = 2.9 \times 1.92, v^* = 0.64, xm = 30, \epsilon = 0.008, \delta = 0.91 \times 0.23. \tag{5.46}$$

The method of generalization via the gamma Mittag-Leffler PDF kernel (see Eqs. (5.21) and (5.22)) leads to the generalized Karma model:

$$\text{Generalized Karma} \begin{cases} \dfrac{du}{dt} & = -u + \left[1 + 4\gamma - \left(\dfrac{Ce^{-at}D^{1-\beta}(e^{at}w)}{v^*}\right)^{xm}\right] \dfrac{u^2 - \delta u^3}{\alpha_1}, \\ \dfrac{dw}{dt} & = \begin{cases} -\lambda e^{-at}D^{1-\alpha}(e^{at}w) - aw, & u < 1 \\ u - 1 - \lambda e^{-at}D^{1-\alpha}(e^{at}w) - aw, & u > 1. \end{cases} \end{cases} \tag{5.47}$$

When we use the gamma Mittag-Leffler probability density function to generalize the memory kernel, it enables the emergence of EADs. An example is shown in Figure 5.5A. Figure 5.5B compares the different kernels. When $\beta < 1$, the fractional kernel is singular, but it decreases rapidly and remains smaller than the exponential kernel within the interval of interest. The comparison between the fractional and the classic trajectory is presented in Figure 5.5C. It is also observed that the fractional AP is faster in the initial repolarization. This is related to a greater numerical mean in the first moments, as mentioned above.

5.3 DISCUSSION OF THE EMERGENCE OF EARLY AFTERDEPOLARIZATIONS

5.3.1 Sensitivity Analysis

It is challenging to explain comprehensively the roles of the four parameters α, β, a, and λ, as they are interrelated in a complex manner. We choose the generalized fractional FHN model Eq. (5.28) to study the emergence of EADs.

As a first analysis, we consider $a = 0$ and $0 < \alpha = \beta \leq 1$, corresponding to the simple Mittag–Leffler case described in Eq. (5.30) and in Figure 5.3. The corresponding memory kernel is given by

$$\kappa(t) = \lambda t^{\alpha-1} E_{\alpha,\alpha}(-\lambda t^{\alpha}). \tag{5.48}$$

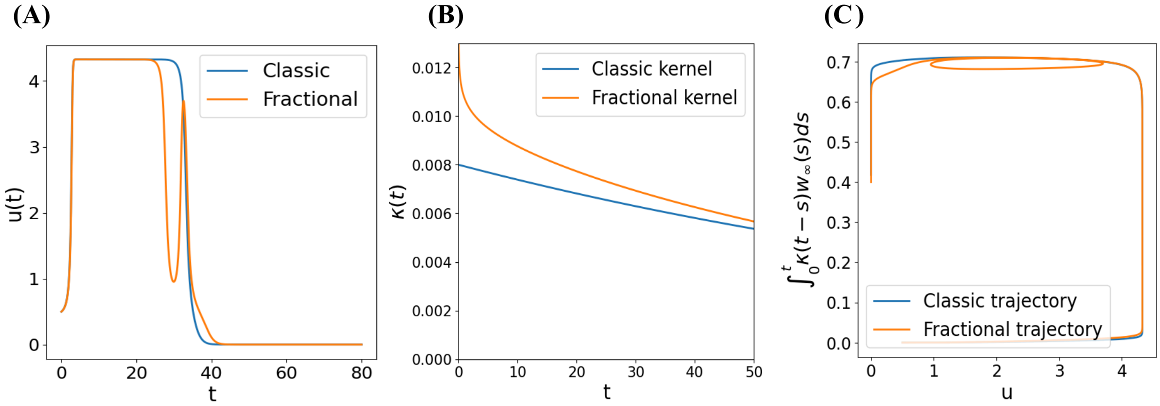

Figure 5.5 – Solution of the model Eq. (5.47) with a gamma Mittag-Leffler distributed memory kernel for parameters $\alpha = \beta = 0.945$, $a = \epsilon$, $\lambda = 0.1 \cdot a$. **(A)** Comparison of memoryless AP and AP with EAD emergence. **(B)** Comparison of exponential and gamma Mittag-Leffler distributed memory kernels. The fractional memory kernel is singular when $\beta < 1$, and it remains above the exponential kernel in the time interval of interest. **(C)** Comparison of classic and fractional trajectories, showing autointersections in the latter.

Figure 5.6A shows a sensitivity analysis and the region where EADs emerge. We analyzed simulations with $\alpha = 0.999$ and λ values of 0.006, 0.012, 0.018, and 0.024, represented by the large black dots on the horizontal dotted line in Figure 5.6A. Starting from a typical AP with $\alpha < 1$ and a Mittag–Leffler memory kernel, EADs can emerge if we decrease α or increase λ. In Figure 5.6B, it is evident that as λ increases, the likelihood of EADs or repolarization failures increases, while the initial repolarization phase becomes faster. This type of kernel cannot be characterized in terms of mean and variance, as these are infinite when $a = 0$. However, useful insights can still be obtained from the numerical mean. Figure 5.6D illustrates the relationship between λ and the numerical mean of the kernel: $\int_0^t s\,\kappa(s)ds$, over time. This relationship is expected, since λ represents the time constant of the Mittag-Leffler part of the kernel, which extends the exponential function and is completely monotonic with parameters $0 < \alpha = \beta \leq 1$ and $\lambda > 0$. Furthermore, the kernels exhibit higher values at initial times when λ is greater. Since $\beta < 1$, all the kernels are singular at zero. We observe that a higher mean in the first moments corresponds to a faster initial repolarization as λ increases.

Next, we investigate simulations with $\lambda = 0.012$ and α values of 0.997, 0.998, 0.999, and 1, denoted by the large black dots on the vertical dotted line in Figure 5.6A. Figure 5.6C indicates that the initial repolarization phase remains consistent across these parameter values. This similarity is supported by Figure 5.6E, where the kernels and their means show minimal variation during the initial repolarization.

We now consider the case where $\lambda = 0$ and $\alpha = 1$, which is the simple gamma case described in Eq. (5.31) and shown in Figure D.1. The memory kernel is given by:

$$\kappa(t) = \frac{a^\beta}{\Gamma(\beta)} t^{\beta-1} e^{-at}. \tag{5.49}$$

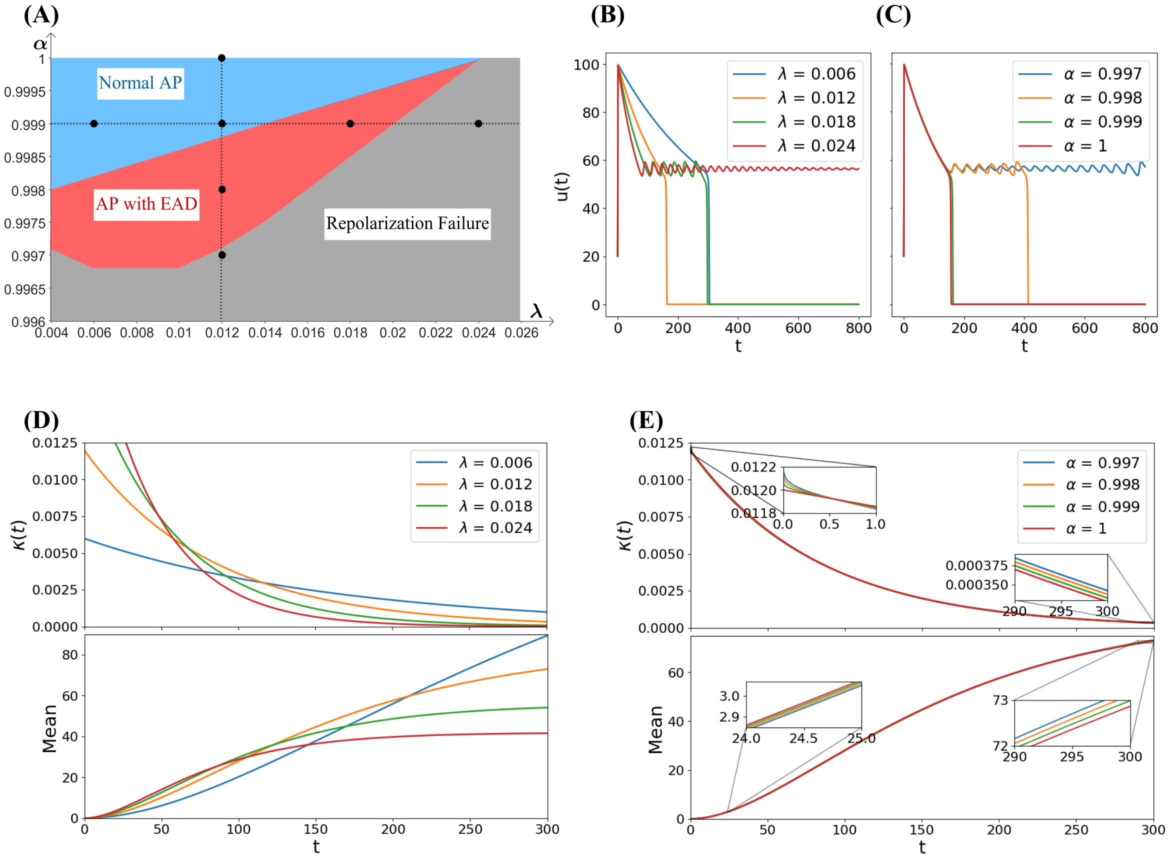

Figure 5.6 – The figure shows simulations for the Mittag-Leffler simple case described in Eq. (5.30) and in Figure 5.3. The standard case is obtained if $\alpha = 1$ and $\lambda = 1/\tau = 0.012$. **(A)** Regions of normal AP, AP with EAD, and repolarization failure in the plane $\lambda - \alpha$. **(B)** Effect of λ on AP behavior with memory kernel Eq. (5.48). **(C)** Effect of α on AP behavior with memory kernel Eq. (5.48). **(D)** Effect of λ on the memory kernel Eq. (5.48). Once $\beta = \alpha < 1$, the kernels are singular. **(E)** The slight effect of α on the memory kernel Eq. (5.48).

This type of kernel will be analyzed in terms of mean and variance in the next section. Figure 5.7A shows the sensitivity analysis and the region of the emergence of EADs. The standard case is obtained if $\beta = 1$ and $a = 1/\tau = 0.012$. We analyze the simulations generated with $\beta = 0.995$ and a values of 0.002, 0.01, 0.018, and 0.024, represented by the large black dots on the horizontal dotted line in Figure 5.7A. In general, for a typical AP with $\beta < 1$ and a gamma memory kernel, EADs can emerge when we decrease β or increase a. In Figure 5.7B, it is evident that as a increases, the likelihood of EADs or repolarization failures increases, while the initial repolarization phase becomes faster. The relationship between a and the mean of the kernel is further illustrated in Figure 5.7D, where the time constant a influences the kernel's behavior. The kernels exhibit higher values at initial times when a is larger, as expected due to a being the time constant of the exponential part of the kernel. Additionally, when $\beta < 1$, all kernels become singular. An increase in a also results in a higher numerical mean at early times, indicating a faster initial repolarization phase. Note that the exact mean of the kernel decreases when a

increases.

Subsequently, we investigate the simulations generated with $a = 0.01$ and β values of 0.975, 0.985, 0.995, and 1, denoted by the large black dots on the vertical dotted line. Figure 5.7C reveals that the initial repolarization phase remains consistent across these parameter values. Note from Figure 5.7E the similarity between the kernels and the means. The exact mean decreases when β decreases.

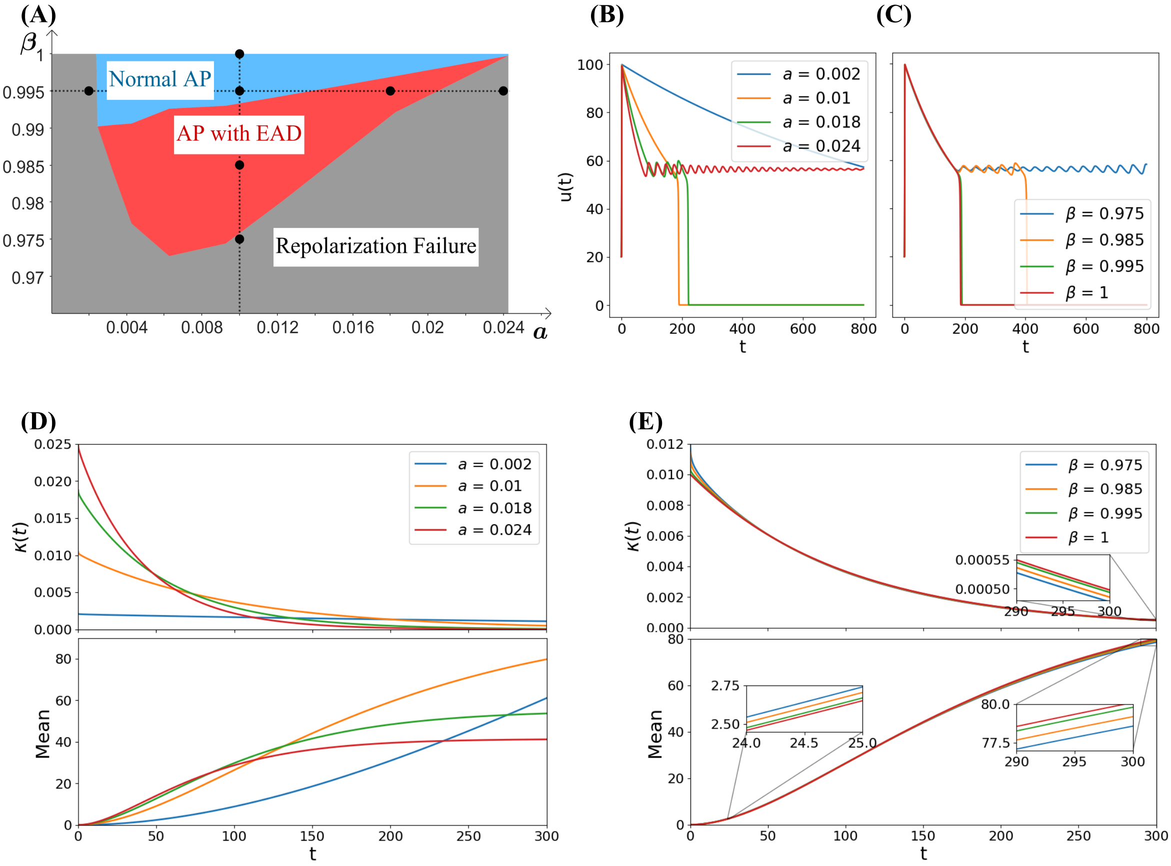

Figure 5.7 – Simulations for $\lambda = 0$ and $\alpha = 1$, the gamma simple case described in Eq. (5.31) and in Figure D.1. **(A)** Regions of normal AP, AP with EAD, and repolarization failure in the plane $a - \beta$. **(B)** Effect of a on AP behavior with memory kernel Eq. (5.49). If a is too small, there is no final repolarization until 800 ms. **(C)** Effect of β on AP behavior with memory kernel Eq. (5.49). The initial repolarization remains similar. **(D)** Effect of a on the memory kernel Eq. (5.49). **(E)** Effect of β on the memory kernel Eq. (5.49). The means are very close at the beginning, but over time, it becomes apparent that the smaller the β, the lower the average.

These two simple cases illustrate the richness of the generalized fractional FHN model in terms of both the shape of the memory kernel and the resulting AP dynamics. Although additional parameters are introduced, which may be challenging to estimate from biological data, the model can remain simpler than high-dimensional formulations. The choice of modeling approach in each case should be guided by further theoretical and experimental investigations.

5.3.2 The Emergence of EADs in terms of Mean and Variance

The aim of this section is to describe the emergence of EADs in terms of the mean and the variance of the memory kernel. For this purpose, we consider $\lambda = 0$ and $\alpha = 1$, which corresponds to the gamma simple case described in Eq. (5.31) and in Figure D.1. The memory kernel for this case is given by Eq. (5.49).

This choice is useful because it simplifies the study of the kernel while retaining fundamental aspects of its generality. In fact, for any positive real values μ and σ^2, there exist parameters a and β such that the mean and variance of the gamma memory kernel are μ and σ^2, respectively, as discussed in previous chapters.

The classic exponential memory kernel is obtained when $\beta = 1$. In the plane of mean × variance, this corresponds to the parabola $\sigma^2 = \mu^2$. Above this parabola, $\beta < 1$, and the memory kernels are weak - singular at the origin. Conversely, below this parabola, $\beta > 1$, and the memory kernels are strong and non-singular. For a fixed μ, when $\sigma^2 \to 0$, the memory kernel converges to the Dirac delta centered at μ. In this case, the model Eq. (5.31) turns into the DDE:

$$\frac{du}{dt} = -Gu(t)\left(1 - \frac{u(t)}{u_{th}}\right)\left(1 - \frac{u(t)}{u_p}\right) - \eta_1 \xi u(t) u(t - \mu). \tag{5.50}$$

When $\mu \to 0$ and $\sigma^2 \to 0$, the memory kernel converges to the Dirac delta centered at 0, and the model Eq. (5.31) simplifies to the ODE:

$$\frac{du}{dt} = -Gu\left(1 - \frac{u}{u_{th}}\right)\left(1 - \frac{u}{u_p}\right) - \eta_1 \xi u^2. \tag{5.51}$$

Figure 5.8A shows three regions in the mean × variance plane. First, there is a region where complete APs occur. Its lower limit corresponds to Dirac delta memory kernels. Then, there is a region in which the APs exhibit EADs, leading to a region of repolarization failure. The emergence of EADs (red region) is negligible for small means. Figure 5.8B illustrates the limit case with Dirac delta kernels, as described in Eq. (5.50). When $\mu = 0$, the model reduces to the ODE (5.51), resulting in no depolarization. Figure 5.8C illustrates the APs generated by the kernels corresponding to the black points in Figure 5.8A, progressing through the regions in a vertical slice. Note that the mean remains the same, and as the variance increases, the AP duration lengthens, making final repolarization more difficult.

The key finding of this analysis is that transitioning from the blue region without EADs to the red region with EADs can be achieved by making slight adjustments either to the left (lower mean) or upwards (higher variance). Starting from the normal AP region, for each μ, if σ^2 increases, there is a small interval where EADs occur. Then, if σ^2 increases more, there is repolarization failure. A leftward shift corresponds to a smaller mean in the kernel, suggesting a shorter memory, while moving upwards maintains the mean but increases the variance, causing the kernel to shift towards the origin (see Figure 5.8).

Biologically, there are two dominant hypotheses regarding the generation mechanisms of EADs (127). One is a calcium-driven mechanism, while the other is a voltage-driven mechanism in which EADs are secondary depolarizations driven by instabilities in the voltage system. In this case, the induction of EADs is attributed to two major factors: reduced repolarization reserve and reactivation of the L-type calcium current. It occurs when outward currents are reduced or inward currents are increased, for example, when potassium currents are reduced.

In the modified FHN models, the fast variable represents the transmembrane voltage, while the slow variable is associated with potassium channel activation. During repolarization, the membrane voltage decreases, and the slow variable follows this change with a delay. If this delay is reduced, the slow variable tracks the decreasing voltage more rapidly, resulting in a lower potassium current because the earlier voltage is smaller. This premature decline in the potassium current can make the membrane more susceptible to reactivation by inward currents, increasing the likelihood of EADs.

Figure 5.9 shows similar results for the MS and Karma fractional models with a gamma memory kernel. However, in these models, the biological interpretation differs from the above. In the fractional MS model (Eq. (5.41)), the convolution term is associated with the inactivation of inward current (whether sodium or calcium). When the memory distribution considers a more recent past, the inward current increases temporarily due to lower recent voltage values compared to distant ones during initial repolarization. This shifts the AP and promotes the emergence of EADs. A similar behavior is observed in the fractional Karma model (Eq. (5.47)).

We hypothesize that similar insights can be applied to the general gamma Mittag-Leffler PDF memory kernel, where the parameters α, β, a, and λ are not constrained, except for the requirement of the PDFs existence. However, establishing a general approach is not easy. Some general kernels can be effectively described using a gamma kernel, but not all. Figure 5.10 illustrates two different APs generated for Eq. (5.28) with kernels of the same mean and variance. The first has four free parameters related to fractionalization, while the second uses a gamma kernel. An important observation is that the general kernel exhibits a behavior that cannot be captured with a gamma kernel. Further discussion about the richness of general kernels can be found in Chapter 3 and Appendix C.

5.3.3 Stability Analysis

From a stability analysis perspective, the transition from repolarization failure to complete AP relates to a change in stability. Our simulations indicate that EADs in the fractional model are associated with unstable focus or unstable limit cycles observed

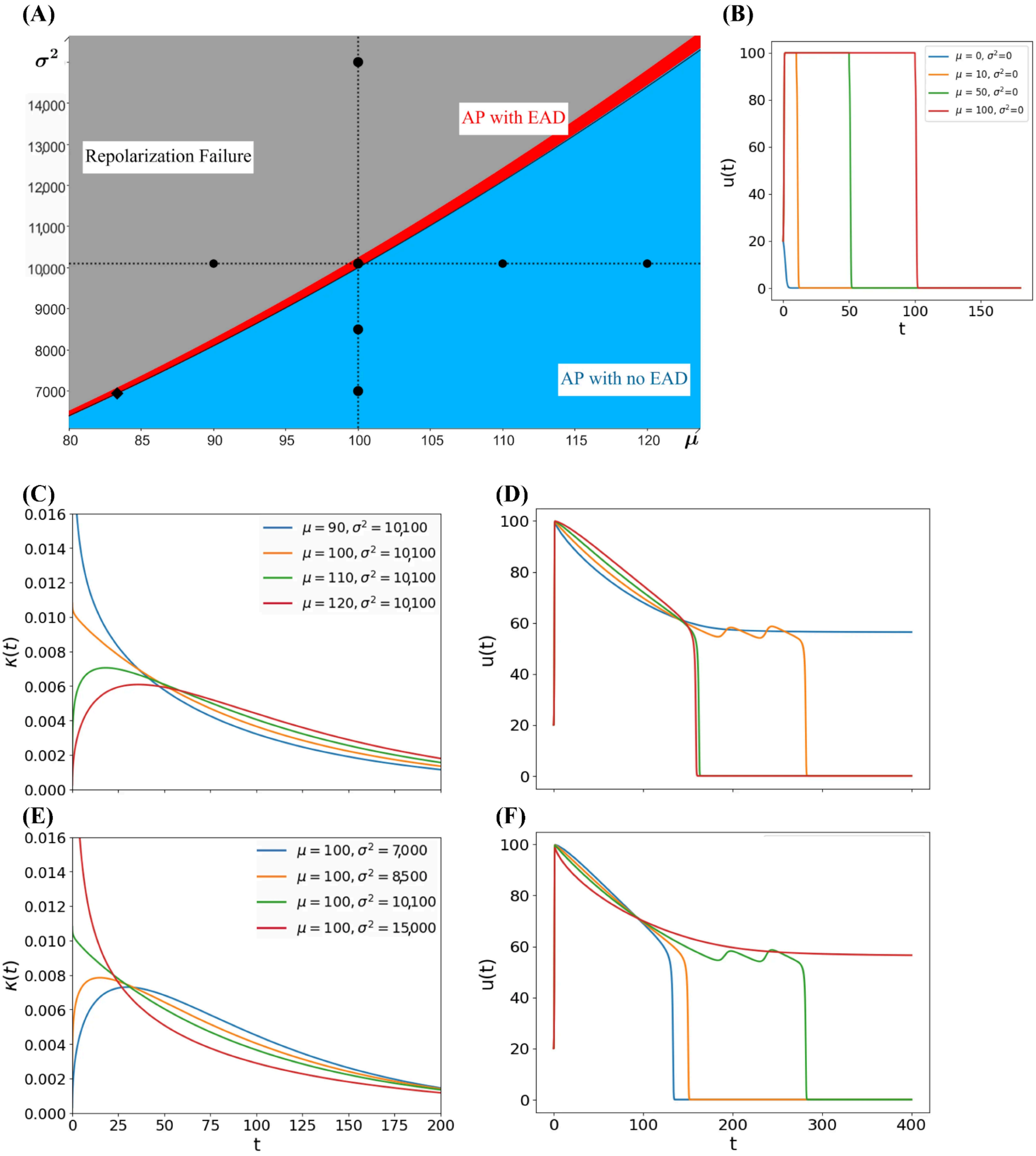

Figure 5.8 – Simulations for the gamma simple case described in Eq. (5.31) and in Figure D.1, respecting the relations in Eq. (3.23). The standard case is obtained in the black diamond, in which $\beta = 1$ and $a = 1/\tau = 0.012$. **(A)** Regions of normal AP, AP with EADs, and repolarization failure in the plane $\mu \times \sigma^2$. The black parabola corresponds to the integer cases in which $\beta = \mu^2/\sigma^2 = 1$. **(B)** Special case in which the model is described by the DDE (5.50). When $\mu = 0$, the model comes down to the ODE (5.51). When $\mu > 0$, the behavior of the model is like a square wave with length μ. **(C)** Gamma kernels generated by the black points in **(A)**, going through the regions in a horizontal slice. For a fixed σ^2, as μ decreases, the more recent past has more weight in the memory kernel. **(D)** APs generated by the gamma memory kernels in **(C)**. **(E)** Gamma kernels generated by the black points in **(A)**, going through the regions in a vertical slice. For a fixed μ, as σ^2 increases, the more recent past has more weight in the memory kernel. **(F)** APs generated by the gamma memory kernels in **(E)**.

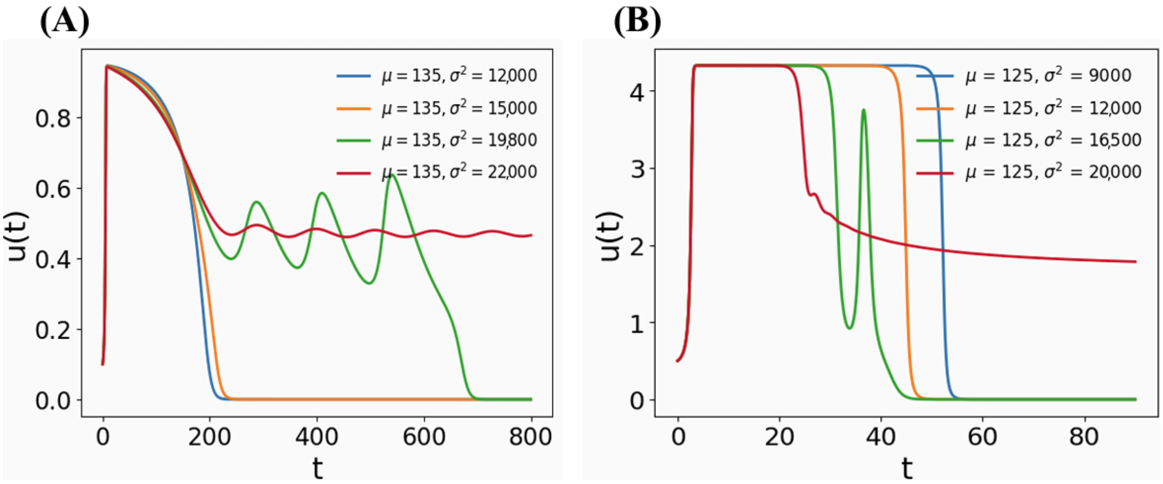

Figure 5.9 – **(A)** APs generated by the MS fractional model Eq. (5.41) with a gamma kernel described by Eq. (3.23). **(B)** APs generated by the Karma fractional model Eq. (5.47) with a gamma kernel described by Eq. (3.23). Maintaining the mean while the variance increases, the final repolarization becomes more difficult in both cases.

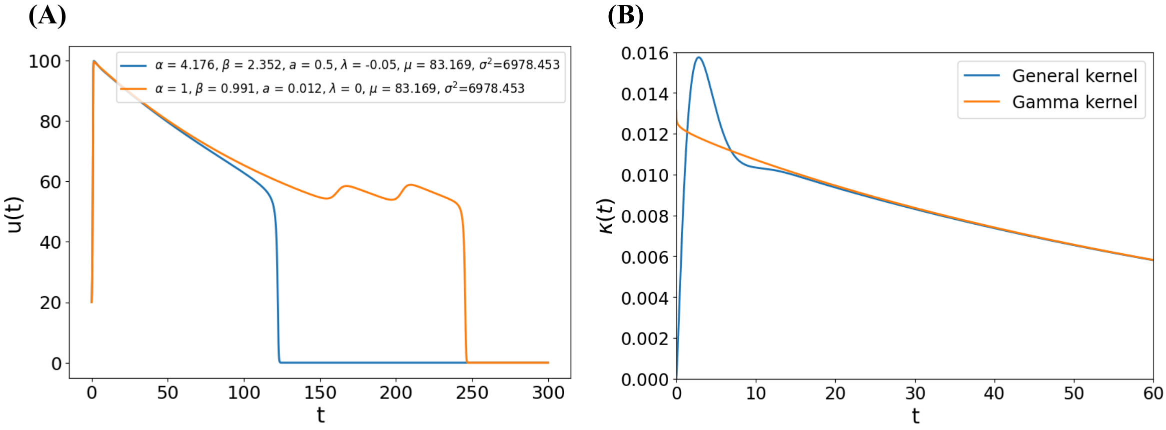

Figure 5.10 – **(A)** APs generated by the FHN fractional model Eq. (5.28). **(B)** Respective memory kernels with the same mean and variance.

in the corresponding integer model. In this context, we consider the time scale τ as the bifurcation parameter in the integer order model Eq. (5.28), and fix $a = 1/\tau$ in the corresponding fractional model Eqs. (5.23) and (5.24).

First, we prove that the fractional system Eq. (5.28) has the same equilibrium point as its equivalent integer system (5.23) and (5.24). Although this is straightforward when the integer-order derivative is replaced by a Caputo fractional derivative, the equilibrium computation when the fractional Riemann-Liouville derivative arises from an integrodifferential perspective is not immediate. In (26), we see an example in which the equilibrium of the fractional equation is not the same as its integer counterpart.

5.3.3.1 Equilibrium Points

The system (5.23) and (5.24) have a trivial equilibrium given by $u^* = w^* = 0$. We now discuss non-trivial equilibria. Note that in equilibrium, we must have $w = \xi u$. Then, if $u \neq 0$, the equilibrium must satisfy

$$-G\left(1 - \frac{u}{u_{th}}\right)\left(1 - \frac{u}{u_p}\right) - \eta_1 \xi u = 0. \tag{5.52}$$

This is a quadratic equation in u and can be written as

$$\frac{G}{u_{th}u_p}u^2 - \left(G\left(\frac{1}{u_{th}} + \frac{1}{u_p}\right) - \eta_1\xi\right)u + G = 0. \tag{5.53}$$

The system can have at most two non-trivial equilibria, given by

$$u_\pm = \frac{-\overline{b} \pm \sqrt{\overline{b}^2 - 4\overline{a}\overline{c}}}{2\overline{a}}; \qquad w_\pm = \xi u_\pm, \tag{5.54}$$

where

$$\overline{a} = \frac{G}{u_{th}u_p}; \qquad \overline{b} = -G\left(\frac{1}{u_{th}} + \frac{1}{u_p}\right) + \eta_1\xi; \qquad \overline{c} = G. \tag{5.55}$$

Next, we aim to calculate the equilibrium points of the fractional system (5.28). Based on a known result under certain assumptions (see, *e.g.*, (67) and Eq. (3.8)), the following asymptotic behavior is derived:

$$\lim_{t\to\infty}[e^{-at}\, D^{1-\beta}(e^{at}f(t))] = a^{1-\beta}f^*, \qquad f^* = \lim_{t\to\infty} f(t). \tag{5.56}$$

Then, in order for an equilibrium $(u^*, \overline{w}^*)$ of the system (5.28) to be valid, it must satisfy the following conditions:

$$-\,Gu^*\left(1 - \frac{u^*}{u_{th}}\right)\left(1 - \frac{u^*}{u_p}\right) - \eta_1 C u^* a^{1-\beta}\overline{w}^* = 0, \tag{5.57}$$

$$\xi u^* - \lambda a^{1-\alpha}\overline{w}^* - a\overline{w}^* = 0. \tag{5.58}$$

Disregarding the trivial equilibrium $(u^*, \overline{w}^*) = (0, 0)$, it is needed to satisfy the condition given by:

$$-\,G\left(1 - \frac{u^*}{u_{th}}\right)\left(1 - \frac{u^*}{u_p}\right) - \eta_1 C a^{1-\beta}\xi\frac{u^*}{\lambda a^{1-\alpha} + a} = 0. \tag{5.59}$$

By definition, C is given by:

$$C = a^\beta + a^{\beta-\alpha}\lambda = \frac{\lambda a^{1-\alpha} + a}{a^{1-\beta}}. \tag{5.60}$$

Then, Eq. (5.59) is equivalent to Eq. (5.52), which concludes the proof that the fractional and integer models have the same set of equilibrium (u^*, w^*). Using Eq. (5.19), we have:

$$w^* = Ca^{1-\beta}\overline{w}^*. \tag{5.61}$$

5.3.3.2 Stability

We study the stability of the integer-order system (5.23) and (5.24). First, we calculate the Jacobian matrix:

$$J = \begin{bmatrix} -G\left(1-\frac{u}{u_{th}}\right)\left(1-\frac{u}{u_p}\right)+Gu\left(\frac{1}{u_{th}}\left(1-\frac{u}{u_p}\right)+\frac{1}{u_p}\left(1-\frac{u}{u_{th}}\right)\right)-\eta_1 w & -\eta_1 u \\ \frac{\xi}{\tau} & -\frac{1}{\tau} \end{bmatrix}. \tag{5.62}$$

In a non-null equilibrium $(u, \xi u)$, we have

$$-G\left(1-\frac{u}{u_{th}}\right)\left(1-\frac{u}{u_p}\right)-\eta_1\xi u = 0. \tag{5.63}$$

Then, the trace of the Jacobian matrix in an equilibrium is given by

$$\mathrm{Tr}(J) = Gu\left(\frac{1}{u_{th}}\left(1-\frac{u}{u_p}\right)+\frac{1}{u_p}\left(1-\frac{u}{u_{th}}\right)\right)-\frac{1}{\tau}. \tag{5.64}$$

In the next step, we compute the determinant of the Jacobian matrix. In an equilibrium $(u, \xi u)$, it is given by

$$\det(J) = -\frac{G}{\tau}u\left(\frac{1}{u_{th}}\left(1-\frac{u}{u_p}\right)+\frac{1}{u_p}\left(1-\frac{u}{u_{th}}\right)\right)+\frac{\eta_1\xi u}{\tau}. \tag{5.65}$$

Thus, in a non-null equilibrium, $\det(J) > 0$ occurs if, and only if,

$$-G\left(\frac{1}{u_{th}}\left(1-\frac{u}{u_p}\right)+\frac{1}{u_p}\left(1-\frac{u}{u_{th}}\right)\right)+\eta_1\xi > 0. \tag{5.66}$$

Note that

$$-G\left(\frac{1}{u_{th}}\left(1-\frac{u}{u_p}\right)+\frac{1}{u_p}\left(1-\frac{u}{u_{th}}\right)\right)+\eta_1\xi \tag{5.67}$$

$$=\frac{2G}{u_{th}u_p}u+\left(-G\left(\frac{1}{u_{th}}+\frac{1}{u_p}\right)+\eta_1\xi\right) \tag{5.68}$$

$$=2\overline{a}u+\overline{b} > 0 \iff u > -\frac{\overline{b}}{2\overline{a}}, \tag{5.69}$$

where $\overline{a} > 0$ and $\overline{b}$ are defined in Eq. (5.55).

Thus, when it exists, (u_-, w_-) is a saddle point. Regarding (u_+, w_+), its existence indicates that it is an unstable point if and only if $\mathrm{Tr}(J) > 0$, which implies:

$$\frac{1}{\tau} < Gu\left(\frac{1}{u_{th}}\left(1-\frac{u}{u_p}\right)+\frac{1}{u_p}\left(1-\frac{u}{u_{th}}\right)\right). \tag{5.70}$$

Since the determinant signal does not depend on τ, a Hopf bifurcation occurs concerning τ when $\mathrm{Tr}(J) = 0$ for (u_+, w_+).

The stability analysis of the equilibrium of the fractional system is not trivial, although the ad hoc replacement of the Caputo fractional derivative in an integer model can have its stability analyzed in a simpler manner (140). Progress in stability studies can be achieved by using integral formulations of the model, as discussed in Appendix B.

5.3.3.3 Emergence of EADs

Recent results (see, for instance, (134, 135)) indicate that oscillatory states in fractional models arise when a bifurcation parameter is taken near Hopf-like bifurcation points. The concept of "Hopf-like" arises due to the impossibility for a fractional model to undergo a classic Hopf bifurcation; in fact, a fractional system cannot have exact periodic solutions (141). However, this concept is used when the integer derivative is replaced on the left side of the ODEs with the Caputo fractional derivative. This is not the case here, but we can gain some insight from simulation results and the stability classification of the integer order counterpart.

Observe that the expression

$$Gu\left(\frac{1}{u_{th}}\left(1-\frac{u}{u_p}\right)+\frac{1}{u_p}\left(1-\frac{u}{u_{th}}\right)\right)=Gu\left(\frac{u_{th}+u_p}{u_{th}u_p}-2\frac{u}{u_{th}u_p}\right) \tag{5.71}$$

is positive precisely in the interval $(0,(u_{th}+u_p)/2)$. This result, together with Eq. (5.70), indicates that a Hopf bifurcation occurs when $\mathrm{Tr}(J)=0$, *i.e.*, when

$$\tau=\tau^*:=\frac{1}{Gu^+\left(\frac{1}{u_{th}}\left(1-\frac{u^+}{u_p}\right)+\frac{1}{u_p}\left(1-\frac{u^+}{u_{th}}\right)\right)}. \tag{5.72}$$

If τ is slightly greater than τ^*, the equilibrium point of the integer model is an unstable spiral. A subcritical Hopf bifurcation occurs at τ^*, and there is an unstable limit cycle when τ is slightly smaller than τ^*. EADs are observed in this neighborhood in our simulations.

With gamma memory kernels, if we set $a=1/\tau$, the mean and the variance are related in the form $\mu/\sigma^2=1/\tau$. EADs are observed when $\mu/\sigma^2\approx 1/\tau^*$ and $\mu^2/\sigma^2\approx \mu/\tau^*<1$. For the parameters of Eq. (5.29), regardless of the value of η_2, we have $\tau^*\approx 52.06$.

In Figure 5.11, we illustrate the behavior of two integer-order solutions and a fractional one. The equilibrium point, shown in red, is an unstable spiral of the integer model. Although the fractional trajectory may enter the spiral region, the non-autonomous nature of the equation allows it to escape and continue evolving. In this example, the yellow fractional and blue classic trajectories have the same initial point and coincide until the vicinity of the equilibrium point.

In Figure 5.12, we show a case where there is an unstable limit cycle. The equilibrium point, shown in red, is a stable spiral of the integer model. The purple solution diverges from the green one, that represents the unstable limit cycle. It is observed that the fractional solution enters the spiral due to the unstable limit cycle but is able to escape it due to the trajectory's ability to self-intersect. As before, in this example, the yellow fractional and blue classical trajectories coincide until they reach the vicinity of the equilibrium point.

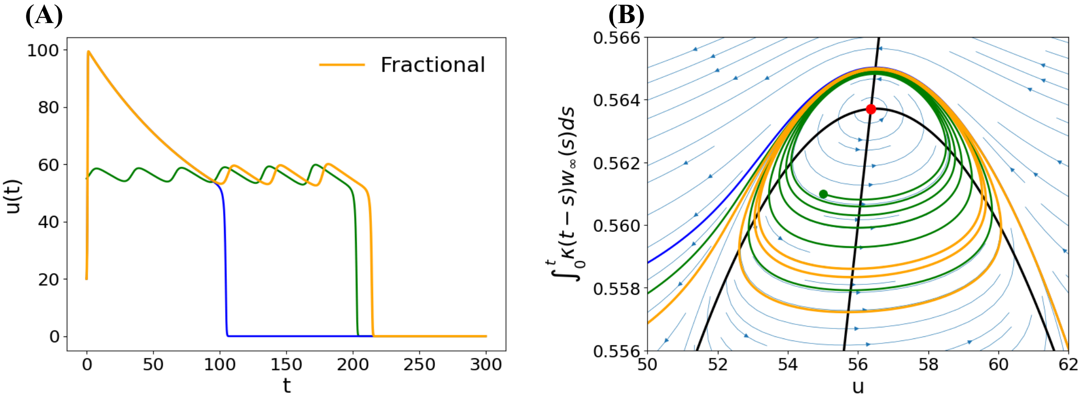

Figure 5.11 – The phase portrait of the solutions in **(A)** is plotted in **(B)** with the parameters of Eq. (5.29), but with $\eta_2 = 0.0191$, so $\tau \approx 52.36$. For the simulation of the fractional model, we consider $a = 1/\tau$, $\mu = 52.15$, $\sigma^2 = \mu\tau$, $\beta = \mu^2/\sigma^2$, $\alpha = 1$, and $\lambda = 0$. The nullclines of the integer-order model are depicted in black, and the red dot represents the equilibrium (u^+, w^+). The green small dot indicates the initial point of the green trajectory, which spirals outwards. The initial condition for the fractional yellow and blue trajectories is $(20, 0)$.

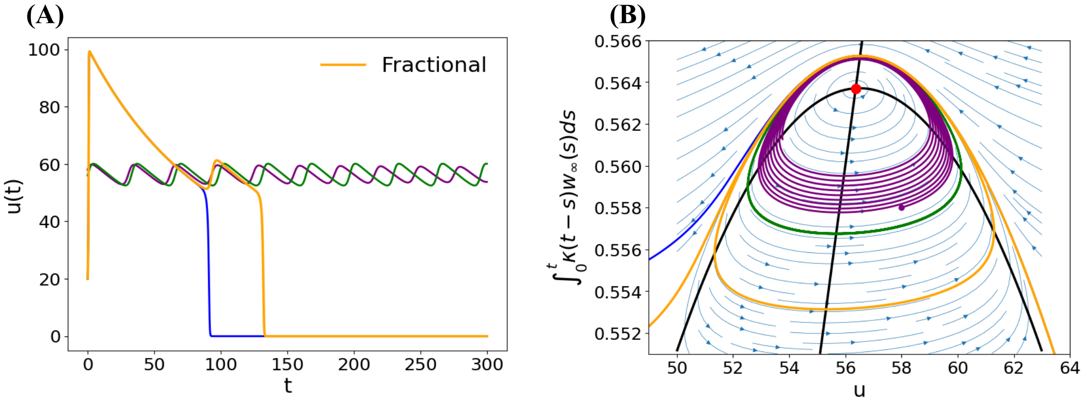

Figure 5.12 – The phase portrait of the solutions in **(A)** is plotted in **(B)** with the parameters of Eq. (5.29), but with $\eta_2 = 0.0191$, so $\tau \approx 43.48$. For the simulation of the fractional model, we consider $a = 1/\tau$, $\mu = 43.45$, $\sigma^2 = \mu\tau$, $\beta = \mu^2/\sigma^2$, $\alpha = 1$, and $\lambda = 0$. The nullclines of the integer-order model are depicted in black, and the red dot represents the equilibrium (u^+, w^+). The purple small dot indicates the initial point of the purple trajectory, which spirals inwards. The initial condition for the fractional yellow and blue trajectories is $(20, 0)$.

These stability observations support the modifications made to the MS and Karma models, as detailed in Appendix E.

5.4 DISCUSSION

This chapter investigates the emergence of EADs by altering the memory kernel of the slow variable in simple two-variable models using tools from FC. Building on the mathematical framework established in previous chapters, we extend HH-type equations with gamma Mittag-Leffler distributed delays to create fractional models. By applying this approach, we observe mixed-mode oscillations in two-variable adapted FHN, MS, and Karma cardiac models, which can be characterized as EADs. Such behavior typically requires at least three variables in autonomous ODE systems.

There are four parameters that play a role in the fractional extension of the models: α, β, a, and λ. The time constant τ is not included in the generalized model, but a and λ are typically associated with it. To discuss the intrinsic relationship between the memory kernel and the generated AP, we conducted a detailed analysis of the sensitivity of parameters for two specific instances of memory kernels: namely, Mittag-Leffler and gamma memory kernels. The emergence of EADs is characterized by changes in the mean and variance of the memory kernel. The analysis reveals that transitioning from a state without EADs to one with EADs can be achieved by a slight decrease in the mean or a slight increase in the variance. Either shift implies that recent voltage values have a greater influence on the potassium current during repolarization, leading to a temporary increase in the AP and triggering EADs. This adjustment in the kernel's characteristics explains the emergence of EADs during repolarization.

Furthermore, we notice that EADs occur when the fractional trajectory passes close to an unstable spiral equilibrium or limit cycle of the integer-order system. The fractional trajectory can enter the spiral but has the ability to escape due to the non-autonomous nature of the fractional formulation, allowing trajectories to intersect themselves. The significance of spiral points in the formation of EADs is consistent with previous findings, such as (142), who showed in a Luo-Rudy cardiac model that EADs arise when the non-resting steady state of the voltage/Ca current subsystem loses stability through a Hopf bifurcation, leading to oscillations terminated by a homoclinic bifurcation. The relationship between oscillations and Hopf-like bifurcations in fractional models has been explored in recent studies (*e.g.*, (129, 130, 131, 132, 133, 134, 135)).

Future work should clarify the relationship between observed mixed-mode oscillations and the parameters α, β, a, and λ from a biological and measurable perspective, exploring the complexity of the gamma Mittag-Leffler probability density function kernels. Additionally, utilizing integral formulations of the model may help formalize stability studies.

6 GENERAL DISCUSSION AND PERSPECTIVES

The unified perspective introduced in Chapter 3 serves as a guiding principle. By viewing different models as arising from specific choices of memory kernels, we can better understand the assumptions underlying each approach, as well as the limitations associated with their use in biological applications.

Having developed and applied the kernel-based framework across different modeling contexts, this chapter discusses central aspects developed throughout the thesis. Particular emphasis is given to good practices and common pitfalls in fractional modeling, kernel-based approaches, and biological applications.

6.1 GOOD PRACTICES AND PITFALLS IN FRACTIONALIZATION

Fractional calculus has attracted significant research interest due to its ability to explicitly capture memory effects by incorporating dependence on past states of systems or processes. However, a mathematically valid fractional equation is not necessarily physically meaningful. The use of fractional derivatives requires careful attention to dimensional consistency, parameter interpretation, and the validity of classical calculus properties.

In our works (33, 143), we analyze compartmental models in which the integer derivative on the left-hand side of ODEs is replaced by fractional derivatives. The Caputo derivative is a common choice, as it preserves the property that the derivative of a constant is zero and allows the use of conventional initial conditions. Although such models can yield useful estimates and interesting mathematical results, a common pitfall is that changing the derivative order does not automatically ensure consistency in parameter definitions, physical units, or conservation laws (see also (65)).

Another class of pitfalls arises from the improper transfer of classical calculus results to the fractional setting. In (144), we discuss properties that are not inherited when integer-order derivatives are replaced by fractional ones, by comparing incorrect and correct formulations of the fractional Barbalat's Lemma. The Mean Value Theorem corollary for monotonicity is another frequent misconception addressed in this context (see also (64)).

Given the distinct nature of fractional calculus as a modeling approach, it raises questions first addressed in (143): *What exactly is fractional modeling?* and *Which phenomena can be effectively described through fractionalization?* Replacing the derivative order is not equivalent to deriving models from distributed waiting-time assumptions. To clarify this distinction, we propose in Chapters 2 and 3 two related forms of fractional modeling in time: fractionalization based on non-exponential dwell-time distributions and fractionalization through delay kernels. Both approaches can be naturally expressed in terms of integral kernels.

From a stochastic viewpoint, the fractional Poisson process has been studied by (44, 45), while distributed Mittag–Leffler waiting times have been discussed since (43, 75). These works show that fractional master equations arise as special cases within the CTRW framework with non-exponential waiting-time distributions. However, translating this theory into biological compartmental models remains nontrivial. An important attempt was made in (56), resulting in fractional compartmental systems without mass imbalance and allowing separate integration of rates of different orders. Nevertheless, issues related to changes in units and physical interpretation remained unclear. These issues were later addressed in (57, 58) through a systematic CTRW-based derivation of fractional compartmental models. Related constructions are further developed in our works (33, 72, 145, 67) and in Chapter 2 and Appendix B of this thesis.

Regarding the kernel-delay approach developed in Chapter 3, gamma-distributed delays have previously been used in practical contexts such as pharmacokinetics (2). However, their explicit connection to fractional calculus had not been previously established. Gamma distributions have also been used in neuronal mean-field interactions (87), delayed driver reaction models (88), and neuronal dynamics (89), while Mittag–Leffler-distributed delays have been employed in tumor drug-response models (90).

Despite these significant contributions, the existing approaches are often presented in a fragmented way. A systematic discussion of methodological principles, good practices, and common pitfalls remains limited. This thesis aims to contribute by organizing and clarifying these aspects within a coherent framework for fractional modeling.

6.2 INTEGRAL KERNELS

The mathematical theory of integral kernels and Mittag–Leffler functions, as developed in previous studies (43, 75, 146, 45, 37), is well established in the literature. Mittag–Leffler distributions have also been examined in applied modeling contexts (147, 148), showing that deviations from exponential behavior in physical phenomena can be effectively described by these functions. However, translating this theoretical framework into practical applications remains a challenge.

In Chapters 2, 3 and 4, we develop a kernel-based perspective that provides a unified framework connecting classical ODEs, chain-trick representations with Erlang or hypoexponential kernels, CTMC-based models with phase-type kernels, and fractional formulations with heavy-tailed or multimodal kernels. Within this framework, the distinction between these approaches lies primarily in the choice of kernel, while preserving physical consistency, particularly in terms of time units. Future research may further strengthen this connection by employing phase-type distribution approximations of fractional kernels, as discussed in Section 7.2.

6.3 APPLICATIONS

We investigated mathematical formulations in various application domains, including population dynamics, epidemiology, and electrophysiology. Simulations were conducted to validate the formulations and gain insights.

Chapter 2 and (55) develop a SIRS model with Mittag–Leffler waiting times, using a method based on Mittag–Leffler kernels to generalize exponential distributions across a broad class of ODE models. We also derived novel analytical results on positivity, monotonicity in the limiting regime, and equilibrium points in a fractional SIR model (26) and Appendix B.

In several developments presented in Chapters 3, 4, and 6, building on previous publications (79, 118, 100), we employed probability density functions associated with the generalized gamma Mittag–Leffler distribution as delay kernels. In addition to analyzing the role of kernel parameters in relation to singularity, monotonicity, and related properties, we demonstrated in (79) and Chapter 3 the ability to reproduce real COVID-19 data using a generalized logistic model and extended the distributed-delay approach to model drug effects in pharmacokinetics.

In electrophysiology, we proposed in (100) and Chapter 4 a simple mathematical model describing a neuronal AP using a single delay differential equation based on sodium and potassium conductances. This framework was further extended to incorporate alternative representations of macroscopic channel memory, such as linear-chain (Erlang) ODE approximations, CTMC-based models, and fractional formulations.

Using the fractional approach, we observed in (118) and Chapter 5 complex phenomena, including mixed-mode oscillations in two-variable adapted FHN, MS, and Karma cardiac models, which can be interpreted as early afterdepolarizations. The possibility of self-intersections in fractional planar trajectories emerged as a central finding, highlighting that such behavior would require at least three variables in autonomous ODE systems.

7 LIMITATIONS AND FUTURE WORK

We outline some limitations that motivate future developments. In Chapter 2, the stability of the equilibria discussed in Section **2.1.2** has not yet been formally established. This issue may be addressed using the theory of Volterra integral equations, as partially explored in Appendix B.

Another limitation concerns the extension from scalar to vector formulations. In Section 2.2, the construction is illustrated for a system, whereas the theoretical development is based on scalar equations, generalizing the exponential waiting time in the equation for I and introducing smooth immunity behavior in the equation for R. We conjecture that Theorem 2.1 extends to vector-valued systems in Eq. (2.3) through matrix-valued Mittag–Leffler functions (78). However, when multiple rate matrices are involved, as in Theorem 2.2, commutativity conditions arise and require careful treatment. While special cases (*e.g.*, diagonal matrices) are tractable, a rigorous analysis in appropriate matrix spaces remains an open problem.

In Chapters 3 and 5, the mechanistic interpretation of the parameters of the gamma Mittag–Leffler memory kernel was application-specific. A systematic biological interpretation of the parameters α, β, a, and λ, including issues of measurability and identifiability, remains an open problem. Further investigation of the integral formulation may also provide a more robust framework for stability analysis, particularly in regimes exhibiting mixed-mode oscillations. The action potential duration (APD) and other critical electrophysiological biomarkers should be incorporated into future research.

Extensions of the theory to partial differential equations, calcium dynamics models, alternans and pacing studies are among the directions for future work. In the next sections, we present preliminary results on two research directions. The first concerns the generation of EADs in the Bueno–Orovio Minimal Model (149) for human ventricular APs, using geometrically inspired adaptations. The second addresses phase-type approximations of the distributions used in this thesis as memory kernels, particularly the gamma Mittag–Leffler distribution.

7.1 EADs IN THE MINIMAL MODEL

In recent studies, such as (150) and (151), the Bueno-Orovio Minimal Model (149) was optimized to reproduce the electrophysiological properties of complex cardiac computational models, such as the ToR-ORd with 44 differential equations (152), that are often very computationally demanding. However, this phenomenological model is not capable of reproducing EADs that arise in drug block and diseases simulated by ORd-type models.

The Minimal Model has four variables and, in principle, does not require nonlocal operators to reproduce oscillations. However, the rigid nullcline $w = 0$ for $u > \theta_w$ constrains the phase-space geometry, preventing the configuration necessary for oscillatory behavior. In Appendix E, we justify the linear adaptations introduced in the MS and Karma models to modify their phase portraits and enable the reproduction of EADs in Chapter 5. These geometric insights motivate the following modification of the third equation of the Minimal Model:

$$\frac{du}{dt} = -(J_{fi} + J_{so} + J_{si}) \tag{7.1}$$

$$\frac{dv}{dt} = (1 - H(u - \theta_v))(\frac{v_\infty - v}{\tau_v^-}) - H(u - \theta_v)\frac{v}{\tau_v^+} \tag{7.2}$$

$$\frac{dw}{dt} = (1 - H(u - \theta_w))(\frac{w_\infty - w}{\tau_w^-}) - H(u - \theta_w)\frac{w - \boldsymbol{f(u)}}{\tau_w^+} \tag{7.3}$$

$$\frac{ds}{dt} = \left(\frac{(1 + \tanh(k_s(u - u_s)))}{2} - s\right)/\tau_s. \tag{7.4}$$

The voltage variables and currents' formulations remain the same as in (149). The new function $f(u)$ introduces flexibility into the nullcline geometry. Particularly, if this function has a simple linear form, $f(u) = \alpha - \beta u$, with α and β positive parameters, EADs can arise, as shown in Figure 7.1. In Figure 7.2, a numerical sensitivity analysis for α and β is presented, describing regions with 0, 1, 2, or 3 peaks after fast depolarization. If the AP does not undergo repolarization until time 1400 ms, we consider it to have failed. APs with 0 and 1 peaks do not exhibit EADs, but correspond to action potentials with and without a pronounced phase 2, respectively.

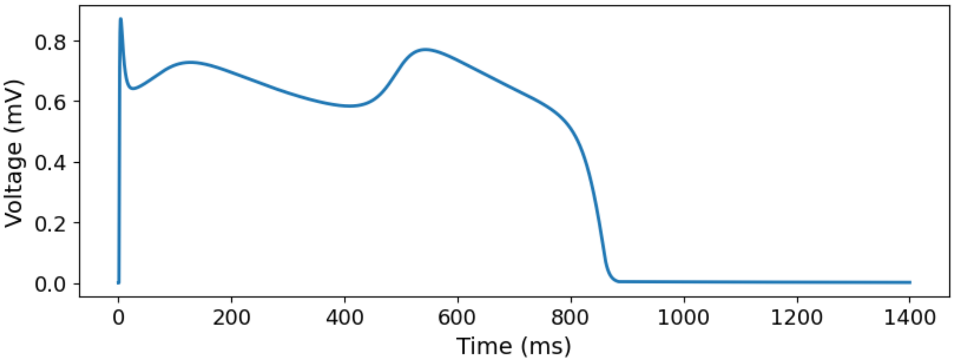

Figure 7.1 – Solution of model Eq. (7.1)-(7.4) with parameters of Table 7.1.

The possibility of exploring the oscillatory regime in the plateau phase of the Minimal Model and other simple cardiac models can help overcome their limitations in reproducing complex electrophysiological properties. By simplifying the model to disregard the variable v, which is more related to fast depolarization, and by removing the Heaviside functions by considering $u > \max\{\theta_v^-, \theta_w, \theta_o, \theta_v\}$, a more focused analysis on the oscillatory regime can be conducted with only 11 parameters. This simplification may serve as a starting point for a more in-depth investigation, including stability analysis and parameter sensitivity. Additionally, fitting EADs of more complex models presents an interesting challenge for future research.

Parameter	**Value**	**Parameter**	**Value**	**Parameter**	**Value**
u_o	0	u_u	1.04	θ_v	0.422
θ_w	0.0845	θ_v^-	0.0033	θ_o	0.0039
τ_{v1}	80	τ_{v2}	1533.3333	τ_{v+}	1.9341
τ_{w1}	43.68	τ_{w2}	18.876	k_{w-}	100
u_{w-}	0.078	τ_{w+}	260	τ_{fi}	0.2482
τ_{o1}	533.3333	τ_{o2}	8	τ_{so1}	61.5754
τ_{so2}	2.0425	k_{so}	3.1474	u_{so}	0.585
τ_{s1}	3.6456	τ_{s2}	15.8667	k_s	4.7683
u_s	0.6557	τ_{si}	11.2821	$\tau_{w\infty}$	0.3033
w^*	1.4	α	5.52	β	6.9

Table 7.1 – Parameters to simulate Figure 7.1. The initial condition is $(u, v, w, s) = (0, 1, 1, 0)$ and a stimulus of amplitude 0.6 is applied between 1 and 2 ms.

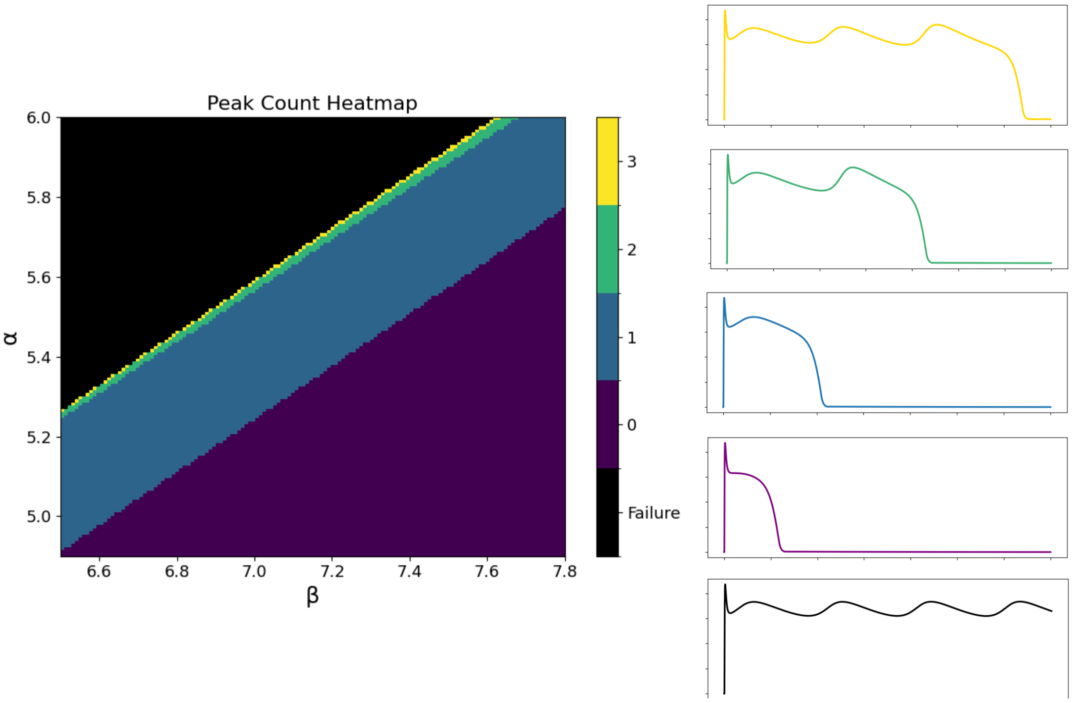

Figure 7.2 – A numerical analysis was conducted to study the emergence of EADs in the model described by Eq. (7.1)-(7.4) by varying α and β while keeping the other parameters fixed as shown in Table 7.1. A representative AP of each region is displayed on the right.

7.2 PHASE-TYPE VS GAMMA MITTAG-LEFFLER DISTRIBUTIONS

There is a significant amount of literature on approximating general distributions with phase-type distributions, which are more analytically tractable due to their Markovian properties. Based on (153), we present the following definition:

Definition 7.1 (Phase-type distribution)**.** *A phase-type distribution F is the distribution of the absorption time in a CTMC with an absorbing last state. It is defined by a generator matrix, T^F, and an initial probability vector, p^F.*

The diagram below illustrates a CTMC with four states (three transient and one absorbing state):

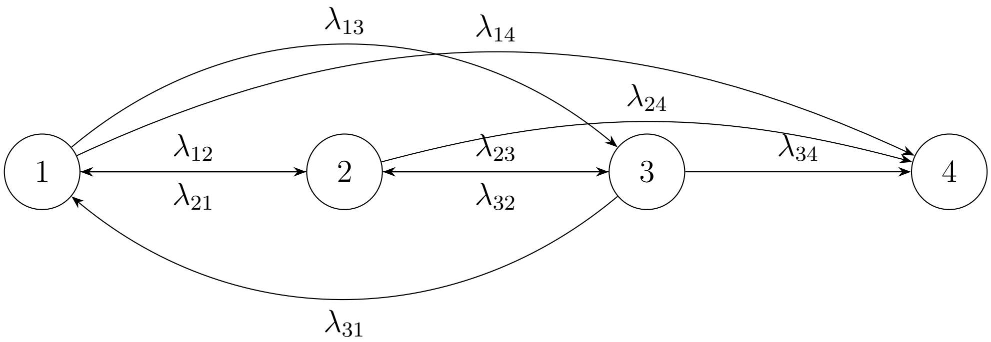

In this case, the phase-type distribution is described by the initial probability vector $p^F = (p_1, p_2, p_3)$ (this means that we start in the i-th state with probability p_i and $p_1 + p_2 + p_3 = 1$) and the generator matrix

$$T^F = \begin{bmatrix} -(\lambda_{12}+\lambda_{13}+\lambda_{14}) & \lambda_{12} & \lambda_{13} \\ \lambda_{21} & -(\lambda_{21}+\lambda_{23}+\lambda_{24}) & \lambda_{23} \\ \lambda_{31} & \lambda_{32} & -(\lambda_{31}+\lambda_{32}+\lambda_{34}) \end{bmatrix}.$$

The set of phase-type distributions is dense in the set of all positive-valued distributions, making it suitable for approximating any positive-valued distribution. There is a extensive literature on how to determine the parameters of phase-type distributions, depending on the available information about the target distribution. The goal is to find a phase-type distribution that approximates either the underlying distribution or a sequence of its moments (154).

In this context, it is interesting to explore the relationship between memory kernels and chains of ODEs using approximations based on phase-type distributions and the generalized linear chain-trick for phase-type distributions (155). A central example is the emergence of EADs in simple cardiac models, which are studied in Chapter 5.

Consider approximating the gamma kernel with parameters $\beta = 0.99$, and $a = 0.012$, as shown in the simulation in Figure D.1. The objective is to derive a phase-type distribution approximation that allows a FHN-type model with three ODEs to generate EADs. The first three moments of the distribution are $E_1 = 82.5$, $E_2 = 13,681.25$, and $E_3 = 3,408,911.458$. By utilizing BuTools (156), a set of useful tools for Markovian performance evaluation, we approximate this gamma distribution by fitting three moments, resulting in a phase-type distribution with the PDF given by:

$$f(t) = a_1 e^{-b_1 t} + a_2 e^{-b_2 t}, \tag{7.5}$$

where

$$a_1 = 0.011895, \quad b_1 = 0.01203019, \quad a_2 = 0.0004086, \quad b_2 = 0.03645471. \tag{7.6}$$

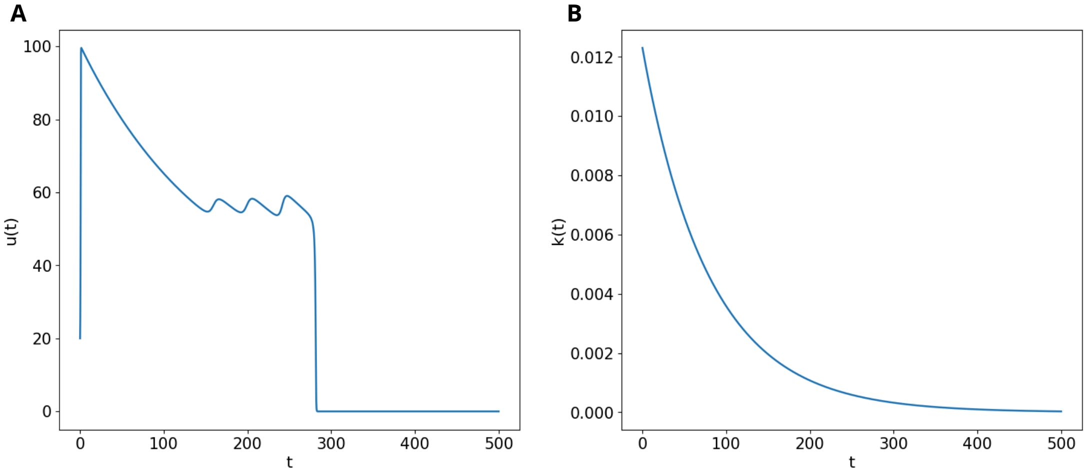

Figure 7.3 – **(A)** Solution of the model (7.7)-(7.9) with a phase-type kernel (7.5), for parameters $a_1 = 0.011895, b_2 = 0.01203019, a_2 = 0.0004086$, and $b_2 = 0.03645471$. **(B)** Corresponding kernel.

By incorporating this kernel into Eq. (5.26), we derive a three-dimensional FHN-type model as follows:

$$\frac{du}{dt} = -Gu\left(1 - \frac{u}{u_{th}}\right)\left(1 - \frac{u}{u_p}\right) - \eta_1 u(w_1 + w_2), \tag{7.7}$$

$$\frac{dw_1}{dt} = \xi a_1 u - b_1 w_1, \tag{7.8}$$

$$\frac{dw_2}{dt} = \xi a_2 u - b_2 w_2. \tag{7.9}$$

This modified model successfully simulates an EAD, as demonstrated in Figure 7.3.

It is possible to prove that any phase-type distribution corresponding to a CTMC of four stages has the form of Eq. (7.5). As a sum of two exponential functions, this PDF cannot be multimodal. Therefore, representing a multimodal gamma Mittag-Leffler kernel, as illustrated in Figure 3.3, requires at least five states, corresponding to four ODEs. However, we have not yet succeeded in approximating these kernels with a phase distribution corresponding to a CTMC of five stages.

Many-state approaches, as pointed out in (2), capture a wide range of data but also present structural limitations. The need to specify the number of compartments a priori and the difficulty of representing complex features with a manageable number of parameters are among them. In contrast, advances in the analytical and numerical correspondence between different classes of memory kernels offer a way to better understand how memory shape and parameter choices influence the observed phenomena, and to clarify under which circumstances distinct modeling strategies are more appropriate. A central aspect of this connection should be the detailed study of the moments of the gamma Mittag–Leffler distribution, for which (85) provides a useful starting point.

8 CONCLUDING REMARKS

Classical biological modeling based on ordinary differential equations typically assumes Markovian or chains of Markovian dwell times and delay distributions, which shape both the interpretation and the dynamics of the phenomenon. In contrast, delayed or fractional formulations often introduce memory as an assumption, approximation, or corrective mechanism rather than as an explicitly analyzed structural component. Moreover, in some fractional approaches, essential biological features, such as dimensional consistency and rate interpretation, may be obscured. Although the Volterra formulation of memory is well established, a unified and biologically consistent framework connecting these paradigms through an explicit interpretation of memory structure has been lacking.

In this thesis, memory is not treated as a theoretical adjustment but is formulated through a kernel that encodes the dynamical organization of the system. Following established results such as (16), memory is expressed as a Volterra convolution between the state variable and a nonnegative kernel κ, normalized to represent a waiting-time probability distribution. This formulation makes explicit that present dynamics depend on a weighted history of past states, with the kernel determining the temporal architecture of memory. Ordinary, delayed, and fractional models then arise as particular structural instances within a continuous kernel spectrum.

In this context, the generalized gamma Mittag–Leffler distribution is introduced as a flexible class of kernels capable of spanning exponential, and heavy-tailed fractional behaviors while preserving statistical interpretability through its moments. Dominant kinetic time scales appear explicitly as kernel parameters, enabling compact analytical and numerical representations without introducing multiple auxiliary ODE states. Thus, complex distributed memory effects can be captured within a finite and structurally coherent formulation, as sumarized in Figure 8.1.

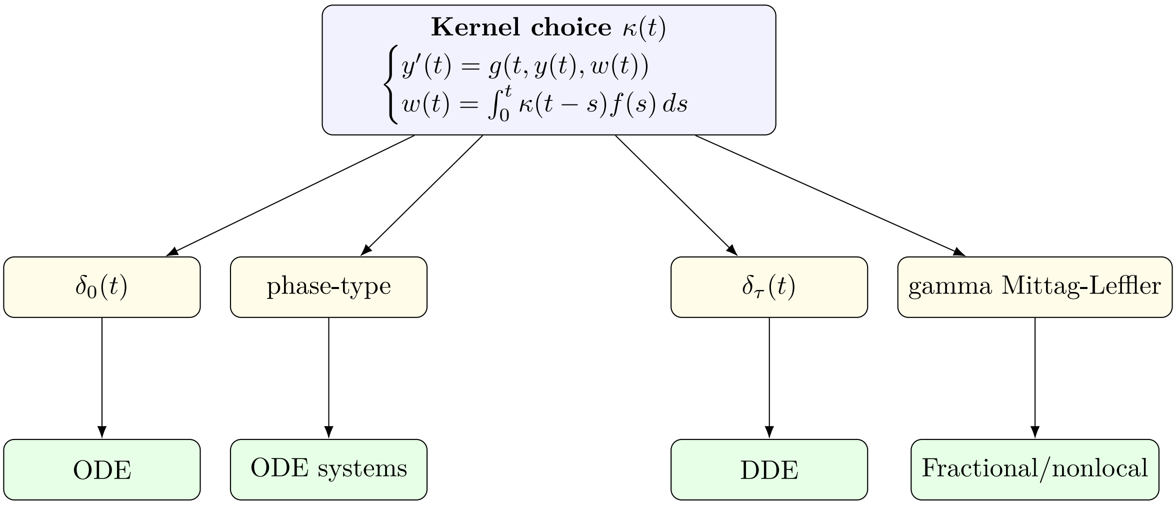

Figure 8.1 – Model classes arising from different choices of memory kernel $\kappa(t)$.

Dynamical consequences of this viewpoint are illustrated by the emergence of complex behaviors in otherwise simple systems. Within the memory-kernel framework, phenomena such as multi-wave epidemic dynamics and oscillatory features in cardiac action potentials, including early afterdepolarizations, arise naturally from the internal temporal organization of the model. Memory modifies phase-space geometry and reorganizes trajectories rather than acting as external forcing. This restructuring may manifest in nontrivial geometric features, such as self-intersections of trajectories in two-dimensional settings.

In electrophysiology, one of the central applications of this thesis, Hodgkin–Huxley or more general Markov ODE formulations remain appropriate when the objective is to resolve explicit state probabilities or microscopic gating mechanisms. By contrast, the delay-kernel perspective emphasizes the macroscopic organization of excitability, refractoriness, stimulus–frequency adaptation, and propagation, while making dominant kinetic time scales explicit as memory parameters. The delay-based ionic representation can also be extended to spatially distributed neuronal models, suggesting further avenues for structural generalization.

Modeling biological systems requires selecting a temporal structure. In most applications, this choice is implicitly Markovian. Although complex memory phenomena can be reproduced by enlarging Markovian state spaces, this strategy involves structural trade-offs, including the ad hoc selection of the number of compartments and limitations in capturing intricate temporal features with a manageable parameter set. This thesis shows that the distinction between Markovian and non-Markovian modeling can be understood within a continuous spectrum of memory kernels. The kernel viewpoint therefore provides a unifying bridge between classical ODE gating (exponential kernels), chain-trick representations (Erlang or hypoexponential kernels), CTMC-based formulations (phase-type kernels), and fractional models characterized by heavy-tailed or multimodal distributions. In this sense, memory is not an auxiliary modification of classical dynamics, but a structural design choice that shapes the modeling of biological systems.

BIBLIOGRAPHY

1 JAIN, L. et al. Population pharmacokinetic analysis of sorafenib in patients with solid tumours. *British journal of clinical pharmacology*, Wiley Online Library, v. 72, n. 2, p. 294–305, 2011.

2 HU, S.; DUNLAVEY, M.; GUZY, S.; TEUSCHER, N. A distributed delay approach for modeling delayed outcomes in pharmacokinetics and pharmacodynamics studies. *Journal of Pharmacokinetics and Pharmacodynamics*, Springer, v. 45, n. 2, p. 285–308, 2018.

3 BARRIO, R.; JOVER-GALTIER, J. A.; MARTÍNEZ, M.; PÉREZ, L.; SERRANO, S. Mathematical birth of early afterdepolarizations in a cardiomyocyte model. *Mathematical Biosciences*, Elsevier, v. 366, p. 109088, 2023.

4 GORENFLO, R.; KILBAS, A. A.; MAINARDI, F.; ROGOSIN, S. V. *Mittag-Leffler functions, related topics and applications.* Berlin: Springer, 2014.

5 BARROS, L. C. d.; LOPES, M. M.; PEDRO, F. S.; ESMI, E.; SANTOS, J. P. C. d.; SÁNCHEZ, D. E. The memory effect on fractional calculus: an application in the spread of COVID-19. *Computational and Applied Mathematics*, Springer, v. 40, n. 3, p. 1–21, 2021.

6 NOORI, H. R. Examples of hysteresis phenomena in biology. In: MAYERGOYZ, I. D.; BERTOTTI, G. (Ed.). *Hysteresis Phenomena in Biology.* Berlin, Heidelberg: Springer, 2013. p. 35–45.

7 BEISNER, B.; HAYDON, D.; CUDDINGTON, K. *Hysteresis. Ecological Models/Encyclopedia of Ecology. V. 3./eds. SE Jorgensen, D. Brian.* Oxford: Elsevier, 2008.

8 FAASSEN, E. J.; VERAART, A. J.; NES, E. H. V.; DAKOS, V.; LÜRLING, M.; SCHEFFER, M. Hysteresis in an experimental phytoplankton population. *Oikos*, Wiley Online Library, v. 124, n. 12, p. 1617–1623, 2015.

9 PIMENOV, A.; KELLY, T.; KOROBEINIKOV, A.; O'CALLAGHAN, M.; POKROVSKII, A. *Systems with hysteresis in mathematical biology via a canonical example. Clustering Algorithms and Mathematical Modeling.* New York: Nova Science Publishers, Inc, 2010.

10 KAHN, O.; LÉTARD, J.-F.; MATHONIÈRE, C. Hysteresis and memory effect in supramolecular chemistry. *Supramolecular Engineering of Synthetic Metallic Materials: Conductors and Magnets*, Kluwer academic publ., p. 127–144, 1998.

11 KERMACK, W. O.; MCKENDRICK, A. G. Contributions to the mathematical theory of epidemics–I. 1927. *Bulletin of Mathematical Biology*, v. 53, n. 1-2, p. 33–55, 1991.

12 LOTKA, A. J. A contribution to quantitative epidemiology. *Journal of the Washington Academy of Sciences*, JSTOR, v. 9, n. 3, p. 73–77, 1919.

13 TOMOVSKI, I.; BASNARKOV, L.; ABAZI, A. Discrete-time non-markovian SEIS model on complex networks. *IEEE Transactions on Network Science and Engineering*, IEEE, v. 9, n. 2, p. 552–563, 2021.

14 BASNARKOV, L.; TOMOVSKI, I.; SANDEV, T.; KOCAREV, L. Non-markovian SIR epidemic spreading model of COVID-19. *Chaos, Solitons & Fractals*, Elsevier, v. 160, p. 112286, 2022.

15 SAXTON, M. J. Single-particle tracking of DNA-binding biomolecules in cells: Power-law distributions of dwell times. *Biophysical Journal*, Elsevier, v. 120, n. 3, p. 359a–360a, 2021.

16 CUSHING, J. M. *Integrodifferential equations and delay models in population dynamics*. Berlin–Heidelberg–New York: Springer Science & Business Media, 1997.

17 CASWELL, H. A simulation study of a time lag population model. *Journal of Theoretical Biology*, Elsevier, v. 34, n. 3, p. 419–439, 1972.

18 MAY, R.; CONWAY, G.; HASSELL, M.; SOUTHWOOD, T. Time delays, density-dependence and single-species oscillations. *The Journal of Animal Ecology*, JSTOR, v. 43, n. 3, p. 747–770, 1974.

19 HEIDEN, U. an der. Delays in physiological systems. *Journal of mathematical biology*, Springer, v. 8, n. 4, p. 345–364, 1979.

20 BOCHAROV, G. A.; RIHAN, F. A. Numerical modelling in biosciences using delay differential equations. *Journal of Computational and Applied Mathematics*, Elsevier, v. 125, n. 1-2, p. 183–199, 2000.

21 VILLALBA-GALEA, C. A.; CHIEM, A. T. Hysteretic behavior in voltage-gated channels. *Frontiers in Pharmacology*, Frontiers Media SA, v. 11, p. 579596, 2020.

22 HODGKIN, A. L.; HUXLEY, A. F. A quantitative description of membrane current and its application to conduction and excitation in nerve. *The Journal of physiology*, Wiley, v. 117, n. 4, p. 500, 1952.

23 ROGERS, J. M.; MCCULLOCH, A. D. A collocation-Galerkin finite element model of cardiac action potential propagation. *IEEE Transactions on Biomedical Engineering*, IEEE, v. 41, n. 8, p. 743–757, 1994.

24 MITCHELL, C. C.; SCHAEFFER, D. G. A two-current model for the dynamics of cardiac membrane. *Bulletin of mathematical biology*, Springer, v. 65, n. 5, p. 767–793, 2003.

25 KARMA, A. Spiral breakup in model equations of action potential propagation in cardiac tissue. *Physical review letters*, APS, v. 71, n. 7, p. 1103, 1993.

26 MONTEIRO, N. Z.; MAZORCHE, S. R.; SANTOS, R. W. dos. Positivity and equilibrium in a fractional SIR model with Mittag-Leffler memory. *Trends in Computational and Applied Mathematics*, SciELO Brasil, v. 25, p. e01789, 2024.

27 RAMEH, R. B.; CHERRY, E. M.; SANTOS, R. W. dos. Single-variable delay-differential equation approximations of the Fitzhugh-Nagumo and Hodgkin-Huxley models. *Communications in Nonlinear Science and Numerical Simulation*, Elsevier, v. 82, p. 105066, 2020.

28 AKIMARU, H.; KAWASHIMA, K. Non-Markovian models. In: *Teletraffic: Theory and Applications*. London: Springer, 1993. p. 39–70.

29 DU, M.; WANG, Z.; HU, H. Measuring memory with the order of fractional derivative. *Scientific reports*, Nature Publishing Group UK London, v. 3, n. 1, p. 3431, 2013.

30 ANGSTMANN, C.; HENRY, B.; MCGANN, A. A fractional order recovery SIR model from a stochastic process. *Bulletin of mathematical biology*, Springer, v. 78, n. 3, p. 468–499, 2016.

31 ANGSTMANN, C.; HENRY, B.; MCGANN, A. A fractional order recovery SIR model from a stochastic process. *Bulletin of Mathematical Biology*, Springer, v. 78, n. 3, p. 468–499, 2016.

32 ANGSTMANN, C. N.; HENRY, B. I.; MCGANN, A. V. A fractional-order infectivity and recovery SIR model. *Fractal and Fractional*, MDPI, v. 1, n. 1, p. 11, 2017.

33 MONTEIRO, N. Z.; MAZORCHE, S. R. Fractional derivatives applied to epidemiology. *Trends in Computational and Applied Mathematics*, SciELO Brasil, v. 22, n. 2, p. 157–177, 2021.

34 JAËCK, F.; MAZLIAK, L.; COLOMBO, E. S. D.; TAZZIOLI, R. *Gösta Mittag-Leffler and Vito Volterra. 40 Years of Correspondence.* Cham: Springer, 2019.

35 WAZWAZ, A.-M. *A First Course In Integral Equations.* Chicago: World Scientific, 2015.

36 SAMKO, S. G.; KILBAS, A. A.; MARICHEV, O. I. *Fractional integrals and derivatives.* Amsterdam: Gordon and Breach Science Publishers, 1993.

37 KOCHUBEI, A. N. General fractional calculus, evolution equations, and renewal processes. *Integral Equations and Operator Theory*, Springer, v. 71, n. 4, p. 583–600, 2011.

38 OLIVEIRA, D.; OLIVEIRA, E. C. D. Hilfer–Katugampola fractional derivatives. *Computational and Applied Mathematics*, Springer, v. 37, n. 3, p. 3672–3690, 2018.

39 OLIVEIRA, D. S.; OLIVEIRA, E. C. de. On the generalized (k, ρ)-fractional derivative. *Progress in Fractional Differentiation and Applications*, v. 4, n. 2, p. 133–145, 2018.

40 SOUSA, J. V. d. C.; OLIVEIRA, E. C. D. On the ψ-hilfer fractional derivative. *Communications in Nonlinear Science and Numerical Simulation*, Elsevier, v. 60, p. 72–91, 2018.

41 LUCHKO, Y. Operational calculus for the general fractional derivative and its applications. *Fractional Calculus and Applied Analysis*, De Gruyter, v. 24, n. 2, p. 338–375, 2021.

42 AL-REFAI, M.; FERNANDEZ, A. Generalising the fractional calculus with sonine kernels via conjugations. *Journal of Computational and Applied Mathematics*, Elsevier, v. 427, p. 115159, 2023.

43 HILFER, R.; ANTON, L. Fractional master equations and fractal time random walks. *Physical Review E*, APS, v. 51, n. 2, p. R848, 1995.

44 REPIN, O.; SAICHEV, A. Fractional Poisson law. *Radiophysics and Quantum Electronics*, Springer, v. 43, n. 9, p. 738–741, 2000.

45 MAINARDI, F.; GORENFLO, R.; SCALAS, E. A fractional generalization of the Poisson processes. *Vietnam Journal of Mathematics*, v. 32, 2004.

46 MICHELITSCH, T. M.; RIASCOS, A. P. Generalized fractional Poisson process and related stochastic dynamics. *Fractional Calculus and Applied Analysis*, Springer, v. 23, n. 3, p. 656–693, 2020.

47 SHI, J.; LIU, F.; KUDREYKO, A.; WU, Z.; SONG, W. Fractional poisson process for estimation of capacity degradation in Li-ion batteries by walk sequences. *Fractal and Fractional*, MDPI, v. 9, n. 9, p. 558, 2025.

48 OLDHAM, K.; SPANIER, J. *The Fractional Calculus theory and applications of differentiation and integration to arbitrary order*. New York: Elsevier, 1974.

49 MILLER, K. S.; ROSS, B. *An introduction to the fractional calculus and fractional differential equations*. New York: Wiley, 1993.

50 PODLUBNY, I. *Fractional differential equations*. San Diego: Elsevier, 1998.

51 KILBAS, A. A.; SRIVASTAVA, H. M.; TRUJILLO, J. J. *Theory and applications of fractional differential equations*. Amsterdam: Elsevier, 2006.

52 DIETHELM, K. *The analysis of fractional differential equations: An application-oriented exposition using differential operators of Caputo type*. Heidelberg: Springer Science & Business Media, 2004.

53 LI, C.; DENG, W. Remarks on fractional derivatives. *Applied mathematics and computation*, Elsevier, v. 187, n. 2, p. 777–784, 2007.

54 PILLAI, R. N. On Mittag-Leffler functions and related distributions. *Annals of the Institute of statistical Mathematics*, Springer, v. 42, n. 1, p. 157–161, 1990.

55 MONTEIRO, N. Z.; SANTOS, R. W. dos; MAZORCHE, S. R. Constructive fractional models through Mittag-Leffler functions. *Computational and Applied Mathematics*, Springer, v. 43, n. 4, p. 177, 2024.

56 DOKOUMETZIDIS, A.; MAGIN, R.; MACHERAS, P. Fractional kinetics in multi-compartmental systems. *Journal of pharmacokinetics and pharmacodynamics*, Springer, v. 37, n. 5, p. 507–524, 2010.

57 ANGSTMANN, C. N.; ERICKSON, A. M.; HENRY, B. I.; MCGANN, A. V.; MURRAY, J. M.; NICHOLS, J. A. A general framework for fractional order compartment models. *SIAM Review*, SIAM, v. 63, n. 2, p. 375–392, 2021.

58 ANGSTMANN, C.; HENRY, B.; JACOBS, B.; MCGANN, A. A time-fractional generalised advection equation from a stochastic process. *Chaos, Solitons & Fractals*, Elsevier, v. 102, p. 175–183, 2017.

59 PINTO, C. M.; CARVALHO, A. R. The role of synaptic transmission in a HIV model with memory. *Applied Mathematics and Computation*, Elsevier, v. 292, p. 76–95, 2017.

60 BONYAH, E.; ATANGANA, A.; CHAND, M. Analysis of 3D IS-LM macroeconomic system model within the scope of fractional calculus. *Chaos, Solitons & Fractals: X*, Elsevier, v. 2, p. 100007, 2019.

61 CHEN, Y.; LIU, F.; YU, Q.; LI, T. Review of fractional epidemic models. *Applied Mathematical Modelling*, Elsevier, v. 97, p. 281–307, 2021.

62 NOROUZI, F.; N'GUÉRÉKATA, G. M. A study of ψ-Hilfer fractional differential system with application in financial crisis. *Chaos, Solitons & Fractals: X*, Elsevier, v. 6, p. 100056, 2021.

63 ZHOU, H.; YANG, S.; ZHANG, S. Modeling non-Darcian flow and solute transport in porous media with the Caputo–Fabrizio derivative. *Applied Mathematical Modelling*, Elsevier, v. 68, p. 603–615, 2019.

64 DIETHELM, K. Monotonicity of functions and sign changes of their Caputo derivatives. *Fractional Calculus and Applied Analysis*, De Gruyter, v. 19, n. 2, p. 561–566, 2016.

65 DOKOUMETZIDIS, A.; MAGIN, R.; MACHERAS, P. A commentary on fractionalization of multi-compartmental models. *Journal of pharmacokinetics and pharmacodynamics*, Springer, v. 37, n. 2, p. 203–207, 2010.

66 DOETSCH, G. *Introduction to the Theory and Application of the Laplace Transformation.* Berlin, Heidelberg: Springer Science & Business Media, 2012.

67 MONTEIRO, N. Z.; MAZORCHE, S. Some remarks on an arbitrary-order SIR model constructed with Mittag-Leffler distribution. *Matemática Contemporânea*, v. 51, p. 25–42, 2022.

68 LUNDBERG, K. H.; MILLER, H. R.; TRUMPER, D. L. Initial conditions, generalized functions, and the Laplace transform troubles at the origin. *IEEE Control Systems Magazine*, IEEE, v. 27, n. 1, p. 22–35, 2007.

69 ORTIGUEIRA, M. D. A new look at the initial condition problem. *Mathematics*, v. 10, n. 10, 2022.

70 LI, C.; ZHANG, F. A survey on the stability of fractional differential equations. *The European Physical Journal Special Topics*, Springer, v. 193, n. 1, p. 27–47, 2011.

71 GALLEGOS, J. A.; DUARTE-MERMOUD, M. A.; AGUILA-CAMACHO, N.; CASTRO-LINARES, R. On fractional extensions of Barbalat lemma. *Systems & Control Letters*, Elsevier, v. 84, p. 7–12, 2015.

72 MONTEIRO, N. Z.; MAZORCHE, S. R. Analysis and application of a fractional SIR model constructed with Mittag-Leffler distribution. In: *Proceedings of the XLII Ibero-Latin-American Congress on Computational Methods in Engineering (CILAMCE).* Online: ABMEC, 2021. CILAMCE 2021.

73 WU, Z.; CAI, Y.; WANG, Z.; WANG, W. Global stability of a fractional order SIS epidemic model. *Journal of Differential Equations*, Elsevier, v. 352, p. 221–248, 2023.

74 HETHCOTE, H. W.; LEWIS, M. A.; DRIESSCHE, P. V. D. An epidemiological model with a delay and a nonlinear incidence rate. *Journal of mathematical biology*, Springer, v. 27, n. 1, p. 49–64, 1989.

75 SCALAS, E.; GORENFLO, R.; MAINARDI, F. Fractional calculus and continuous-time finance. *Physica A: Statistical Mechanics and its Applications*, Elsevier, v. 284, n. 1-4, p. 376–384, 2000.

76 AMMI, M. R. S.; TAHIRI, M.; TORRES, D. F. Global stability of a caputo fractional sirs model with general incidence rate. *Mathematics in Computer Science*, Springer, v. 15, n. 1, p. 91–105, 2021.

77 DUTTA, P.; SANTRA, N.; SAMANTA, G.; SEN, M. De la. Nonlinear sirs fractional-order model: analysing the impact of public attitudes towards vaccination, government actions, and social behavior on disease spread. *Mathematics*, MDPI, v. 12, n. 14, p. 2232, 2024.

78 POPOLIZIO, M. On the matrix Mittag–Leffler function: theoretical properties and numerical computation. *Mathematics*, MDPI, v. 7, n. 12, p. 1140, 2019.

79 MONTEIRO, N. Z.; SANTOS, R. W. dos; MAZORCHE, S. R. Bridging the gap between models based on ordinary, delayed, and fractional differentials equations through integral kernels. *Proceedings of the National Academy of Sciences*, National Academy of Sciences, v. 121, n. 19, p. e2322424121, 2024.

80 VOLTERRA, V. Leçons sur la Théorie Mathématique de la Lutte pour la Vie. *Gauthier-Villars, Paris*, v. 193, n. 1, 1931.

81 BERETTA, E.; BREDA, D. Discrete or distributed delay? Effects on stability of population growth. *Math. Biosci. Eng*, v. 13, n. 1, p. 19–41, 2016.

82 ALLEN, E. J. Derivation and computation of discrete-delay and continuous-delay SDEs in mathematical biology. *Mathematical Biosciences & Engineering*, Mathematical Biosciences & Engineering, v. 11, n. 3, p. 403–425, 2013.

83 FARGUE, D. Réducibilité des systèmes héréditaires à des systèmes dynamiques. *CR Acad. Sci. Paris B*, v. 277, p. 471–473, 1973.

84 OLIVA, W. M.; ROCHA, C. Reducible Volterra and Levin–Nohel retarded equations with infinite delay. *Journal of Dynamics and Differential Equations*, Springer, v. 22, p. 509–532, 2010.

85 NAIR, S. S. An overview of generalized gamma Mittag–Leffler model and its applications. *Axioms*, MDPI, v. 4, n. 3, p. 365–384, 2015.

86 CHILDERS, D.; MILLER, S. *Probability and Random Processes*. Hoboken, NJ: Wiley-Interscience, 2004.

87 KASLIK, E.; KOKOVICS, E.-A.; RĂDULESCU, A. Stability and bifurcations in Wilson-Cowan systems with distributed delays, and an application to basal ganglia interactions. *Communications in Nonlinear Science and Numerical Simulation*, Elsevier, v. 104, p. 105984, 2022.

88 SIPAHI, R.; ATAY, F. M.; NICULESCU, S.-I. Stability of traffic flow behavior with distributed delays modeling the memory effects of the drivers. *SIAM Journal on Applied Mathematics*, SIAM, v. 68, n. 3, p. 738–759, 2008.

89 KARMESHU; GUPTA, V.; KADAMBARI, K. Neuronal model with distributed delay: analysis and simulation study for gamma distribution memory kernel. *Biological cybernetics*, Springer, v. 104, p. 369–383, 2011.

90 BYUN, J. H.; ROH, Y.; YOON, I.-S.; KIM, K. S.; JUNG, I. H. Fractional transit compartment model for describing drug delayed response to tumors using Mittag-Leffler distribution on age-structured PKPD model. *Plos one*, Public Library of Science, v. 17, n. 11, p. e0276654, 2022.

91 DEVAKUMAR, K. P. *COVID-19 dataset*. Aug 2020. Disponível em: <https://www.kaggle.com/datasets/imdevskp/corona-virus-report>.

92 HERSKOVITS, J.; MAZORCHE, S. R. A feasible directions algorithm for nonlinear complementarity problems and applications in mechanics. *Structural and Multidisciplinary Optimization*, Springer, v. 37, n. 5, p. 435–446, 2009.

93 REIS, R. F. et al. Characterization of the COVID-19 pandemic and the impact of uncertainties, mitigation strategies, and underreporting of cases in South Korea, Italy, and Brazil. *Chaos, Solitons & Fractals*, Elsevier, v. 136, p. 109888, 2020.

94 LUCHKO, Y. General fractional integrals and derivatives with the Sonine kernels. *Mathematics*, MDPI, v. 9, n. 6, p. 594, 2021.

95 LEONOV, A.; NAGORNOV, O.; TYUFLIN, S. Modeling of mechanisms of wave formation for COVID-19 epidemic. *Mathematics*, MDPI, v. 11, n. 1, p. 167, 2022.

96 CHAN, T.-L.; YUAN, H.-Y.; LO, W.-C. Modeling COVID-19 transmission dynamics with self-learning population behavioral change. *Frontiers in public health*, Frontiers, v. 9, p. 768852, 2021.

97 KHARAZMI, E. et al. Identifiability and predictability of integer-and fractional-order epidemiological models using physics-informed neural networks. *Nature Computational Science*, Nature Publishing Group, v. 1, n. 11, p. 744–753, 2021.

98 SILVA, P. J. et al. Optimized delay of the second COVID-19 vaccine dose reduces ICU admissions. *Proceedings of the National Academy of Sciences*, National Acad Sciences, v. 118, n. 35, p. e2104640118, 2021.

99 RAHMAN, B.; BLYUSS, K. B.; KYRYCHKO, Y. N. Dynamics of neural systems with discrete and distributed time delays. *SIAM Journal on Applied Dynamical Systems*, SIAM, v. 14, n. 4, p. 2069–2095, 2015.

100 MONTEIRO, N. Z.; SANTOS, R. W. Revisiting the modeling of cell electrophysiology using a delay-based equation. *Nonlinear Dynamics*, 2026. DOI 10.1007/s11071-026-12392-0.

101 BORON, W. F.; BOULPAEP, E. L. *Medical Physiology*. 3rd. ed. Philadelphia, PA: Elsevier Health Sciences, 2016. NCBI Bookshelf, National Center for Biotechnology Information, US National Library of Medicine. ISBN 9781455733286.

102 ARMSTRONG, C. M.; BEZANILLA, F. Currents related to movement of the gating particles of the sodium channels. *Nature*, v. 242, p. 459–461, 1973.

103 KEENER, J.; SNEYD, J. *Mathematical physiology: II: Systems physiology.* New York: Springer, 2009.

104 CAMARDO, J. S.; GREENSPAN, A. M.; HOROWITZ, L. N.; SPIELMAN, S. R.; JOSEPHSON, M. E. Strength-interval relation in the human ventricle: effect of procainamide. *The American journal of cardiology*, Elsevier, v. 45, n. 4, p. 856–860, 1980.

105 KANDEL, S. M.; ROTH, B. J. The strength-interval curve in cardiac tissue. *Computational and Mathematical Methods in Medicine*, Wiley Online Library, v. 2013, n. 1, p. 134163, 2013.

106 FITZHUGH, R. Impulses and physiological states in theoretical models of nerve membrane. *Biophysical Journal*, Elsevier, v. 1, n. 6, p. 445–466, 1961.

107 KORSBO, N.; JÖNSSON, H. It's about time: Analysing simplifying assumptions for modelling multi-step pathways in systems biology. *PLoS computational biology*, Public Library of Science San Francisco, CA USA, v. 16, n. 6, p. e1007982, 2020.

108 GLASS, D. S.; JIN, X.; RIEDEL-KRUSE, I. H. Nonlinear delay differential equations and their application to modeling biological network motifs. *Nature communications*, Nature Publishing Group UK London, v. 12, n. 1, p. 1788, 2021.

109 BEGUERISSE-DÍAZ, M.; DESIKAN, R.; BARAHONA, M. Linear models of activation cascades: analytical solutions and coarse-graining of delayed signal transduction. *Journal of The Royal Society Interface*, The Royal Society, v. 13, n. 121, p. 20160409, 2016.

110 SHIFERAW, Y.; WATANABE, M.; GARFINKEL, A.; WEISS, J.; KARMA, A. Model of intracellular calcium cycling in ventricular myocytes. *Biophysical journal*, Elsevier, v. 85, n. 6, p. 3666–3686, 2003.

111 HOU, S.; HEINEMANN, S. H.; HOSHI, T. Modulation of BKCa channel gating by endogenous signaling molecules. *Physiology*, American Physiological Society, v. 24, n. 1, p. 26–35, 2009.

112 BOLCH, G.; GREINER, S.; MEER, H. D.; TRIVEDI, K. S. *Queueing networks and Markov chains: modeling and performance evaluation with computer science applications.* New York: John Wiley & Sons, 2006.

113 ROSS, S. M. *Introduction to probability models.* Boston, MA: Academic press, 2014.

114 SALGADO-GARCÍA, R. Open Markov chains: Cumulant dynamics, fluctuations and correlations. *Entropy*, v. 23, n. 2, p. 256, 2021.

115 HILLE, B. *Ion Channels of Excitable Membranes.* 3rd. ed. Sunderland, MA: Sinauer Associates, 2001. ISBN 978-0-87893-321-1.

116 RUDY, Y.; SILVA, J. R. Computational biology in the study of cardiac ion channels and cell electrophysiology. *Quarterly reviews of biophysics*, Cambridge University Press, v. 39, n. 1, p. 57–116, 2006.

117 ASMUSSEN, S.; ALBRECHER, H. *Applied Probability and Queues*. 2nd. ed. New York: Springer, 2008. (Applications of Mathematics, v. 51).

118 MONTEIRO, N. Z.; SANTOS, R. W. dos; MAZORCHE, S. R. Ion channel memory drives cardiac early afterdepolarizations in fractional models. *Mathematics*, MDPI, v. 13, n. 10, p. 1585, 2025.

119 SHARMA, S. K. et al. Neuronal model with distributed delay: Emergence of unimodal and bimodal ISI distributions. *IEEE transactions on nanobioscience*, IEEE, v. 12, n. 1, p. 1–12, 2012.

120 TIWARI, K.; SENAPATI, D. Stochastic FitzHugh–Nagumo neuron model with gamma distributed delay kernel. *Chaos, Solitons & Fractals*, Elsevier, v. 196, p. 116378, 2025.

121 THOMPSON, R. *Using delay-differential equations for modeling calcium cycling in cardiac myocytes*. Tese (Doutorado) — Rochester Institute of Technology, 2013.

122 NAKABAYASHI, J.; SASAKI, A. Optimal phosphorylation step number of intracellular signal-transduction pathway. *Journal of theoretical biology*, Elsevier, v. 233, n. 3, p. 413–421, 2005.

123 CRANEFIELD, P. F. Action potentials, afterpotentials, and arrhythmias. *Circulation research*, Am Heart Assoc, v. 41, n. 4, p. 415–423, 1977.

124 CHARPENTIER, F.; DROUIN, E.; GAUTHIER, C.; MAREC, H. L. Early after/depolarizations and triggered activity: mechanisms and autonomic regulation. *Fundamental & clinical pharmacology*, Wiley Online Library, v. 7, n. 1, p. 39–49, 1993.

125 HUANG, X.; SONG, Z.; QU, Z. Determinants of early afterdepolarization properties in ventricular myocyte models. *PLoS computational biology*, Public Library of Science, v. 14, n. 11, p. e1006382, 2018.

126 STEIN, J.; GREENE, D.; FENTON, F.; SHIFERAW, Y. Mechanism of arrhythmogenesis driven by early after depolarizations in cardiac tissue. *bioRxiv*, 2024.

127 WANG, R.; QU, Z.; HUANG, X. Dissecting the roles of calcium cycling and its coupling with voltage in the genesis of early afterdepolarizations in cardiac myocyte models. *PLOS Computational Biology*, Public Library of Science, v. 20, n. 2, p. e1011930, 2024.

128 KÜGLER, P.; ERHARDT, A. H.; BULELZAI, M. Early afterdepolarizations in cardiac action potentials as mixed mode oscillations due to a folded node singularity. *PLoS One*, Public Library of Science, v. 13, n. 12, p. e0209498, 2018.

129 NGUEUTEU, G.; YAMAPI, R.; WOAFO, P. Quasi-static transient and mixed mode oscillations induced by fractional derivatives effect on the slow flow near folded singularity. *Nonlinear Dynamics*, Springer, v. 78, p. 2717–2729, 2014.

130 ABDELOUAHAB, M. S.; LOZI, R. Hopf-like bifurcation and mixed mode oscillation in a fractional-order FitzHugh-Nagumo model. In: AIP PUBLISHING. *AIP Conference Proceedings*. Melville, NY, 2019. v. 2183, n. 1.

131 TEKA, W. W.; UPADHYAY, R. K.; MONDAL, A. Spiking and bursting patterns of fractional-order Izhikevich model. *Communications in Nonlinear Science and Numerical Simulation*, Elsevier, v. 56, p. 161–176, 2018.

132 LOZI, R.; ABDELOUAHAB, M.-S.; CHEN, G. Mixed-mode oscillations based on complex Canard explosion in a fractional-order Fitzhugh-Nagumo model. *Applied Mathematics and Nonlinear Sciences*, v. 5, n. 2, p. 239–256, 2020.

133 MBOUNA, S. G. N. Fractional calculus-based generalization of the FitzHugh-Nagumo model: Biophysical justification, dynamical analysis and neurocomputational implications. In: WANG, Z. (Ed.). *Nonlinear Systems – Recent Developments and Advances*. London: IntechOpen, 2022.

134 GAO, X.-L.; ZHANG, H.-L.; WANG, Y.-L.; LI, Z.-Y. Research on pattern dynamics behavior of a fractional vegetation-water model in arid flat environment. *Nonlinear Dynamics*, 2024.

135 HE, K.; SONG, J.; ZHAO, N.; LIU, S. Hopf bifurcation and dynamical transitions in a fractional-order FitzHugh-Rinzel model with multiple time delays. *Communications in Nonlinear Science and Numerical Simulation*, Elsevier, v. 141, p. 108471, 2025.

136 FITZHUGH, R. Impulses and physiological states in theoretical models of nerve membrane. *Biophysical Journal*, Elsevier, v. 1, n. 6, p. 445–466, 1961.

137 FRANZONE, P. C.; PAVARINO, L. F. A parallel solver for reaction–diffusion systems in computational electrocardiology. *Mathematical models and methods in applied sciences*, World Scientific, v. 14, n. 06, p. 883–911, 2004.

138 DIETHELM, K.; KIRYAKOVA, V.; LUCHKO, Y.; MACHADO, J.; TARASOV, V. E. Trends, directions for further research, and some open problems of Fractional Calculus. *Nonlinear Dynamics*, Springer, p. 1–26, 2022.

139 FENTON, F. H.; CHERRY, E. M. Models of cardiac cell. *Scholarpedia*, v. 3, n. 8, p. 1868, 2008. Revision #91508.

140 AHMED, E.; EL-SAYED, A. M.; EL-SAKA, H. A. Equilibrium points, stability and numerical solutions of fractional-order predator–prey and rabies models. *Journal of Mathematical Analysis and Applications*, Elsevier, v. 325, n. 1, p. 542–553, 2007.

141 TAVAZOEI, M. S.; HAERI, M. A proof for non existence of periodic solutions in time invariant fractional order systems. *Automatica*, Elsevier, v. 45, n. 8, p. 1886–1890, 2009.

142 TRAN, D. X. et al. Bifurcation and chaos in a model of cardiac early afterdepolarizations. *Physical Review Letters*, APS, v. 102, n. 25, p. 258103, 2009.

143 MAZORCHE, S. R.; MONTEIRO, N. Z. Modelos epidemiológicos fracionários: o que se perde, o que se ganha, o que se transforma? *Proceeding Series of the Brazilian Society of Computational and Applied Mathematics*, v. 8, n. 1, 2021.

144 MONTEIRO, N. Z.; MAZORCHE, S. R. Limitations and applications in a fractional Barbalat's Lemma. *Fractional Calculus and Applied Analysis*, Springer, v. 26, n. 1, p. 253–275, 2022.

145 MONTEIRO, N. Z.; MAZORCHE, S. R. Numerical study of the parameters in an arbitrary order SIR model built with Mittag-Leffler distribution. *CQD Revista Eletrônica Paulista de Matemática*, v. 22, n. 2, 2022.

146 BERNARD, S.; BÉLAIR, J.; MACKEY, M. C. et al. Sufficient conditions for stability of linear differential equations with distributed delay. *Discrete and Continuous Dynamical Systems Series B*, AIMS PRESS, v. 1, n. 2, p. 233–256, 2001.

147 GEORGIOU, N.; KISS, I. Z.; SCALAS, E. Solvable non-Markovian dynamic network. *Physical Review E*, APS, v. 92, n. 4, p. 042801, 2015.

148 HAUBOLD, H. J.; MATHAI, A. M.; SAXENA, R. K. Mittag-Leffler functions and their applications. *Journal of applied mathematics*, Hindawi, v. 2011, 2011.

149 BUENO-OROVIO, A.; CHERRY, E. M.; FENTON, F. H. Minimal model for human ventricular action potentials in tissue. *Journal of theoretical biology*, Elsevier, v. 253, n. 3, p. 544–560, 2008.

150 SILVA, J. G. R. *Modelo matemático-computacional reduzido para potencial de ação, dinâmica de cálcio e tensão ativa de cardiomiócitos*. Tese (Doutorado) — Universidade Federal de Juiz de Fora, Juiz de Fora, 2024. Programa de Pós-Graduação em Modelagem Computacional.

151 BARBOSA, M. U. *Do complexo ao mínimo: otimização de parâmetros para reprodução eficiente de curvas de restituição e do potencial de ação*. Dissertação (Mestrado) — Universidade Federal de Juiz de Fora, Juiz de Fora, 2025. Programa de Pós-Graduação em Modelagem Computacional.

152 TOMEK, J. et al. Development, calibration, and validation of a novel human ventricular myocyte model in health, disease, and drug block. *elife*, eLife Sciences Publications, Ltd, v. 8, p. e48890, 2019.

153 OSOGAMI, T.; HARCHOL-BALTER, M. Closed form solutions for mapping general distributions to quasi-minimal PH distributions. *Performance Evaluation*, Elsevier, v. 63, n. 6, p. 524–552, 2006.

154 SHERZER, E.; RESHEFF, Y.; TELEK, M. An unconstrained optimization approach to moment fitting with phase type distributions. *arXiv preprint arXiv:2505.20379*, 2025.

155 HURTADO, P. J.; KIROSINGH, A. S. Generalizations of the 'linear chain trick': incorporating more flexible dwell time distributions into mean field ode models. *Journal of mathematical biology*, Springer, v. 79, n. 5, p. 1831–1883, 2019.

156 HORVÁTH, G.; TELEK, M. Butools 2: a rich toolbox for markovian performance evaluation. In: *Proceedings of the 9th International Conference on Performance Evaluation Methodologies and Tools (VALUETOOLS 2016)*. Spain: ACM, 2016. BuTools is a collection of computational methods useful for phase-type and MAP analysis. Disponível em: <https://webspn.hit.bme.hu/ telek/tools/butools/index.php?page=2>.

157 MONTEIRO, N. Z.; MAZORCHE, S. R. Estudos numéricos em um modelo SIR fracionário. *Proceeding Series of the Brazilian Society of Computational and Applied Mathematics*, v. 9, n. 1, 2022.

158 HETHCOTE, H. W. The mathematics of infectious diseases. *SIAM review*, SIAM, v. 42, n. 4, p. 599–653, 2000.

159 CORLESS, R. M. et al. On the Lambert W function. *Advances in Computational Mathematics*, Springer, v. 5, n. 1, p. 329–359, 1996.

160 HETHCOTE, H. W.; TUDOR, D. W. Integral equation models for endemic infectious diseases. *Journal of mathematical biology*, Springer, v. 9, n. 1, p. 37–47, 1980.

161 EL-SAYED, A.; EL-MESIRY, A.; EL-SAKA, H. On the fractional-order logistic equation. *Applied Mathematics Letters*, Elsevier, v. 20, n. 7, p. 817–823, 2007.

162 ABDELJAWAD, T.; AL-MDALLAL, Q. M.; JARAD, F. Fractional logistic models in the frame of fractional operators generated by conformable derivatives. *Chaos, Solitons & Fractals*, Elsevier, v. 119, p. 94–101, 2019.

163 ABDELJAWAD, T.; HAJJI, M. A.; AL-MDALLAL, Q. M.; JARAD, F. Analysis of some generalized ABC–fractional logistic models. *Alexandria Engineering Journal*, Elsevier, v. 59, n. 4, p. 2141–2148, 2020.

164 MENDONÇA, A. K. F.; SOUZA, G. M.; PAIXÃO, D. N. dos S.; AMORIM, R. G. G. de; RISPOLI, V. de C. Fractional logistic equation applied to Brazilian COVID-19 data. *CQD-Revista Eletrônica Paulista de Matemática*, p. 1–10, 2022.

165 HUTCHINSON, G. E. et al. Circular causal systems in ecology. *Ann. NY Acad. Sci*, v. 50, n. 4, p. 221–246, 1948.

166 KRAMER, A. M.; DENNIS, B.; LIEBHOLD, A. M.; DRAKE, J. M. The evidence for Allee effects. *Population Ecology*, Springer, v. 51, n. 3, p. 341–354, 2009.

167 BEREC, L.; ANGULO, E.; COURCHAMP, F. Multiple Allee effects and population management. *Trends in Ecology & Evolution*, Elsevier, v. 22, n. 4, p. 185–191, 2007.

A APPENDIX A – PROOF OF THE THEOREMS OF SECTION 2.1

In this appendix, we present proofs of the theorems from Section 2.1. These results are derived using Laplace transform techniques and properties of fractional operators.

The fundamental equation is given by:

$$y = \int_0^t \kappa(t-\tau)g(y,\tau)d\tau + \kappa(t)y_0. \tag{A.1}$$

Theorem A.1. *If the kernel in Eq.* (2.6) *is given by* $\kappa(t) = E_\alpha(-(rt)^\alpha)$*, the corresponding differential model is given by:*

$$y' = -r^\alpha D^{1-\alpha}y + g(y,t), \tag{A.2}$$

in terms of the Riemann-Liouville fractional derivative.

In terms of the Caputo fractional derivative, the model can be written as:

$${}^C D^\alpha y = -r^\alpha y + I^{1-\alpha}g(y,t). \tag{A.3}$$

Proof. If the kernel in Eq. (A.1) is given by $\kappa(t) = E_\alpha(-(rt)^\alpha)$, we write:

$$y = \int_0^t E_\alpha(-(r(t-\tau))^\alpha)g(y,\tau)d\tau + E_\alpha(-(rt)^\alpha)y_0. \tag{A.4}$$

Taking the derivative using Leibniz's rule and the identity

$$E_{\alpha,\alpha}(z) = \sum_{k=0}^{\infty} \frac{k!}{\Gamma(\alpha k+\alpha)}\frac{z^k}{k!} = \sum_{k=0}^{\infty} \frac{(\alpha k+\alpha)k!}{\Gamma(\alpha k+\alpha+1)}\frac{z^k}{k!} = \alpha E^2_{\alpha,1+\alpha}(z), \tag{A.5}$$

it follows from Lemma 1.1 that

$$y' = g(y,t) + \int_0^t -r^\alpha(t-\tau)^{\alpha-1}E_{\alpha,\alpha}\left(-\left(r(t-\tau)\right)^\alpha\right)g(y,\tau)d\tau - r^\alpha y_0 t^{\alpha-1}E_{\alpha,\alpha}(-(rt)^\alpha). \tag{A.6}$$

Using the convolution property of the Laplace transform, we obtain:

$$y' = g(y,t) - r^\alpha \mathcal{L}^{-1}\left[\mathcal{L}\left[t^{\alpha-1}E_{\alpha,\alpha}(-(rt)^\alpha)\right]\mathcal{L}\left[g(y,t)\right]\right] - r^\alpha y_0 t^{\alpha-1}E_{\alpha,\alpha}(-(rt)^\alpha). \tag{A.7}$$

Then, using Proposition 1.4 and applying the convolution property once again, we obtain:

$$\begin{aligned}
y' &= g(y,t) - r^\alpha \mathcal{L}^{-1}\left[\frac{1}{s^\alpha + r^\alpha}\mathcal{L}\left[g(y,t)\right]\right] - r^\alpha y_0 t^{\alpha-1}E_{\alpha,\alpha}(-(rt)^\alpha) \\
&= g(y,t) - r^\alpha \mathcal{L}^{-1}\left[s^{1-\alpha}\mathcal{L}[E_\alpha(-(rt)^\alpha)]\mathcal{L}\left[g(y,t)\right]\right] - r^\alpha y_0 t^{\alpha-1}E_{\alpha,\alpha}(-(rt)^\alpha) \\
&= g(y,t) - r^\alpha \mathcal{L}^{-1}\left[s^{1-\alpha}\mathcal{L}\left[\int_0^t E_\alpha(-(r(t-\tau))^\alpha)g(y,\tau)d\tau\right]\right] - r^\alpha y_0 t^{\alpha-1}E_{\alpha,\alpha}(-(rt)^\alpha) \\
&= g(y,t) - r^\alpha \mathcal{L}^{-1}\left[s^{1-\alpha}\mathcal{L}\left[y - y_0 E_\alpha(-(rt)^\alpha)\right]\right] - r^\alpha y_0 t^{\alpha-1}E_{\alpha,\alpha}(-(rt)^\alpha).
\end{aligned} \tag{A.8}$$

From Proposition 1.2, we obtain:

$$y' = g(y,t) - r^{\alpha} D^{1-\alpha} y + r^{\alpha} y_0 D^{1-\alpha} E_{\alpha}(-(rt)^{\alpha}) - r^{\alpha} y_0 t^{\alpha-1} E_{\alpha,\alpha}(-(rt)^{\alpha}),$$

where $D^{1-\alpha} := D_{0+}^{1-\alpha}$ is the Riemann-Liouville derivative operator. From Lemma 1.2, we can write:

$$y' = g(y,t) - r^{\alpha} D^{1-\alpha} y + r^{\alpha} y_0 t^{\alpha-1} E_{\alpha,\alpha}(-(rt)^{\alpha}) - r^{\alpha} y_0 t^{\alpha-1} E_{\alpha,\alpha}(-(rt)^{\alpha}), \tag{A.9}$$

which yields the fractional model (A.2).

By considering the hypothesis of Lemma 1.3 and applying the Riemann-Liouville integral operator $I^{1-\alpha} := I_{0+}^{1-\alpha}$ to the model (A.2), or even applying the Laplace Transform in Eq. (A.8), multiplying by $s^{\alpha-1}$ and proceeding (Propositions 1.1 and 1.3), we obtain the Caputo version of the model, given by Eq. (A.3).

The dimensional consistency is preserved, and in the latter case a fractional integral of the function g appears on the right-hand side. □

Theorem A.2. *If the kernel in Eq.* (A.1) *is given by* $\kappa(t) = E_{\alpha}(-(r_1 t)^{\alpha}) e^{-r_2 t}$, *the corresponding differential model is given by:*

$$y' = -r_1^{\alpha} e^{-r_2 t} D^{1-\alpha}(e^{r_2 t} y) - r_2 y + g(y,t), \tag{A.10}$$

in terms of the Riemann-Liouville fractional derivative.

In terms of the Caputo fractional derivative, the model can be written as:

$$e^{-r_2 t}\, {}^{C}D^{\alpha}(e^{r_2 t} y) = -r_1^{\alpha} y + e^{-r_2 t} I^{1-\alpha}(e^{r_2 t} g(y,t)). \tag{A.11}$$

Proof. Using the chosen kernel, we write:

$$y = \int_0^t E_{\alpha}(-(r_1(t-\tau))^{\alpha}) e^{-r_2(t-\tau)} g(y,\tau) d\tau + E_{\alpha}(-(r_1 t)^{\alpha}) e^{-r_2 t} y_0. \tag{A.12}$$

Taking the derivative via Leibniz's rule and using the Laplace convolution property, we obtain:

$$\begin{aligned}
y' &= g(y,t) - r_1^{\alpha} e^{-r_2 t} \mathcal{L}^{-1}\left[\mathcal{L}\left[t^{\alpha-1} E_{\alpha,\alpha}\left(-\left(r_1 t\right)^{\alpha}\right)\right] \mathcal{L}\left[e^{r_2 t} g\right]\right] \\
&\qquad - y_0 r_1^{\alpha} t^{\alpha-1} E_{\alpha,\alpha}(-(r_1 t)^{\alpha}) e^{-r_2 t} - r_2 y \\
&= g(y,t) - r_1^{\alpha} e^{-r_2 t} \mathcal{L}^{-1}\left[s^{1-\alpha} \frac{s^{\alpha-1}}{s^{\alpha} + r_1^{\alpha}} \mathcal{L}\left[e^{r_2 t} g\right]\right] \\
&\qquad - y_0 r_1^{\alpha} t^{\alpha-1} E_{\alpha,\alpha}(-(r_1 t)^{\alpha}) e^{-r_2 t} - r_2 y \\
&= g(y,t) - r_1^{\alpha} e^{-r_2 t} \mathcal{L}^{-1}\left[s^{1-\alpha} \mathcal{L}\left[e^{r_2 t} y - y_0 E_{\alpha}(-(r_1 t)^{\alpha})\right]\right] \\
&\qquad - y_0 r_1^{\alpha} t^{\alpha-1} E_{\alpha,\alpha}(-(r_1 t)^{\alpha}) e^{-r_2 t} - r_2 y \\
&= g(y,t) - r_1^{\alpha} e^{-r_2 t} D^{1-\alpha}(e^{r_2 t} y) + y_0 r_1^{\alpha} t^{\alpha-1} E_{\alpha,\alpha}(-(r_1 t)^{\alpha}) e^{-r_2 t} \\
&\qquad - y_0 r_1^{\alpha} t^{\alpha-1} E_{\alpha,\alpha}(-(r_1 t)^{\alpha}) e^{-r_2 t} - r_2 y,
\end{aligned} \tag{A.13}$$

which yields the fractional model (A.10).

The model can also be written as:

$$(e^{r_2 t}y)' = -r_1^\alpha D^{1-\alpha}(e^{r_2 t}y) + e^{r_2 t}g(y,t). \tag{A.14}$$

Applying the Riemann–Liouville integral operator to this equation yields the Caputo fractional form:

$${}^C D^\alpha(e^{r_2 t}y) = -r_1^\alpha e^{r_2 t}y + I^{1-\alpha}(e^{r_2 t}g(y,t)). \tag{A.15}$$

By introducing the variable changes $\overline{y} = e^{r_2 t}y$ and $\overline{g}(\overline{y},t) = e^{r_2 t}g(y,t) = e^{r_2 t}g(\overline{y}e^{-r_2 t},t)$, we can express the Caputo-type model as:

$${}^C D^\alpha(\overline{y}) = -r_1^\alpha \overline{y} + I^{1-\alpha}(\overline{g}(\overline{y},t)). \tag{A.16}$$

Dimensional consistency is again preserved. If $r_2 = 0$, we have $\kappa(t) = E_\alpha(-(rt)^\alpha)$, and we recover the fractional differential equations (A.2) and (A.3). □

Theorem A.3. *If $y \to y^*$ as $t \to \infty$ in Eq.* (A.2)*, then*

$$\lim_{t\to\infty} g(y,t) = 0 \tag{A.17}$$

if $\alpha < 1$.

On the other hand, if $y \to y^*$ as $t \to \infty$ in Eq. (A.3) *under the same assumptions, then we must have:*

$$y^* = r^{-\alpha} \lim_{t\to\infty} I^{1-\alpha}g(y,t). \tag{A.18}$$

Proof. The proof is straightforward in Eq. (A.3). In Eq. (A.2), since the term $D^{1-\alpha}y$ vanishes as $y \to y^*$ and $\alpha < 1$, the equilibrium in Eq. (A.2) requires Eq. (A.17). □

Theorem A.4. *If $y \to y^*$ when $t \to \infty$ in Eq.* (A.10) *and Eq.* (A.11)*, then*

$$y^* = (r_1^\alpha r_2^{1-\alpha} + r_2)^{-1} \lim_{t\to\infty} g(y,t). \tag{A.19}$$

Proof. In Eq. (A.10), the asymptotic equilibrium is given by

$$0 = -r_1^\alpha \lim_{t\to\infty}[e^{-r_2 t}D^{1-\alpha}(e^{r_2 t}y)] - r_2 y^* + \lim_{t\to\infty} g(y,t). \tag{A.20}$$

From Eq. (3.8), it follows that, in Eq. (A.20), the asymptotic equilibrium respects

$$0 = -r_1^\alpha r_2^{1-\alpha} y^* - r_2 y^* + \lim_{t\to\infty} g(y,t), \tag{A.21}$$

which implies

$$y^* = (r_1^\alpha r_2^{1-\alpha} + r_2)^{-1} \lim_{t\to\infty} g(y,t). \tag{A.22}$$

Note the indeterminacy in the case $r_2 = 0$, the case that recovers Eq. (A.2). Moreover, if $\alpha = 1$, we have:

$$y^* = (r_1 + r_2)^{-1} \lim_{t\to\infty} g(y,t) = r^{-1} \lim_{t\to\infty} g(y,t), \tag{A.23}$$

as expected.

At the same time, we can calculate the asymptotic equilibrium using Eq. (A.11):

$$\lim_{t\to\infty} [e^{-r_2 t}\, {}^C D^{1-\alpha}(e^{r_2 t} y)] = -r_1^\alpha y^* + \lim_{t\to\infty} [e^{-r_2 t}\, I^{1-\alpha}(e^{r_2 t} g(y,t))]. \tag{A.24}$$

Let G be the Laplace transform of g. This limit can be evaluated using Laplace transform techniques and a binomial expansion. For the Riemann-Liouville integral,

$$\begin{aligned}\mathcal{L}[e^{-r_2 t}\, I^{1-\alpha}(e^{r_2 t} g(y,t))] &= (s + r_2)^{\alpha-1} G((s - r_2) + r_2) \\ &= (s + r_2)^{\alpha-1} G(s) \\ &= r_2^{\alpha-1} G(s) + (\alpha - 1) r_2^{\alpha-2} s G(s) + \mathcal{O}(s^2) G(s).\end{aligned} \tag{A.25}$$

Assuming all limits involved are finite, the Final Value Theorem (66) implies:

$$\begin{aligned}\lim_{t\to\infty} [e^{-r_2 t}\, I^{1-\alpha}(e^{r_2 t} g(y,t))] &= \lim_{s\to 0} [r_2^{\alpha-1} s G(s) + (\alpha - 1) r_2^{\alpha-2} s^2 G(s) + \mathcal{O}(s^3) G(s)] \\ &= r_2^{\alpha-1} \lim_{t\to\infty} g(y,t).\end{aligned} \tag{A.26}$$

Finally, for the Caputo derivative,

$$\begin{aligned}\mathcal{L}[e^{-r_2 t}\; {}^C D^{\alpha}(e^{r_2 t} y)] &= (s + r_2)^\alpha Y((s - r_2) + r_2) - (s + r_2)^{\alpha-1} y_0 \\ &= (s + r_2)^\alpha Y(s) - (s + r_2)^{\alpha-1} y_0 \\ &= r_2^\alpha Y(s) + \alpha r_2^{\alpha-1} s Y(s) + \mathcal{O}(s^2) Y(s) - (s + r_2)^{\alpha-1} y_0.\end{aligned} \tag{A.27}$$

Applying the Final Value Theorem once again, we obtain:

$$\begin{aligned}\lim_{t\to\infty} [e^{-r_2 t}\, {}^C D^{\alpha}(e^{r_2 t} y)] &= \lim_{s\to 0} [r_2^\alpha s Y(s) + \alpha r_2^{\alpha-1} s^2 Y(s) + \mathcal{O}(s^3) Y(s) - s(s + r_2)^{\alpha-1} y_0] \\ &= r_2^\alpha y^*.\end{aligned} \tag{A.28}$$

Then, in Eq. (A.24), the asymptotic equilibrium respects:

$$r_2^\alpha y^* = -r_1^\alpha y^* + r_2^{\alpha-1} \lim_{t\to\infty} g(y,t), \tag{A.29}$$

which leads to the same result as Eq. (A.19). □

Theorem A.5. *The mean waiting time for y in the model described by Eq.* (A.10) *or Eq.* (A.11) *is given by:*

$$\eta = \frac{r_2^{\alpha-1}}{r_2^\alpha + r_1^\alpha}. \tag{A.30}$$

It is undefined if $r_2 = 0$, i.e., the mean waiting time is not finite in the case of Eq. (A.2) *and Eq.* (A.3).

Proof. The cumulative distribution function of the random variable representing the waiting time of individuals or materials, denoted as y, is given by $F(t) = 1 - E_\alpha(-(r_1 t)^\alpha)e^{-r_2 t}$. The corresponding probability density function is given by:

$$f(t) = r_1^\alpha t^{\alpha-1} E_{\alpha,\alpha}(-(r_1 t)^\alpha)e^{-r_2 t} + r_2 E_\alpha(-(r_1 t)^\alpha)e^{-r_2 t}. \tag{A.31}$$

The mean waiting time is given by the expectation of this random variable:

$$\eta = \int_0^\infty t r_1^\alpha t^{\alpha-1} E_{\alpha,\alpha}(-(r_1 t)^\alpha)e^{-r_2 t} dt + \int_0^\infty r_2 t E_\alpha(-(r_1 t)^\alpha)e^{-r_2 t} dt. \tag{A.32}$$

Integrating by parts yields:

$$\begin{aligned}\int_0^\infty t r_1^\alpha t^{\alpha-1} E_{\alpha,\alpha}(-(r_1 t)^\alpha)e^{-r_2 t} dt = &\int_0^\infty E_\alpha(-(r_1 t)^\alpha)e^{-r_2 t} dt \\ &- \int_0^\infty r_2 t E_\alpha(-(r_1 t)^\alpha)e^{-r_2 t} dt.\end{aligned} \tag{A.33}$$

It follows from Eqs. (A.32)-(A.33) and Proposition 1.4 that:

$$\eta = \int_0^\infty E_\alpha(-(r_1 t)^\alpha)e^{-r_2 t} dt = \mathcal{L}[E_\alpha(-(r_1 t)^\alpha)](r_2) = \frac{r_2^{\alpha-1}}{r_2^\alpha + r_1^\alpha}. \tag{A.34}$$

In particular, η is undefined when $r_2 = 0$ and $\alpha < 1$, which corresponds to the case in Eq. (A.2) where the mean waiting time is not finite. However, if $\alpha = 1$, we have $\eta = 1/r$, which corresponds to the integer case. □

B APPENDIX B – POSITIVITY AND EQUILIBRIUM IN A FRACTIONAL SIR MODEL

This appendix to Chapter 2 is based on the results presented in (26), where an alternative construction of the SIR model proposed in (32) is introduced. The time required to remove an individual from the infectious compartment, as well as the infectivity, exhibit memory effects governed by Mittag–Leffler distributions. This alternative construction clarifies how the proposed generalizations act, starting from the classical SIR model. Using integrodifferential techniques, we establish novel analytical results concerning positivity, monotonicity in a limiting case, and equilibrium points. These results are also verified numerically.

The compartmental SIR (Susceptible-Infected-Removed) model was introduced by Kermack and McKendrick in 1927 (11). The SIR model proposed in (32) has been studied in detail in (33, 67) and related works. Here, we provide a brief overview for completeness.

B.1 THE MODEL

B.1.1 An overview

The main idea of the construction is that, if there are $S(t)$ susceptible individuals at time t in a population of size N, then the expected number of new infections per infected individual is given by $\sigma(t,t')\frac{S(t)}{N}\Delta T$ in a time step ΔT. Here, $\sigma(t,t')$ is the transmission function of an individual first infected at time $t' < t$.

The survival function $\Phi(t,t')$ gives the probability that a person first infected at time $t' < t$ remains infected at time t. Considering that there is no disease before $t = 0$, the flow of individuals into the infectious compartment I at time t is recursively given by

$$q^+(I,t) = \int_0^t \sigma(t,t')\frac{S(t)}{N}\Phi(t,t')q^+(I,t')dt' + i_0\sigma(t,0)\frac{S(t)}{N}\Phi(t,0), \tag{B.1}$$

where i_0 is the initial condition: the number of infectious individuals at time 0.

The transmission function $\sigma(t,t')$ depends on both the present time t, e.g., due to cultural or containment measures, and the age of infection $t - t'$. The dependence on t is expressed by an extrinsic infectivity ω, independent of the individual. On the other hand, there is an intrinsic infectivity ρ that depends on the infection age. So,

$$\sigma(t,t') = \omega(t)\rho(t - t'). \tag{B.2}$$

For the survival function, it is assumed that natural death and recovery or death due to the disease of an infected individual are independent. Then,

$$\Phi(t,t') = \phi(t - t')\theta(t,t'), \tag{B.3}$$

where $\phi(t-t')$ is the probability that an individual first infected in t' still has the disease at time t. Furthermore, $\theta(t,t')$ is the probability that an individual first infected in t' has not yet died a natural death by time t, and is given by

$$\theta(t,t') = e^{-\int_{t'}^{t} \gamma(u)du}, \tag{B.4}$$

where γ is the vital rate.

Individuals in compartment I at time t must have entered this compartment at some previous time and remained there until t. Therefore, we can express the number of infected individuals as follows:

$$I(t) = \Phi(t,0)i_0 + \int_0^t \Phi(t,t')q^+(I,t')dt'. \tag{B.5}$$

Writing $\psi(t) = -d\phi(t)/dt$, we derive Eq. (B.5) through Leibniz's rule, obtaining

$$\begin{aligned}\frac{dI(t)}{dt} &= \omega(t)\frac{S(t)}{N}\left(\int_0^t \rho(t-t')\Phi(t,t')q^+(I,t')dt' + \rho(t)\Phi(t,0)i_0\right)\\ &- \int_0^t \psi(t-t')\theta(t,t')q^+(I,t')dt' - \psi(t)\theta(t,0)i_0 - \gamma(t)I(t). \end{aligned}\tag{B.6}$$

The dependence on $q^+(I,t')$ is removed by defining memory kernels for infectivity and recovery. Henceforth, we consider $i_0 = 1$ for simplicity. Eq. (B.5) can be rewritten as

$$\frac{I(t)}{\theta(t,0)} - \phi(t) = \int_0^t \phi(t-t')\frac{q^+(I,t')}{\theta(t',0)}dt'. \tag{B.7}$$

Using the Laplace transform in the first integral of (B.6), we can write

$$\mathcal{L}\{\rho(t)\phi(t)\}\mathcal{L}\left\{\frac{q^+(I,t)}{\theta(t,0)}\right\} = \mathcal{L}\left\{\int_0^t K_I(t-t')\left(\frac{I(t')}{\theta(t',0)}\right)dt' - \rho(t)\phi(t)\right\}, \tag{B.8}$$

where the infectivity memory kernel is defined as

$$K_I(t) = \mathcal{L}^{-1}\left\{\frac{\mathcal{L}\{\rho(t)\phi(t)\}}{\mathcal{L}\{\phi(t)\}}\right\}. \tag{B.9}$$

In the same way, based on the second integral of Eq. (B.6), we write:

$$\mathcal{L}\{\psi(t)\}\mathcal{L}\left\{\frac{q^+(I,t)}{\theta(t,0)}\right\} = \mathcal{L}\left\{\int_0^t K_R(t-t')\left(\frac{I(t')}{\theta(t',0)}\right)dt' - \psi(t)\right\}, \tag{B.10}$$

where the recovery memory kernel is defined by

$$K_R(t) = \mathcal{L}^{-1}\left\{\frac{\mathcal{L}\{\psi(t)\}}{\mathcal{L}\{\phi(t)\}}\right\}. \tag{B.11}$$

Fractional derivatives are incorporated into the model by choosing $\psi(t)$ as a power-law-type function and $\rho(t)$ consistently defined with $\psi(t)$.

$$\psi(t) = \frac{t^{\alpha-1}}{\tau^\alpha}E_{\alpha,\alpha}\left(-\left(\frac{t}{\tau}\right)^\alpha\right), \tag{B.12}$$

for $0 < \alpha \leq 1$, where τ is a scale parameter. The corresponding survival function is

$$\phi(t) = E_{\alpha,1}\left(-\left(\frac{t}{\tau}\right)^{\alpha}\right). \tag{B.13}$$

We can calculate the Laplace transform of the removal memory kernel defined by the Mittag-Leffler function, obtaining:

$$\mathcal{L}\{K_R(t)\} = \frac{\mathcal{L}\{\psi(t)\}}{\mathcal{L}\{\phi(t)\}} = s^{1-\alpha}\tau^{-\alpha}. \tag{B.14}$$

The Laplace transform of the kernel implies that a convolution with the recovery memory kernel can be written as

$$\int_0^t K_R(t-t')\frac{I(t')}{\theta(t',0)}dt' = \tau^{-\alpha}D^{1-\alpha}\left(\frac{I(t)}{\theta(t,0)}\right). \tag{B.15}$$

Another fractional derivative is incorporated into the infectivity memory kernel by considering

$$\rho(t) = \frac{1}{\phi(t)}\frac{t^{\beta-1}}{\tau^{\beta}}E_{\alpha,\beta}\left(-\left(\frac{t}{\tau}\right)^{\alpha}\right). \tag{B.16}$$

Since $\rho(t) \geq 0$ is necessary, we take $0 < \alpha \leq \beta \leq 1$. Using Eq. (B.16), we obtain the Laplace transform of the infectivity kernel:

$$\int_0^t K_I(t-t')\frac{I(t')}{\theta(t',0)}dt' = \tau^{-\beta}D^{1-\beta}\left(\frac{I(t)}{\theta(t,0)}\right). \tag{B.17}$$

Substituting Eqs. (B.15) and (B.17) into the master equation Eq. (B.6) and rewriting, the fractional SIR model from (32):

$$S'(t) = \gamma(t)N - \frac{\omega(t)S(t)\theta(t,0)}{N\tau^{\beta}}D^{1-\beta}\left(\frac{I(t)}{\theta(t,0)}\right) - \gamma(t)S(t), \tag{B.18}$$

$$I'(t) = \frac{\omega(t)S(t)\theta(t,0)}{N\tau^{\beta}}D^{1-\beta}\left(\frac{I(t)}{\theta(t,0)}\right) - \frac{\theta(t,0)}{\tau^{\alpha}}D^{1-\alpha}\left(\frac{I(t)}{\theta(t,0)}\right) - \gamma(t)I(t), \tag{B.19}$$

$$R'(t) = \frac{\theta(t,0)}{\tau^{\alpha}}D^{1-\alpha}\left(\frac{I(t)}{\theta(t,0)}\right) - \gamma(t)R(t). \tag{B.20}$$

B.1.2 Another approach for constructing a fractional SIR model

The function $\psi(t) = -\dfrac{d\phi(t)}{dt}$ can be related to the continuous random variable X, which represents the waiting time of an individual in the infectious compartment in the absence of vital dynamics. Indeed, the cumulative distribution function of X is $F(t) = P(X \leq t) = 1 - \phi(t)$. Therefore, the probability density function of X is $\psi(t) = -d\phi(t)/dt$. The distribution F is a Mittag–Leffler distribution, $F(t;\alpha,\tau) = 1 - E_{\alpha}\left(-\left(\frac{t}{\tau}\right)^{\alpha}\right)$. If $\alpha < 1$, the expectation is infinite. This corresponds, for instance, to situations in which long waiting times are not negligible. However, if $\alpha = 1$, it reduces to the exponential distribution. For exponentially distributed waiting times, the first moment of the random variable X exists, and τ coincides with the mean waiting time in the infectious compartment in the absence of vital dynamics. If $\gamma(t) \equiv \gamma > 0$, the effective mean waiting time in the infectious compartment, accounting for both recovery and natural death, is finite and given by $\gamma^{\alpha-1}/(\gamma^{\alpha}+\tau^{-\alpha})$ for any $\alpha \in (0,1]$ (55). In this section, we show how to recover, from the theory presented in Chapter 2, the same fractional model constructed via CTRW in the previous section.

Assuming constant rates of vital dynamics (γ), infectivity (σ), and mean removal time (τ), the SIR model can be written as

$$\begin{cases} S'(t) = \gamma N - \sigma \dfrac{S(t)}{N} I(t) - \gamma S(t), \\ I'(t) = \sigma \dfrac{S(t)}{N} I(t) - \frac{1}{\tau} I(t) - \gamma I(t), \\ R'(t) = \frac{1}{\tau} I(t) - \gamma R(t). \end{cases} \tag{B.21}$$

From the second equation, we can write

$$I = \int_0^t e^{-\gamma(t-t')} e^{-(t-t')/\tau} \sigma \frac{S(t')}{N} I(t') dt' + e^{-\gamma t} e^{-t/\tau} i_0. \tag{B.22}$$

We generalize $e^{-t/\tau}$, which corresponds to an exponentially distributed waiting time in the infectious compartment, with a Mittag-Leffler probability $E_\alpha\left(-\left(\frac{t}{\tau}\right)^{\alpha}\right)$.

This generalization yields a fractional SIR model with general recovery time as in (30). However, as discussed in the previous subsection, in (32) there is also a generalization of the transmission function: in fact, the infectivity σ is seen as a function with an extrinsic term $\omega(t)$, depending on the present time (for instance, cultural and political measures), and an intrinsic term $\rho(t-t')$, depending on the age of infection:

$$\sigma(t,t') = \omega(t)\rho(t-t'). \tag{B.23}$$

In the absence of memory, *i.e.*, when the infectivity does not depend on the infection age, ρ is constant.

Note that a person that becomes infectious in a time t' is still infectious in t if:

- It is alive (probability $e^{-\gamma(t-t')}$), and
- It is not removed (probability $E_\alpha\left(-\left(\frac{(t-t')}{\tau}\right)^{\alpha}\right)$).

Therefore, the flux of new infectious individuals is given recursively by:

$$\begin{aligned} q^+(t) =& \frac{S(t)}{N}\omega(t) \int_0^t e^{-\gamma(t-t')} E_\alpha\left(-\left(\frac{(t-t')}{\tau}\right)^{\alpha}\right) \rho(t-t') q^+(t') dt' \\ &+ \frac{S(t)}{N}\omega(t) e^{-\gamma t} E_\alpha\left(-\left(\frac{t}{\tau}\right)^{\alpha}\right) \rho(t) i_0. \end{aligned} \tag{B.24}$$

Aiming to use the Laplace Transform of Mittag-Leffler functions in Eq. (B.24) and considering that the intrinsic infectivity is positive and monotonically decreasing with time, we consider:

$$\rho(t) = \frac{1}{E_\alpha\left(-\left(\frac{t}{\tau}\right)^\alpha\right)} \frac{t^{\beta-1}}{\tau^\beta} E_{\alpha,\beta}\left(-\left(\frac{t}{\tau}\right)^\alpha\right), \tag{B.25}$$

with $0 < \alpha \leq \beta \leq 1$. Then,

$$\begin{aligned} q^+(t) =& \frac{S(t)}{N}\omega(t) \int_0^t e^{-\gamma(t-t')} \frac{(t-t')^{\beta-1}}{\tau^\beta} E_{\alpha,\beta}\left(-\left(\frac{(t-t')}{\tau}\right)^\alpha\right) q^+(t')dt' \\ &+ \frac{S(t)}{N}\omega(t) e^{-\gamma t} \frac{t^{\beta-1}}{\tau^\beta} E_{\alpha,\beta}\left(-\left(\frac{t}{\tau}\right)^\alpha\right) i_0. \end{aligned} \tag{B.26}$$

Observe that:

$$\int_0^t e^{-\gamma(t-t')} \frac{(t-t')^{\beta-1}}{\tau^\beta} E_{\alpha,\beta}\left(-\left(\frac{(t-t')}{\tau}\right)^\alpha\right) q^+(t')dt' \tag{B.27}$$

$$= \frac{e^{-\gamma t}}{\tau^\beta} \mathcal{L}^{-1}\left[\mathcal{L}\left[t^{\beta-1} E_{\alpha,\beta}\left(-\left(\frac{t}{\tau}\right)^\alpha\right)\right] \mathcal{L}\left[e^{\gamma t} q^+(t)\right]\right] \tag{B.28}$$

$$= \frac{e^{-\gamma t}}{\tau^\beta} \mathcal{L}^{-1}\left[\frac{s^{\alpha-\beta}}{s^\alpha + \tau^{-\alpha}} \mathcal{L}\left[e^{\gamma t} q^+(t)\right]\right] \tag{B.29}$$

$$= \frac{e^{-\gamma t}}{\tau^\beta} \mathcal{L}^{-1}\left[s^{1-\beta} \mathcal{L}\left[\int_0^t E_\alpha\left(-\left(\frac{(t-t')}{\tau}\right)^\alpha\right) e^{\gamma t'} q^+(t')dt'\right]\right] \tag{B.30}$$

$$= \frac{e^{-\gamma t}}{\tau^\beta} D^{1-\beta}(e^{\gamma t} Y), \tag{B.31}$$

where

$$Y(t) = \int_0^t E_\alpha\left(-\left(\frac{(t-t')}{\tau}\right)^\alpha\right) e^{-\gamma(t-t')} q^+(t')dt'. \tag{B.32}$$

Note that Y represents the total number of individuals who entered the I compartment in each $0 < t' \leq t$ and remain alive and infectious at time t. So,

$$\begin{aligned} I(t) &= E_\alpha\left(-\left(\frac{t}{\tau}\right)^\alpha\right) e^{-\gamma t} i_0 + Y(t) \\ &= E_\alpha\left(-\left(\frac{t}{\tau}\right)^\alpha\right) e^{-\gamma t} i_0 + \int_0^t E_\alpha\left(-\left(\frac{(t-t')}{\tau}\right)^\alpha\right) e^{-\gamma(t-t')} q^+(t')dt'. \end{aligned} \tag{B.33}$$

This implies that:

$$D^{1-\beta}(e^{\gamma t} Y) = D^{1-\beta}(e^{\gamma t} I) - i_0 D^{1-\beta}\left(E_\alpha\left(-\left(\frac{t}{\tau}\right)^\alpha\right)\right) \tag{B.34}$$

$$= D^{1-\beta}(e^{\gamma t} I) - i_0 t^{\beta-1} E_{\alpha,\beta}\left(-\left(\frac{t}{\tau}\right)^\alpha\right). \tag{B.35}$$

It follows from (B.26) and (B.35) that:

$$q^+(t) = \frac{S(t)\omega(t) e^{-\gamma t} D^{1-\beta}(e^{\gamma t} I)}{N \tau^\beta}. \tag{B.36}$$

Finally, differentiating (B.33) using Leibniz's rule and the identity

$$E_{\alpha,\alpha}(z) = \sum_{k=0}^{\infty} \frac{k!}{\Gamma(\alpha k+\alpha)} \frac{z^k}{k!} = \sum_{k=0}^{\infty} \frac{(\alpha k+\alpha)k!}{\Gamma(\alpha k+\alpha+1)} \frac{z^k}{k!} = \alpha E^2_{\alpha,1+\alpha}(z), \tag{B.37}$$

we get:

$$I'(t) = q^+(t) - \frac{e^{-\gamma t} D^{1-\alpha}(e^{\gamma t} I)}{\tau^\alpha} - \gamma I(t) \tag{B.38}$$

$$= \frac{S(t)\omega(t)e^{-\gamma t} D^{1-\beta}(e^{\gamma t} I)}{N\tau^\beta} - \frac{e^{-\gamma t} D^{1-\alpha}(e^{\gamma t} I)}{\tau^\alpha} - \gamma I(t). \tag{B.39}$$

This is the master equation of the fractional SIR model (B.18)-(B.20) with constant vital rate $\gamma(t) \equiv \gamma$:

$$S'(t) = \gamma N - \frac{S(t)\omega(t)e^{-\gamma t} D^{1-\beta}(e^{\gamma t} I)}{N\tau^\beta} - \gamma S(t), \tag{B.40}$$

$$I'(t) = \frac{S(t)\omega(t)e^{-\gamma t} D^{1-\beta}(e^{\gamma t} I)}{N\tau^\beta} - \frac{e^{-\gamma t} D^{1-\alpha}(e^{\gamma t} I)}{\tau^\alpha} - \gamma I(t), \tag{B.41}$$

$$R'(t) = \frac{e^{-\gamma t} D^{1-\alpha}(e^{\gamma t} I)}{\tau^\alpha} - \gamma R(t). \tag{B.42}$$

In the next section, we prove the non-negativity of solutions for positive initial conditions. Furthermore, we show that, in the limiting case where the vital dynamics is null, the compartments S and R are monotonic.

B.2 MONOTONICITY IN THE LIMITING CASE AND NON-NEGATIVITY

The solution of the fractional SIR model constructed in the previous section is expected to be non-negative, since the compartments represent populations. We now establish the following result:

Proposition B.1. *Let* $\gamma(t) \equiv \gamma \geq 0$. *Assuming that the solution of the system* (B.18)-(B.20) *exists uniquely with initial conditions* $S(0) \geq 0, I(0) = i_0 > 0$ *and* $R(0) = N - S(0) - I(0) \geq 0$, *and is continuous for* $t > 0$, *we have:*

- $S(t), I(t), R(t)$, $D^{1-\beta}\left(\frac{I(t)}{\theta(t,0)}\right)$ *and* $D^{1-\alpha}\left(\frac{I(t)}{\theta(t,0)}\right)$ *are non-negative;*
- $S(t), I(t), R(t) \leq N$ *for all* t.

Proof. We first prove the positivity of $S(t)$ for both $\gamma > 0$ and $\gamma = 0$. Initially, consider $\gamma > 0$. Suppose, by contradiction, that the set $\{t > 0;\ S(t) < 0\}$ is non-empty. Let $T > 0$ be the infimum of this set. By continuity of the solution, we have $S(T) = 0$. From Eq. (B.18), we have $S'(T) = \gamma N > 0$. Thus, there is an interval $(T, T+\epsilon)$ such that $S'(T) > 0$ and S is increasing in this interval, which is a contradiction, since T is defined as the infimum of the set $\{t > 0;\ S(t) < 0\}$, and so there is a sequence in $\{t > 0;\ S(t) < 0\}$ that converges to T from the right. Therefore, $S(t) > 0$ for all t.

In the case $\gamma = 0$, we can write:

$$S'(t) = -q^+(I,t) = -\int_0^t \sigma(t,t')\frac{S(t)}{N}\Phi(t,t')q^+(I,t')dt' - i_0\sigma(t,0)\frac{S(t)}{N}\Phi(t,0), \tag{B.43}$$

$$\frac{S'(t)}{S(t)} = \frac{1}{N}\int_0^t \sigma(t,t')\Phi(t,t')S'(t')dt' - \frac{1}{N}i_0\sigma(t,0)\Phi(t,0), \tag{B.44}$$

$$\log(|S(s)|) = \frac{1}{N}\int_0^s \left[\int_0^t \sigma(t,t')\Phi(t,t')S'(t')dt' - i_0\sigma(t,0)\Phi(t,0)\right] dt + \log(S(0)), \tag{B.45}$$

$$|S(s)| = e^{f(s)}S(0) = \begin{cases} e^{f(s)}S(0), & S(0) \geq 0 \\ -e^{f(s)}S(0), & S(0) < 0 \end{cases}, \tag{B.46}$$

where

$$f(s) = \frac{1}{N}\int_0^s \left[\int_0^t \sigma(t,t')\Phi(t,t')S'(t')dt' - i_0\sigma(t,0)\Phi(t,0)\right] dt. \tag{B.47}$$

Since $S(0) \geq 0$, Eq. (B.46) implies that $S(t) \geq 0$ for all t.

Given that $S(t) \geq 0$ and that σ and Φ are positive functions, Eq. (B.1) or Eq. (B.26) gives $q^+(I,t) \geq 0$ for all t. From Eq. (B.5) or Eq. (B.33) it follows that $I(t) \geq 0$ for all t. Now, applying the inverse Laplace Transform to Eq. (B.8), we have

$$\int_0^t K_I(t-t')\frac{I(t')}{\theta(t',0)}dt' = \int_0^t \rho(t-t')\phi(t-t')\frac{q^+(I,t')}{\theta(t',0)}dt' + \rho(t)\phi(t)i_0. \tag{B.48}$$

It follows from the positivity of ρ, ϕ, θ and $q^+(I,t)$ that

$$\int_0^t K_I(t-t')\frac{I(t')}{\theta(t',0)}dt' > 0, \tag{B.49}$$

for all t. Therefore, from Eq. (B.17), we have $D^{1-\beta}\left(\frac{I(t)}{\theta(t,0)}\right) > 0$, for all t. The same can be concluded for $D^{1-\alpha}\left(\frac{I(t)}{\theta(t,0)}\right)$.

Finally, suppose, by contradiction, that the set $\{t > 0;\ R(t) < 0\}$ is non-empty. Let $T \geq 0$ be the infimum of this set. Since the solution is continuous and $R(0) \geq 0$, we must have $R(T) = 0$. Then,

$$R'(T) = \frac{\theta(T,0)}{\tau^\alpha}\left(D^{1-\alpha}\left(\frac{I(t)}{\theta(t,0)}\right)\right)(T) > 0. \tag{B.50}$$

Thus, there is an interval $(T, T+\epsilon)$ such that $R'(t) > 0$ and R is increasing in this interval, which is a contradiction, since there is a sequence in $\{t > 0;\ R(t) < 0\}$ that converges to T from the right. Therefore, $R(t) \geq 0$ for all t.

Since $S(t) + I(t) + R(t) = N$, it follows from $S(t)$, $I(t)$, $R(t) \geq 0$ that $S(t)$, $I(t)$, $R(t) \leq N$, which completes the proof.

□

For the limit case in which $\gamma = 0$, we also have the following result:

Proposition B.2. *Considering the limiting system* (B.18)-(B.20) *for which* $\gamma(t) \equiv 0$, *the functions* $S(t)$ *and* $R(t)$ *are non-increasing and non-decreasing, respectively.*

Proof. Since $S(t)$, $D^{1-\beta}\left(\frac{I(t)}{\theta(t,0)}\right)$, and $D^{1-\alpha}\left(\frac{I(t)}{\theta(t,0)}\right)$ are non-negative, if $\gamma(t) \equiv 0$, then $S'(t) \leq 0$ and $R'(t) \geq 0$. Thus, S and R are non-increasing and non-decreasing, respectively. □

We note that this property is consistent with epidemiological expectations, but it cannot be guaranteed for *ad hoc* fractional SIR models, where the integer order derivative is replaced by the Caputo derivative:

$$\begin{cases} {}^{C}D^{\alpha}_{0+}S(t) = -\sigma \dfrac{S(t)}{N} I(t), \\ {}^{C}D^{\alpha}_{0+}I(t) = \sigma \dfrac{S(t)}{N} I(t) - \frac{1}{\tau} I(t), \\ {}^{C}D^{\alpha}_{0+}R(t) = \frac{1}{\tau} I(t). \end{cases} \tag{B.51}$$

In fact, Figure B.1 illustrates the solution of the system (B.51). It highlights the non-monotonic behavior of the compartments S and R in the model without vital dynamics. This issue is not resolved by simply balancing the units of the parameters. On the other hand, in Figure B.2 the system (B.18)-(B.20) is numerically solved. We observe that monotonicity is preserved in the model for arbitrary orders, as observed in Proposition B.2, even when $\alpha \neq \beta$. Therefore, any oscillations observed in this model arise exclusively from vital dynamics. In the simulations, we consider a population $N_0 = 10^6$, initial conditions $S(0) = N_0 - 1$, $I(0) = 1$ and $R(0) = 0$, and $dt = 0.1$ for both simulations. Our previous works (143, 157) provide a detailed discussion about the *ad hoc* fractionalization (B.51).

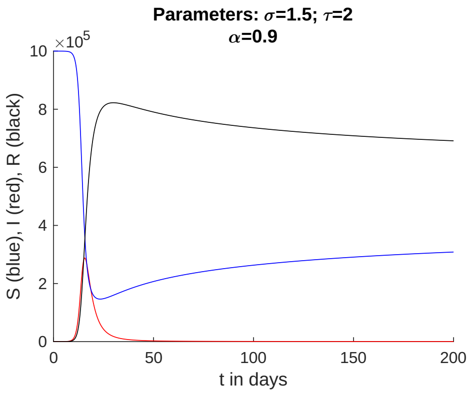

Figure B.1 – Non-monotonic behavior of S and R in system (B.51).

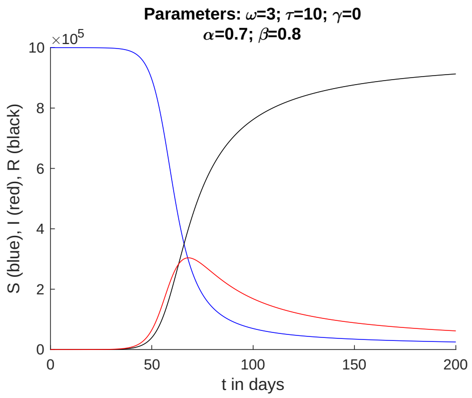

Figure B.2 – Monotonicity of S and R in Eq. (B.18)-(B.20) for $\gamma(t) \equiv 0$.

The next section addresses equilibrium points. In particular, we study their relationship with the basic reproduction number and approaches to stability analysis.

B.3 EQUILIBRIUM POINTS AND STABILITY

Classical epidemiological ODE models such as Eq. (B.21) are time-invariant. Their local behavior allows the parameters to define the disease dynamics independently of the time in which one begins the modeling. However, this property does not hold for the model (B.18)–(B.20). Different past histories modify the future dynamics. Its nonlocal behavior also implies unexpected behavior of the reproduction number $\Re(t)$. The reproduction number at time t can be defined as the expected number of individuals infected by a person first infected in time t. The basic reproduction number is this number for $t = 0$, *i.e.*, the average number of secondary infections that occur when an infectious individual is introduced into a completely susceptible population (158). The definition of reproduction numbers in the proposed model is non-intuitive. In (32), an integral construction for the basic reproduction number is proposed. In (67), we extend the reproduction number proposal to any time t and also propose the S-variable reproduction numbers. These discussions have central implications in equilibrium analysis and peak conditions. For instance, the peak does not occur when $\Re(t) = 1$, nor $\Re^S(t) = 1$ (67). This reflects the nonlocal nature of the model.

For this thesis, we only use the basic reproduction number (32):

$$\Re_0 = \int_0^\infty \sigma(t)\Phi(t)dt = \frac{\omega\gamma^{\alpha-\beta}}{\tau^\beta\gamma^\alpha + \tau^{\beta-\alpha}}. \tag{B.52}$$

For the equilibrium calculation of the system (B.40)-(B.42), we consider $\gamma(t) \equiv \gamma$ constant, so $\theta(t, 0) = e^{-\gamma t}$. Taking the limit when $t \to \infty$, we calculate the limits of the form $\lim\limits_{t\to\infty} e^{-\gamma t} D^{1-\alpha}(I(t)e^{\gamma t})$ according to Eq. (3.8). Assuming $\lim\limits_{t\to\infty} \omega(t) = \omega^*$, we obtain a disease-free state,

$$S^* = N, \quad I^* = 0, \quad R^* = 0, \tag{B.53}$$

and, if $\omega^* > 0$, an endemic state:

$$\begin{aligned} S^* &= \frac{((\tau\gamma)^{\beta-\alpha} + (\tau\gamma)^\beta)N}{\omega^*}, \qquad I^* = \frac{N(\tau\gamma)^\alpha}{1 + (\tau\gamma)^\alpha} - \frac{N(\tau\gamma)^\beta}{\omega^*}, \\ R^* &= \frac{N}{1 + (\tau\gamma)^\alpha} - \frac{N(\tau\gamma)^{\beta-\alpha}}{\omega^*}. \end{aligned} \tag{B.54}$$

Particularly, when $\omega(t) \equiv \omega$, this result is the same as that obtained in (32). Note that the viability of the endemic equilibrium in Eq. (B.54) requires

$$\omega^* > (\tau\gamma)^{\beta-\alpha} + (\tau\gamma)^\beta, \tag{B.55}$$

which is related to the basic reproduction number Eq. (B.52).

In fact, if $\omega(t) \equiv \omega$, the criterion for the viability given in Eq. (B.55) can be rewritten as $\Re_0 > 1$. Furthermore, the value S^* of the endemic state given in Eq. (B.54)

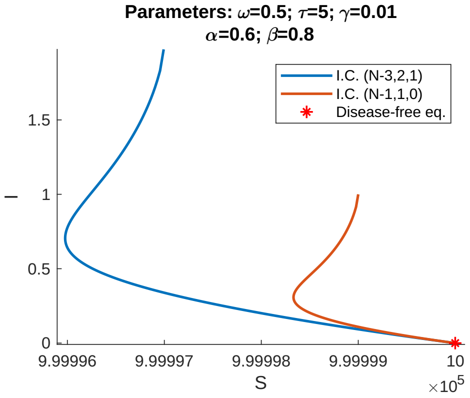

Figure B.3 – Trajectories $\Re_0 < 1$.

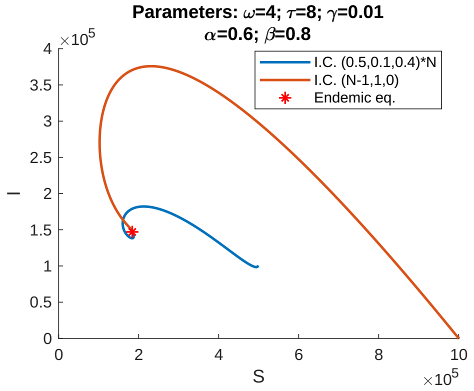

Figure B.4 – Trajectories $\Re_0 > 1$.

is of the form $S^* = N/\Re_0$. Thus, $\Re_0$ has an essential relationship with the final size of the infection.

Until now, we have proven that **if there are asymptotically stable equilibria for the case $\gamma > 0$, then they are given by Eqs.** (B.53)-(B.54). A limiting case in which $\gamma = 0$ is studied in (72):

Theorem B.1. *If $\omega(t) \equiv \omega$, $\gamma(t) \equiv 0$, $i_0 > 0$ and $\alpha = \beta$ in the system* (B.18)-(B.20), *then the solution asymptotically approaches equilibrium $(S, I, R)_\infty$, where*

$$R_\infty = N + \frac{N}{\omega} W_0 \left(\frac{-S_0 \omega e^{-\omega}}{N} \right), \tag{B.56}$$

and

$$S_\infty = S_0 \exp\left(-\frac{\omega}{N} R_\infty \right) = -\frac{N}{\omega} W_0 \left(\frac{-S_0 \omega e^{-\omega}}{N} \right), \quad I_\infty = N - S_\infty - R_\infty = 0. \tag{B.57}$$

W_0 represents the principal branch of Lambert's function W (159), and $S_0 = S(0)$. Lambert's function W, also known as the omega function or product logarithm, is a multivalued function defined by the equation $W(z)e^{W(z)} = z$, where z is a complex number.

Proof. See (72). ☐

For $\gamma > 0$, the disease-free state is expected to be an asymptotically stable equilibrium when $\omega^* < (\tau\gamma)^{\beta-\alpha} + (\tau\gamma)^{\beta}$, while the endemic state is expected to be asymptotically stable if $\omega^* > (\tau\gamma)^{\beta-\alpha} + (\tau\gamma)^{\beta}$. These hypotheses are formulated, for constant $\omega(t)$, in (32).

To develop our results, based on (160), we need the integral forms of the infectious and recovered compartments:

$$I(t) = \Phi(t,0)i_0 + \int_0^t \Phi(t,t')\frac{\omega(t')S(t')\theta(t',0)}{N\tau^\beta}\left(D^{1-\beta}\left(\frac{I(t)}{\theta(t,0)}\right)\right)(t')dt', \tag{B.58}$$

$$R(t) = F(t)\theta(t,0)i_0 + \int_0^t F(t-t')\theta(t,t')\frac{\omega(t')S(t')\theta(t',0)}{N\tau^\beta}\left(D^{1-\beta}\left(\frac{I(t)}{\theta(t,0)}\right)\right)(t')dt', \tag{B.59}$$

on with $F(t) = 1-\phi(t)$.

The following results are demonstrated:

Theorem B.2. *If* $\omega(t)$ *is bounded with* $\lim\limits_{t\to\infty}\omega(t) = \omega^*$, $\gamma(t)\equiv\gamma$ *and* $\beta = 1$ *in the system* (B.18)-(B.20)*, the disease-free equilibrium of Eq.* (B.53) *is globally asymptotically stable if* $\omega^* < (\tau\gamma)^{1-\alpha} + (\tau\gamma)$.

Proof. We define the constant A such that

$$A = \int_0^\infty \frac{\omega^*}{\tau}\Phi(t)dt = \frac{\omega^*}{(\tau\gamma)+(\tau\gamma)^{1-\alpha}} < 1. \tag{B.60}$$

Let $J = \lim\limits_{t\to\infty}\sup I(t)$ and suppose, by contradiction, that $J > 0$. Thus, it is possible to choose ϵ small enough such that $2\epsilon + A(1+\epsilon)(J+\epsilon) < J$. Indeed, defining the continuously increasing function $E(t) = 2t + A(1+t)(J+t)$, we have $E(0) = AJ < J$ and $\lim\limits_{t\to\infty}E(t) = \infty$, so there is $\epsilon_J > 0$ such that $E(\epsilon_J) = J$. Therefore, we just need to choose $\epsilon \in (0,\epsilon_J)$.

We have $\lim\limits_{t\to\infty}\Phi(t,0)i_0 = 0$. Furthermore, we know that $\lim\limits_{t\to\infty}\sup I(t) = J$ and $\lim\limits_{t\to\infty}\omega(t) = \omega^*$. Thus, choosing ϵ, we can choose a time $t_1 > 0$ sufficiently large such that $\Phi(t,0)i_0 < \epsilon/2$, $I(t) < J+\epsilon$ and $\omega(t) < (1+\epsilon)\omega^*$ for $t > t_1$. Choosing t_1, since $\lim\limits_{t\to\infty}\theta(t,0) = 0$, we can choose t_2 large enough such that $Nt_1\theta(t,0)\omega_m/\tau < \epsilon$ for $t > t_2$, where ω_m is the maximum value reached by $\omega(t)$. So, for $t > t_1+t_2$, we have $t - t_1 > t_2$ and

$$\begin{aligned} I(t) &= \Phi(t,0)i_0 + \int_0^t \Phi(t,t')\frac{\omega(t')S(t')I(t')}{N\tau}dt' \\ &< \frac{\epsilon}{2} + \int_0^{t_1}\Phi(t,t')\frac{\omega(t')S(t')I(t')}{N\tau}dt' + \int_{t_1}^t \Phi(t,t')\frac{\omega(t')S(t')I(t')}{N\tau}dt'. \end{aligned} \tag{B.61}$$

Now, we recall that $S(t), I(t) \leq N$. In the first integral we use $\Phi(t,0) = \phi(t)\theta(t,0) \leq \theta(t,0)$. In the second integral, we use that $I(t) < J+\epsilon$ and $\omega(t) < (1+\epsilon)\omega^*$ for $t > t_1$, obtaining

$$I(t) < \frac{\epsilon}{2} + N\int_0^{t_1}\theta(t,t')\frac{\omega_m}{\tau}dt' + (J+\epsilon)(1+\epsilon)\int_{t_1}^t \Phi(t,t')\frac{\omega^*}{\tau}dt'. \tag{B.62}$$

Finally, as $t - t_1 > t_2$, we have $\theta(t,t_1) < \theta(t_2)$. Furthermore, by the definition of A, we have $\int_{t_1}^t \Phi(t,t')\omega^*/\tau dt' < A$. Therefore, by choosing ϵ, t_1 and t_2, it follows that, for all $t > t_1 + t_2$, we have

$$\begin{aligned} I(t) &< \frac{\epsilon}{2} + Nt_1\theta(t_2)\frac{\omega_m}{\tau} + A(1+\epsilon)(J+\epsilon) \\ &< \frac{3\epsilon}{2} + A(1+\epsilon)(J+\epsilon) < J - \frac{\epsilon}{2}, \end{aligned} \tag{B.63}$$

a contradiction. It follows that $J = 0$ and $\lim\limits_{t\to\infty} I(t) = 0$.

Remembering that, under the conditions of the statement, we have

$$S'(t) = \gamma N - \frac{\omega(t)S(t)I(t)}{N\tau} - \gamma S(t), \tag{B.64}$$

then $\lim\limits_{t\to\infty} I(t) = 0$ implies that $\lim\limits_{t\to\infty} S(t) = N$. Therefore, $\lim\limits_{t\to\infty} R(t) = \lim\limits_{t\to\infty}(N - I(t) - S(t)) = 0$. ☐

Theorem B.3. *If* $\omega(t) \equiv \omega$, $\gamma(t) \equiv \gamma$ *and* $\beta = 1$ *in the system* (B.18)-(B.20)*, the endemic equilibrium of Eq.* (B.54) *is locally asymptotically stable whenever it is feasible, that is, when* $\omega > (\tau\gamma)^{1-\alpha} + (\tau\gamma)$.

Proof. We analyze the local stability of the endemic equilibrium by translating it to the origin and applying a general stability result for nonlinear Volterra integral equations. This requires verifying that the associated characteristic equation has no roots with non-negative real part.

With the hypotheses of the statement, Eq. (B.54) resumes to

$$S^* = \frac{((\tau\gamma)^{1-\alpha} + \tau\gamma)N}{\omega}, \qquad I^* = \frac{N(\tau\gamma)^{\alpha}}{1 + (\tau\gamma)^{\alpha}} - \frac{N\tau\gamma}{\omega}, \tag{B.65}$$

$$R^* = \frac{N}{1 + (\tau\gamma)^{\alpha}} - \frac{N(\tau\gamma)^{1-\alpha}}{\omega}. \tag{B.66}$$

Moreover, if $\beta = 1$ and ω is constant, then $\sigma(t) \equiv \omega/\tau$. We also have

$$\frac{N}{S^*} = \Re_0 = \int_0^\infty \sigma(t)\Phi(t,0)dt = \frac{\omega}{\tau}\int_0^\infty \Phi(t,0)dt = \frac{\omega}{(\tau\gamma)^{1-\alpha} + \tau\gamma}. \tag{B.67}$$

Thus,

$$\begin{aligned} I^* &= \left(\int_0^\infty \sigma(t')\Phi(t')dt' \cdot \frac{S^*}{N}\right) I^* = \int_0^\infty \Phi(t')\frac{S^*I^*\omega}{N\tau}dt' \\ &= \int_0^t \Phi(t-t')\frac{S^*I^*\omega}{N\tau}dt' + \int_t^\infty \Phi(t')\frac{S^*I^*\omega}{N\tau}dt'. \end{aligned} \tag{B.68}$$

Observe, from $F(t) = 1 - \phi(t)$ and $\phi(t)\theta(t,0) = \Phi(t,0)$, that

$$\int_0^\infty \frac{\omega}{\tau}F(t')\theta(t',0)dt' = \int_0^\infty \frac{\omega}{\tau}\theta(t',0)dt' - \int_0^\infty \frac{\omega}{\tau}\Phi(t')dt' \tag{B.69}$$

$$\begin{aligned} &= \frac{\omega}{\tau\gamma} - \frac{\omega}{(\tau\gamma)^{1-\alpha} + \tau\gamma} \\ &= (\tau\gamma)^{-\alpha}\int_0^\infty \frac{\omega}{\tau}\Phi(t')dt', \end{aligned} \tag{B.70}$$

i.e.,

$$\frac{N}{S^*} = (\tau\gamma)^{\alpha} \int_0^{\infty} \frac{\omega}{\tau} F(t')\theta(t', 0)dt'. \tag{B.71}$$

Returning to Eq. (B.65), we note that $R^* = (\tau\gamma)^{-\alpha} I^*$. So, we write

$$\begin{aligned} R^* &= ((\tau\gamma)^{-\alpha} I^*) \left((\tau\gamma)^{\alpha} \int_0^{\infty} \frac{\omega}{\tau} F(t')\theta(t', 0)dt' \cdot \frac{S^*}{N} \right) \\ &= \int_0^{\infty} F(t')\theta(t', 0) \frac{S^* I^* \omega}{N\tau} dt' \\ &= \int_0^{t} F(t - t')\theta(t, t') \frac{S^* I^* \omega}{N\tau} dt' + \int_t^{\infty} F(t')\theta(t', 0) \frac{S^* I^* \omega}{N\tau} dt'. \end{aligned} \tag{B.72}$$

We let $V = I - I^*$ and $W = R - R^*$ to translate the equilibrium to the origin. Then, by Eqs. (B.58), (B.59), (B.68), and (B.72), and observing that

$$SI - S^*I^* = S^*V - I^*(V + W) - V(V + W), \tag{B.73}$$

we get

$$\begin{aligned} &\begin{bmatrix} V \\ W \end{bmatrix} = \begin{bmatrix} f_1(t) \\ f_2(t) \end{bmatrix} + \\ &\int_0^t \begin{bmatrix} \Phi(t, t')\omega/N\tau & 0 \\ F(t - t')\theta(t, t')\omega/N\tau & 0 \end{bmatrix} \times \begin{bmatrix} (S^*V - I^*(V + W) - V(V + W))(t') \\ (V + W)(t') \end{bmatrix} dt', \end{aligned} \tag{B.74}$$

on with

$$\begin{bmatrix} f_1(t) \\ f_2(t) \end{bmatrix} = \begin{bmatrix} \Phi(t, 0)i_0 - \int_t^{\infty} \Phi(t') \frac{S^* I^* \omega}{N\tau} dt' \\ F(t)\theta(t, 0)i_0 - \int_t^{\infty} F(t')\theta(t', 0) \frac{S^* I^* \omega}{N\tau} dt' \end{bmatrix}. \tag{B.75}$$

The nonlinear Volterra integral system of Eq. (B.74) can be written in matrix form as:

$$X(t) = F(t) + \int_0^t A(t - t')G(X(t'))dt', \tag{B.76}$$

where

$$X = \begin{bmatrix} V \\ W \end{bmatrix}; F = \begin{bmatrix} f_1 \\ f_2 \end{bmatrix}; A = \begin{bmatrix} \Phi\omega/N\tau & 0 \\ F\theta\omega/N\tau & 0 \end{bmatrix}; \tag{B.77}$$

$$G(X) = \begin{bmatrix} S^*V - I^*(V + W) - V(V + W) \\ V + W \end{bmatrix}. \tag{B.78}$$

This allows us to apply stability results from (160). We write the following characteristic equation of the linearization of Eq. (B.76):

$$\det \left(\text{Identity} - \int_0^{\infty} e^{-\lambda t} B(t)dt \right) = 0, \tag{B.79}$$

where J is the Jacobian of G evaluated at 0:

$$J = \begin{bmatrix} S^* - I^* - 2V & -I^* - V \\ 1 & 1 \end{bmatrix}_{V=W=0} = \begin{bmatrix} S^* - I^* & -I^* \\ 1 & 1 \end{bmatrix}, \tag{B.80}$$

and $B(t) = A(t)J$.

The stability analysis of the origin uses a result cited in (160): *If the solutions of Eq.* (B.76) *exist in* $[0,\infty)$ *and are bounded,* $F(t) \in C[0,\infty)$*,* $F(t) \to 0$ *when* $t \to \infty$*,* $A(t) \in L^1[0,\infty)$*,* $G(X) \in C^1(\mathbb{R}^2)$*,* $G(0) = 0$*,* J *is non-singular and Eq.* (B.79) *does not have roots with non-negative real parts, then the origin is a locally asymptotically stable equilibrium.*

Most of the conditions are straightforward. In particular, $F(t) \to 0$ due to the existence of the Laplace transform of the Mittag-Leffler function. We need to prove that there are no characteristic roots of Eq. (B.79) with a non-negative real part.

Since the second column of $A(t)$ is zero, $A(t)$ has rank one, and therefore $B(t) = A(t)J$ also has rank one, and can be decomposed in an outer product. Note that:

$$M(\lambda) := \int_0^\infty e^{-\lambda t} B(t) dt = \left(\int_0^\infty e^{-\lambda t} \begin{bmatrix} \Phi\omega/N\tau \\ F\theta\omega/N\tau \end{bmatrix} (t) dt \right) \begin{bmatrix} S^* - I^* & -I^* \end{bmatrix}. \tag{B.81}$$

Then, using the identity for rank-one matrices $\det(I - uv^T) = 1 - v^T u$, we obtain:

$$\det\left(\text{Identity} - M(\lambda)\right) = 1 - \begin{bmatrix} S^* - I^* & -I^* \end{bmatrix} \left(\int_0^\infty e^{-\lambda t} \begin{bmatrix} \Phi\omega/N\tau \\ F\theta\omega/N\tau \end{bmatrix} (t) dt \right). \tag{B.82}$$

Substituting the expressions of $\Phi(t,0)$ and $\theta(t,0)$, we obtain the scalar characteristic equation:

$$1 - \int_0^\infty e^{-\lambda t} e^{-\gamma t} (1 - F(t)) S^* \frac{\omega}{N\tau} dt + \int_0^\infty e^{-\lambda t} e^{-\gamma t} I^* \frac{\omega}{N\tau} dt = 0. \tag{B.83}$$

The condition $\omega > (\tau\gamma)^{1-\alpha} + (\tau\gamma)$ is equivalent to

$$\Re_0 = \frac{N}{S^*} = \int_0^\infty \Phi(t,0) \frac{\omega}{\tau} dt = \int_0^\infty e^{-\gamma t} (1 - F(t)) \frac{\omega}{\tau} dt > 1. \tag{B.84}$$

Suppose, by contradiction, that $\mathrm{Re}(\lambda) \geq 0$, then

$$\int_0^\infty e^{-\gamma t} (1 - F(t)) \frac{\omega}{\tau} dt = \frac{N}{S^*} > \mathrm{Re}\left(\int_0^\infty e^{-\lambda t} e^{-\gamma t} (1 - F(t)) \frac{\omega}{\tau} dt \right). \tag{B.85}$$

Thus,

$$1 > \mathrm{Re}\left(\int_0^\infty e^{-\lambda t} e^{-\gamma t} (1 - F(t)) S^* \frac{\omega}{N\tau} dt \right). \tag{B.86}$$

For Eq. (B.83) to hold, it must be that

$$\mathrm{Re}\left(\int_0^\infty e^{-\lambda t} e^{-\gamma t} I^* \frac{\omega}{N\tau} dt \right) < 0. \tag{B.87}$$

However, if $\mathrm{Re}(\lambda) > -\gamma$, we have

$$\int_0^\infty e^{-\lambda t} e^{-\gamma t} I^* \frac{\omega}{N\tau} dt = \frac{\omega I^*}{(\lambda+\gamma)N\tau}. \tag{B.88}$$

Since $\lambda = a + bi$ with $a \geq 0$, we have

$$\frac{\omega I^*}{(\lambda+\gamma)N\tau} = \frac{\omega I^*}{N\tau} \cdot \frac{1}{(a+\gamma)+bi} \cdot \frac{(a+\gamma)-bi}{(a+\gamma)-bi} = \frac{\omega I^*}{N\tau} \cdot \frac{(a+\gamma)-bi}{(a+\gamma)^2+b^2}, \tag{B.89}$$

following that

$$\mathrm{Re}\left(\frac{\omega I^*}{(\lambda+\gamma)N\tau}\right) = \frac{\omega I^*(a+\gamma)}{N\tau((a+\gamma)^2+b^2)} > 0, \tag{B.90}$$

a contradiction with Eq. (B.87). Therefore, the characteristic equation has no roots with non-negative real part. By the cited result, the origin is locally asymptotically stable, and thus the endemic equilibrium (S^*, I^*, R^*) is locally asymptotically stable. □

We hypothesize that the region with $i_0 > 0$ is a region of attraction for (S^*, I^*, R^*), even for $\beta < 1$. Figures B.3 and B.4 illustrate Theorems B.2 and B.3, with different initial conditions and $\beta < 1$.

Furthermore, a recent study by (73) provides a global analysis of the equilibria of an SIS model related to the model in equations (B.18)-(B.20) with $\beta = 1$, with the main difference being the existence of an input depending on I in the S compartment. Their geometric approach to global stability problems may extend the results of Theorem B.3 globally, although this extension is not straightforward. Also, (73) uses an approximation for the fractional derivative of I that needs to be further explored in the case of the SIR model. More general memory kernels, such as those described in Chapters 3-5 using gamma Mittag-Leffler distributions, provide opportunities for generalizing the model to several types of diseases.

C APPENDIX C – ADDITIONAL RESULTS AND DISCUSSIONS FOR CHAPTER 3

In this appendix, we offer further discussions related to Chapter 3, including integro-differential asymptotic results, a concise parametric study of the gamma Mittag-Leffler PDF, key features and distinctions of the general approach compared to classical models, and some extensions.

C.1 INTEGRO-DIFFERENTIAL ASYMPTOTIC RESULTS

The logistic model with gamma Mittag-Leffler distributed delays is given by:

$$\begin{cases} y' = ry(1 - Ce^{-at}D^{1-\beta}(e^{at}w)), \\ w' = y - \lambda e^{-at}D^{1-\alpha}(e^{at}w) - aw. \end{cases} \tag{C.1}$$

As cited before, in FDEs, stability conditions are not intuitively related to classical integer-order results due to nonlocality and other intrinsic features. For instance, the Barbalat's Lemma states that, if the uniformly continuous nonnegative function $f(t)$ in $[0, \infty]$ is such that $\int_0^t f(\tau)d\tau < C$, for some constant C and all $t > 0$, then $f(t) \to 0$ when $t \to \infty$. It is often used in Lyapunov's theory, but is not trivial in FDEs (144).

Moreover, in Eq. (3.4), the equations involve two orders of derivatives: 1 (classical) and $1 - \alpha$ (or $1 - \beta$). Therefore, there are many difficulties regarding classical equilibrium analysis.

Some progress can be made with integro-differential theory. In fact, following (16), **the integro-differential equation in Eq.** (3.1) **has a unique positive equilibrium given by** $y^* = 1$**.** This aligns with the main text. The work (16) also proved that for the Erlang PDF kernel $Ct^{\beta-1}e^{-at}$ with $\beta = 2$, the equilibrium $y^* = 1$ is locally asymptotically stable with relatively short delays when the mean μ is such that $\mu < 4/r$. Recall from Eq. (3.1) that r is the speed of dynamics. The equilibrium is unstable for "long" delays, that is, $\mu > 4/r$.

In general, if μ is the finite mean of a gamma Mittag-Leffler distribution with respect to the memory kernel $\kappa(t)$ in Eq. (3.1), an adaptation of the theory from (16) provides the following result: **The equilibrium** $y^* = 1$ **is locally asymptotically stable if** $r\mu$ **is sufficiently small.**

Note that this result cannot be stated if μ is infinite, as in the case of the Mittag-Leffler distributed delays model Eq. (3.20). Another fundamental point is that $y^* = 1$ is not necessarily unstable for "long" delays. For example, this does not happen in the case of the weak memory kernel $\kappa(t) = Ce^{-at}$. The perspective adopted by (16), and encompassed by the generalized kernel and fractional formulations developed here, is that delays in the response of a species' growth rate tend to destabilize the dynamics. This destabilization may manifest as sustained oscillations or as a slower convergence to equilibrium for larger values of μ. In this context, the fractional case—whose mean waiting time is infinite—naturally exhibits a very slow approach to equilibrium, as illustrated in Figures 3.1B and C.17.

C.2 STUDY OF THE GAMMA MITTAG-LEFFLER PDF KERNEL

In this section, we discuss how the parameters α, β, a, and λ affect the memory kernel described in Eq. (3.2).

Figure C.1A-B shows how α and β affect the memory kernel for $a = 0.012$ and $\lambda = 0.15 \cdot a$, which are chosen from simulations of the fractional FHN model (see Section 5.2). To analyze the effect of α in Figure C.1A, we keep β constant at 0.95. Decreasing α causes the kernel to decrease more rapidly in its initial stages, while slightly increasing the weight of the right tail. Conversely, to investigate the influence of β in Figure C.1B, we fix α at 0.7. As β increases within the specified time range, the kernel exhibits lower values at earlier times, with the right tail becoming more prominent. The kernels exhibit a singularity at time 0 when β is less than 1. Note that, with the time range and the set of parameters considered, the fractional order β has a more significant impact on the memory kernel.

On the other hand, Figure C.1C-D discusses how a and λ impact the memory kernel (3.2) for $\alpha = 0.7$ and $\beta = 0.95$. To analyze the effect of a in Figure C.1C, we keep λ constant at 0.0018. In the time interval of interest, as a decreases, the early stages of the kernel have smaller values, but the decay is slower. To analyze the effect of λ, we keep a constant at 0.012. Figure C.1D shows that λ affects the kernel in a similar way to a, but with less intensity. The parameters a and λ relate to the velocity of the model and can be understood as a type of time constant.

Finally, Figure C.1E-F discusses how α and β impact the memory kernel (3.2) for a strong kernel, with $\beta > 1$. Reducing the value of α results in a lower peak but a wider distribution with a slightly heavier tail on the right. Decreasing β brings the kernel closer to the origin.

C.3 WHAT IS GAINED?

As observed in the development of the model, Eq. (3.4) encompasses gamma- and Mittag-Leffler-distributed delays, ODE systems based on Erlang PDF kernels, and, in the limit, the classical logistic model and the DDE. This framework enables the consideration of the characteristics of each of these memory kernels in a unified manner, while also extending and combining some of these properties.

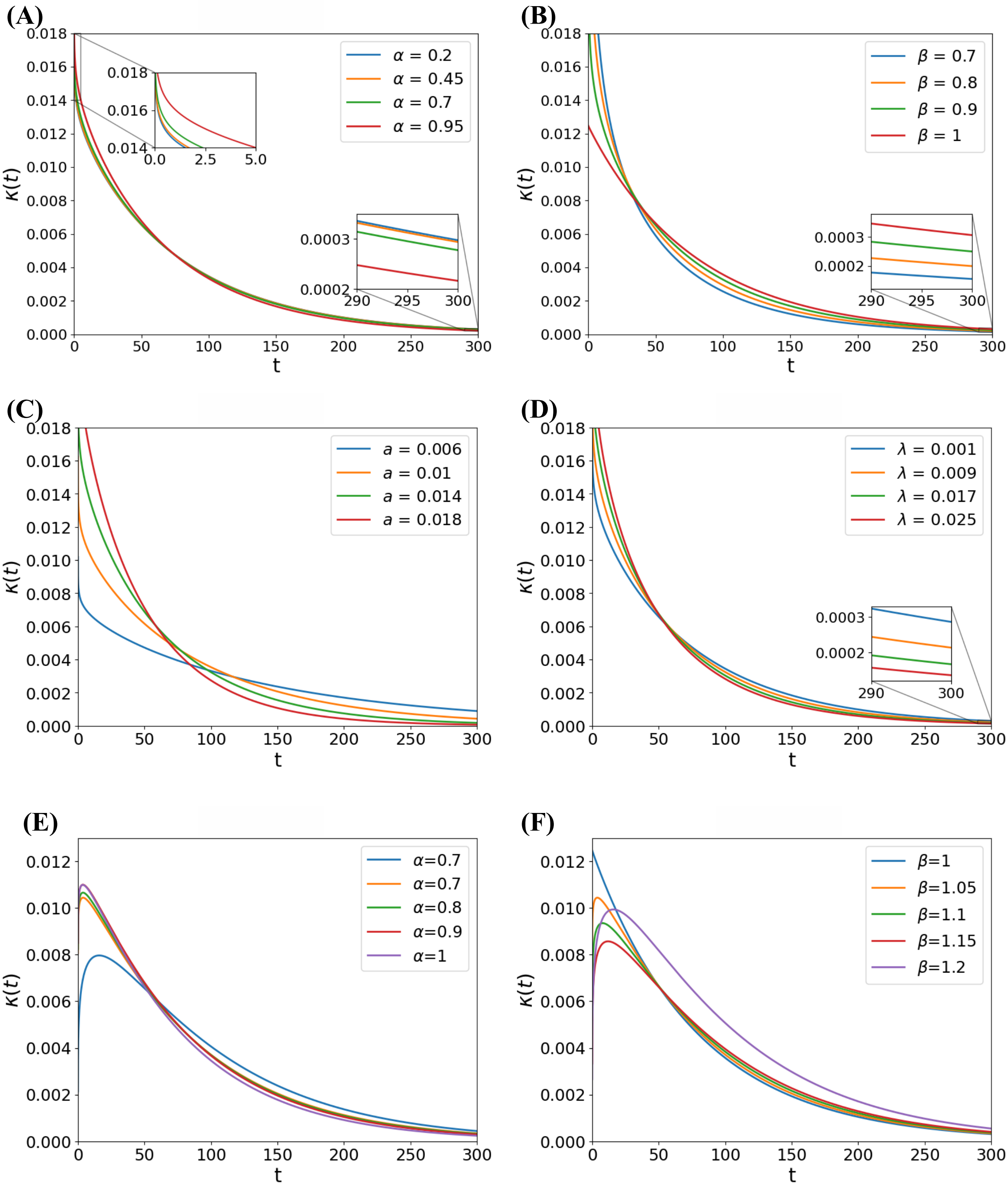

Figure C.1 – For panels **(A)-(D)**, we fix three of the four parameters: $\alpha = 0.7$, $\beta = 0.95$, $a = 0.012$, and $\lambda = 0.0018$. We consider $\beta = 1.2$ in panel **(E)** and $\alpha = 0.7$ in panel **(F)**. In the specified time interval: (**A**) Effect of α: Decreasing α leads to a faster decrease in the kernel at the beginning, with a slightly heavier right tail. **(B)** Effect of β: Increasing β results in smaller values in the early moments of the kernel, with a heavier right tail. **(C)** Effect of a: Decreasing a causes smaller values in the early stages of the kernel but a slower decay. **(D)** Effect of λ: It affects the kernel similarly to a, but with less impact within our range of study. **(E)** Effect of α - Strong kernels: Decreasing α leads to a smaller peak, although more spread out with a slightly heavier right tail. **(F)** Effect of β - Strong kernels: Decreasing β causes the kernel to shift towards the origin.

C.3.1 Extending and flexing features

Figures C.2a to C.2b illustrate an extension of the logistic response for Erlang PDF kernel with a mean of $\mu = 1$. The Erlang PDF is independent of α, with $\beta = a \in \mathbb{N}$ and $\lambda = 0$. In Figures C.2a to C.2b, we allow β to vary from 1 to 4, varying a from $\beta - 0.5$ to $\beta + 2$, α from 1 to 4, and λ such that the mean is maintained equal to 1.

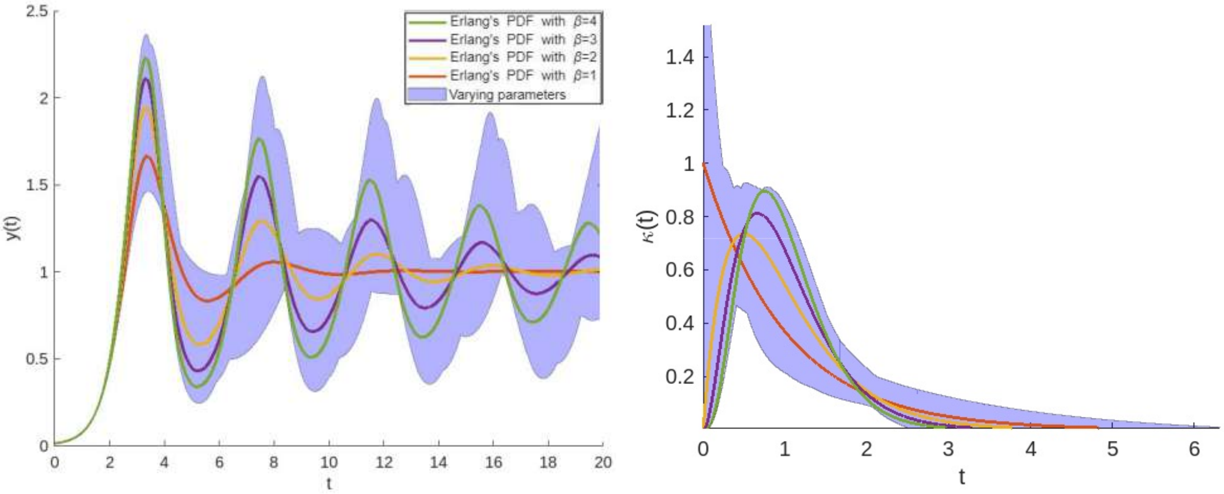

(a) Logistic responses.

(b) Erlang PDF kernels.

Figure C.2 – The extension of the logistic response for Erlang PDF kernels.

The extension characterizes singular kernels when $\beta = 1$, as well as heavier right tails. It enables increasing overshoot and minimum after overshoot in the responses, along with peak translation. In general, the inclusion of fractional orders α and β, together with parameter combinations, allows for a fine-grained representation of real-world data features.

C.3.2 Linking features

The general framework clarifies the transition of kernel properties. For instance, diagram C.3 illustrates how one can transition between a Mittag-Leffler-distributed delayed model and an ODE system through generalizations allowed by the memory kernel (3.2).

Figure C.4 shows an example of how to transition between a Mittag-Leffler-distributed delayed model with $\alpha = \beta = 0.8$ and $\lambda = 0.5$ to an ODE system generated by an Erlang PDFs memory kernel with $\beta = a = 2$.

C.3.3 Combining features

In Figure 3.3.B, the fit to Brazil's COVID-19 data shows a singular, but non-monotonic memory kernel. This kernel combines the features of Mittag-Leffler and Erlang PDF kernels with the presence of a singularity, Mittag-Leffler type decay, and a peak. This occurs due to the different velocities of factors e^{-at} (exponential decay)

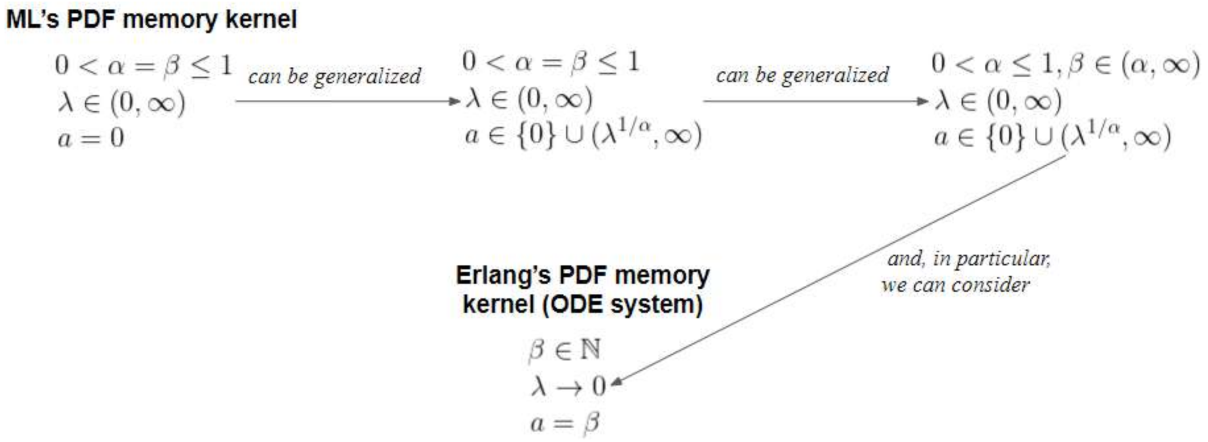

Figure C.3 – Scheme illustrating the transition between a Mittag-Leffler-distributed delayed model and an ODE system through generalizations enabled by the memory kernel in Eq. (3.2).

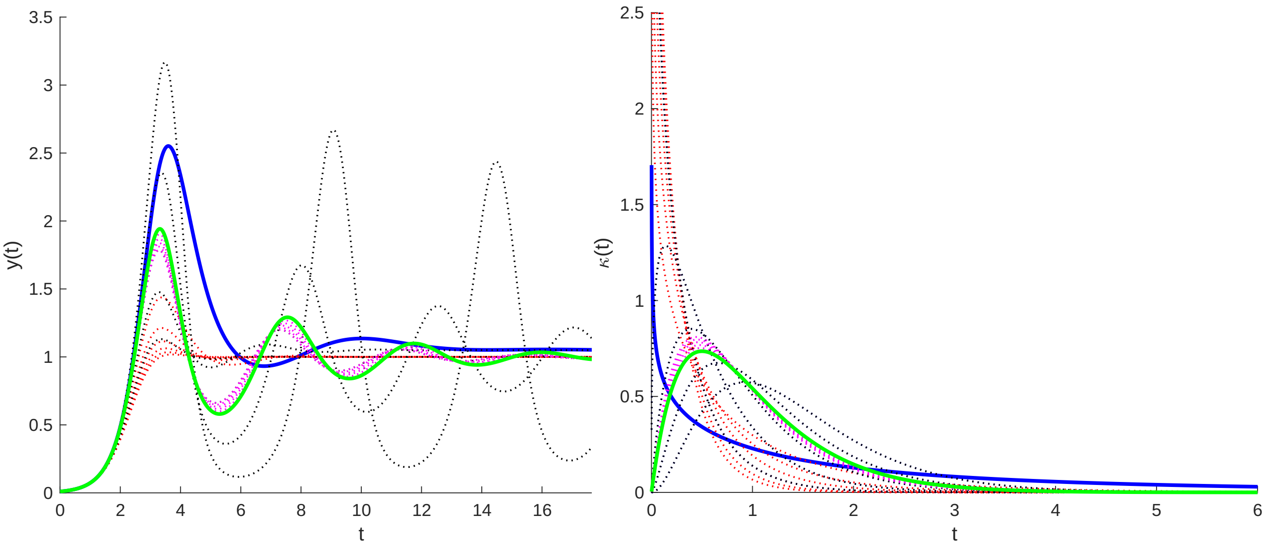

(a) Logistic response transition. (b) Memory kernel transition.

Figure C.4 – In blue, the ML's PDF response and kernels with $\alpha = \beta = 0.8$ and $\lambda = 0.5$. The red dotted lines illustrate the first generalization, with a ranging from 0.5 to 3. The black dotted lines show curves obtained with the second generalization, with β ranging from 0.8 to 3, and $a = 2$. The magenta dotted lines represent $\lambda \to 0$ when $a = \beta = 2$, and the solid green curves correspond to Erlang PDF response and kernel with $\beta = 2$.

and $E_{\alpha,\beta}(-\lambda t)$ (Mittag-Leffler growth when $\lambda < 0$), which can induce oscillations in the product $e^{-at}E_{\alpha,\beta}(-\lambda t)$, as shown in Figure C.5.

In fact, singular non-monotonic kernels (see Figure C.6 for $a = 3$, $\beta = 0.1$, and mean $\mu = 1$) and strong kernels with more than one peak (see Figure C.7a-C.7b for $\alpha = 20$, $a = 5$, and mean $\mu = 1$) are possible with the general kernel (3.2). This behavior cannot be achieved with Mittag-Leffler distributed delays, DDE models, or ODE models.

We notice this behavior, in general, when α is large. These oscillations can be

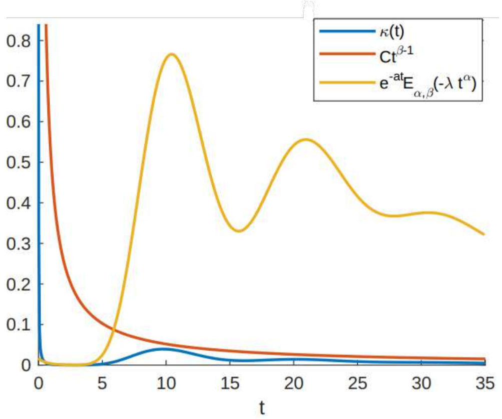

Figure C.5 – Kernel for fitting Brazil's COVID-19 data: $\kappa(t) = Ct^{\beta-1}e^{-at}E_{\alpha,\beta}(-\lambda t^{\alpha})$.

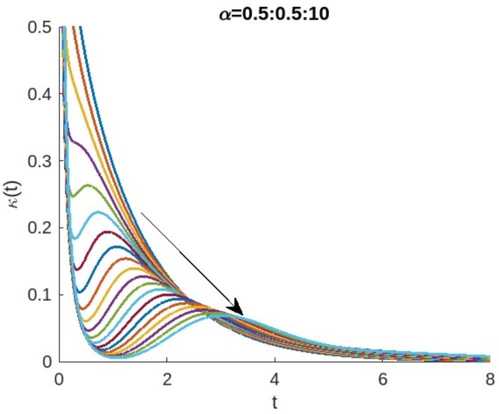

Figure C.6 – Weak nonmonotonic kernels. The arrow indicates the direction of growth of α.

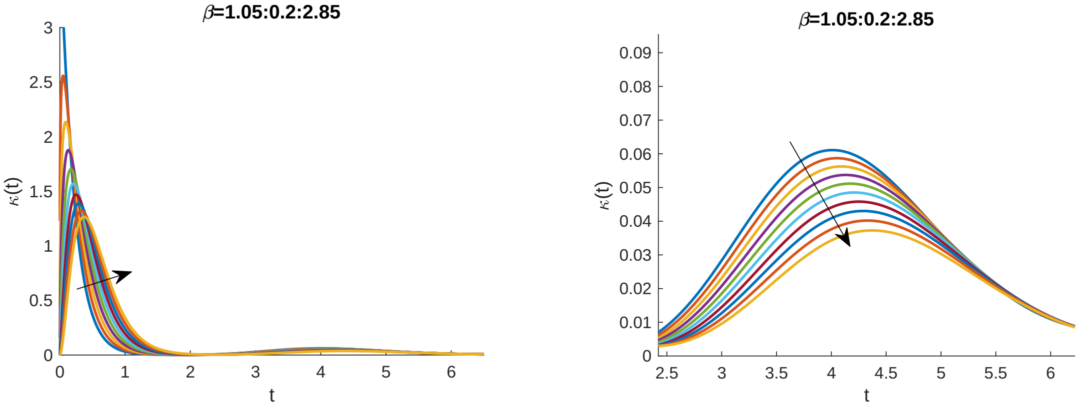

(a) Strong kernels with more than one peak.

(b) Zoom in Fig C.7a.

Figure C.7 – Strong kernels with more than one peak. The arrow indicates the growth direction of β.

understood by analyzing the Mittag-Leffler series (1.11). Note that:

$$\kappa(t) = Ct^{\beta-1}e^{-at}E_{\alpha,\beta}(-\lambda t^{\alpha}) = Ct^{\beta-1}e^{-at}\sum_{k=0}^{\infty}\frac{(-\lambda)^k t^{\alpha k}}{\Gamma(\alpha k+\beta)}$$

$$= Ce^{-at}\sum_{k=0}^{\infty}\frac{(-\lambda)^k t^{\alpha k+\beta-1}}{\Gamma(\alpha k+\beta)}. \tag{C.2}$$

For $a > 0$, each term $\dfrac{e^{-at}t^{\alpha k+\beta-1}}{\Gamma(\alpha k+\beta)}$ is proportional to the PDF of a gamma distribution with mean $(\alpha k+\beta)/a$, mode equal to 0 if $\alpha k+\beta < 1$, and mean $(\alpha k+\beta-1)/a$ if $\alpha k+\beta \geq 1$, and variance $(\alpha k+\beta)/a^2$. When $\lambda < 0$, $\kappa(t)$ is the sum of scaled gamma PDFs $\kappa_k(t)$, for $k = 0, 1, \ldots$, defined as:

$$\kappa_k(t) = \frac{C|\lambda|^k e^{-at}t^{\alpha k+\beta-1}}{\Gamma(\alpha k+\beta)}. \tag{C.3}$$

When α is large and a is relatively small, the distance α/a between successive modes is large compared to the standard deviation $\sqrt{\alpha k+\beta}/a$ of κ_k for small k. In this case, different peaks can appear in the sum, as illustrated in Figure C.8-C.9.

According to the second hypothesis of the gamma Mittag–Leffler distribution (3.2), if $\alpha > 1$, the parameter λ must satisfy $-a^\alpha < \lambda \leq 0$. If $\mu = 1$, this requires $\beta < a$. Therefore, β must be small for different peaks to appear in general kernels. In Figure C.10, we present a multimodal kernel with mean $\mu = 15.475$.

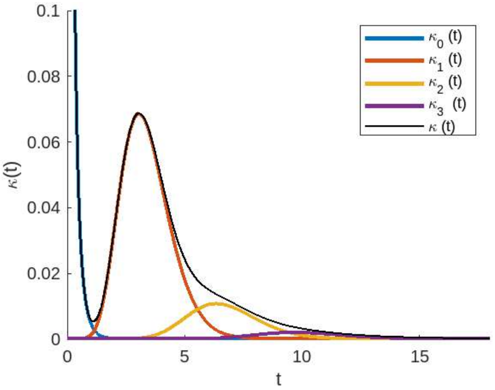

Figure C.8 – Memory kernel Eq. (3.2) and contributions Eq. (C.3) for $a = 3$, $\alpha = 10$, $\beta = 0.1$, and mean $\mu = 1$.

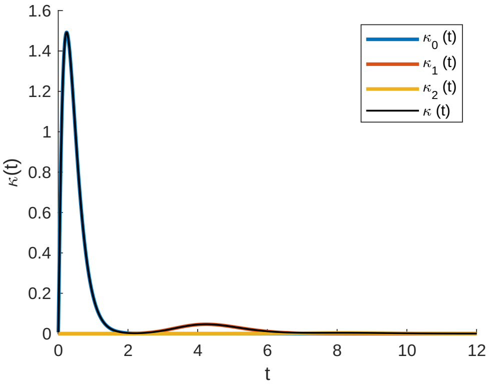

Figure C.9 – Memory kernel Eq. (3.2) and contributions Eq. (C.3) for $a = 5$, $\alpha = 20$, $\beta = 2.2$, and mean $\mu = 1$.

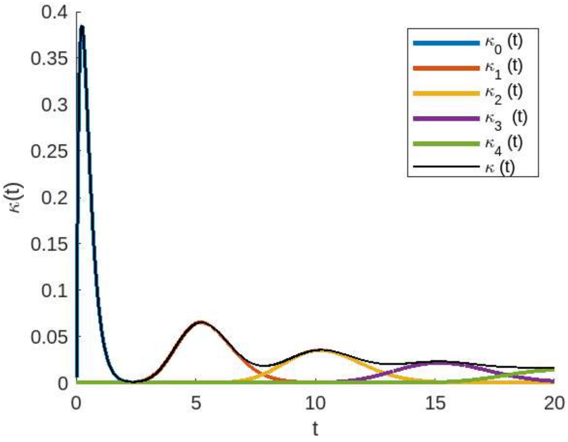

Figure C.10 – Memory kernel Eq. (3.2) and contributions Eq. (C.3), for $a = 4, \alpha = 20, \beta = 1.9, \lambda = -3 \cdot 4^{19}$.

When $\alpha \leq 1$, we can have $0 \leq \lambda < a^\alpha$. Then, the series (C.2) becomes alternating in sign. Examples are shown in Figure C.11, for a weak memory case, and in Figure C.12, for a strong memory case. In these cases, we do not obtain multimodality.

When $a = 0$, $\alpha = \beta$, and $\lambda > 0$, we have a Mittag-Leffler PDF, in which

$$\kappa(t) = Ct^{\alpha-1}E_{\alpha,\alpha}(-\lambda t^\alpha) = C\sum_{k=0}^{\infty}\frac{(-\lambda)^k t^{\alpha(k+1)-1}}{\Gamma(\alpha(k+1))}. \tag{C.4}$$

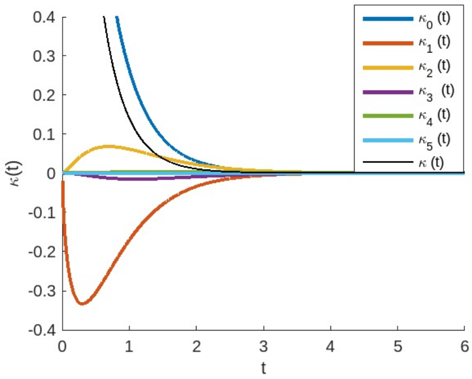

Figure C.11 – Memory kernel (3.2) and contributions (C.3) for $a = 2$, $\alpha = \beta = 0.8$, and $\lambda = 0.5$.

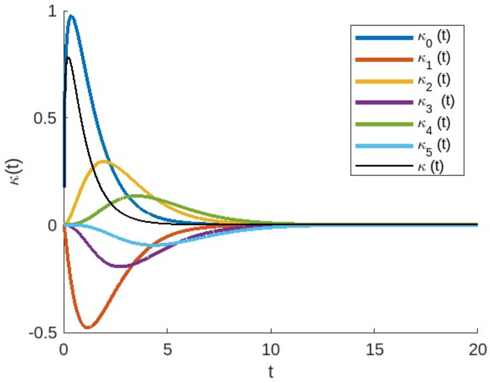

Figure C.12 – Memory kernel (3.2) and contributions (C.3) for $a = 1$, $\alpha = 0.8$, $\beta = 1.35$, and mean $\mu = 1$.

In this case, $\kappa(t)$ is a weighted sum of power functions of t:

$$\kappa_k(t) = \frac{C(-\lambda)^k t^{\alpha(k+1)-1}}{\Gamma(\alpha(k+1))}. \tag{C.5}$$

When $\alpha = 1$, Eq. (C.2) represents the Taylor series for $e^{-\lambda t}$. Figures C.13a-C.13b illustrate the kernels Eq. (C.5) and the partial sums $k_0 + \cdots + k_n$ up to $n = 6$.

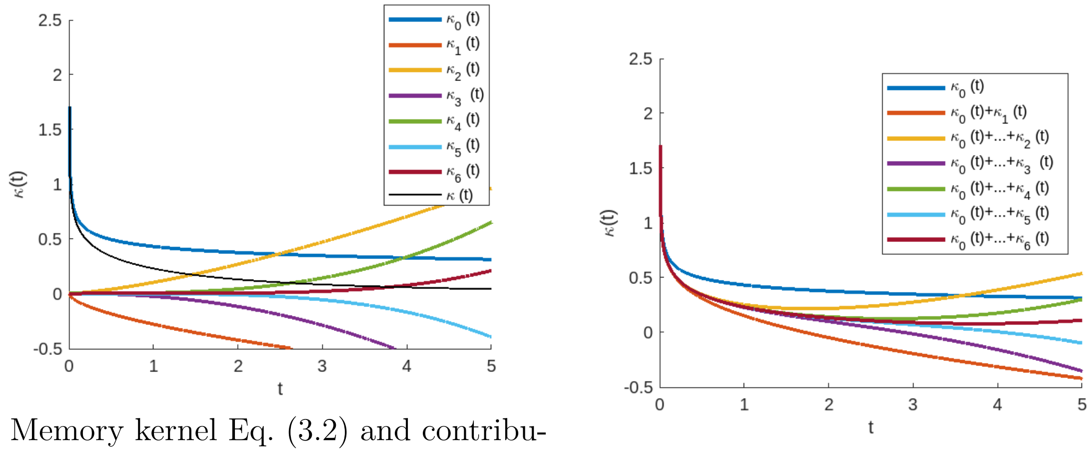

(a) Memory kernel Eq. (3.2) and contributions Eq. (C.5).

(b) Partial sums $k_0 + \cdots + k_n$.

Figure C.13 – Memory kernel (3.2) and contributions (C.5) for $a = 0$, $\alpha = \beta = 0.8$, and $\lambda = 0.5$. The Mittag-Leffler PDF memory kernel is monotonic (4), *i.e.*, it does not exhibit oscillations.

An illustrative map of the classification of kernels is shown in Figure 3.2. In the following subsections, we explore specific dynamics and examples that are useful for better understanding the model parameters and their application in real-world problems.

C.3.4 ODE system

The PDF of the Erlang distribution is obtained by setting $\lambda = 0$ and $\beta \in \mathbb{N}^*$. In this case, $C = a^\beta$. Then, for each $\beta \in \mathbb{N}$ and respective $a = a_\beta$, the memory kernel is given by:

$$\kappa_\beta(t) = \frac{(a_\beta)^\beta\, t^{\beta-1} e^{-a_\beta t}}{(\beta-1)!}, \tag{C.6}$$

where a_β is chosen depending on β. The mean is given by $\mu = \beta/a_\beta$. In Figures C.14a-C.14b, we maintain $\mu = 1$, so $a_\beta = \beta$. The number of ODEs of the logistic framework is determined by $\beta + 1$, as discussed. The equilibrium $y^* = 1$ is illustrated in Figures C.14a and C.15a.

For $\beta = 1$, this is equivalent to considering exponentially distributed delays. However, for $\beta > 1$, a bell-shaped kernel becomes increasingly peaked as β increases. The presence of delays implies overshoot, and, according to Figure C.14a, the amplitude and quantity of oscillations in the solution increase as β increases. In fact, as discussed in the main text, the variance increases as β increases, and long delays lead to instabilities.

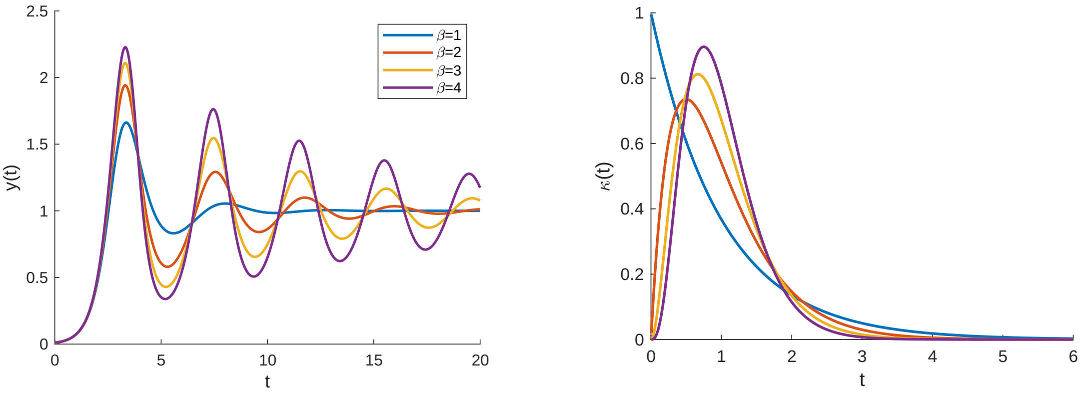

(a) Logistic responses.

(b) Erlang kernels.

Figure C.14 – Logistic responses to memory kernels $(\beta^\beta t^{\beta-1} e^{-\beta t})/(\beta-1)!$ varying β.

Next, in Figure C.15b, we present kernels varying the mean of the distribution for $\beta = 2$. The values $a = 0.6$ to $a = 1.4$ correspond to means $\mu = 3.33$ to $\mu = 1.43$, respectively. Note that the kernels are squeezed to the left when a increases because the mean of the distribution decreases. This diminishes the overshoot and subsequent oscillations, as shown in Figure C.15a. As stated by (16), the equilibrium $y^* = 1$ is locally asymptotically stable with relatively short delays, when the average μ is such that $\mu < 4/r = 2$, while it is unstable for “long” delays, that is, $\mu > 4/r = 2$.

C.3.5 DDE

The classical case is obtained from Eq. (3.4) by setting $\alpha = \beta = 1$ and $\lambda = 0$, in the limiting case where $C = a \to \infty$. The simple DDE case is obtained from Eq. (3.4) by setting $\beta \in \mathbb{N}^*$ and $\lambda = 0$, in the limiting case where $\beta = a \to \infty$, as the kernel approaches δ_μ with $\mu > 0$. The delay parameter μ introduces oscillations, and there is a threshold for μ above which the population exhibits periodic behavior. Figure C.16a illustrates the increasing overshoots and number of oscillations as μ increases, leading to periodic

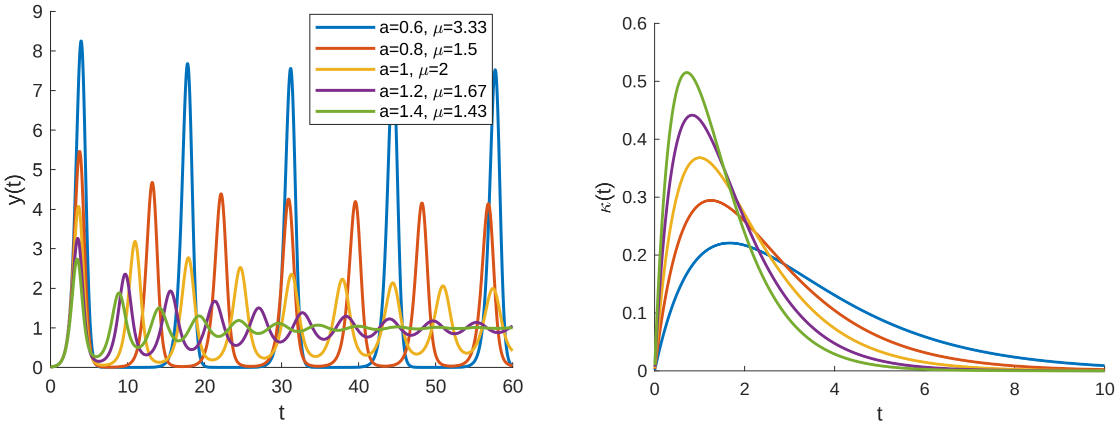

(a) Logistic responses.

(b) Erlang kernels.

Figure C.15 – Logistic responses to memory kernels a^2te^{-at} varying a.

behavior. In Figure C.16b, we show δ_μ for different μ values, representing the mean. For $\mu = 0$, there is no delay, corresponding to the classical case of the logistic model.

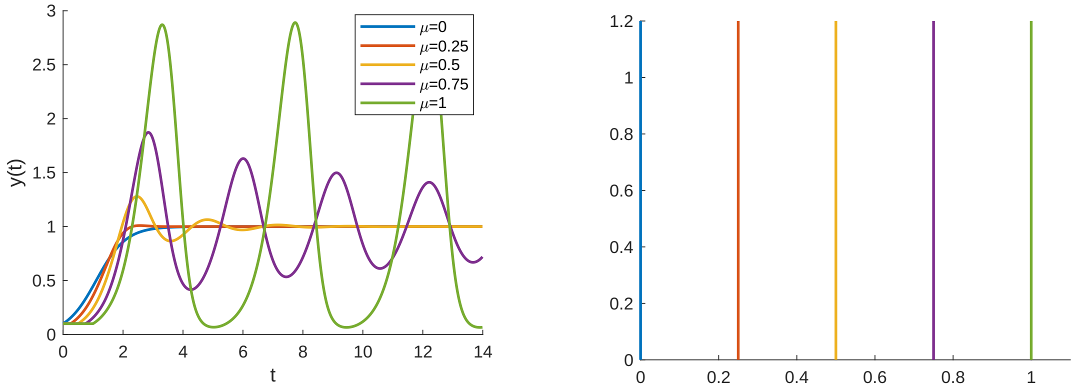

(a) Logistic responses.

(b) Kernels δ_μ varying μ.

Figure C.16 – Logistic response to δ_μ memory kernels, varying the delay μ.

C.3.6 Fractional systems

By choosing $\lambda > 0$, $0 < \alpha = \beta \leq 1$, and $a = 0$, we can consider the logistic model with Mittag-Leffler distributed delays. In Figures C.17a and C.17b, we observe the impact of the order α for $\lambda = 1$. In this case, there is no finite mean. For all values of α, the kernel shows that the population growth rate is primarily influenced by the present, with a decreasing influence from the past. The order α signifies the extent of influence from the recent past: smaller α values emphasize recent history more prominently (above the exponential), with a rapid decrease in influence up to a certain point (below the exponential). However, the influence persists for longer durations due to the denser right tail associated with smaller α values. Despite the singularity at 0 for $\alpha < 1$, the integral of the kernel remains equal to 1 as it is a PDF. This preserves the key characteristics of logistic behavior, such as equilibria. Nevertheless, the convergence to the limit is slow due to the heavy right tail.

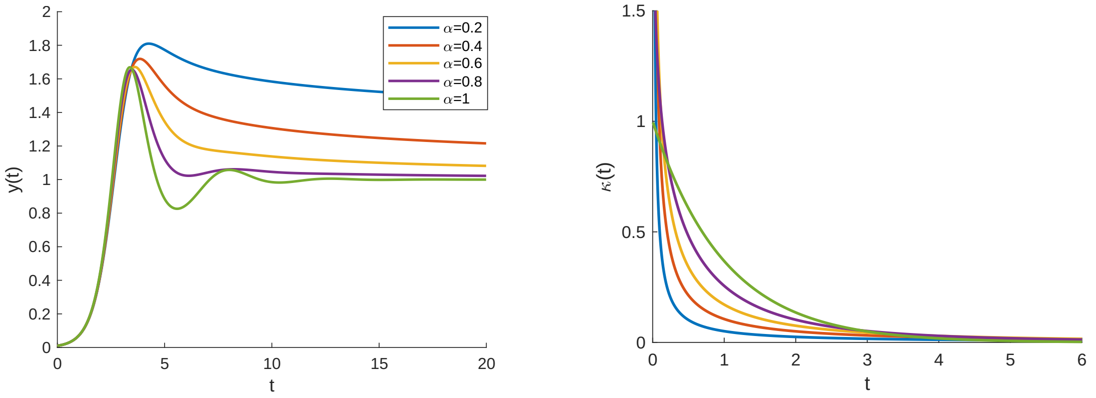

(a) Logistic responses.

(b) Mittag-Leffler PDF kernels.

Figure C.17 – Logistic responses to memory kernels $Ct^{\alpha-1}e^{-at}E_{\alpha,\alpha}(-\lambda t^{\alpha})$, for $\lambda = 1$, varying α.

Next, we consider the case where $-a^{\alpha} < \lambda \leq 0$, $a > 0$, and $\alpha, \beta > 0$ in the kernel given in Eq. (3.2). In the first scenario, we set $\alpha = 0.1$ and $a = 3$, while varying β. In these simulations, we keep the mean $\mu = 1$, so λ is recalculated as $\lambda = a^{\alpha}(a-\beta)/(\beta-\alpha-a)$ when β changes. We explore different values of β ranging from 1.8 to 3, resulting in several strong memory kernels, as illustrated in Figure C.18b. This shift in the distribution's mode from the current to another point leads to increased overshoot and oscillatory behavior, as depicted in Figure C.18a.

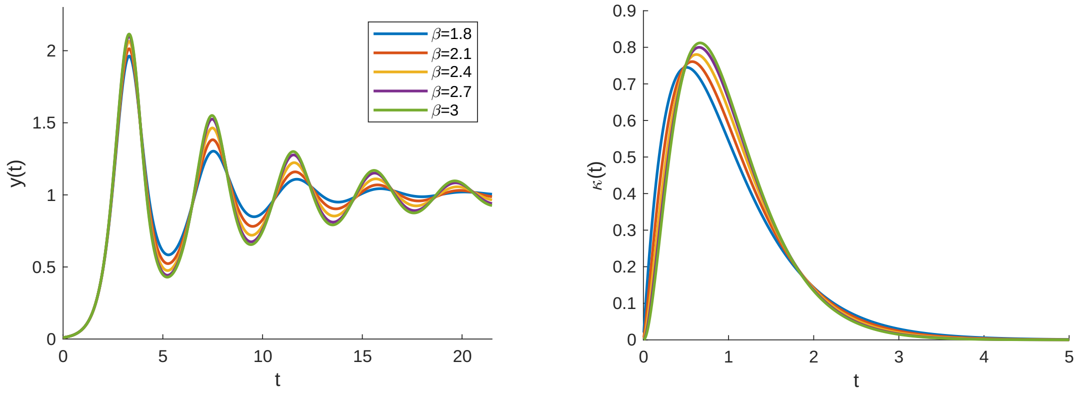

(a) Logistic responses.

(b) General kernels.

Figure C.18 – Logistic responses with kernels $Ct^{\beta-1}e^{-at}E_{\alpha,\beta}(-\lambda t^{\alpha})$, mean $\mu = 1$, $a = 3$ and $\alpha = 0.1$. The values of β and λ to investigate their impact on the responses.

Then, we consider $\alpha = 0.8$, $a = 3$, and vary β. The mean $\mu = 1$ is maintained, so λ is recalculated as $\lambda = a^{\alpha}(a-\beta)/(\beta-\alpha-a)$. We vary β from 0.35 to 0.95, as shown in Figure C.19b. The effect is similar to that of the Mittag-Leffler distributed delays case, but in this case, we have a finite mean and a faster approach to equilibrium.

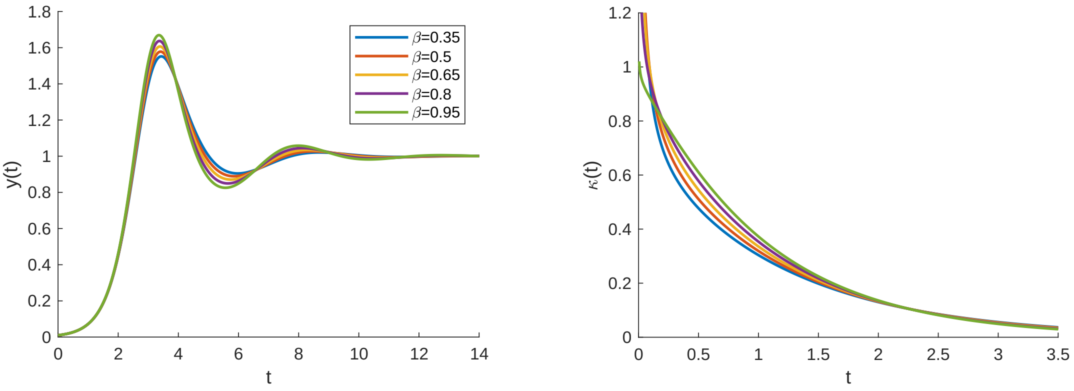

(a) Logistic responses.

(b) General kernels.

Figure C.19 – Logistic responses with kernels $Ct^{\beta-1}e^{-at}E_{\alpha,\beta}(-\lambda t^{\alpha})$, with $\mu = 1$, $a = 3$, and $\alpha = 0.8$. The parameters β and λ are varied to investigate their impact on the response.

As stated, an adaptation of the theory from (16) shows that the equilibrium $y^* = 1$ is locally asymptotically stable if $r\mu$ is sufficiently small. On the other hand, increasing $r\mu$ may not lead to instability. For instance, if $\kappa(t)$ has a finite mean and is monotonically decreasing, the maximum response of the growth rate to density changes is instantaneous, while the delayed response to past population densities is monotonically decreasing, and instability may not occur (16). In Figure C.20a and C.20b, we keep $\mu = 1$ and vary r in the last two simulations, with $a = 3, \alpha = 0.1, \beta = 2.5$, and $a = 3, \alpha = 0.8, \beta = 0.5$. Observe that increasing $r\mu$ in the first case destabilizes the equilibrium, but not in the last case.

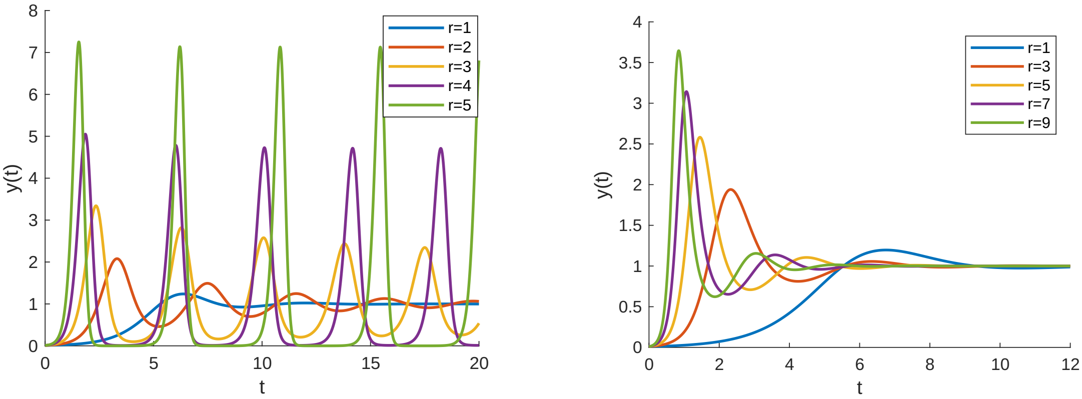

(a) Varying $r\mu$, by increasing r.

(b) Varying $r\mu$, by increasing r.

Figure C.20 – The destabilizing effect of increasing $r\mu$ is observed when $\kappa(t)$ is not monotonic. The models are simulated with $a = 3$, $\alpha = 0.1$, $\beta = 2.5$, and $a = 3$, $\alpha = 0.8$, $\beta = 0.5$, respectively.

Finally, we consider $\alpha = 5.5$, $a = 2$, and vary β, while maintaining a mean $\mu = 1$ by varying λ for each β. We vary β from 0.1 to 0.9, as shown in Figure C.21b. Unlike the Mittag-Leffler-distributed delayed case, the kernels in this scenario are non-monotonic, even with mode zero, as discussed in Section C.3. In Figure C.21a, observe that there is no considerable minimum after overshoot in this case, but the equilibrium is quickly approximated.

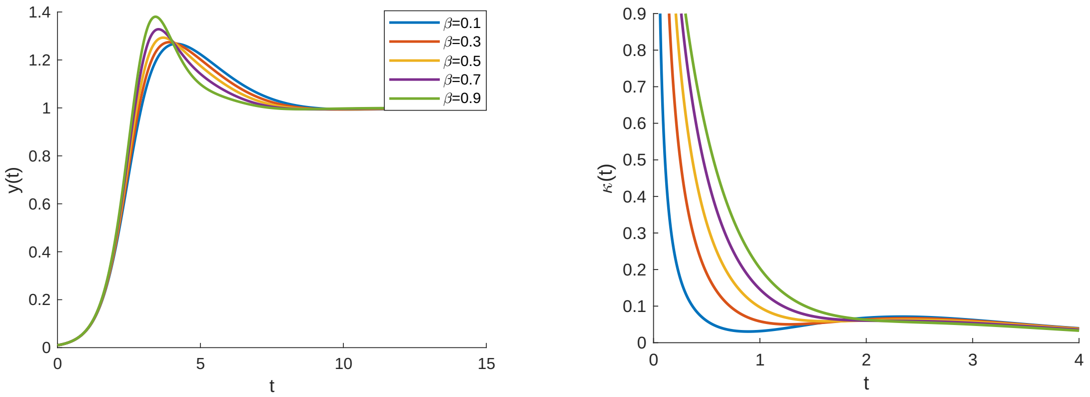

(a) Logistic responses.

(b) General kernels.

Figure C.21 – Logistic responses with kernels $Ct^{\beta-1}e^{-at}E_{\alpha,\beta}(-\lambda t^{\alpha})$, mean $\mu = 1$, $a = 2$ and $\alpha = 5.5$. The values of β and λ are varied to investigate their impact on the responses.

C.3.7 Oscillation quantitative analysis

The kernels shown in Figure 3.1 generate the logistic responses shown in Figure 3.1.A-B. Denoting the kernels as κ_i, where $i \in \{a, b, c, d, e, f\}$, Table C.1a indicates the maximum overshoot, while Table C.1b indicates the minimum after overshoot of each logistic response.

κ	**Maximum overshoot**
κ_a	Monotonic without overshoot
κ_b	(4.394, 2.927)
κ_c	(3.319, 1.942)
κ_d	(3.667, 3.010)
κ_e	(3.316, 2.174)
κ_f	(3.922, 1.324)

(a) Maximum overshoot (t, y)

κ	**Minimum after overshoot**
κ_a	Monotonic without overshoot
κ_b	(6.102, 0.066)
κ_c	(5.297, 0.580)
κ_d	(7.081, 0.882)
κ_e	(5.274, 0.388)
κ_f	(8.72, 0.989)

(b) Minimum after overshoot (t, y)

Table C.1 – Oscillations in logistic responses varying memory kernels.

C.4 ON THE FRACTIONAL-ORDER LOGISTIC EQUATIONS

The fractional-order logistic equation

$$^{C}D^{\alpha}y(t) = ry(t)(1 - y(t)) \tag{C.7}$$

is well studied in (161) and several related references, where $^{C}D^{\alpha}$ denotes the Caputo fractional derivative. Recent generalizations to other fractional derivatives can be found in (162, 163).

Although fractional logistic-type models have been successfully applied in practice, as shown in (164), establishing the biological meaning of dimensions and orders can be challenging. To the best of our knowledge, the fractional logistic equation (C.7) has a monotonic solution and does not exhibit oscillations. This suggests the presence of a different type of memory mechanism that is not yet fully understood, as delays typically lead to oscillations (16, 165).

An essential observation is that the monotonicity of solutions for (C.7) cannot be proven as easily as in the classical case, since the sign of the fractional derivative is not a sufficient condition to indicate growth or decrease of the function. Therefore, the rate interpretation is compromised. For example, in the SIR model without vital dynamics, replacing the integer derivative with Caputo fractional derivatives results in non-monotonic behavior for the susceptible and recovered compartments when $\alpha < 1$ (see Appendix B).

C.5 IMMEDIATE EXTENSIONS

C.5.1 Allee Effect

We may consider the possibility of an Allee effect in the logistic general system. In many ecological systems, there is a positive correlation between the growth rate and the population abundance at low densities, known as the Allee effect. This effect can be caused by several mechanisms such as mating limitation, cooperative defense, and predator satiety (166). The strong Allee effect considered here leads to an extinction threshold, where a species cannot survive at very low densities. While the simultaneous action of multiple mechanisms generating the Allee effect is possible (167), most cases focus on the Allee effect related to birth. The logistic or cubic model with the Allee effect is represented by:

$$y'(t) = ry(t)\left(\frac{y(t)}{A} - 1\right)(1 - y(t)), \tag{C.8}$$

where r and $A < 1$ are positive parameters, with A being the critical point below which the species faces extinction. The equilibria $y = 0$ and $y = 1$ are stable, while $y = A$ is unstable.

The approach presented in Chapter 3 can be extended to the cubic general fractional logistic model as shown in Eq. (C.9):

$$\begin{cases} y' = ry\left(\dfrac{y(t)}{A} - 1\right)(1 - Ce^{-at}D^{1-\beta}(e^{at}w)), \\ w' = y - \lambda e^{-at}D^{1-\alpha}(e^{at}w) - aw. \end{cases} \tag{C.9}$$

C.5.2 Kernels as the sum of the PDFs

Another extension can be constructed by defining the kernel as a weighted sum of the PDFs $f_1, \cdots, f_n$ given in Eq. (3.2), namely

$$f(t) = \sum_{i=1}^{n} \epsilon_i f_i; \qquad \sum_{i=1}^{n} \epsilon_i = 1. \tag{C.10}$$

In this case, the general model in Eq. (3.4) can be expressed as

$$\begin{cases} y' = ry\left(1 - \sum_{i=1}^{n} \epsilon_i C_i e^{-a_i t} D^{1-\beta_i}(e^{a_i t} w_i)\right), \\ w_i' = y - \lambda_i e^{-a_i t} D^{1-\alpha_i}(e^{a_i t} w_i) - a_i w_i, \text{for } i = 1, \cdots, n, \end{cases} \tag{C.11}$$

where w_i are auxiliary variables representing different memory terms.

This construction accommodates more complex memory kernels while preserving the structural properties of the model. Even in this general setting, $y^* = 1$ remains the unique nontrivial equilibrium. The cubic extension follows analogously.

D APPENDIX D – EADS EXAMPLES IN THE FRACTIONAL FHN MODEL

In this appendix, we present examples of the emergence of EADs for specific simplifications and combinations of the fractional FHN model. Upon solving system (5.31), a comparison between a classical and a modified AP is shown in Figure D.1A, while Figure D.1B compares the kernels. When $\beta < 1$, the memory kernel is singular, and over the interval of interest, the only significant difference between the kernels occurs at early times. This example illustrates that EADs can arise from minimal changes to an exponential memory kernel.

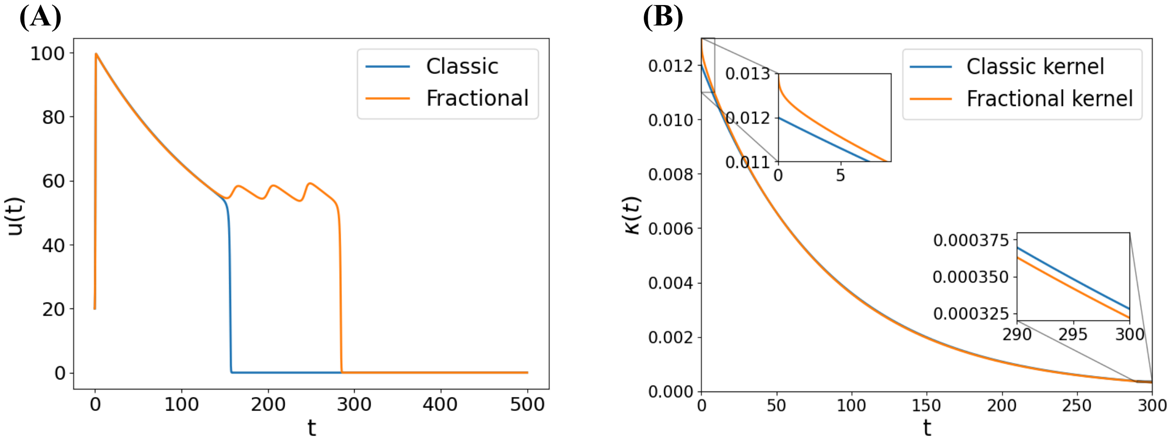

Figure D.1 – Solution of system (5.31) with a gamma memory kernel, for parameters $\alpha = 1$, $\beta = 0.99$, $a = \eta_2 \cdot \eta_3$, and $\lambda = 0$. **(A)** Comparison of a memoryless AP and an AP exhibiting EADs, showing similar initial repolarization. **(B)** Comparison of the exponential and gamma-distributed memory kernels given by $a^{\beta}t^{\beta-1}e^{-at}$. They intersect but remain very similar. The fractional memory kernel is singular when $\beta < 1$.

Figure D.2A shows the emergence of EADs in an example with $\alpha = 0.95$ and $\beta = 1$ (system (5.32) and (5.33)). Figure D.2B compares the kernels. When $\beta = 1$, the kernel is non-singular, although it is larger than the classical kernel at early times. Note that the fractional AP is faster during the initial repolarization. This is related to a larger numerical mean over the initial time interval. With a longer delay, the gating variable w reaches a higher voltage earlier and may be relatively larger than anticipated.

Several other combinations of parameters allow for different mixed-mode oscillations. In particular, Figure D.3 provides additional examples.

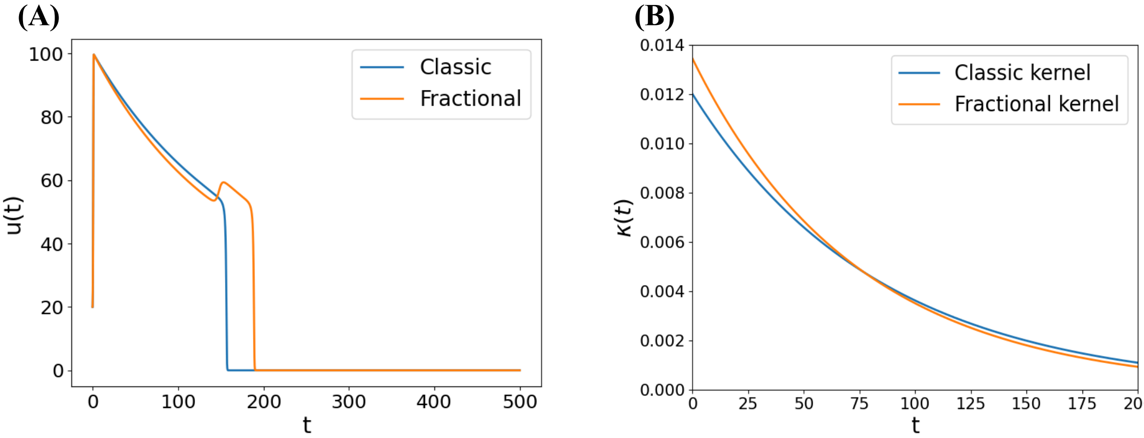

Figure D.2 – Solution of system (5.32)–(5.33) with parameters $\alpha = 0.95$, $\beta = 1$, $a = \eta_2 \cdot \eta_3$, $\lambda = 0.15 \cdot a$. **(A)** Comparison of a memoryless AP and an AP exhibiting EADs, showing faster initial repolarization in the fractional case. **(B)** Comparison of the exponential and fractional memory kernels given by $(a + a^{1-\alpha}\lambda)e^{-at}E_\alpha(-\lambda t^\alpha)$. The fractional memory kernel is non-singular when $\beta = 1$. Over the interval of interest, it initially lies above the exponential kernel, then crosses it and decays more rapidly.

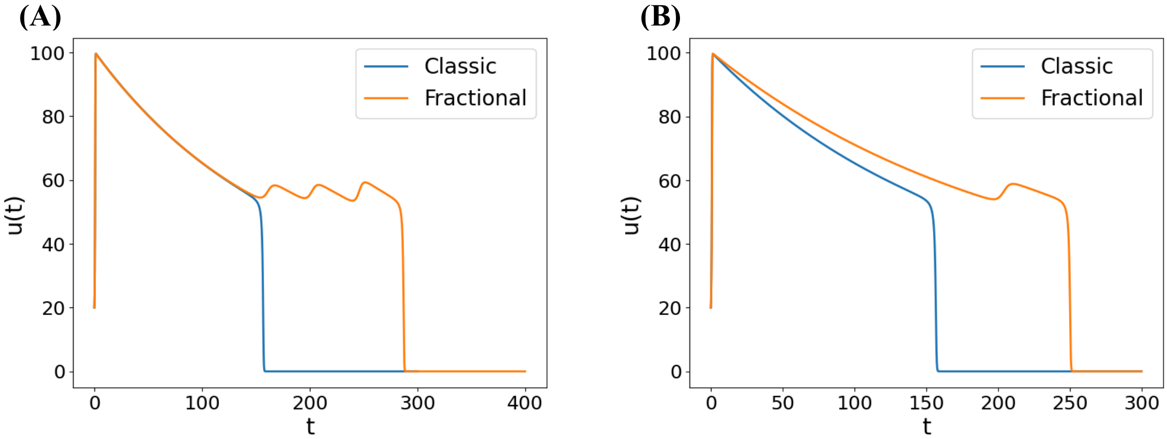

Figure D.3 – Comparison of a memoryless AP and an AP exhibiting EADs for the following parameters: **(A)** $\alpha = 0.99$, $\beta = 0.992$, $a = 0.01$, $\lambda = 0.002$. **(B)** $\alpha = 0.985$, $\beta = 0.995$, $a = 0.008$, $\lambda = 0.0015$.

E APPENDIX E – JUSTIFICATION OF THE ADAPTATIONS IN THE MS AND KARMA MODELS

In this appendix, we justify our adaptations of the MS and Karma models based on the stability observations discussed in Section **5.3.3**. Figure E.1 shows the phase portraits of the integer FHN, MS, and Karma models for parameter sets that induce EADs. The geometry of the phase portraits in Figure E.1B and C does not permit the existence of a spiral equilibrium. In these cases, there are two equilibria located on the line $w = 0$.

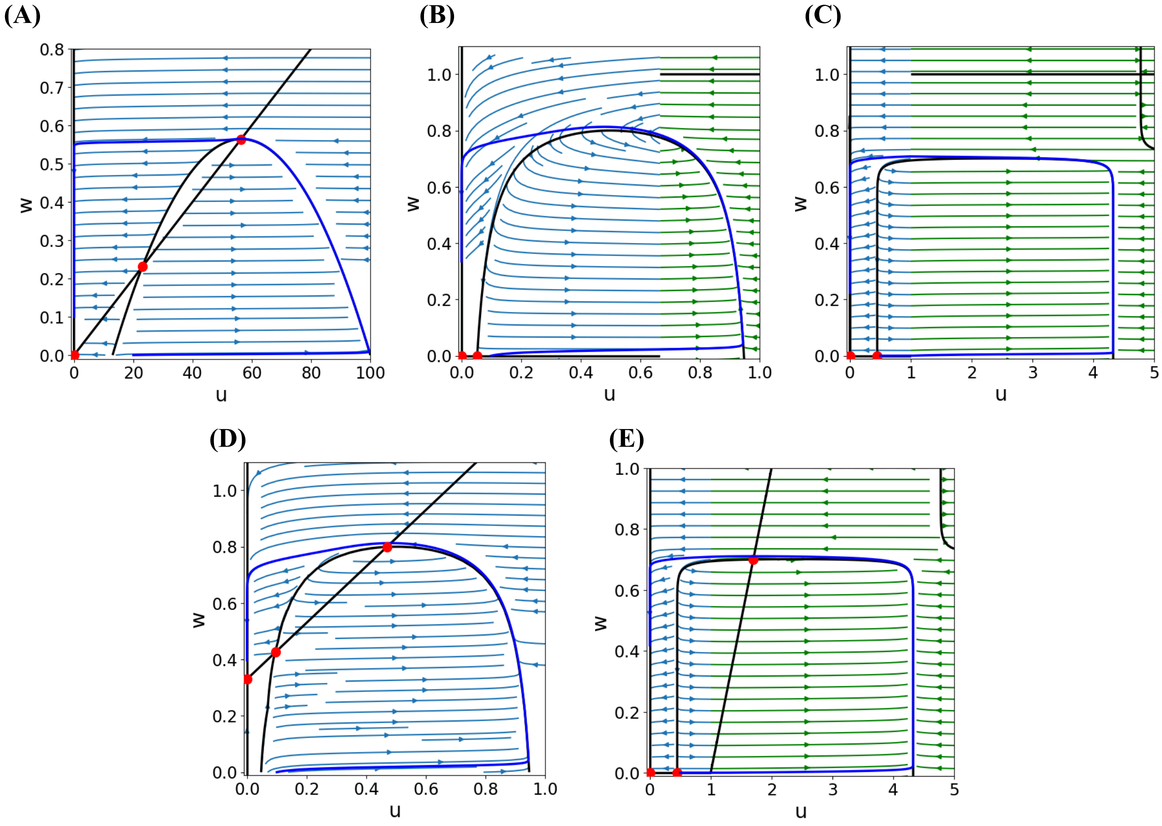

Figure E.1 – Phase portraits with vector fields. Nullclines are shown in black, model trajectories in blue, and equilibrium points as red dots. **(A)** Phase portrait of the integer-order FHN model defined by Eqs. (5.23) and (5.24), with parameters given in Eq. (5.29). **(B)** Phase portrait of the integer-order classical MS model defined by Eqs. (5.34) and (5.35), after the change of variable $w \to 1 - w$, with parameters given in Eq. (5.40). **(C)** Phase portrait of the integer-order classical Karma model defined by Eqs. (5.42)and (5.43), with parameters given in Eq. (5.46). **(D)** Phase portrait of the integer-order linear MS model defined by Eqs. (5.36) and (5.37). **(E)** Phase portrait of the integer-order linear Karma model defined by Eqs. (5.44) and (5.45). Note that the curved nullclines are nontrivial due to the term w^{xm} in the first equation. Additional equilibria may exist outside the range considered here.

The adaptations of the MS and Karma models were designed to reproduce the geometric features of the phase portrait in Figure E.1A. In particular, this configuration exhibits three equilibria, two of which arise from the intersection of a linear and a parabolic nullclines. Numerical simulations indicate that the third equilibrium in Figures E.1D and

E is an unstable spiral. Overall, the geometry resembles that of the FHN model, with three equilibria, two of which lie on the curved nullcline. These geometric insights motivate a modification of the third equation of the Bueno-Orovio Minimal Model to enable the reproduction of EADs, as discussed in Section 7.1.